Computational Modelling of Small-Scale River Morphodynamics

Computational Modelling of Small-Scale River Morphodynamics

Proefschrift

ter verkrijging van de graad van doctor
aan de Technische Universiteit Delft,
op gezag van de Rector Magnificus prof.ir. K.C.A.M. Luyben,
voorzitter van het College voor Promoties,
in het openbaar te verdedigen

op maandag 4 juni 2012 om 10.00 uur

door

Mohamed NABI
werktuigbouwkundig ingenieur
geboren te Najaf, Irak

Dit manuscript is goedgekeurd door de promotor:
Prof.dr.ir H.J. de Vriend

Copromotor:
dr.ir. E. Mosselman

Samenstelling promotiecommissie:

Rector Magnificus	voorzitter
Prof.dr.ir. H.J. de Vriend	Technische Universiteit Delft, promotor
Dr.ir. E. Mosselman	Technische Universiteit Delft, copromotor
Prof.dr. Y. Shimizu	Hokkaido University
Dr. J.M. Nelson	USGS
Prof.dr.ir. L. van Rijn	Deltares
Prof.dr. S.J.M.H. Hulscher	Universiteit Twente
Prof.dr.ir. G.S. Stelling	Technische Universiteit Delft
Prof.dr.ir. C. Vuik	Technische Universiteit Delft, reservelid

The project has been funded by Delft Cluster within the work package "River Morphology" project 4.30 "Safety against flooding", with a subsidy from Rijkswaterstaat Waterdienst.

Keywords: River morphodynamics, sediment transport, Hysteresis, Hydrograph, Large Eddy simulation, turbulent flow, Multigrid, Unstructured Cartesian grid, Immersed boundaris.

ISBN 978-9-461-91299-2

Typeset by LaTeX
Printed by Ipskamp Drukkers B.V., the Netherlands.

Preface

The present thesis reports on results of a PhD research project on computational modelling of subaqueous dunes in rivers. This research was carried out in the Section of Hydraulic Engineering at Delft University of Technology and focused on detailed numerical simulation of bed morphodynamics under turbulent flow by means of Large Eddy Simulation (LES).

The project was part of the work package "River Morphology" of Delft Cluster project 4.30 "Safety against flooding", financed by the Netherlands government and supported by Rijkswaterstaat Waterdienst, and it was embedded in a joint research programme including experimental research, numerical research, and field measurement. The main aim of this research was the prediction of flood water levels and the impact assessment of measures to increase the safety from flooding.

This thesis consists of two main parts: one describing the numerical methodology for hydrodynamics, sediment transport and morphodynamics, and the other one presenting and validating results for flow, sediment and morphology in open-channel flows. Hereby, this thesis provides a broad image of small-scale morphodynamics in open-channel flows in general, enhancing the insight in river-bed morphodynamics and facilitating further development of parameterized relations for practical engineering.

Mohamed Nabi
June 2012

Summary

Alluvial open channel beds often exhibit statistically periodic irregularities, known as dunes. Dunes have considerable effects on sediment transport and flow resistance. When growing during a flood, the dunes create more resistance and flood levels may rise significantly. Accurate prediction of dune properties therefore contributes to effective flood risk management.

Recently, significant progress has been made in understanding bedform dynamics, thanks to significant advances in monitoring flow and bedform morphology in laboratory and field, as well as in their numerical modelling. Nowadays, numerical modelling captures not only the characteristics of the mean flow field, but also those of turbulence, including coherent flow structures above non-flat beds. These advances enable radical progress in modelling and understanding the behaviour of alluvial bedforms.

Sediment motion can nowadays be measured and simulated in detail. The effect of turbulent flow on sediment particles can be understood in a more physics-based way. Sediment transport can be linked to bed topography and the bed deformations can be studied by considering the motion of sediment particles in the flow. This gives insight into the evolution and migration of ripples and dunes under turbulent flow and the effects they have on floods.

Generation and migration of dunes are determined by sediment transport, which in its turn is influenced by the turbulence structures above and behind the dunes. This kind of physical phenomena involves a wide range of time scales. Often, the measurements cannot capture the smallest time scales, whence many experimental studies consider only statistical properties under homogenous steady-state conditions. Consequently, models based on such measurements can only be empirical. They usually fall short in computing the physical nature of the phenomena in unsteady flows. Therefore, a rigorous physics-based numerical model is needed.

This study concentrates on detailed simulations of flow, sediment transport and bedform morphodynamics. Based on these simulations the governing physics behind these phenomena are studied. This is achieved by developing a detailed three-dimensional numerical model for hydrodynamics, sediment transport and morphodynamics. The model simulates the time- dependent water flow by Large Eddy Simulation (LES) on a locally refined Cartesian grid. The sediment is con-

sidered as rigid spherical particles moving in the water under gravity and flow-induced forces. The change of bed (morphodynamics) is the net result of pick-up and deposition of sediment on each portion of the bed. The model is validated against theoretical and experimental results of previous studies published in the literature.

The resulting model is complex and time-consuming, especially in time-varying flow conditions, such as a flood wave. Therefore, the insights and data obtained with it were used to develop parametric models that can be used operationally at larger spatial and temporal scales.

In a number of three-dimensional simulations over two-dimensional bedforms the form drag resulting from the bedforms is compared with existing theoretical, empirical and semi-empirical formulae. It is found that the numerical results agree very well with these formulae. Bedforms in nature, however, are usually three-dimensional. When comparing simulated flows over three-dimensional dunes and with the two-dimensional case, the form drag on three-dimensional dunes turns out to be very different. Based on this finding, the form drag is parameterized for two- and three-dimensional dunes. Furthermore, the generation and migration of dunes under steady flow conditions is studied, and the results are compared with former experimental studies. This comparison shows a very good agreement between the numerical and experimental findings.

Dune evolution during floods often shows a hysteresis, with different dune heights at the same discharge during the rising and falling stage of the flood wave. As flow resistance in the main channel of a river is mainly controlled by dune dimensions, the hysteresis in dune height is reflected in the time-evolution of the flow resistance during floods, thus yielding a dynamic roughness. Limited knowledge on this phenomenon, combined with computational limitations, usually keep dynamic roughness behaviour from being included in flood simulation models. To understand the physics behind this hysteresis effect, channels with different discharges and different grain sizes are simulated. It is shown that the hysteresis in the form drag is a function of both variables. Extension of the simulations to the upper flat bed regime shows that the model captures most of the physical phenomena in this regime and yields a flat bed as observed in experiments and in the field.

Samenvatting

De bedding van alluviale rivieren vertoont vaak statistisch periodieke oneffenheden, bekend als beddingvormen (ribbels als ze klein zijn, duinen als ze groter zijn). Met name duinen hebben aanzienlijke invloed op het sedimenttransport en de weerstand die de stroming ondervindt. Al groeiend tijdens een hoogwater veroorzaken ze steeds meer weerstand en kunnen ze leiden tot aanzienlijk hogere waterstanden. Nauwkeurige voorspelling van de eigenschappen van duinen draagt daarom bij tot effectieve beheersing van overstromingsrisico's.

De laatste tijd is aanmerkelijke vooruitgang geboekt in het begrijpen van de dynamica van beddingvormen, dankzij belangrijke stappen voorwaarts, zowel in het waarnemen van water- en sedimentbeweging en morfologische verschijnselen in het laboratorium en het veld als in de numerieke modellering van deze verschijnzelen. De huidige numerieke modellen beschrijven niet alleen de eigenschappen van de gemiddelde stroming, maar ook die van de turbulentie, inclusief coherente structuren boven een niet-vlakke bedding. Dit maakt het mogelijk grote vooruitgang te boeken in de modellering van en het inzicht in het gedrag van alluviale beddingvormen.

Sedimentbeweging kan tegenwoordig in detail gemeten en berekend worden. Het effect van turbulente stroming op sedimentkorrels wordt fysisch doorgrond. Sedimenttransport wordt gekoppeld aan bodemligging en veranderingen daarin volgen uit het gedrag van de bewegende korrels. Dit geeft inzicht in de vorming en verplaatsing van ribbels en duinen in turbulente stroming en in de effecten daarvan op hoogwaters.

De vorming en verplaatsing van beddingvormen worden bepaald door het transport van sediment en dat wordt op zijn beurt benvloed door de turbulentiestructuren boven en achter de beddingvormen. Dit soort verschijnselen beslaat een breed scala van ruimte- en tijdschalen. De kleinste daarvan worden meestal niet zichtbaar in metingen, reden waarom veel experimenteel onderzoek alleen kijkt naar de statistische eigenschappen onder homogene, stationaire condities. Daardoor kunnen modellen die gebaseerd zijn op dit type onderzoek ook slechts empirisch van aard zijn. Zulke modellen schieten tekort in de beschrijving van de fysica, met name in tijdsafhankelijke situaties. Daarom is er behoefte aan een rigoureus op fysische basiswetten gebaseerd numeriek model.

Dit onderzoek concentreert zich op de gedetailleerde simulatie van turbulente

stroming, sedimenttransport en morfodynamiek van beddingvormen. Met behulp van deze simulaties wordt de fysica die aan deze verschijnselen ten grondslag ligt bestudeerd. Daartoe is een gedetaileerd drie-dimensionaal numeriek model ontwikkeld dat tijdsafhankelijke turbulente stroming beschrijft via Large Eddy Simulation (LES) op een lokaal verfijnd Cartesiaans rekenrooster. Het sediment wordt gemodelleerd als starre, bolvormige deeltjes die door het water bewegen onder invloed van zwaartekracht en door de stroming uitgeoefende krachten. De bodemliggingsverandering (morfodynamiek) is het netto resultaat van het oppikken en afzetten van sediment op het desbetreffende deel van de bodem. Het model is gevalideerd met behulp van theoretische en experimentele resultaten van eerder gepubliceerd onderzoek.

Het resulterende model is complex en rekenintensief, vooral onder in de tijd varirende condities, zoals bij een hoogwatergolf. Daarom zijn de inzichten en de gegevens die met dit model zijn verkregen vertaald in parametrische modellen voor operationaal gebruik op grotere ruimte- en tijdschalen.

In een aantal driedimensionale simulaties over tweedimensionale duinen is de vormweerstand die door de beddingvormen teweeg wordt gebracht vergeleken met bestaande theoretische, empirische en semi-empirische formules. Het is vastgesteld dat de numerieke resultaten goed overeen komen met deze formules. Beddingvormen in de natuur zijn echter meestal driedimensionaal. Vergelijking van berekende stromingen over twee- en driedimensionale duinpatronen leert, dat de vormweerstand bij driedimensionale duinpatronen sterk afwijkt van die bij tweedimensionale. Op grond hiervan is de vormweerstand geparametriseerd voor twee- en driedimensionale duinen. Daarnaast zijn de vorming en verplaatsing van duinen onder stationaire stromingscondities onderzocht en zijn de resultaten vergeleken met die van eerder experimenteel onderzoek. Deze vergelijking toont een zeer goede overeenkomst tussen de numerieke en experimentele bevindingen.

Duingroei tijdens hoogwater vertoont vaak een hysterese-effect, met een verschil in duinhoogte bij dezelfde afvoer bij was en bij val van het hoogwater. Aangezien de stromingsweerstand in de hoofdgeul van een rivier in hoge mate wordt bepaald door de afmetingen van de duinen, komt dit hysterese-effect terug in het verloop van de weerstand tijdens de hoogwatergolf (dynamische ruwheid). Beperkte kennis van dit verschijnsel en beperkte rekencapaciteit leiden er vaak toe, dat deze dynamische ruwheid niet wordt meegenomen in hoogwaterberekeningen. Om inzicht te krijgen in de fysica die aan dit hysterese-effect ten grondslag ligt, zijn simulaties met verschillende afvoeren en verschillende korrelgrootten uitgevoerd. Daaruit blijkt, dat het effect afhankelijk is van beide gevarieerde grootheden. Uitbreiding van de simulaties naar het upper flat-bed regime laat zien, dat het model de relevante fysische verschijnselen grotendeels weergeeft en, net als waargenomen in experimenten en in het veld, uiteindelijk een vlak bed geeft.

Contents

Chapter 1

Introduction

1.1 Background

The water levels during river floods, and hence the risk of flooding, depend on the hydraulic roughness of the river. One of the components of this roughness is produced by statistically periodic irregularities on the river bed called "bedforms": ripples if they are small, dunes if they are larger. The development of dunes and the associated hydraulic roughness during a flood is complex. Initially dunes grow higher and make the river bed rougher, but in later stages the dunes grow longer and make the bed smoother. Then, new bedforms may develop on top of the elongated dunes that increase the roughness again.

Bedforms are the result of sediment pick-up and deposition. The sediment transport over bedforms in open-channel flow is strongly affected by the complex turbulence structures caused by flow separation at the dune crest. The three-dimensionality of turbulence and the effect of turbulence on the sediment transport and morphological process form a complex problem which remains to be completely solved. At present, there is still limited and mostly empirical knowledge about the effect of dunes on the hydraulic roughness of rivers. Several researchers proposed methods to predict the dune dimensions based on parametric methods (Yalin, 1992; Raudkivi, 1997), empirical relations (Julien and Klaassen, 1995; Van Rijn, 1984c), and theoretical interpretations (Onda and Hosoda, 2004). Existing experimental studies are limited to the formation of dunes in steady-state flow regimes (Allen, 1965; Blom et al., 2003; Klaassen, 1990). Wilbers (2004) has shown for several floods in the River Rhine in the Netherlands that none of these predictors is able to correctly predict the dune dimensions, let alone their time-evolution. He developed an empirical method to predict dune development for unsteady flows. This method was applied successfully to three sections of the River Rhine branches, but it cannot be generalized. The method gives limited insight into the physical mechanisms underlying dune development during floods.

Existing numerical studies on the morphology of bedforms are limited to the

Figure 1.1: Flume experiment for dunes at Delft Hydraulics (Blom et al., 2003)

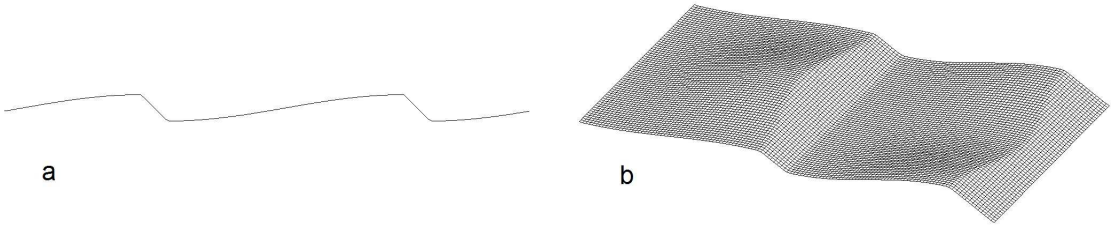

Figure 1.2: Schematic configurations of (a) two-dimensional and (b) three-dimensional dunes. The three dimensional dunes consist of alternatingly convex and concave parts.

approximation of two-dimensional fluid flow in the vertical plane, with two-dimensional dunes development (Giri and Shimizu, 2006; Niemann et al., 2011) or with fixed bed (Yoon and Patel, 1996; Zedler and Street, 2001; Shimizu et al., 2001; Yue et al., 2006; Grigoriadis et al., 2009). The nature of flow over three-dimensional dunes is very different from that over two-dimensional ones, to the degree that the real-life application of some results from two-dimensional studies requires careful attention (Best, 2005). Field observations suggest an urgent requirement for a fuller analysis of dune three-dimensionality, both in laboratory experiments and in numerical models.

Figure (1.1) shows a flume experiment at Delft Hydraulics (Blom et al., 2003). Considering the centre-line of the flume gives a two-dimensional form of the dunes as shown in Figure (1.2a). The real shape of dunes, however, is not as two-dimensional as shown in that figure. Figure (1.2b) shows the three-dimensional

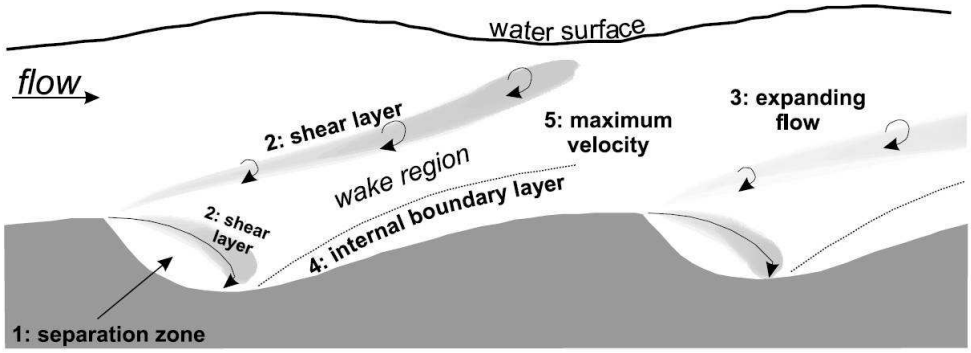

Figure 1.3: Schematic diagram of the principal regions of flow over dunes (Best, 2005)

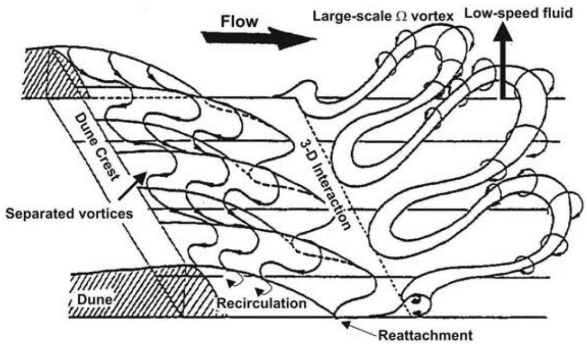

Figure 1.4: Models of vortex topology associated with dunes proposed by Nezu and Nakagawa (1993)

topography of a typical dune. The dunes in this particular case consist of two parts, a two-dimensional base form with a three-dimensional form on top of it. The second part is alternatingly concave and convex (Best, 2005). This difference between two- and three-dimensional dune topography is so large that they are hard to compare.

Figure (1.3) shows a schematic diagram of the principal regions of flow over dunes. Five such regions can be distinguished, namely (1) separation zone, (2) shear layer, (3) expanding flow, (4) internal boundary layer and (5) maximum velocity region (Best, 2005). Figure (1.4) shows the vortex topology associated with dunes proposed by Nezu and Nakagawa (1993). Coherent structures of turbulence such as horseshoe structures have a large influence on sediment entrainment, and hence on the deformation of dunes (Yalin, 1992). As can be seen from these figures, the structure of turbulence on and behind the dunes is so complicated, that it cannot be described by simple models.

1.2 State of the art

Dunes are among the most common alluvial bedforms and their occurrence and morphology have received considerable attention over the past three decades (Dinehart, 1989; Gabel, 1993; Dalrymple and Rhodes, 1995; Roden, 1998; Carling, 1999; Carling et al., 2000a,b; Ten Brinke et al., 1999; Wewetzer and Duck, 1999; Wilbers, 2004).

Best (2005) presents a comprehensive review of past investigations on river dunes. Most of these investigations analyze flow and turbulence structures over bed forms in laboratory experiments (Benjamin, 1959; Nelson et al., 1993; Best et al., 1997; Schmeeckle et al., 1999; Blom et al., 2003; Schindler and Robert, 2005; Fernandez et al., 2006). These studies have corroborated the significance of fluid dynamics for bed forms through the strong coupling between the bed morphology and the flow field.

A variety of approaches has been developed in order to analyze bed-form-induced morphology in alluvial channels and the development of dunes (Kennedy, 1963; Engelund, 1970; Engelund and Fredsøe, 1982; Coleman and Melville, 1994, 1996; Fredsøe, 1974, 1996; Lisle et al., 1997; Baas, 1999; Smith, 1970; Kobayashi and Madsen, 1985; McLean and Smith, 1986; Nelson and Smith, 1989). Most of them are based on linear stability theory, but some used weakly nonlinear stability analysis (Ji and Mendoza, 1997; Yamaguchi and Izumi, 2005). Notable examples of field observations are those by Itakura et al. (1986), Kishi and Kuroki (1972), Dinehart (1989) and Carling et al. (2000a,b). All these studies revealed the influence of temporal variability on bed form development.

The recent development of high-performance computers and the associated reduction in computational time has made the application of high-resolution numerical models feasible, particularly for modelling flow and turbulence characteristics over bed forms. Shimizu et al. (2001) , for instance, developed computational codes for a three-dimensional direct numerical simulation of flow and turbulence over two-dimensional fixed dunes. The numerical model was able to reproduce coherent structures induced by separation at the dune crest. Numerical computations carried out by Richards and Taylor (1981), Mendoza-Cabrales (1987), Zijlema et al. (1995), Yoon and Patel (1996), Barr et al. (2004), Yue et al. (2005), Yue et al. (2006), Stoesser et al. (2008) and Grigoriadis et al. (2009) also yielded realistic descriptions of flow field and turbulence over bed forms. However, these numerical studies do not include bed form dynamics, rather treated the bedforms as part of a rigid (inerodible) bed.

Morphodynamic numerical models are being increasingly employed in river engineering research studies (Jang and Shimizu, 2005; Olsen, 2003; Shimizu, 2002; Darby et al., 2002; Shimizu and Itakura, 1989; Giri and Shimizu, 2006; Giri et al., 2007; Shimizu et al., 2009; Niemann et al., 2011). Despite the considerable amount of work in this area, rather slow progress has been made regarding the numerical computation of bed form dynamics. Nakayama and Shimizu (2001) carried

out a numerical study on suspended sediment transport over bed forms. The computed time-averaged suspended sediment concentration was found to be in good agreement with the Rouse vertical distribution curve, as well as with laboratory measurements. Tjerry and Fredsøe (2005) conducted a numerical study on dune morphology as a continuation of previous investigations by Fredsøe (1982) and Fredsøe and Tjerry (2001). This study is basically focused on the shape and dimensions of fully developed sand dunes as well as their relationship with the bed shear stress distribution and sediment transport mechanism. In their work, a hydrodynamic model with a conventional $k - \varepsilon$ turbulence closure was used. The flow model was coupled with sediment transport descriptions based on the Meyer-Peter-Müller equation. In addition, they implemented the Reynolds stress model (RSM) to simulate a flow experiment with a backward facing step. They found that the so-called "local maximum" in the bed shear stress in the wake region could be better reproduced using RSM rather than $k - \varepsilon$ closure.

Most existing morphological models have been developed using empirical or semi-empirical relationships for sediment transport rate and dispersion of suspended sediment that are essentially based on temporally or spatially averaged boundary shear stress. Some researchers (Schmeeckle and Nelson, 2003) pointed out the incompatibility of these relationships with the actual sediment transport phenomena, particularly in the high-turbulence zone near the bed. Nonetheless, these approaches still remain pertinent for practical applications based on bulk sediment fluxes.

Onda and Hosoda (2004) attempted to simulate bedform development numerically. They proposed a depth-averaged flow model considering vertical acceleration with a description of the bottom shear stress based on a potential flow approximation. In order to compute the water surface profile over dunes, a numerical technique proposed earlier by Hosoda and Tada (1994) was used. Using this model, flow resistance cannot be reproduced, due to the hydrostatic pressure assumption in cases where the spatial depth gradient is greater than a standard (small) value, like at the lee side of a dune. They attempted to eliminate this deficiency by introducing a reduction factor to treat vertical acceleration terms in case of high depth gradients. They used the sediment pickup and deposition functions proposed by Nakagawa and Tsujimoto (1980) to simulate sand dune formation. However, this approach does not reproduce flow separation behind the dune crest and, thereby, its effects on the flow field and the sediment transport. Jerolmack and Mohrig (2005) proposed a nonlinear stochastic surface evolution model to simulate bed form growth. In this model, the temporal variation of the bed shear stress was treated as a stochastic variable and its morphodynamic importance was explored by adding a noise term. The authors succeeded in simulating the qualitative features of bed form evolution. However, their proposed model does not consider fluid dynamics of bed forms and is therefore physically incomplete. Giri and Shimizu (2006) have developed a vertical two-dimensional RANS model with an enhanced $k - \varepsilon$ turbulence closure

with nonlinear terms. Their model includes a free surface and they were able to obtain migrating dune-shape bed forms even at relatively high Froude numbers. However, the sediment transport is divided into a pickup and a deposition description, and the latter works by distributing the deposition of sediment over a certain region, thereby obtaining an artificial filtering effect. The step length of the sediment motion is parameterized as a function of sediment size, and the effect of the shear stress on the step length is ignored. In their later work (Shimizu et al., 2009) the step length is considered as a function of the local bed shear stress, but no proper parameterizations were used. Dune length and height are strongly related to the parameterization factor, which is still unknown.

Recently, Niemann et al. (2011) have continued the work proposed by Fredsøe and Tjerry (2001), but implemented a $k-\omega$ closure. They have shown that $k-\omega$ closure yields better results than standard $k-\varepsilon$ for turbulence in recirculation zones. This model estimates the sediment transport based on time-averaged bed shear stress (Meyer-Peter-Müller equation) in which the time varying characteristics are filtered. Moreover, to avoid numerical instabilities, an artificial filter on the bed form was applied, which influences the results. Consequently, a reliable and more complete approach for bed form morphodynamic modelling is needed to advance our understanding of bed-form-induced flow, sediment transport and bed evolution mechanisms in alluvial streams.

According to the author's knowledge, there is still no complete three-dimensional model for simulation of morphodynamical behaviour of river-bed. More sophisticated physics-based approaches are needed to overcome the shortcomings of the existing models.

1.3 Objective

The objective of the present study is to understand and predict the physical mechanisms underlying the generation and behaviour of dunes, and to derive parameterized formulations for their statistically steady and unsteady morphodynamical behaviour. This is achieved by developing a detailed three-dimensional numerical model for simulating the development and migration of dunes in open channels. The numerical model consists of three components: (1) a detailed eddy-resolving hydrodynamic model, (2) a physics-based sediment transport model based on individual grain motion, and (3) a sediment balance module yielding the bed deformation (morphodynamics). The model aims at giving better insight into the development of the hydraulic roughness, and hence the water levels, during river floods. The insights thus obtained will allow the development of parameterized models for larger spatial and temporal scales that can be used in operational models for flood early warning systems and the determination of design water levels.

1.4 Research questions

In accordance with the objective stated above, the following research questions have been formulated:

Q1: What kind of solver is suitable for the simulation of detailed hydrodynamics on time scales typical of the growth and decay of dunes?

Q2: What physics-based model can describe the motion of sediment with sufficient accuracy?

Q3: How to model the river bed morphology?

Q4: What is the relation between sediment size, variable discharge and bed morphology?

Q5: How to derive parameterized relations from the simulated phenomena?

1.5 Methodology and thesis outline

Chapter 2: An efficient eddy-resolving hydrodynamic model is a key ingredient for the simulation of detailed hydrodynamics on time scales for growth and decay of dunes. This chapter focuses on the implementation of an accurate and cost-efficient hydrodynamic model for problems with moving boundaries and, more specifically, evolving bedforms in rivers (**Q1**). The hydrodynamic model is validated against theoretical, numerical and experimental results from literature.

Chapter 3: This chapter focuses on the subaqueous behaviour of sediment in the presence of ripples and dunes. Four different modes of sediment movement are discussed, namely pick-up, transport, deposition and sliding. The sediment models are validated against theoretical investigations and are found to be in good agreement with published results (**Q2**).

Chapter 4: The deformation of the bed is discussed in this chapter. Sediment pick-up and deposition are considered as sink and source terms for the deformation of the bed (**Q3**). The simulated results are compared with experimental results and a good agreement is found between them.

Chapter 5: In this chapter, results for different configurations of two- and three-dimensional bedforms are discussed and parameterized relations are derived (**Q4**-**Q5**). The parameterized relations are compared with past theoretical and experimental investigations.

Chapter 6: In this chapter, the bedforms for different configurations are simulated and the results are compared with the measurements. Moreover, the effect of sediment size on the bedform topography is studied (**Q4**).

Chapter 7: In this chapter, results for different combinations of sediment sizes and discharge hydrographs are discussed, the variation of the drag force under discharge hydrographs is investigated (**Q4**), and some phenomena such as flatbed regime under variable discharge are simulated. The results are compared with existing empirical diagrams.

Chapter 8: Finally, the answers to the research questions (**Q1**-**Q5**) are summarized, supplemented with recommendations for practical application and further research.

Chapter 2

Hydrodynamic model

2.1 Introduction

The ability to handle problems with complex geometries is one of the main issues in computational fluid dynamics. There are two techniques to deal with this kind of problems: unstructured and structured grid methods. The former method builds an unstructured grid which usually fits the boundary geometry. The boundaries can be applied directly and accurately and it does not need any forcing approach. This method has the benefit of handling complex geometries in an easy way. This technique is suitable for fixed boundaries, whereas in moving boundary problems, the grid has to be rebuilt after each time step. Therefore, unstructured grid methods can be expensive for problems with moving boundaries.

The structured grid method can fit complex geometries (boundary fitted methods) or use fixed Cartesian grids in a fixed frame. The main advantage of boundary-fitted grids is that imposition of boundary conditions is greatly simplified. However, the physical domain must be mapped onto a computational domain and the grid must be regenerated after each deformation of the boundaries. Therefore this method requires much computational effort. Furthermore, generation of a suitable grid for complex geometries can be troublesome and sometimes cannot be applied without multi-block techniques. All of these issues lead to complexity and possibly instability in the computational system.

Methods based on Cartesian grids received special attention in the last decade because it can handle complex geometries quite easily using a simple structure of Cartesian grids. Here the grid is fixed and it does not coincide with the body surface. The boundaries cannot be applied directly and explicitly as in boundary-fitted grids. There are two remedies for this kind of problems: using cut-cell techniques or using ghost-cell immersed boundary methods. In the former approach, the cells which intersect the boundaries are cut. This approach has been used for inviscid (Bayyuk, 1996; Quirk, 1994) and viscous flow computations including fixed and moving boundaries (Mittal et al., 2008; Udaykumar et al., 2001; Ye et al.,

1999; Kirkpatrick et al., 2003). This approach imposes the boundaries accurately, but its drawback lies in the wide variety of ways in which the cells can be cut by the boundaries. It causes difficulties in programming and also decreases the computational efficiency. In the ghost-cell immersed boundary techniques, the flow at the boundary is forced, using simple interpolation, which does not increase the computation time significantly. This method has been applied for viscous flows with fixed (Gilmanov et al., 2003; Tseng and Ferziger, 2003; Balaras, 2004) and moving boundaries (Fadlun et al., 2000; Yang and Balaras, 2006). These examples show that the ghost-cell immersed boundary method can be applied successfully for problems with very complex geometries.

Structured Cartesian grids are still expensive for simulation of phenomena at large large time and space scales, because the entire domain must be structurally divided, whereas in most cases this is not necessary. The regions with high gradients usually form a small fraction of the domain. A locally refined Cartesian grid is therefore preferable, with the grid locally refined in regions with high gradients. This method has been successfully applied for inviscid (Aftosmis et al., 1998; Clarke et al., 1986; Zeeuw and Powell, 1993; Waymel et al., 2006) and viscous flows (Martin et al., 2008; Iaccarino and Verzicco, 2003). Aftosmis et al. (1998) consider the grid as fully unstructured and discretise the equations on a single grid, whereas Ham et al. (2002) treat the grid as multi-level grid and use a hierarchical tree data structure. In a multi-level grid, each higher-level grid covers a sub-domain of the coarser grid. Some authors have suggested (Coirier and Powell, 1996) or demonstrated (Berger et al., 2000; Ham et al., 2002) that the grid hierarchical tree structure is amenable to multigrid methods. However, the multigrid methods are more efficient than the Krylov space methods for large matrices (Saad, 2003).

In this study, we solve the flow on a Cartesian grid with local refinementing. The grid can be refined in high-gradient regions such as regions with no-slip boundary conditions. The no-slip condition on the immersed body surface is satisfied by providing momentum forcing inside the body; hence a ghost-cell immersed boundary method is applied. The current method shares some features with the methods of Balaras (2004), particularly in terms of the identification and interpolation of the immersed boundary.

The current chapter focuses on describing the numerical methods for the hydrodynamic part of the solver, validating the accuracy of the applied approach and demonstrating the capabilities of the solver in some complex configurations.

2.2 The governing equations

Starting point for the analysis of the flow are the conservation equations for mass, momentum and energy completed with auxiliary relations to close the system. For the general form of these equations we refer to Batchelor (2000). The general

form of the mass and momentum conservation equations is as follows.

$$\frac{\partial \rho}{\partial t} + \frac{\partial \rho u_j}{\partial x_j} = 0 \tag{2.1}$$

$$\frac{\partial \rho u_i}{\partial t} + \frac{\partial \rho u_i u_j}{\partial x_j} = -\frac{\partial p}{\partial x_i} + \frac{\partial}{\partial x_j} e_{ij} + \rho f_i \tag{2.2}$$

where x_i's are the coordinates, t the time, p is the pressure, ρ the density, u_i the velocity component in x_i-direction, f_i the volume force in x_i-direction and e_{ij} the viscous stress tensor.

We assume isothermal flow; therefore the equation for the conservation of energy is not needed. We can also use the incompressible form of Navier-Stokes equations because the compressibility of water is negligible. Such flow is governed by a set of conservation equations of mass and momentum as follows.

$$\frac{\partial u_j}{\partial x_j} = 0 \tag{2.3}$$

$$\frac{\partial u_i}{\partial t} + \frac{\partial u_i u_j}{\partial x_j} = -\frac{1}{\rho}\frac{\partial p}{\partial x_i} + \frac{1}{\rho}\frac{\partial}{\partial x_j} e_{ij} + f_i \tag{2.4}$$

For an incompressible Newtonian fluid the viscous stress tensor is given by

$$e_{ij} = \mu \left(\frac{\partial u_i}{\partial x_j} + \frac{\partial u_j}{\partial x_i} - \frac{2}{3}\delta_{ij}\frac{\partial u_k}{\partial x_k} \right) \tag{2.5}$$

where μ is the dynamic viscosity and δ is Kronecker-delta. The dynamic viscosity μ is constant because the flow is isothermal. The density ρ is also constant because of the incompressibility of the fluid. Usually μ is combined with ρ to form the kinematic viscosity ν. Equations (2.3) and (2.4) all together are called the Navier-Stokes equations for an incompressible, isothermal flow.

2.3 Discretization

2.3.1 Spatial discretization

The derivatives of diffusion and advection terms of momentum equations are discretized using a second-order finite-volume method. All derivatives for advection terms are discretized by central differencing. The pressure and velocities are discretized on a staggered grid to avoid checkerboard-type oscillations. It means, the pressure is located in the centre and the velocities are located on the faces of the cells.

2.3.2 Temporal discretization

The time integration of Equation (2.4) can be obtained in two different ways, namely explicit or implicit. Implicit and explicit forms of time integration both have their advantages and drawbacks. The explicit methods are cheap per time step, and easy to program. However, the explicit methods are restricted to small CFL numbers. It makes the simulation of problems for large periods impractical.

In order to remove the CFL restrictions, implicit methods can be a good choice. Fully implicit time integrations are unconditionally stable, but they require more calculations per time iteration. In each time step, they form a matrix, which must be solved iteratively. In the presence of advection terms (non-linear terms), the solution of this matrix requires a relatively large number of iterations.

On the other hand, turbulent flows are multi-scale phenomena. The time step in direct numerical simulation (DNS) model has to satisfy the smallest scales in turbulence, and it is not allowed to exceed the Kolmogorov time scale. The smallest time scale of a turbulent regime is usually one order larger than the time following from the CFL restrictions in explicit methods, which makes the use of explicit methods not feasible. Furthermore, applying a fully implicit integration can be very expensive for small time steps (in order of Kolmogorov time scale).

As a remedy an alternative method can be employed. This method applies an implicit time integration for the diffusion term (linear term), and integrates the advection terms (nonlinear terms) explicitly. This gives us a so called IMEX (implicit-explicit) scheme. The resulting scheme is cheaper because the implicit operator is now linear and time-independent. To maintain second-order accuracy in time, it is attractive to use for the explicit part not the forward Euler scheme, but a second order explicit scheme, such as the Adams-Bashforth scheme.

Finally, to solve Equations (2.3) and (2.4) at second-order accuracy, a two-step fractional step method is applied. The solution advances in time using the Adams-Bashforth-Crank-Nicolson method, which conserves the second-order accuracy in time. The diffusion term is discretized using an implicit Crank-Nicolson scheme, whereas for the advection term a second-order Adams-Bashforth scheme is employed. This eliminates the viscous stability constraint which can be quite severe when simulating viscous flows. In the framework of the two-step fractional step method, an estimation of the velocity field $\vec{u}^*$ can be obtained by the predictor part as

$$\frac{1}{\Delta t}\left(\vec{u}^* - \vec{u}^{n-1}\right) + \frac{3}{2}C\left(\vec{u}^{n-1}\right) - \frac{1}{2}C\left(\vec{u}^{n-2}\right) + \frac{1}{2}D\left(\vec{u}^* + \vec{u}^{n-1}\right) + Gp^{n-1/2} = \vec{f}\left(t^{n-1/2}\right) \tag{2.6}$$

where n is the index for time steps. C, D and G are spatial operators for the advection, diffusion and pressure respectively. $\vec{f}$ is a forcing term that must be

determined in a way that $\vec{u}^{n+1}$ satisfies the boundary conditions immersed in the computational domain. The resulting velocity field $\vec{u}^*$ is not divergence free and the velocity and pressure must be corrected by a pressure correction term

$$\vec{u}^{n+1} = \vec{u}^* - (\Delta t/\rho)\,\nabla \delta p \tag{2.7}$$

$$p^{n+1} = p^n + \delta p \tag{2.8}$$

The pressure correction can be realized by solving the following Poisson equation

$$\nabla^2 \delta p = \frac{\rho}{\Delta t} \nabla \vec{u}^* \tag{2.9}$$

Wesseling (2000) has derived a suitable stability condition for the Adams-Bashforth-Cranck-Nicolson method as follows

$$\Delta t \leq \max\left[\tau_1,\ \min\left(\tau_2,\ \max\left(\tau_3,\ \tau_4\right)\right)\right] \tag{2.10}$$

with

$$\tau_1 = \frac{8}{3} q_3 \nu / \sum_j u_j^2$$

$$\tau_2 = \frac{1}{2} / \sum_j \Delta x_j^{-2} \left[2\nu + (1-\xi)\left|u_j \Delta x_j\right|\right]$$

$$\tau_3 = q_1 (3\nu)^{1/3} \left(\sum_j u_j^4 / \Delta x_j^2\right)^{-1/3}$$

$$\tau_4 = q_2 \sqrt{3} / \sum_j \left|u_j\right| / \Delta x_j$$

where ξ is equal to unity for central differencing of the advection term, q_1, q_2 and q_3 are 1, 0 and 0.5 for $\xi = 1$ respectively.

2.4 Immersed-boundary method

An approach which has been gaining popularity in recent years is the Cartesian grid method. In this method the governing equations are discretized on a Cartesian grid which cannot fit the immersed boundaries. Cut-cell techniques and ghost-cell methods are the most popular remedies to this problem. In cut-cell techniques, the intersecting cells are cut, yielding arbitrarily shaped cells, which add complexity to the computational model. The ghost-cell methods force

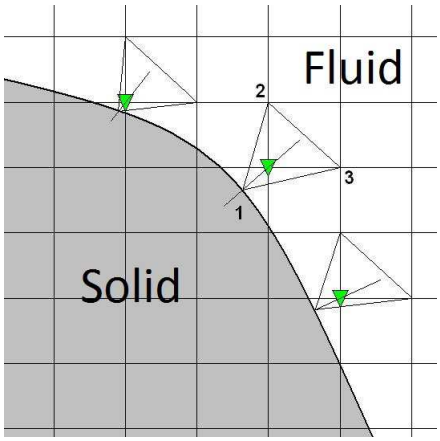

Figure 2.1: Interpolation stencil in 2D. The ghost nodes are interpolated linearly using two nearest points in the fluid and a point on the boundary.

the fluid at the immersed boundaries. It is easy to implement and requires less computational effort than the cut-cell techniques. The ghost-cell method implemented in this study is based on the application of direct forcing on the immersed boundaries. The approach is similar to the forcing used by Mohd-Yusof (1997) and Fadlun et al. (2000). The force is a function of time and space, and is defined in such a way that the desired boundary conditions are satisfied at every time step. The locations of this force are not coincident with the grid points; hence it must be extrapolated to these nodes. The magnitude of the forcing function that will enforce the boundary conditions can be derived from the Navier-Stokes equations in the following form

$$\frac{u_G^{n+1} - u_i^n}{\Delta t} = RHS_i + f_i \tag{2.11}$$

where RHS is the right hand side of the Navier-Stokes equations and includes the advection, diffusion and pressure terms. u_G^{n+1} is the velocity on the immersed boundaries, and f_i is the forcing function. The force f_i in Equation (2.11) is correct if the positions of unknowns are located exactly on the boundaries. This is not the case for the complex geometries. Many different interpolation and extrapolation techniques have been adopted to determine the forcing term on the ghost cells. In general, they can be classified into two categories: (a) schemes that allocate the ghost cells inside the fluid in the vicinity of the boundary (Balaras, 2004), and (b) techniques that consider the first cells in the solid as ghost cells (Tseng and Ferziger, 2003).

In the present study, the former category is used, where the ghost cells are located in the fluid in the vicinity of the boundary. Ghost cells are defined as the cells which are in the fluid and have minimally one neighbour cell located in the

solid. To determine the locations of nodes, an integer flag is used. The nodes with flag -1 are located in the solid, whereas the fluid nodes are indicated by flag 1. The ghost nodes are determined by flag zero. There are several ways to build a construction for the ghost cells to be constrained and satisfy the boundary conditions. In the present work a second-order construction is used, which is flexible in complex geometries, and can also handle the moving boundaries. Figure (2.1) shows the interpolation stencil in a two-dimensional case. The ghost nodes can be interpolated linearly by considering the two nearest points in the fluid and a point on the intersection of the boundary interface with the normal line passing through the ghost node. In the two-dimensional case, the construction forms a triangle, whereas it is a tetrahedron in a three-dimensional situation. This interpolation is robust and removes the numerical instabilities which can be generated by higher order polynomial interpolations. A linear interpolation can be described as

$$u = a_0 + \sum_{i=1}^{N} a_i x_i \tag{2.12}$$

where N represents the dimension and a_i's are the coefficients of the linear interpolation. The coefficients can be expressed as

$$a = B^{-1} u \tag{2.13}$$

where B is a matrix (3×3 for 2D, and 4×4 for 3D) for which the elements can be calculated from the coordinates of the interpolation points. Equation (2.13) can be rewritten for 3D forms as

$$\begin{bmatrix} a_1 \\ a_2 \\ a_3 \\ a_0 \end{bmatrix} = \begin{bmatrix} x_1 & y_1 & z_1 & 1 \\ x_2 & y_2 & z_2 & 1 \\ x_3 & y_3 & z_3 & 1 \\ x_4 & y_4 & z_4 & 1 \end{bmatrix}^{-1} \begin{bmatrix} u_1 \\ u_2 \\ u_3 \\ u_4 \end{bmatrix} \tag{2.14}$$

In the above algorithm, boundary conditions for the pressure near the interface are not imposed explicitly, but they are essentially implicit in the source term of the Poisson equation (Balaras, 2004).

2.5 Mesh refinement

One difficulty with the Cartesian approach, apart from the difficulties arising from immersed boundaries, is the problem of resolution. A simple Cartesian grid treats all portions of flow equally; all cells in the grid are rectangles or cuboids, and all have the same size (Figure 2.2). Flows of interest are almost never that

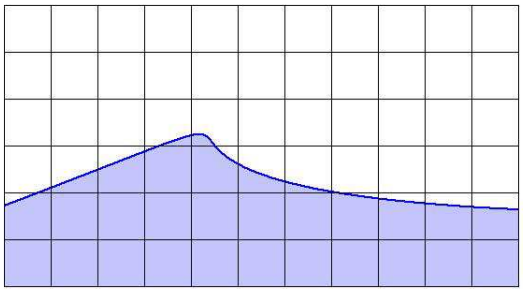

Figure 2.2: Simple Cartesian grid for flow over a dune.

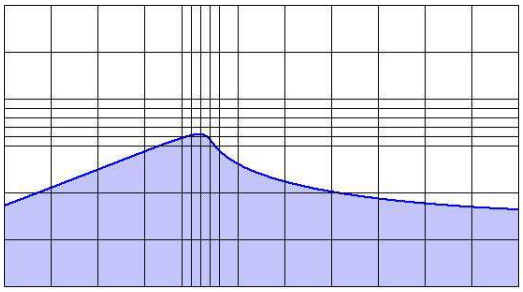

Figure 2.3: Refinement by compression/stretching.

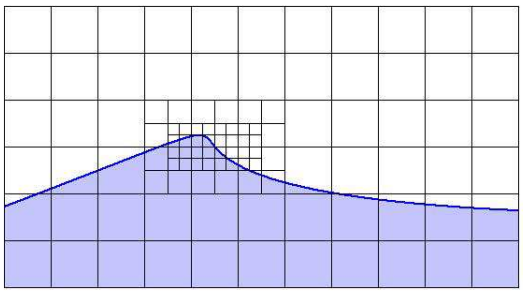

Figure 2.4: Refinement by patches.

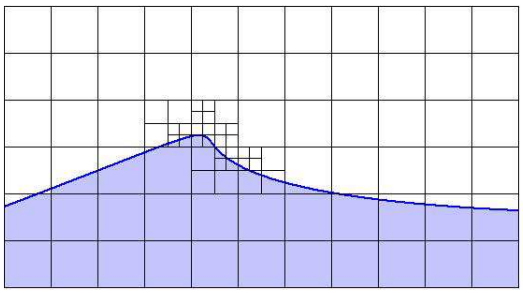

Figure 2.5: Refinement by cells.

isotropic. To resolve real geometries, and real flows, it is virtually always necessary to allow the grid to adapt in some way.

One way to adapt the grid is to keep the grid Cartesian, i.e. successive points lie along a line of constant x (or y or z), but the spacing is allowed to vary so that certain features of the geometry or flow are better resolved than others. This complicates the flow solver somewhat, as non-constant grid spacing must be accounted for, but the basic structure of the code is unchanged. Figure (2.3) shows a simple example; the grid is refined in the vicinity of the forward stagnation point. It is clear from the figure that there is an inefficiency associated with this type of refinement. Clustering grid points near the stagnation point leads to clustering away from the body as well.

Another approach to adaptive refinement is to select a rectangular region in which refinement is desired, and overlay the grid in that region with a patch of finer grid. This approach, depicted in Figure (2.4), leads to a Cartesian grid away from the patch, and a Cartesian grid inside the patch, but requires special treatment on both sides of the boundary of the patch. This patch-overlay can be done recursively, so that large variations in cell size can be achieved. In Figure (2.4), a 2×3 patch of the base grid has been refined one level. Following that, a 2×4 sub-patch of that patch has been refined by one level. The resulting grid

resolves the forward stagnation point, and the area of refinement is kept local.

A third approach is local unstructured refinement, as depicted in Figure (2.5). This approach can be viewed as a non-rectangular patch refinement. Its advantage over the patch refinement is economical use of cells; more flexibility to capture the high-gradient variations and the relative independence from the other cells; its disadvantage is that the grid does not have the (i, j, k) structure that the unstretched or stretched Cartesian approach has globally, and the patch-refinement approach has locally. But this method has great flexibility to treat flows with high gradients and flows with complex geometries.

In order to optimize the use of computational resources, we use an adaptive multi-levels Cartesian mesh, with local refinement as shown in Figure (2.5), in which more grids cells can be placed in high-gradient regions such as near boundaries. Figure (2.6) shows such kind of grid over a dune. The gradient of flow in boundary layers is high; hence the grid has the finest resolution in the vicinity of the solid boundaries. The grid generation process starts from a relatively coarse Cartesian grid encompassing the overall domain. The grid generation then proceeds by successive refinements. Each coarse cell is divided into eight equal children cells (4 children in 2D) to form the next level of refinement (see Figure 2.6). Data structures that work well for this refinement scheme, as well as other data structures, are described in the next section.

2.6 Data structure

The data structure of a code is the roadmap for the information contained in the code. It shows what information is stored, and how to access it. For a typical structured-grid code, the data structure can entirely be contained in an (i, j, k) index. Unstructured grid codes usually have a significantly more complicated data structure. Of primary concern is the connectivity of the grid. Some information must be stored to determine which cells are neighbours of a given cell.

The set of refined Cartesian cells is commonly managed in two ways: the hierarchical tree data structure and the fully unstructured approach. In the fully unstructured approach, each cell is connected to one or four neighbours in each direction. The drawbacks of this approach can be listed as below,

- The stencil of discretization will differ from the standard form. It is called discretization pollution. By incorporating the neighbour cells, related to the local topology of the grid, different forms of discretization can be achieved.
- The symmetric structure of the matrix for the pressure correction can be destroyed because of hanging nodes. Some efficient solvers such as CG algorithm are not applicable for this purpose. The use of GMRES or BiCGStab is quite expensive. The Algebraic Multigrid techniques are also not efficient for non-symmetric matrices.

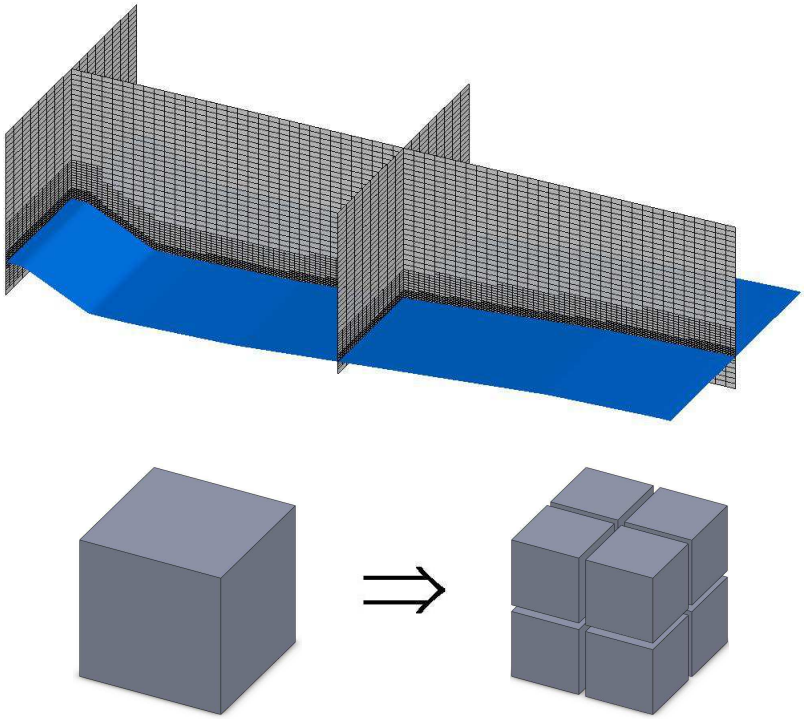

Figure 2.6: Multi-level Cartesian grid over a dune. The cells of the coarse grid are split into 8 children to form the fine grid.

To avoid the first shortcoming, approaches based on least-square interpolation are employed (Koh et al., 2003; Mavriplis, 2003; Capizzano, 2007). It is shown that the discretization based on least-square interpolations, leads to numerical instabilities. To avoid the instabilities, different kinds of limiters are used (Berger et al., 2005; Pereira and Silva, 2005; Mandal and Subramanian, 2008). These limiters are non physical based operators and they are employed to damp the numerical wiggles. The solution by this method has less significant physics-based results for the unsteady state of the flow. The use of a hierarchical data structure is an alternative solution. At this method, the finer cells are considered as separate grids that are located in subdomains of the coarser grids. Figure (2.7) shows a fully unstructured, and a multi-level grid. At the multi-levels grid, the sub-grids can be treated separately and they form a kind of nested grids.

Coirier and Powell (1996) used the hierarchical tree structure in their Euler and Navier-Stokes solver, demonstrating that the tree structure provides a logical means of finding cell-to-cell connectivity and allows straightforward isotropic refinement and coarsening through tree growth and pruning. Further, even though the tree traverses required to determine neighbour connectivity are based on logical recursive routines, the calculation time required for computing quantities involving the neighbours (e.g. residual calculations) will be greater than for

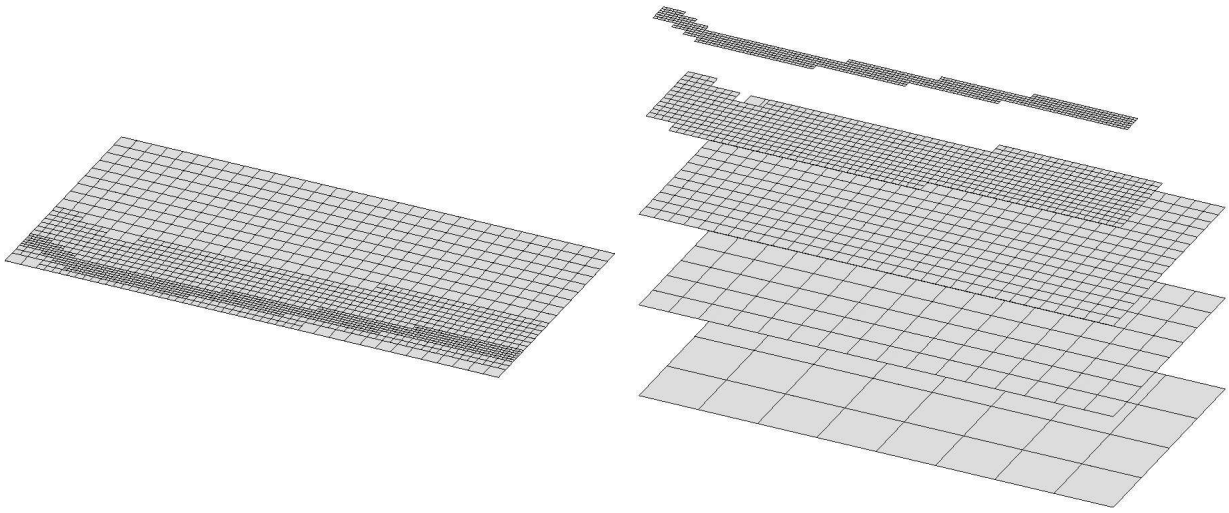

Figure 2.7: A fully unstructured (left) and a multi-level grid (right).

the fully unstructured approach, where the neighbour references are explicitly stored. Here we use the hierarchical tree data structure approach combined with an unstructured approach by defining local pointers for neighbours to avoid the searching problems. This method conserves the parent-child communications and keeps the advantages of unstructured grids.

Finally, we point out that the solution of viscous incompressible flows requires that careful attention be paid to the velocity-pressure coupling to prevent non-physical oscillations in the solution. This is normally accomplished by using variants of the staggered grid method. In this case, the calculation and storage of face-based data are required. The storage and management of faces between cell neighbours requires the definition of new tree structures for faces. The tree structures for faces are managed in a comparable way as those for the cells. Three kinds of faces (perpendicular to x- y- and z coordinates) require three extra trees. In a three-dimensional mesh, the cells form an octree and the faces form three quad-tree data structures.

Therefore, the neighbour relations for three-dimensional grids are managed as follows

- Each cube is connected by six pointers to the six covering faces.
- A pointer connects the cell to its parent on the coarser level.
- Each cell has eight pointers to be connected to its children which are located on the finer grid.
- The faces have two pointers, connected to the cubes.
- Each face includes four pointers to connect to its children (faces located in the finer level).

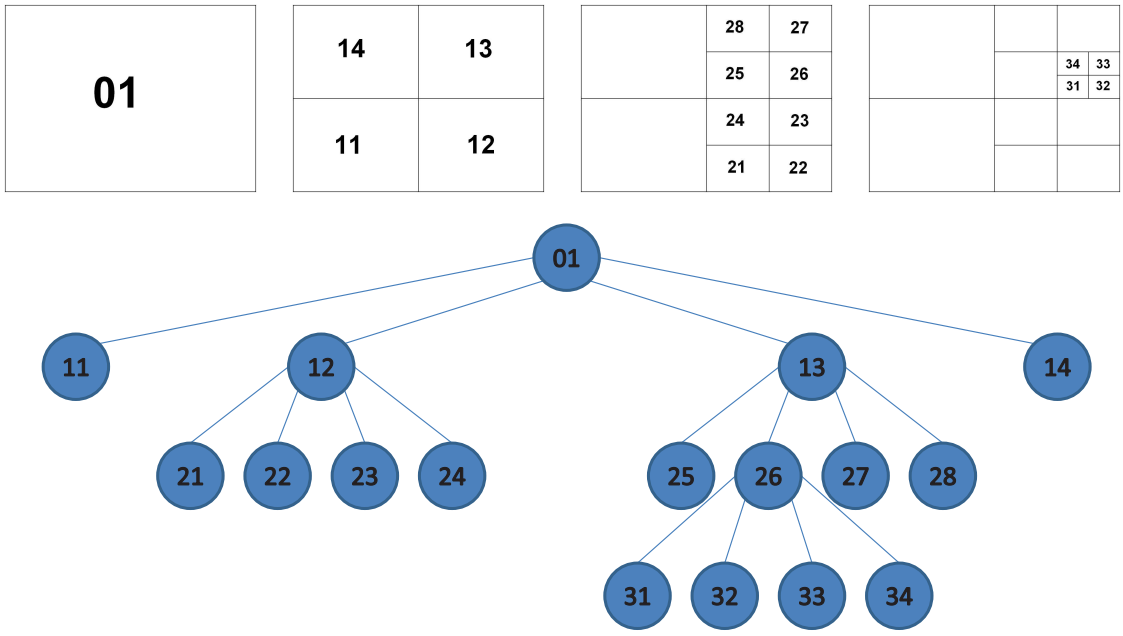

Figure 2.8: Data structure for multi-level Cartesian grid. Tree data structure is defined to identify the inter-grid connections.

- One pointer connects the face to the parent at the coarser level.

Figure (2.8) shows the structure of cell-face-cell connections in two dimensions. Furthermore, the boundary conditions for any grid level are defined by ghost cells and ghost faces. The ghost cells and ghost faces are managed in such a way, that they surround all subdomains. The values on the ghost cells and ghost faces can be interpolated from the values on the coarser grid. A high-order interpolation is necessary to conserve the order of accuracy. We here implemented at least third-order interpolation to conserve the second-order accuracy of the model.

By this kind of data structure, the parent-children connectivity can be directly employed to find the related cells and faces on the finer and coarser grids, which makes the implementation of a multigrid method straightforward. This kind of multigrid techniques is more efficient than the Krylov space methods on a single unstructured grid, because of the presence of hanging nodes on the single grid, resulting from the local refining. The hanging nodes can breach the symmetry of coefficient matrices.

2.7 Multigrid

Multigrid techniques are generally accepted as fast and efficient methods for solving many types of partial differential equations, and particularly elliptic problems whose discretization results in a K-matrix (Wesseling, 2004). Multigrid methods exhibit an optimal complexity and are, in theory, independent of the mesh size (Saad, 2003). Here, we are interested in the combination of adaptivity and multigrid. Actually, adaptive grid refinement turns out to be fully compatible with the multigrid structure and philosophy. Brandt (1977) has introduced multilevel adaptive refinement (MLAT). McCormick and Thomas (1986) introduced the fast adaptive composite grid method (FAC), which can be regarded as an alternative to the MLAT approach. MLAT and FAC are closely related. The main difference between MLAT and FAC is the composite grid orientation of FAC. The grid composition is explicit in FAC, whereas MLAT composes the grid in an implicit way. Once the sequence of local refinement regions has been defined and constructed, MLAT can be more suitable for our purpose. The adaptive grid refinement techniques start with a coarse grid covering the whole computational domain. Finer grids are then introduced locally only in a sub-domain in order to improve the accuracy of the solution. Adaptive multigrid differs from standard multigrid in the sense of the structure of the grid hierarchy. In standard multigrid techniques, all grids are global (cover the whole computational domain), whereas in adaptive multigrid techniques, the fine grids can be global or cover the domain partially.

One of the most important parts of a multigrid algorithm is the smoothing process. Several smoothers for the Navier-Stokes equations problem have been studied in literature. These approaches fall into two categories: (1) coupled smoothing (Vanka, 1986; Thompson and Ferziger, 1989; Oosterlee, 1997), in which the momentum and continuity equation are satisfied simultaneously, and (2) distributive smoothing (Brandt and Yavneh, 1992; Thomas et al., 1999), in which the momentum equations are solved in a first step, and then the velocities and pressures are corrected in order to satisfy the continuity equation. In stretched grid problems and flows with strong gradients, coupled smoothing has advantages over the distributive approach because the momentum and continuity are satisfied simultaneously (Vanka, 1986). However the computational cost of the coupled method is much higher than that of the distributive one, because the matrices (local small matrices) have to be inverted in each cell, and the velocity components have to be updated twice.

In particular, we have chosen the distributive approach with Gauss-Seidel smoothing. It complies well with the fractional-step approach and the multigrid techniques can be applied for both momentum and pressure. The main difference between the momentum and the pressure correction equation comes from the nonlinearity of the advection terms in the momentum equations. The momentum equations cannot be solved by a linear multigrid approach in a direct

way, without global linearization. The nonlinearity of the momentum equations brings the motivation to apply different kind of multigrid cycles. Here we apply FAS (Full Approximation Storage) for the momentum equation. It is additionally observed that FAS can lead to higher stability for the linear problems, especially in multi-level adaptive approaches. Therefore, FAS is applied for both momentum and pressure. The time iterations can be described by the following algorithm.

1. Solve the momentum equations
   (a) Apply one FAS cycle for momentum in x-direction.
   (b) Apply one FAS cycle for momentum in y-direction.
   (c) Apply one FAS cycle for momentum in z-direction.
   (d) Calculate the scalar fields, like turbulence closure.
   (e) Check the residual. If it is not converged, go to a.
2. Apply MG/FAS cycles for the pressure correction, until convergence
3. Correct the velocity field and pressure.
4. Go to step 1.

The local iteration process in step 1 is very fast if an implicit-explicit method (i.e. Crank-Nicolson-Adams-Bashforth method) is used, and it is seen that the momentum converges by very few multigrid cycles per time iteration. This feature makes the solution of the implicit-explicit method time efficient. The FAS algorithm can be described as follows:

FAS multigrid cycle; MGFAS (u_0, u, k, γ)
if level $=$ *coarsest*
Solve the coarsest grid by a fast solver
else
Pre-smoothing with ν_1 *iterations;* $S\,(\bar{u}, u, f, \nu_1, k)$
Compute the defect on Ω_k*;* $r_k = f_k - N_k u_k$
Restrict the defect from Ω_k *to* Ω_{k-1}*;* $r_{k-1} = I_k^{k-1} r_k$
Restrict u from Ω_k *to* Ω_{k-1}*;* $u_{k-1} = \hat{I}_k^{k-1} u_k$
Keep the values of u_{k-1}*;* $u'_{k-1} = u_{k-1}$
Compute the right-hand side for Ω_{k-1}*;* $f_{k-1} = r_{k-1} + N_{k-1} u_{k-1}$
Do loop 1 *to* γ*; MGFAS* (u_0, u, k, γ)
Compute the correction on Ω_{k-1}*;* $c_{k-1} = u_{k-1} - u'_{k-1}$
Interpolate the correction from Ω_{k-1} *to* Ω_k*;* $c_k = I_{k-1}^k c_{k-1}$
Compute the corrected approximation on Ω_k*;* $u_k^{new} = u_k + c_k$
Apply post-smoothing with ν_2 *iterations;* $S\,(u, u, f, \nu_2, k)$
endif

However, the efficiency of the multigrid methods degenerates dramatically in presence of anisotropies. Typically these anisotropies may occur when the coefficients of the discrete operator vary by orders of magnitude or when a highly anisotropic grid is used (Trottenberg et al., 2001). Highly anisotropic grids cannot be treated efficiently by standard coarsening and pointwise smoothers. The reason is that pointwise relaxation has a smoothing effect only with respect to the "strong coupling" in the operator and damps the errors only in the coarsest direction.

Trottenberg et al. (2001) has proposed two techniques to avoid this difficulty, (1) semicoarsening and (2) line smoothers. The former technique keeps the pointwise relaxation, but modifies the grid coarsening according to the direction with strongly coupled unknowns. The coarse grid is defined by doubling the mesh size only in that direction in which the errors are smooth. The line smoother technique keeps the standard multigrid coarsening, but changes the relaxation procedure from pointwise to linewise. That is, all unknowns on a line are updated collectively. Linewise relaxations are thus block iterations in which each block of unknowns corresponds to a line. The collective solution of all equations corresponding to a line means the solution of a tridiagonal system of equations.

In the present work, the latter technique (linewise smoothing) is applied, because of its simplicity in programming. Moreover, the tridiagonal matrices can be solved by a direct and cost-efficient algorithm, the so-called Thomas algorithm. The smoother applies linewise GS (Gauss Seidel) iterations in the normal direction.

Another difficulty which arises in adaptive grids, is defining the boundary conditions. The boundaries for the fine grids (which can be not global) fall in the regions inside the computational domain. The boundaries must be interpolated from the coarser grid in any multigrid-cycle. The order of interpolation must be higher than the order of accuracy of the computational scheme. Here we adopt at least a third-order interpolation to conserve the second-order accuracy of the scheme. Figure (2.9) shows a fine grid located on a coarser grid. The ghost cells (which surround the grid), must be interpolated from the coarser grid. Figure (2.9 left) shows the ghost cells in a two-dimensional grid, for the pressure, whereas in Figure (2.9 right) the ghost faces on which the velocity component u (in x-direction) is located, are shown. The difference in interpolations for pressure and velocities is due to the grid staggering.

Considering Figure (2.9 left), the pressure on ghost-cells at the fine grid (yellow cells), must be interpolated from nine surrounding points on the coarser grid (27 points in 3D) for the case of third order interpolation. In two-dimensional cases, bi-quadratic interpolation, and in three-dimensional cases, tri-quadratic interpolation is employed. The interpolations for the velocities are different than that for the pressure, due to their locations. For velocities at ghost faces, which are connected to a parent-face, a quadratic interpolation is employed. For the suspended faces (without a parent-face) a combination of quadratic and cubic in-

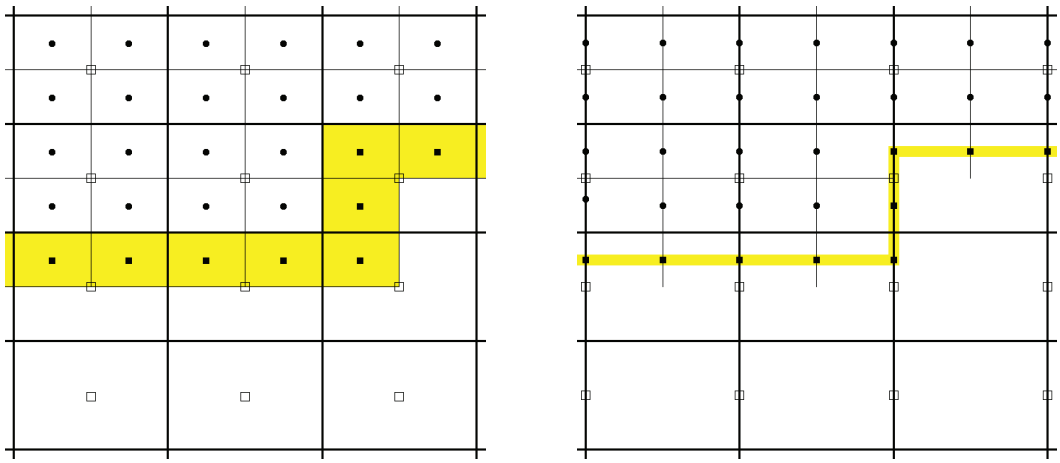

Figure 2.9: The ghost cells and ghost faces located on the interfaces of two successive grids. The values for these cells are interpolated from the coarser grid, for pressure (left) and for velocity u (right).

terpolations is employed to conserve the symmetry of interpolations. The ghost faces are indicated by ■ in Figure (2.9 right).

2.8 Moving boundaries

The general algorithm outlined in Section 2.4 is directly applicable to flows with moving boundaries. For moving boundaries, the forcing approach and the related interpolations must be re-evaluated after every time that the location of the interface is updated. In flows with moving boundaries, however, complications arise which are usually related to the time advancement scheme. This is due to the fact that the role of the grid points near the interface changes from timestep to timestep, as the solid body moves through the fixed grid. The forcing points can change from fluid to solid points, and vice versa.

The solution of the momentum equation at timestep n, requires physical values of the velocity vector and pressure, as well as their derivatives from timestep $n-1$ at all fluid points. Due to the fact that the interface changes location, it is possible that some of the required values from timestep $n-1$ are not physical. Due to the CFL restriction of the present scheme the boundaries cannot move by more than one grid cell in each timestep, which results in two possible changes in the flags of the points near the interface.

After that the boundary changes location, three different situations may occur:

1. The interface does not pass any grid point. In this case, the grid points do not change role and no stability errors arise.

2. The interface moves towards the fluid and passes some grid points. The forcing point becomes to be solid and the nearest fluid points become forcing points. Because the new solid points have a history from the previous timestep, no stability errors can arise.

3. The interface moves towards the solid and passes some grid points. The forcing points become fluid and the solid points become forcing points. Because the new solid points have no history from the previous timestep, stability problems may arise.

Situation 3 is shown in Figure (2.10) for a two-dimensional case. In the left part of Figure (2.10) the derivative $\partial vu/\partial y$ in the momentum equation for u_1 makes use of velocities v_1 and v_2. The values of v_1 and v_2 are both physical because they are located outside the solid. In a later stage, the boundary moves toward the solid (see Figure 2.10right) and the role of u_2 changes (from forcing to fluid point). The same derivative now makes use of v_3 and v_4, while v_3 is located in the solid and has no physical value. This phenomenon can also be observed for the pressure derivatives in the momentum equations. At the first stage, pressure p_1 is used for the calculation of the control volume related to velocity u_1. After deformation of the boundary, pressure p_2 is used for u_2. Pressure p_2 has no physical value because it was calculated at time step n, when it was located in the solid.

To avoid such instabilities, we apply a field-extension procedure, in which the velocity and pressure fields are extrapolated at the first point in the solid phase at the end of each deformation. We call these points pseudo-fluid points. In this way, not only the velocity and pressure at the forcing points at substep $n-1$, but also their derivatives will have physical values, eliminating problems in the computation of the momentum derivatives in the next step.

The values of the velocity at the pseudo-fluid points are construed using a procedure which is similar to the procedure applied by Tseng and Ferziger (2003). Central to this procedure is using the image of the pseudo-fluid node inside the flow domain to ensure positive weighting coefficients. The point I is the image of the pseudo-fluid point through the boundary as shown in Figure (2.10). The flow variable is evaluated at the image point using the same interpolation scheme as described in Section 2.4. The value at the pseudo-fluid point can be determined as

$$\varphi_p = 2\varphi_b - \varphi_I \tag{2.15}$$

Unlike the velocities, the pressure on the immersed boundaries cannot be determined explicitly. The boundary condition for pressure is of the Neumann type and can be expressed in normal derivative form as

$$\frac{\partial p}{\partial n} = 0 \tag{2.16}$$

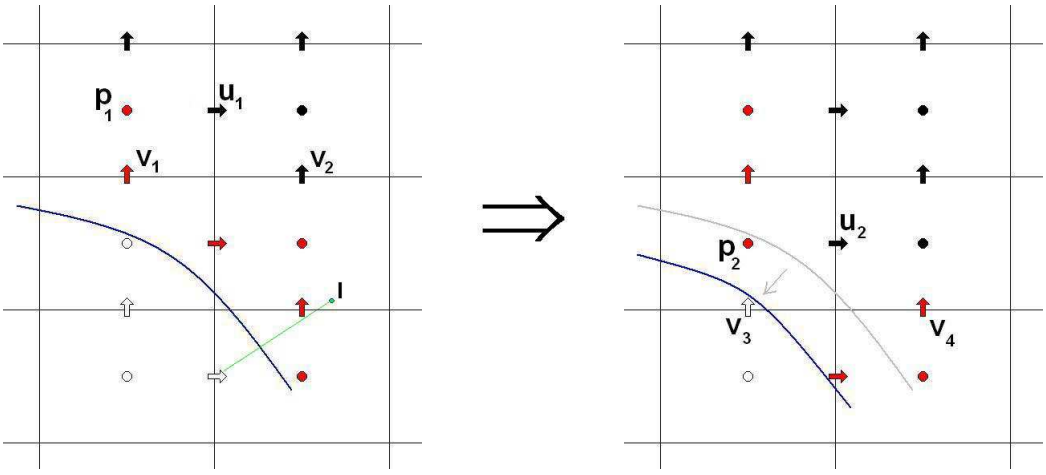

Figure 2.10: Moving the boundary can bring nonphysical values for the derivatives in the momentum equations. The role of u changes from ghost-cell to fluid cell, and it gives non-physical values of $\partial vu/\partial y$.

The normal derivative of pressure can then be expressed as:

$$\frac{\partial p}{\partial n} = \frac{\partial p}{\partial x_i} n_i \tag{2.17}$$

where n_i's denote the components of normal unit vector, $\vec{n}$. A linear interpolation for pressure can be described as

$$p = a_0 + \sum_{i=1}^{N} a_i x_i \tag{2.18}$$

where N represents the dimension and a_i the coefficients of the linear interpolation. Differentiation of Equation (2.18) yields:

$$\frac{\partial p}{\partial x_i} = a_i \tag{2.19}$$

Substituting Equation (2.19) into (2.17) yields

$$a_i n_i = \frac{\partial p}{\partial n} = 0 \tag{2.20}$$

By considering Equation (2.18) for extra points in the fluid phase (2 points in 2D, or 3 points in 3D), the coefficients can be expressed as

$$a = B^{-1} P \tag{2.21}$$

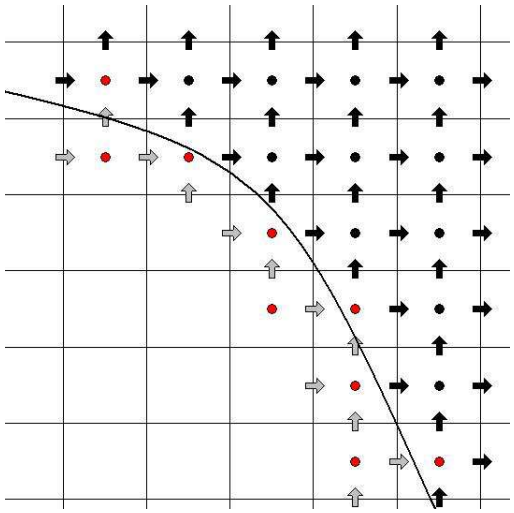

Figure 2.11: Extension to some nodes on the pressure grid that have been classified as boundary nodes on the velocity grid.

where B is a matrix (3×3 for 2D, and 4×4 for 3D) whose elements can be computed from Equation (2.20) and the coordinates of the interpolation points. Equation (2.21) can be rewritten in an expanded form in 3D, as

$$\begin{bmatrix} a_1 \\ a_2 \\ a_3 \\ a_0 \end{bmatrix} = \begin{bmatrix} n_x & n_y & n_z & 0 \\ x_1 & y_1 & z_1 & 1 \\ x_2 & y_2 & z_2 & 1 \\ x_3 & y_3 & z_3 & 1 \end{bmatrix}^{-1} \begin{bmatrix} \partial p/\partial n \\ p_1 \\ p_2 \\ p_3 \end{bmatrix} \tag{2.22}$$

Applying Equation (2.21) for an image point of pressure located in the fluid, the pressure value of the pseudo-fluid point can be determined as

$$p_p = p_I \tag{2.23}$$

where p_p is the pseudo-fluid pressure and p_I is the pressure at the image point.

We should also note that, due to the staggering of the mesh, the selection of points on the pressure grid where the field extension is performed is not only based on their relative location with respect to the interface, but also on their association to velocity values that are non-physical. As a result the pressure is also extended to some nodes on the pressure grid that would have been classified as boundary nodes on the velocity grid as shown in Figure (2.11) by red circles.

2.9 Moving grid

The motion of boundaries imposes us to adapt the grid in a way to be able to enforce a fine mesh around the boundaries. It can be realized by defining an adaptive grid in which the refining criteria are based on the distance to the solid boundaries. After each movement of the solid boundaries, the grid cells must be refined or coarsened to conserve the grid topology regarding to the boundaries. It can be done by defining coarsening and refining algorithms. Refining adds new children-cells and faces to their associated parents, whereas the coarsening removes the children from the parents.

The new children cells and faces include no predefined values of variables (e.g. velocities and pressure etc.) and they must be interpolated from their parent's level. Here we apply a third-order interpolation to conserve the the second-order accuracy of the computational scheme. For coarsening, no interpolation is necessary because they are predefined from the last time step.

2.10 Turbulence closure

Three major tools are available for simulation of turbulent flows - RANS (Reynolds Averaged Navier-Stokes), DNS (Direct Numerical Simulation) and LES (Large Eddy Simulation). RANS removes the turbulence fluctuations by statistically averaging of the velocity and the pressure fields. The results of RANS are not accurate enough for understanding the physics behind the sediment transport and deformation of dunes. The turbulence fluctuations have a significant effect on pickup of sediment and evolution of dunes.

DNS is the most accurate method. It solves all scales of turbulence in both space and time, from the largest scale down to the Kolmogorov microscale. The DNS approach tries to solve the Navier-Stokes equations such that all persisting eddies are resolved. If the Reynolds number of the flow becomes very large, small flow structures will develop. Due to viscous forces in the flow, very small eddies die rather quickly. The size of the smallest persisting eddies is given by the Kolmogorov law. To capture all eddies, one would need a mesh size of $h \sim Re^{-3/4}$. The total number of mesh cells in a uniform mesh in three dimensions is $N = h^{-3} \sim Re^{9/4}$. The number of grid points increases rapidly with the Reynolds number in DNS. It means the performance of a DNS is possible on present day computers only for low Reynolds numbers and simple geometries. Therefore DNS is not a useful tool for the present purpose.

LES is an alternative method, which is computationally less expensive than DNS, and gives reasonably accurate results compared to DNS. LES has the advantage over DNS of allowing a wide range of Reynolds numbers. Henn and Sykes (1999) showed that LES agrees quite well with experimental results for flow over wavy surfaces, even when the ripples are large enough to cause sepa-

ration. In the present study, LES has been applied as turbulence closure, because of its advantages over RANS and DNS.

The governing equations for the fluid are the full three-dimensional, unsteady, incompressible Navier-Stokes equations written in terms of primitive variables. These equations are given below in terms of volume filtered variables.

$$\frac{\partial \bar{u}_j}{\partial x_j} = 0 \tag{2.24}$$

$$\frac{\partial \bar{u}_i}{\partial t} + \frac{\partial \bar{u}_i \bar{u}_j}{\partial x_j} = -\frac{1}{\rho}\frac{\partial \bar{P}}{\partial x_i} + \frac{\partial}{\partial x_j}\left\{2\left(\nu + \nu_t\right) S_{ij}\right\} \tag{2.25}$$

where x_i's are the coordinates, t is the time, $\bar{P}$ the modified pressure, ρ the density, $\bar{u}_i$ the filtered velocity component in x_i-direction, ν and ν_t the molecular and turbulent viscosities and S_{ij} is the resolved strain rate tensor:

$$S_{ij} = \frac{1}{2}\left(\frac{\partial \bar{u}_i}{\partial x_j} + \frac{\partial \bar{u}_j}{\partial x_i}\right) \tag{2.26}$$

In large eddy simulation, the large eddies are solved directly, ignoring the smaller eddies. The smaller eddies are then modelled separately. LES uses volume filtering, allowing to filter eddies which are smaller than the grid cell volume. The filter is defined as

$$\mathbf{f}\left(\mathbf{x}, t\right) = \int f\left(\mathbf{y}, t\right) G_\Delta\left(\mathbf{x} - \mathbf{y}\right) d\mathbf{y} \tag{2.27}$$

The effect of the small scales upon the resolved part of turbulence appears in the sub-grid-scale (SGS) stress term

$$\tau_{ij} = \overline{u_i u}_j - \bar{u}_i \bar{u}_j \tag{2.28}$$

which must be modelled. It is set proportional to the strain-rate tensor S_{ij}, characterizing the local deformation of the resolved velocity field. The model is written as

$$\tau_{ij} = -2\nu_T S_{ij} + \frac{1}{3}\tau_{kk}\delta_{ij} \tag{2.29}$$

And finally, the eddy viscosity is determined as

$$\nu_t = \left(C_S \overline{\Delta}\right)^2 \left|\overline{S}\right| \tag{2.30}$$

where

$$|\overline{S}| = \sqrt{2\overline{S}_{ij}\overline{S}_{ij}} \tag{2.31}$$

$$\overline{\Delta} = (\Delta x.\Delta y.\Delta z)^{1/3} \tag{2.32}$$

The value of C_S is constant in Smagorinsky's model. The value of C_S can be determined using the turbulence spectrum. Its value is approximately 0.17 in isotropic turbulent flow (Lilly, 1967).

Smagorinsky's model is too dissipative in the presence of walls; moreover, it does not work in particular for the transition in a boundary-layer developing on a flat plate. It artificially relaminarizes the flow if the upstream perturbation is not high enough. This is due to the heavy influence in the eddy viscosity of the velocity gradient in the direction normal to the wall and to an improper behaviour of the model at the wall. Smagorinsky's model ignores the backscatter of energy, and dissipates all the energy which is transferred from the large to the small eddies.

To avoid excessive dissipation, the effect of SGS is modelled using a dynamic sub-grid scale model (SGS model) as well as a classical log-law model. Depending on the configuration of the boundaries, one of these models can be selected. For smooth boundaries, or boundaries with roughness smaller than the thickness of the viscous sub-layer, the sub-grid scale model has advantages, as it is more accurate than the classical wall model, especially in the accurate simulation of the boundary layer. As the roughness height exceeds the thickness of the viscous sub-layer, the use of dynamic sub-grid scale model is impractical, and the classic wall model has to be applied.

2.10.1 Dynamic sub-grid scale model

In dynamic models for subgrid-scale stresses, the model coefficient C_S is determined during the calculation progress. This is accomplished by defining a test filter, the width of which is larger than the grid filter width $\overline{\Delta}$. The test-grid level SGS stress tensor takes the following form:

$$T_{ij} = \widehat{\overline{u_i}\overline{u}_j} - \widehat{\overline{u}}_i\widehat{\overline{u}}_j \tag{2.33}$$

The Germano identity tensor is defined as

$$L_{ij} = T_{ij} - \widehat{\tau}_{ij} = \widehat{\overline{u}_i}\widehat{\overline{u}}_j - \widehat{\overline{u}}_i\widehat{\overline{u}}_j \tag{2.34}$$

where

$$\widehat{\tau}_{ij} = \widehat{\overline{u_i u}_j} - \widehat{\overline{u}_i}\widehat{\overline{u}_j} \tag{2.35}$$

where the hat represents the test-grid filtering process based on a characteristic filter size of $\widehat{\overline{\Delta}}$. Applying Smagorinsky's model for T_{ij} and τ_{ij} gives

$$\tau_{ij} = -2C_S^2\Delta^2 \left|\overline{S}\right| \overline{S}_{ij} \tag{2.36}$$

$$T_{ij} = -2C_S^2 \left(2\Delta\right)^2 \left|\widehat{\overline{S}}\right| \widehat{\overline{S}}_{ij} \tag{2.37}$$

Substitution of these expressions into the Germano identity leads to an overdetermined system of five equations and one unknown. These five equations cannot be satisfied simultaneously. The resulting error is defined as

$$e_{ij} = L_{ij} - 2\Delta^2 \left(C_S^2 \widehat{\left|\overline{S}\right| \overline{S}_{ij}} - 4C_S^2 \widehat{\left|\overline{S}\right|} \widehat{\overline{S}}_{ij} \right) \tag{2.38}$$

Different approaches have been used to minimize the error. The commonly used minimization approach is based on a least-square method. Ghosal et al. (1995), constrained C_S^2 to have no variation in a homogenous plane, and derived the following relation by applying least-square minimization.

$$C_S^2 = \frac{\left\langle L_{ij} M_{ij} \right\rangle}{\left\langle L_{kl} M_{kl} \right\rangle} \tag{2.39}$$

Here $\langle . \rangle$ denotes averaging in a homogenous plane. The averaging in a homogenous plane damps the sharp fluctuations of C_S which tends to destabilize the numerical simulation (leads to negative eddy viscosity).

For a rectangular channel, the homogenous planes are parallel to the walls. $L_{ij}M_{ij}$ can be easily averaged to be used in Equation (2.17). But this is not the case for problems with complex geometries. The homogenous plane does not usually exist or cannot be found. An alternative method, proposed by Meneveau et al. (1996), is based on accumulation of the required statistics over the fluid-particle trajectory. Averaging along fluid-particle trajectories eliminates the need for homogenous directions. This feature makes the averaging suitable for problems with complex geometries. In this approach the coefficient C_S is determined based on a Lagrangian averaging model (Meneveau et al., 1996) and has been defined as

$$C_S^2 = \frac{I_{LM}}{I_{MM}} \tag{2.40}$$

where

$$I_{LM} = \int_{-\infty}^{t} L_{ij}M_{ij}W\left(t-t'\right)dt' \tag{2.41}$$

$$I_{MM} = \int_{-\infty}^{t} M_{ij}M_{ij}W\left(t-t'\right)dt' \tag{2.42}$$

Here W is a weighting function. It is a free parameter defining the extent backward along the pathline over which we choose to minimize the error. Meneveau et al. (1996) have chosen the weighting function as

$$W\left(t-t'\right) = T^{-1}e^{-(t-t')/T} \tag{2.43}$$

so that the integrals (2.42) and (2.43) will be the solution of the following equations.

$$\frac{DI_{LM}}{Dt} = \frac{\partial I_{LM}}{\partial t} + \bar{\mathbf{u}}.\nabla I_{LM} = \frac{1}{T}\left(L_{ij}M_{ij} - I_{LM}\right) \tag{2.44}$$

$$\frac{DI_{MM}}{Dt} = \frac{\partial I_{MM}}{\partial t} + \bar{\mathbf{u}}.\nabla I_{MM} = \frac{1}{T}\left(M_{ij}M_{ij} - I_{MM}\right) \tag{2.45}$$

where time scale T controls the memory length of the Lagrangian averaging. Meneveau determined this time scale as follows

$$T = 1.5\Delta\left(I_{LM}I_{MM}\right)^{-1/8} \tag{2.46}$$

Equations (2.44) and (2.45) must be discretized in a Lagrangian field. The resulting equations are derived as follows

$$I_{LM}^{n+1}\left(\mathbf{x}\right) = H\left\{\varepsilon\left[L_{ij}M_{ij}\right]^{n+1}\left(\mathbf{x}\right) + \left(1-\varepsilon\right)I_{LM}^{n}\left(\mathbf{x}-\bar{\mathbf{u}}^{n}\Delta t\right)\right\} \tag{2.47}$$

$$I_{LM}^{n+1}\left(\mathbf{x}\right) = \varepsilon\left[M_{ij}M_{ij}\right]^{n+1}\left(\mathbf{x}\right) + \left(1-\varepsilon\right)I_{MM}^{n}\left(\mathbf{x}-\bar{\mathbf{u}}^{n}\Delta t\right) \tag{2.48}$$

$$\varepsilon = \frac{\Delta t/T^{n}}{1+\Delta t/T^{n}} \tag{2.49}$$

$$T^{n} = 1.5\Delta\left(I_{LM}^{n}I_{MM}^{n}\right)^{-1/8} \tag{2.50}$$

$H\left(x\right)$ is the ramp function ($H\left(x\right)=1$ if $x \geq 0$, and zero otherwise).

A tri-linear interpolation is used to approximate the values of $I_{LM}^{n}\left(\mathbf{x}-\bar{\mathbf{u}}^{n}\Delta t\right)$ and $I_{MM}^{n}\left(\mathbf{x}-\bar{\mathbf{u}}^{n}\Delta t\right)$, along the fluid trajectory. The tri-linear interpolation can

introduce some numerical diffusion into (2.47) and (2.48). The resulting diffusion can be reduced by employing a higher order interpolation, although no significant adverse effect can be observed.

2.10.2 The log-law wall model

In the dynamic SGS model, the grid has to be refined to reach the viscous sub-layer near solid walls. If the viscous sub-layer does not exist (because of high roughness), the use of a log-law wall model has advantages over the SGS model. This approach interpolates the velocity close to the solid boundaries by a logarithmic function. As there is no need to refine the grid to resolve the viscous sub-layer, it is computationally more efficient than the SGS model. The essence of this approach is the determination of the shear velocity u_* by a logarithmic relation from the near-wall flow region and the subsequent imposition of a shear stress u_*^2 as a surface force in the momentum equations for the grid cells adjacent to the wall.

For a hydraulically rough solid wall, the log-law has the following form

$$\frac{u}{u_*} = \frac{1}{\kappa} \ln \frac{z}{z_0} \tag{2.51}$$

in which u is the velocity parallel to the wall at a distance of z from the wall and κ is the von Kármán constant. The value of z_0 is defined as $z_0 = k_s/30$ where k_s represents the roughness height. The diameter of the sand particles is related to the roughness height k_s as 2.5 times the sand particles diameter (Van Rijn, 1984c).

For hydraulically smooth solid walls, the standard log-law wall model with viscous sub-layer ($z^+ \leq 5$), the buffer layer ($5 < z^+ < 30$) and the logarithmic layer ($z^+ \geq 30$) is given by

$$u^+ = \begin{cases} z^+ & z^+ \leq 5 \\ 5.0 \ln z^+ - 3.05 & 5 < z^+ < 30 \\ 2.5 \ln z^+ + 5.20 & z^+ \geq 30 \end{cases} \tag{2.52}$$

where u^+ and z^+ represent the non-dimensional parallel velocity to the wall and the non-dimensional normal distance to the wall respectively.

2.11 Numerical experiments

2.11.1 Stokes flow with source

The linear Stokes problem is obtained from the Navier-Stokes equations by ignoring the advection terms. For a constant viscosity ν equations (2.3) and (2.4) yield

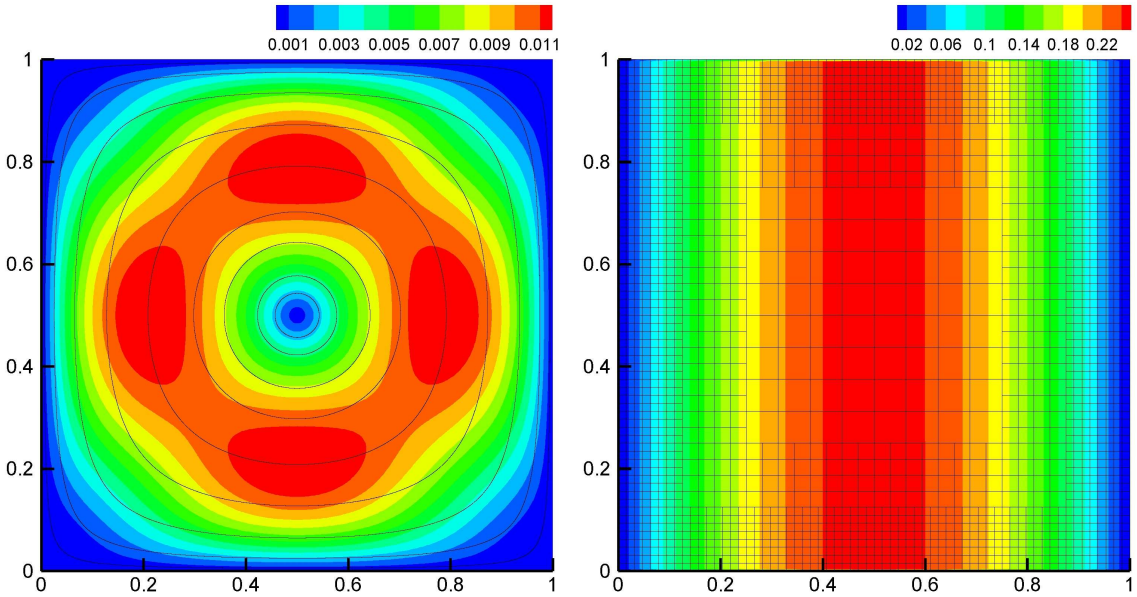

Figure 2.12: Stokes flow with source: computed velocity field (left) and pressure field (right). For visualization purposes, the grid presented is coarser than the grid used in the computation of this figure.

$$\frac{\partial u_j}{\partial x_j} = 0 \tag{2.53}$$

$$\frac{\partial u_i}{\partial t} + \frac{1}{\rho}\frac{\partial p}{\partial x_i} - \nu\frac{\partial^2 u_i}{\partial x_j} = f_i \tag{2.54}$$

This example, taken from Donea and Huerta (2003), has a closed-form analytical solution which is used to determine the convergence rate. A unit viscosity is assumed ($\nu = 1$) and the computational domain is given by the unit square $(0,1) \times (0,1)$. The source functions are given by

$$\begin{aligned} f_x = {} & (12 - 24y)\, x^4 + (-24 + 48y)\, x^3 + \left(-48y + 72y^2 - 48y^3 + 12\right) x^2 \\ & + \left(-2 + 24y - 72y^2 + 48y^3\right) x + 1 - 4y + 12y^2 - 8y^3 \end{aligned} \tag{2.55}$$

$$\begin{aligned} f_y = {} & \left(8 - 48y + 48y^2\right) x^3 + \left(-12 + 72y - 72y^2\right) x^2 \\ & + \left(4 - 24y + 48y^2 - 48y^3 + 24y^4\right) x - 12y^2 + 24y^3 - 12y^4 \end{aligned} \tag{2.56}$$

with zero Dirichlet boundary condition for velocity around the domain. The exact solution to this problem is

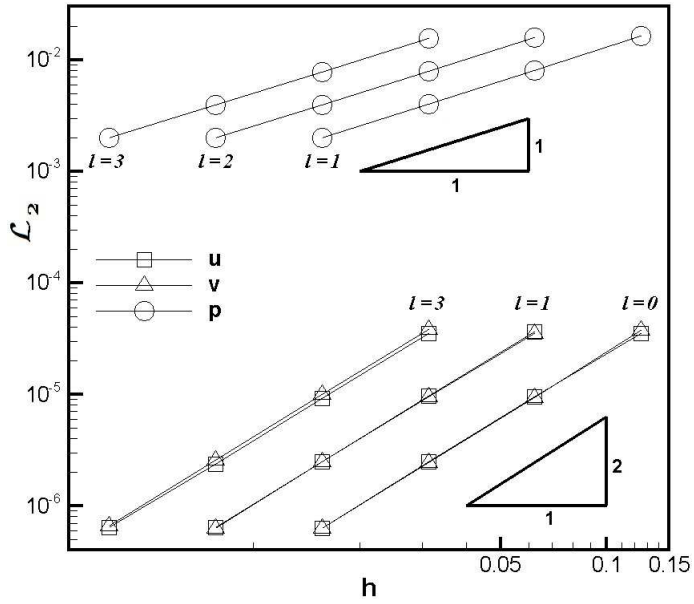

Figure 2.13: Error in the $\mathcal{L}_2$-norm for the velocities in Stokes flow with source. $h = \Delta x = \Delta y$ and l indicates the level number.

$$u = x^2 (1-x)^2 \left(2y - 6y^2 + 4y^3\right) \tag{2.57}$$

$$v = -y^2 (1-y)^2 \left(2x - 6x^2 + 4x^3\right) \tag{2.58}$$

$$p = x (1-x) \tag{2.59}$$

The problem is solved for four different grid resolutions, namely 8×8, 16×16, 32×32 and 64×64 for the base grid. All grids are locally refined by two more levels (three levels grids) in the vicinity of the boundaries.

Figure (2.12) shows the computed flow and pressure field with grid resolution of 64×64. The computed velocity and pressure fields are reasonably smooth. The $\mathcal{L}_2$ error norm for the velocities are shown in Figure (2.13). This norm is defined as

$$\mathcal{L}_2 = \sqrt{\frac{1}{n} \sum_{i=1}^{n} (\varphi_{i,e} - \varphi_{i,s})^2} \tag{2.60}$$

where n is the number of grid points and $\varphi_{i,e}$ and $\varphi_{i,s}$ indicate the exact and numerical solution, respectively. A convergence rate of order two is observed for

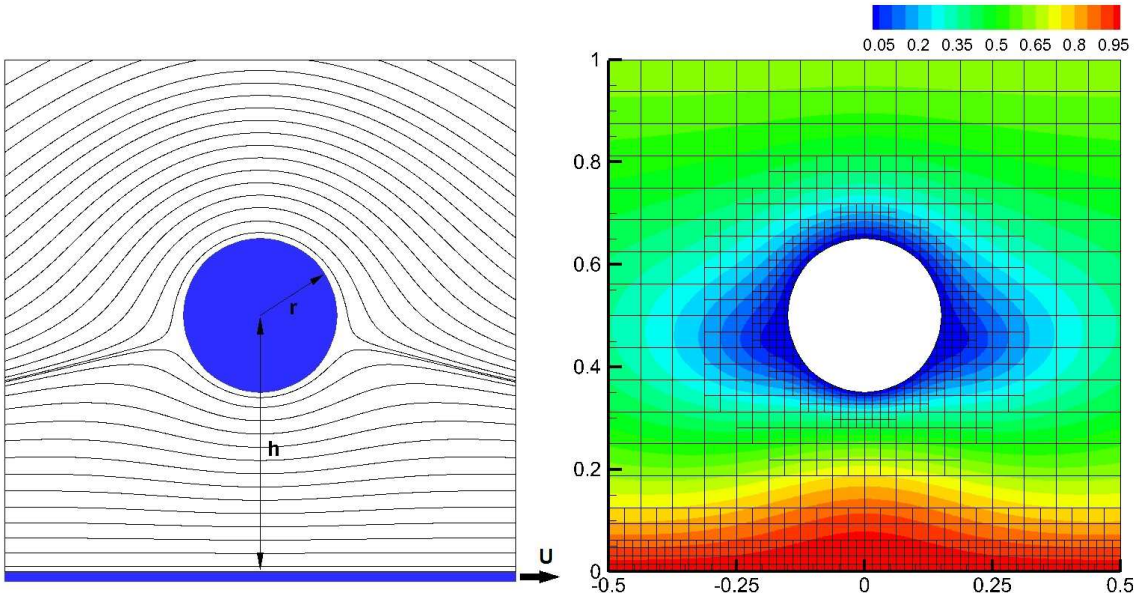

Figure 2.14: Computational domain for Wannier flow and the computed streamlines (left) and the computed velocity field (right). For visualization purposes, the grid presented is coarser than the grid used in the computation of this figure.

the velocity field (meaning that the scheme is second-order accurate for the velocities), whereas the pressure converges at a rate slightly better than one (meaning that the pressure scheme is first-order accurate).

2.11.2 Wannier flow

In order to verify the accuracy of the model including ghost-cell immersed boundaries, Stokes flow around a cylinder in the vicinity of a moving wall is simulated. This problem has been solved analytically by Wannier (1950). Wannier obtained the exact solution for Stokes flow past a spinning cylinder located in the vicinity of an infinite wall moving in the horizontal direction. The flow is bounded by the wall at one side and extends to infinity in other directions (see Figure 2.14). In our validation study we have considered the case where the cylinder is not spinning. The exact solution for this situation is given by

$$\psi = A \ln \frac{x^2 + (s+y)^2}{x^2 + (s-y)^2} + B \frac{y\,(s+y)}{x^2 + (s+y)^2} + B \frac{y\,(s-y)}{x^2 + (s-y)^2} + Dy$$
$$+ Fy \ln \frac{x^2 + (s+y)^2}{x^2 + (s-y)^2} \tag{2.61}$$

where ψ is the stream function. The various parameters are defined as

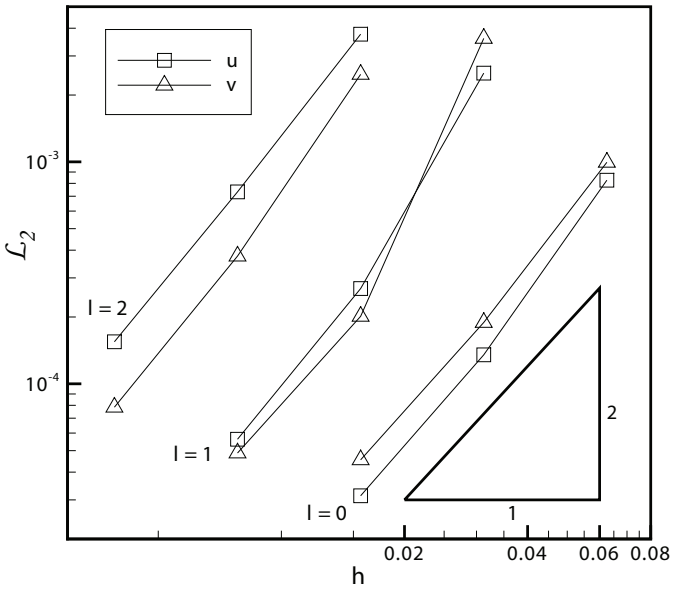

Figure 2.15: Error in the $\mathcal{L}_2$-norm for the velocities in Wannier flow with source. $h = \Delta x = \Delta y$ and l indicates the level number.

$$A = -\frac{Uh}{\ln(\gamma)} \quad , \quad B = \frac{2(h+s)U}{\ln(\gamma)}$$

$$C = \frac{2(h-s)U}{\ln(\gamma)} \quad , \quad D = -U \quad , \quad F = \frac{U}{\ln(\gamma)}$$

$$\alpha = x^2 + (s+y)^2 \quad , \quad \beta = x^2 + (s-y)^2$$

$$s^2 = h^2 - r^2 \quad , \quad \gamma = \frac{(h+s)}{(h-s)}$$

The components of velocity can be derived from the stream function.

$$u = -\frac{2(A+Fy)}{\alpha}\left[(s+y) + \frac{\alpha}{\beta}(s-y)\right] - D - F\ln\left(\frac{\alpha}{\beta}\right)$$
$$-\frac{B}{\alpha}\left[(s+2y) - \frac{2y(s+y)^2}{\alpha}\right] - \frac{C}{\beta}\left[(s-2y) + \frac{2y(s-y)^2}{\beta}\right] \tag{2.62}$$

$$v = \frac{2x}{\alpha\beta}(A+Fy)(\beta-\alpha) - \frac{2Bxy(s+y)}{\alpha^2} - \frac{2Cxy(s-y)}{\beta^2} \tag{2.63}$$

where u and v are the components of velocity in x- and y-directions respectively.

In the above expressions, U is the velocity of the wall, r the radius of the cylinder, and h the distance of the wall from the center of the cylinder. All boundary conditions have been calculated analytically from equations (2.62) and (2.63). The flow is calculated for three different grid resolutions, namely 16×16, 32×32 and 64×64 as base grid. All grids are locally refined by two more levels (three levels grids) around the cylinder and the moving wall. The results of the current simulation is compared with the Wannier relations, and the $\mathcal{L}_2$ norm is plotted in Figure (2.15) to determine the global accuracy of the model and it shows a convergence rate of slightly more then two for velocities.

2.11.3 Flow around a circular cylinder

The simulation of flow around a cylinder is an interesting task, because its behaviour can change dramatically as a function of Reynolds number. In high Reynolds numbers, the flow separates and forms vortex shedding, which is called Kármán vortex street. This flow has been studied extensively numerically and experimentally.

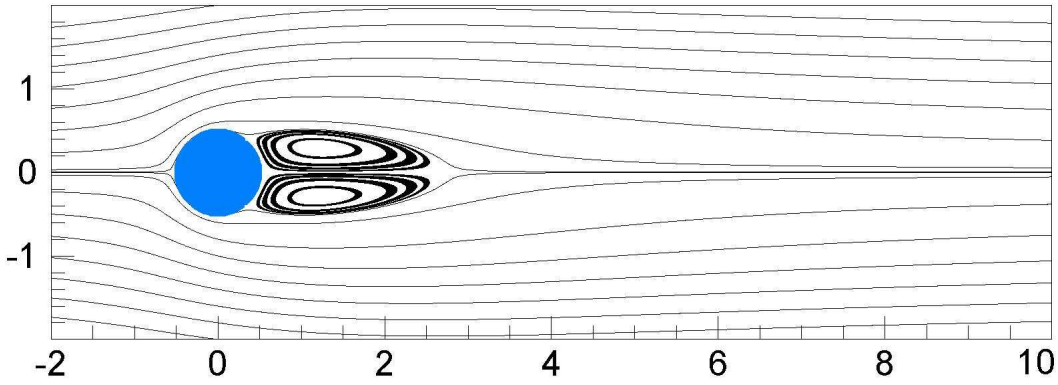

Figure 2.16: Streamlines for $Re = 40$ cylinder.

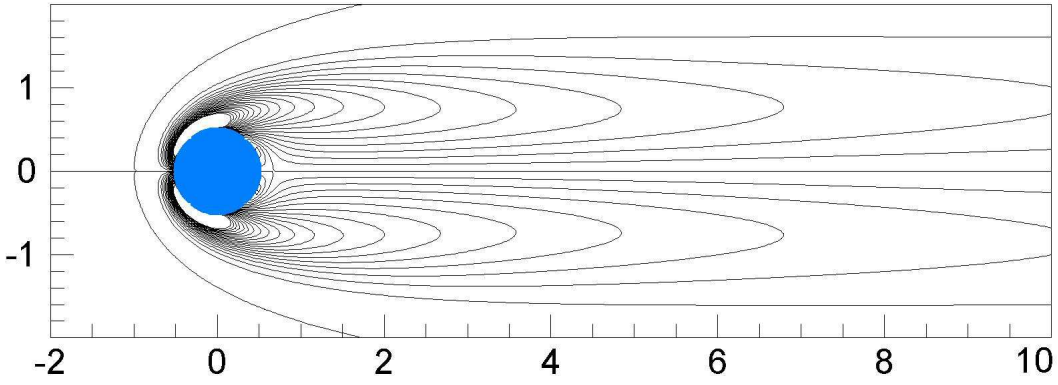

Figure 2.17: Vorticity for $Re = 40$ cylinder. Contour values are $-4 : 0.2 : 4$.

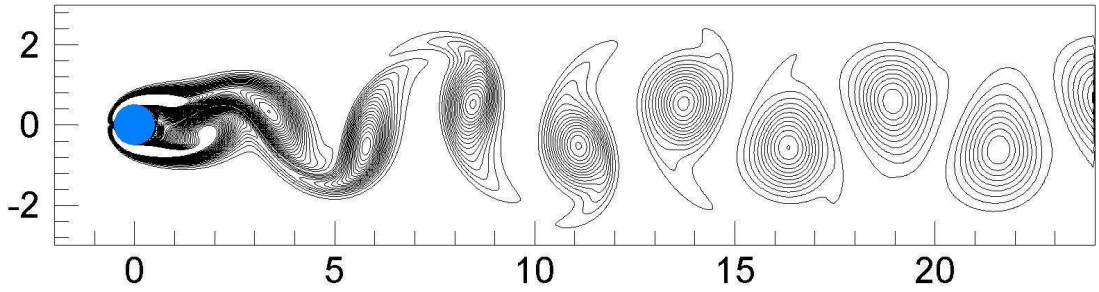

Figure 2.18: Vortex street behind cylinder at $Re = 100$. Contour values are $-2.5 : 0.1 : 2.5$.

Table 2.1: Summary of results for $Re = 20$ and $Re = 40$.

	$Re = 20$			$Re = 40$		
	L	θ	C_D	L	θ	C_D
Ye et al. (1999)	0.9	–	2.0	2.3	–	1.5
Tseng and Ferziger (2003)	–	–	–	2.21	–	1.53
Pan (2006)	0.85	–	2.01	2.13	–	1.5
Xu and Wang (2006)	0.92	44.2	2.23	2.21	53.5	1.66
Tritton (1959)	–	–	2.22	–	–	1.48
Coutanceau and Bouard (1977)	0.73	42.3	–	1.89	52.8	–
Fornberg (1980)	0.91	–	2.00	2.24	–	1.50
Dennis and Chang (1970)	0.94	43.7	2.05	2.35	53.8	1.52
Calhoun (2002)	0.91	45.5	2.19	2.18	54.2	1.62
Russell and Wang (2003)	0.94	43.3	2.13	2.29	53.1	1.60
Present	0.93	44.2	2.21	2.22	53.5	1.58

The simulation has been performed at three different Reynolds numbers $Re = 20$, 40 and 100, based on the freestream velocity and the diameter of the cylinder. This flow has been solved by Tritton (1959), Dennis and Chang (1970), Coutanceau and Bouard (1977), Fornberg (1980), Ye et al. (1999), Kim et al. (2001), Calhoun (2002), Tseng and Ferziger (2003), Russell and Wang (2003), Pan (2006) and Xu and Wang (2006).

The non-dimensional far-field stream velocity was held constant at $U_\infty = 1\,\mathrm{m/s}$. The base calculations were done on a 1024×512 grid. Figures (2.16) and (2.17) show the streamlines and the vorticity contours for $Re = 40$, respectively. Figure (2.18) shows the expected trailing von Kármán vortex street at $Re = 100$. This particular simulation was run to a non-dimensional time of 150 to ensure full development of the quasi-steady-state condition.

Table (2.1) shows a summary of results for steady-state solutions. We compared the length of the trailing bubble, the angle of separation, and the drag coefficient. These geometric results compare very favorably with both experimental and previous computational results.

2.11.4 Driven cavity flow

The three-dimensional lid-driven cavity flow is a simple viscous incompressible flow case that has many features suitable for testing the performance of the present hydrodynamic model, including primary and secondary vortices, wall boundary layers, and flow separation and reattachment. This test considers the incompressible Navier-Stokes problem on the cubic domain $\Gamma\,(0,1) \times (0,1) \times (0,1)$ with pure Dirichlet boundary conditions, imposing $\vec{u} = [1,0,0]^{-1}$ on the upper boundary at $y = 1$, and $\vec{u} = [0,0,0]^{-1}$ elsewhere on $\partial\Gamma$, defining length- and velocity scales $L_{ref} = 1$ and $U_{ref} = 1$, respectively. The viscosity ν is adjusted in order to obtain Reynolds numbers of 100, 400 and 1000, respectively. The computational domain is discretized by uniform cubes with mesh size $h_e = 1/128$ including only one grid level. The simulations begin from zero velocity and continue until a steady state flow has been achieved.

Figure (2.19) presents the velocity profiles along the vertical centreline of the cubic cavity for Reynolds numbers 100, 400 and 1000. These predictions are compared with those by Goda (1979), Ku et al. (1987) and Mahallati and Militzer (1993) for $Re = 100$ and 400, while for $Re = 1000$, results from Ku et al. (1987) and Mahallati and Militzer (1993) are available. Figure (2.19) shows the present results have a very good agreement with the results obtained by Ku et al. (1987). Figure 2.20 presents the velocity profile along the horizontal centreline for Reynolds numbers 100, 400 and 1000. These profiles are compared with Ku et al. (1987) and it is clear that the present results are in a good agreement with Ku's results.

2.11.5 Flow in a straight channel

The unsteady Navier-Stokes equations are solved at a Reynolds number of 3300, based on the mean centre-line velocity and channel half-width. The computational domain in streamwise and transverse directions is chosen to be $4\pi\delta \times 2\pi\delta$, where δ is the channel half-width. These configurations are identical with the configurations chosen by Kim et al. (1987). The aim is to validate the model by comparing the velocity profile close to the solid boundaries and the root-mean-square velocity fluctuations profiles with the DNS simulation by Kim et al. (1987).

The flow is solved until homogenous turbulence is obtained. The averaging begins after the flow has reached its statistically steady state. The averaging is done over 15 large-eddy time cycles to obtain the time-mean values of the velocity and the turbulence statistics. It is taken into account that the first grid points close to the wall are within the viscous sublayer, $u^+ = y^+$ for $y^+ < 5$. This is a necessary condition for the dynamic models in LES to be valid in wall-bounded turbulent flows because near-wall eddy structures scale with the viscous length scale (Pope, 2004).

Figure (2.21) shows the velocity profile normalized by the wall shear velocity

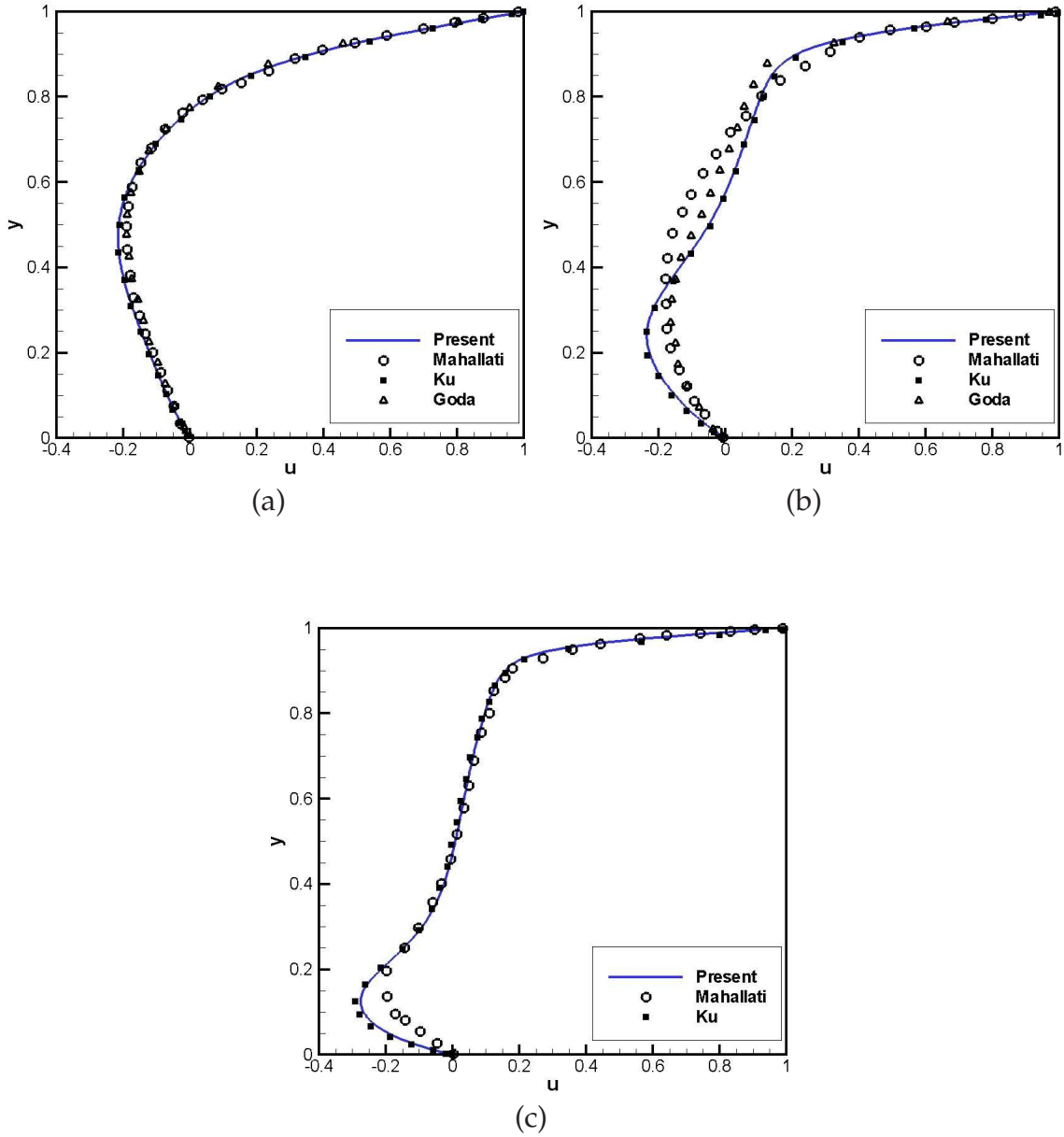

Figure 2.19: Velocity profile on the vertical centreline of the cubic cavity for: (a) $Re = 100$; (b) $Re = 400$; (c) $Re = 1000$

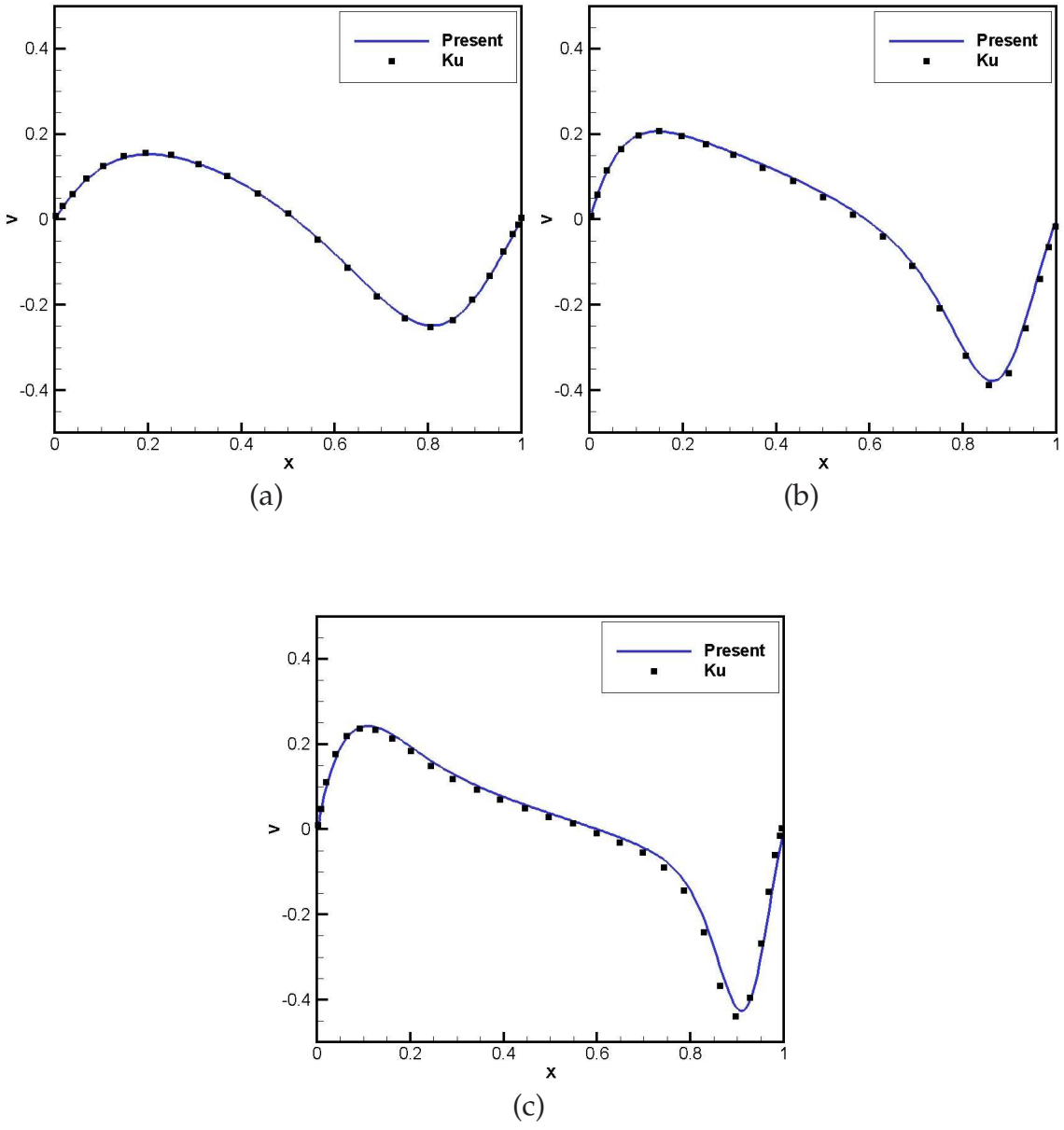

Figure 2.20: Velocity profile on the horizontal centreline of the cubic cavity for: (a) $Re = 100$; (b) $Re = 400$; (c) $Re = 1000$

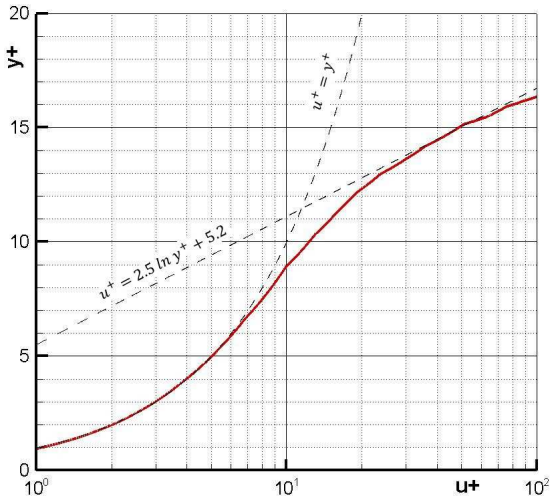

Figure 2.21: Mean velocity profile in the vicinity of the lower wall, compared with the log-law of the wall.

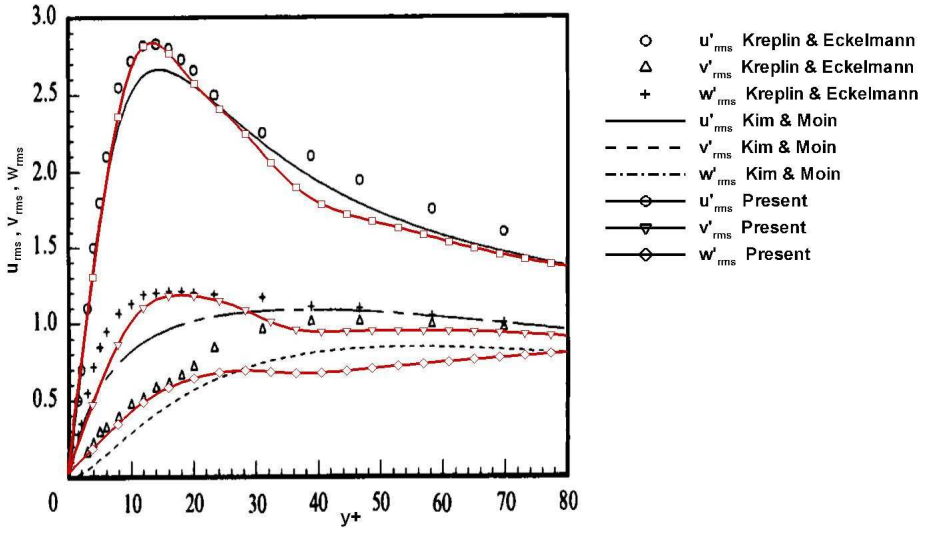

Figure 2.22: Root-mean-square velocity fluctuations normalized by the wall shear velocity, compared with measurements by Kreplin and Eckelmann (1979) and DNS results by Kim et al. (1987).

u_* in the vicinity of the bottom wall. It is shown that the profile of u^+ is close to the theoretical value (log-law).

Turbulence intensities normalized by the wall shear velocity are shown in Figure (2.22) as a function of the wall-coordinate. All these results show a good agreement with the theory and the DNS results by Kim et al. (1987), as well as with the experimental measurements conducted by Kreplin and Eckelmann (1979).

2.11.6 Flow over a sinuous bed

In this section the results of LES over a two-dimensional sinuous bed are presented. The bed is considered as a sinusoidal wavy form with wave height and length of 2δ and λ respectively. A wave slope $2\delta/\lambda = 0.1$ is considered, corresponding with well-separated crests. The maximum height of the channel is $H = \lambda$ and the size of the domain in streamwise and transverse directions is considered 2λ. The mean channel height and the bulk velocity are used as the length and velocity scales. The bulk velocity is defined as the average velocity in x-direction in a plane parallel to the yz-plane at a position with a height of $H - \delta$.

$$U = \frac{1}{(H-\delta)\, L_z} \int_A u dA \tag{2.64}$$

where L_z is the length in the transverse direction. The Reynolds number has been set to 6760 based on the length scale H and velocity scale U. This simulation is similar to the DNS simulation by Maaß and Schumann (1996) and the LES simulation by Balaras (2004).

Periodic boundary conditions have been imposed in streamwise and transverse directions. On the roof, a non-slip boundary is imposed. A ghost-cell immersed boundary method is used to enforce the non-slip condition on the bottom. The present problem is simulated using a base grid $32 \times 32 \times 32$ in streamwise, normal and transverse directions, with three levels of refining (four-levels grid). It means the size of the smallest cells in x-direction is

$$\Delta x_{finest} = \frac{\Delta x_0}{2^{4-1}} = \frac{\Delta x_0}{8} \tag{2.65}$$

Because of isotropy of the grid, the sizes in y- and z-directions are $\Delta y_0/8$ and $\Delta z_0/8$. Δx_0, Δy_0 and Δz_0 are the sizes of a cell on the base grid (without refining). The finest cells are located in the vicinity of the non-slip boundaries. Figure (2.23) illustrates the computational domain and the grid with three levels of refining (four-levels grid). The flow is driven by a pressure gradient in x-direction. After each time step, the bulk velocity is calculated and the pressure gradient is determined in a way that the bulk velocity remains constant.

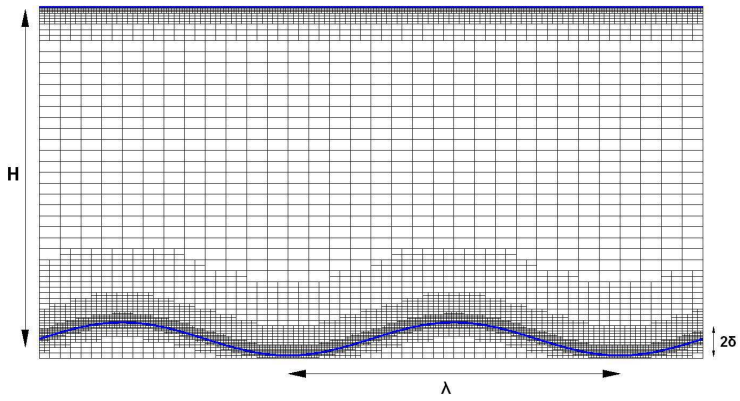

Figure 2.23: Computational domain and the underlying grid for flow in a wavy-bed channel. A four-levels grid is used.

Figures (2.24) and (2.25) show the profiles of average velocities in streamwise and normal directions, respectively. The intersections are parallel to the yz-plane and located at $x/\lambda = 0.1, 0.3, 0.5$ and 0.7. The length is normalized by λ and the velocities are normalized by the bulk velocity U. All these figures show that the DNS simulation by Maaß and Schumann (1996) and LES simulations by Balaras (2004) are in good agreement with the present numerical results.

2.11.7 Flow over a fixed dune

In this section the results of LES over a two-dimensional fixed dune are presented. The set-up of the simulation performed was selected from the laboratory experiment undertaken by Balachandar et al. (2002). In this experiment, the measurements were made on the 17th dune of a train of 22 two-dimensional dunes that were attached to the bottom of the flume. These configurations were also solved numerically by Yue et al. (2006) and Stoesser et al. (2008). Therefore we use it as validation case for the present work. Figure (2.26) shows the configuration of the selected dune. The Reynolds and Froude numbers, based on water depth L and free-surface velocity U_0 at the inlet of the domain are considered to be 5.7×10^4 and 0.44 respectively. The non-dimensional wavelength is $\lambda/h = 20$, and the non-dimensional water depth is $L/h = 6$.

This simulation is similar to the LES simulation by Yue et al. (2006). Periodic boundary conditions have been applied in streamwise and spanwise directions. The free surface is approximated by a free-shear boundary condition. A ghost-cell immersed boundary method is used to enforce the non-slip condition on the bed. The present problem is simulated using a multi-levels grid with initial cells of $32 \times 32 \times 16$ in streamwise, normal and spanwise direction respectively. Three refining levels are considered and the finest grid is located in the vicinity of the

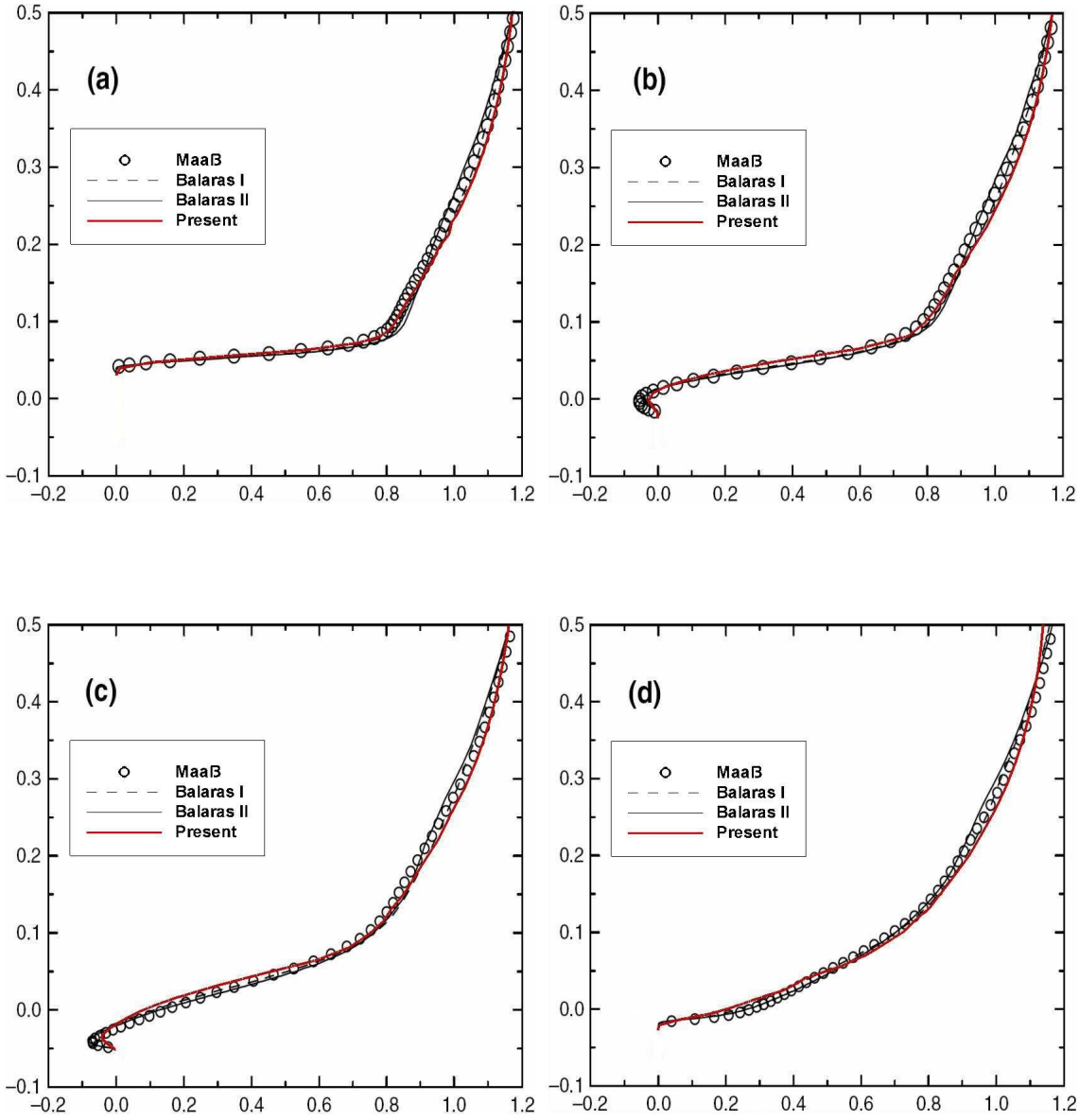

Figure 2.24: Mean streamwise velocity profiles at different streamwise locations at (a) $x/\lambda = 0.1$, (b) $x/\lambda = 0.3$, (c) $x/\lambda = 0.5$, and (d) $x/\lambda = 0.7$.

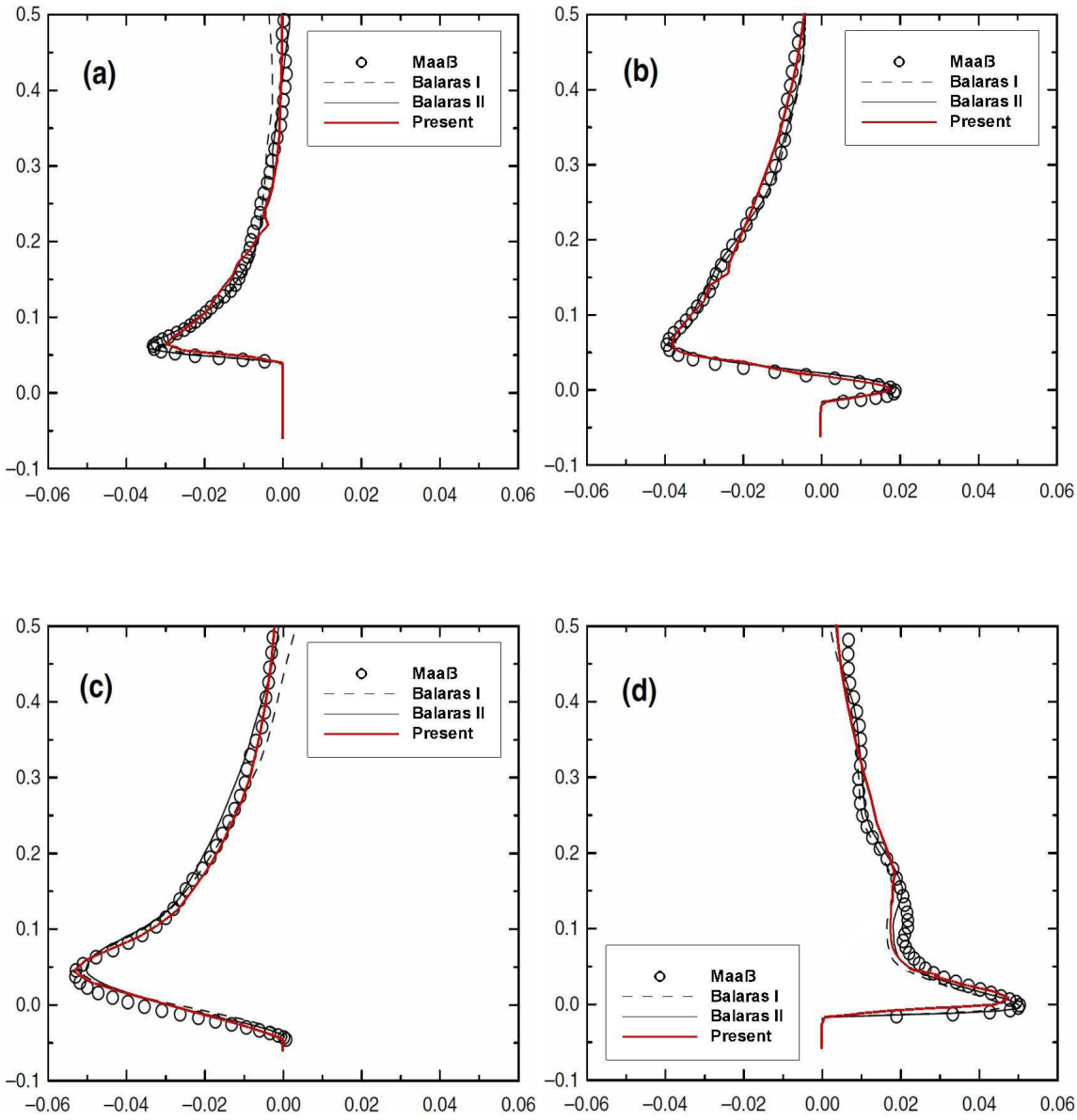

Figure 2.25: Mean normal velocity profiles at different streamwise locations at (a) $x/\lambda = 0.1$, (b) $x/\lambda = 0.3$, (c) $x/\lambda = 0.5$, and (d) $x/\lambda = 0.7$.

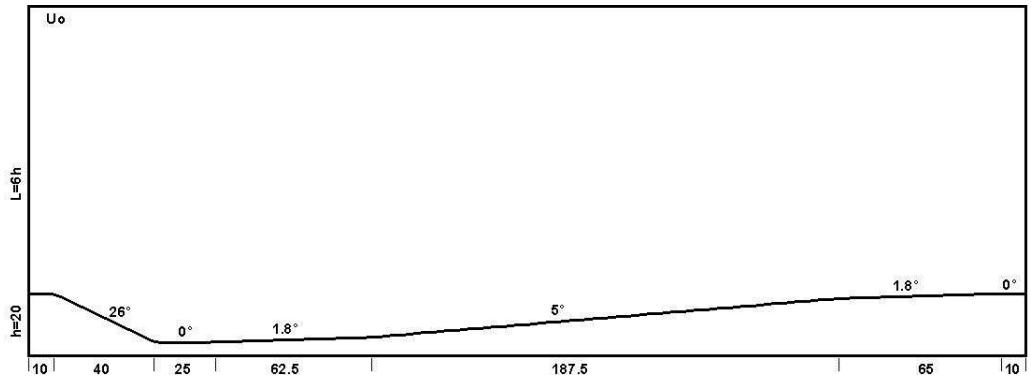

Figure 2.26: Dune geometry in a vertical plan.

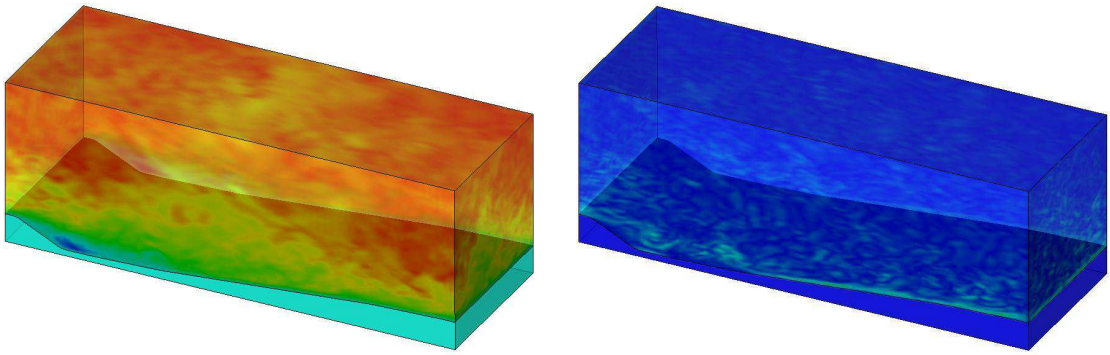

Figure 2.27: Instantaneous streamwise velocity (left) and vorticity (right) on a fixed dune.

bed.

Figure (2.27) shows the instantaneous streamwise velocity and vorticity of the current dune. Figure (2.28) shows the average velocity profiles in four different intersections. The intersections are parallel to the yz plane and located at $x/h =$ 4, 5, 12 and 18. h is defined as the height of the dune. The first two intersections are located after the dune crest inside the recirculation zone. The last station is just before the dune crest at $x/h = 18$. The lengths are normalized by h and the velocities are normalized by the reference free-surface velocity U_0.

The results are compared with the experimental measurements of Balachandar et al. (2002) and the LES simulation of Yue et al. (2006). From Figure (2.28), it is clear that the present results are in good agreement with experimental and numerical results obtained before.

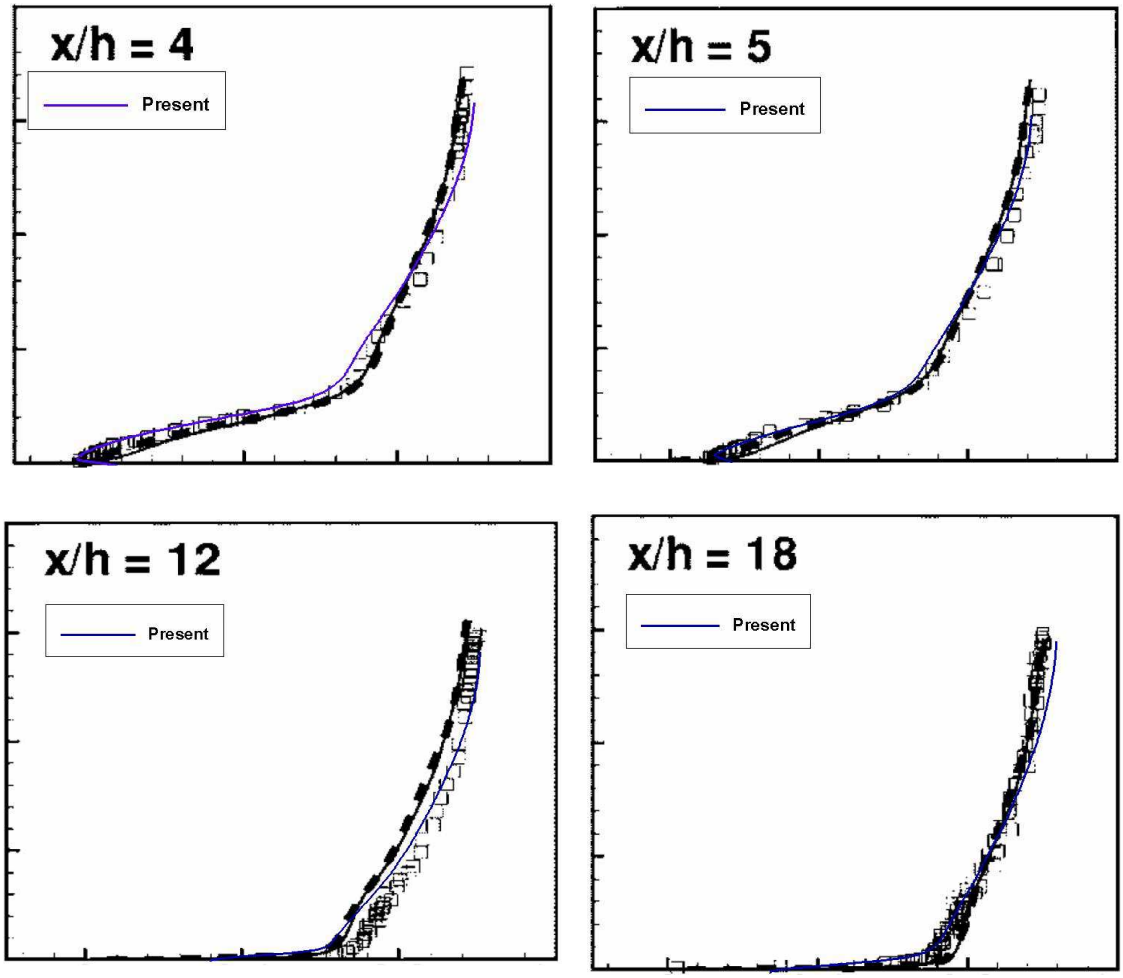

Figure 2.28: Mean wall-normal velocity profiles at different streamwise locations: □ LES of Yue et al. (2006), - - - Balachandar et al. (2002) and — the present LES, for (a) $x/h = 4$, (b) $x/h = 5$, (c) $x/h = 12$, (d) $x/h = 18$.

Chapter 3

Sediment pick-up, transport and deposition

3.1 Introduction

Morphological changes are due to deposition and erosion of sediment. Morphological modelling without a sediment transport model is therefore difficult to imagine. The formation of ripples, dunes, bars and other alluvial forms is governed by flow-induced sediment motion, the structure of the bed and sediment-bed interactions. Given the small particle size, turbulence at Kolmogorov scales is relevant to sediment motion. The lack of accurate physics-based models of sediment transport at these scales makes the prediction of small-scale alluvial processes such as ripple and dune formation difficult. Rolling and saltation of sediment grains over the bed in turbulent flow are inherently complex problems. Turbulence produces near-bed velocity and pressure fluctuations that give rise to fluctuations in the forces on and the resultant motion of sediment particles, due to which sediment may be picked up and transported by the fluid. On the other hand, the presence of sediment particles in the flow may generate or suppress turbulence, thus creating a dynamic feedback system.

In the past, sediment transport has mainly been described in terms of bulk fluxes related to mean flow properties. Some of these sediment transport formulae include a threshold of motion: the critical shear stress. Shields (1936) was a pioneer in describing this critical shear stress in unidirectional shear flow. White (1940), Iwagaki (1956), Coleman (1967), Wiberg and Smith (1987), Zanke (1990), Ling (1995), Dey (1999), Dey and Debnath (2000), McEwan and Heald (2001), Paphitis (2001), Papanicolaou et al. (2001), Kleinhans and van Rijn (2002), Wu and Chou (2003) and Dey and Papanicolaou (2008) addressed the issue of incipient motion as a function of the mean bed shear stress via a deterministic analysis of noncohesive sediment particles on a loose sediment bed. In contrast to this deterministic view, the stochastic view is that turbulent stress variations are responsible for the initial dislodgment of sediment. Einstein and El-Samni (1949),

Paintal (1971), Nelson et al. (1995), Cheng and Chiew (1998) and Papanicolaou et al. (2002) deal with sediment entrainment based on stochastic approaches.

Schmeeckle and Nelson (2003) applied Direct Numerical Simulation (DNS) for bedload transport. The difficulty arising in this kind of simulations is how to define the lift force applied on the sediment particles. The phenomenon of particle lift is still not completely understood and adequate experimental results are not available to determine a reliable quantitative relationship. Saffman (1965) considered the lift force on a small sphere in an unbounded, linear shear flow. He assumed the particle and shear Reynolds numbers to be much smaller than unity and the particle Reynolds number to be much smaller than the shear Reynolds number. Harper and Chang (1968) extended Saffman's analysis to arbitrary three-dimensional bodies in linear shear flow. Drew (1978) performed a similar analysis for a small sphere in two-dimensional strain flow. McLaughlin (1991) extended Saffman's analysis to situations in which the particle Reynolds number is not necessarily small compared to the shear Reynolds number. Kurose and Komori (1999) studied the lift and drag forces on a rotating sphere in a linear shear flow. They applied Direct Numerical Simulation (DNS), and investigated the effects of both shear and rotational speed on the drag and lift forces for particle Reynolds numbers $1 \leq Re_p \leq 500$. They showed their DNS results to be in good agreement with McLaughlin's results.

Here we develop a high-resolution 3D numerical model for morphodynamic processes on small temporal and spatial scales, based on large eddy simulation, direct numerical simulation of sediment particle motion, and adaptive grid refinement and submerged boundary techniques for mobile beds. In this chapter we present the submodel for sediment motion, which consists of modules for pick-up, transport over the bed, transport in the water column and deposition. The sediment is modelled as rigid spherical particles in the turbulent flow. Depending on the shear stresses, the particles slide as a sheet layer over the bed or separate from the bed while jumping or being suspended by the flow. We test the sediment submodel against well-established analytical and empirical relations and find that the model correctly reproduces the settling velocity of a single particle in stagnant water, the angle of repose after avalanching and the Rouse profile for the concentration of suspended sediments. Furthermore, computed sediment transport rates are within the range of values predicted by empirical transport formulae and agree in particular with the formulae of Meyer-Peter and Müller (1948) and Wiberg and Smith (1987).

3.2 Particles model versus conservation form

Two common techniques are commonly employed to consider the particulate sediment behaviour, either a conservation equation for sediment fluxes (Eulerian) or tracking the motion of individual particles in a Lagrangian framework.

In the former approach, the sediment is considered as a continuous medium (fluid) moving in the main fluid (here water). Similar to the fluid, a conservation form for sediment can be derived, including diffusion and advection terms. This approach simulates the sediment as a cloud of concentration. The main advantage of this method is the low computational costs; only one extra equation needs to be solved.

The Lagrangian approach is computationally more expensive. In this approach, the sediments are considered as small discrete particles moving in the fluid. The motion of sediment particles is governed by the hydrodynamic and gravity forces. As a result, two equations must be solved for each particle, describing the velocity and the trajectory of the particle, respectively.

The Lagrangian approach is more suitable for problems which include a finite number of sinks or sources of sediment. The physical phenomena of sediment transport are incorporated directly, which can be mentioned as the main advantage of this approach. The detailed motion of the particles such as jumping, rolling and sliding can be explicitly simulated, which gives a better insight into the detailed behaviour of the sediment.

Although the techniques based on a Lagrangian framework are relatively expensive, they have numerous advantages over Eulerian methods. Therefore, we apply this approach in the present study. This choice enables us to simulate the physical behaviour of particles such as their discontinuous jumping with the proper step length. To predict the trajectory of each solitary particle, the forces applied on the particle must be determined, as explained in the next section.

3.3 Forces on a single particle

A particle immersed in a fluid is subject to gravity and fluid forces. In the next sections, these forces are formulated.

3.3.1 Drag force

The drag force is caused by pressure gradients and viscous skin friction. As both are proportional to the relative flow velocity squared, the drag force can be expressed as

$$\vec{F}_{drag} = C_D \frac{\pi}{8} d^2 \rho \left(\vec{u}_f - \vec{v}_p\right) \left|\vec{u}_f - \vec{v}_p\right| \tag{3.1}$$

where ρ is the mass density of the fluid, d is the particle diameter, C_D is the drag coefficient, $\vec{v}_p$ is the particle velocity, and $\vec{u}_f$ is the flow velocity in the centre of the particle, if the particle would be absent. Figure (3.1) shows the relation between the drag coefficient C_D and the particle Reynolds number Re_p ($Re_p = \left|\vec{u}_f - \vec{v}_p\right| d/\nu$), with ν denoting the kinematic viscosity. This figure is taken from

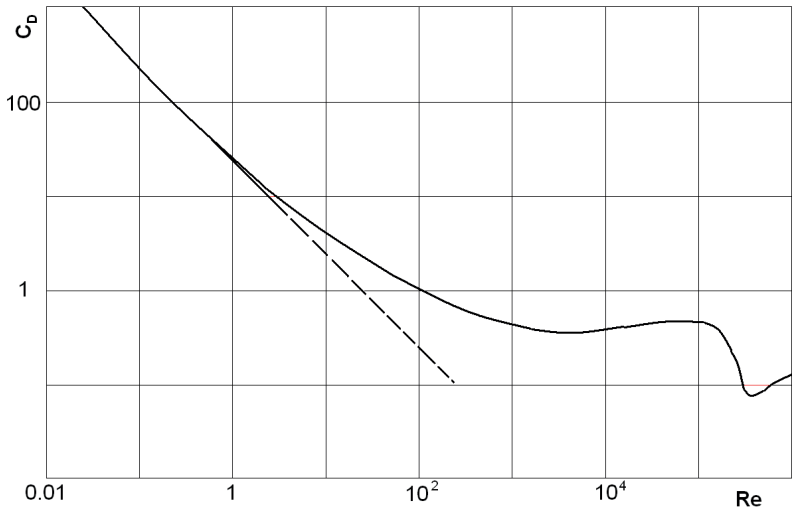

Figure 3.1: The dependence of the drag coefficient on the particle Reynolds number. The line indicates a linear relation for relatively low particle Reynolds numbers (Morsi and Alexander, 1972).

the experimental studies of Morsi and Alexander (1972) for non-rotating spheres. Their experiments showed that C_D can be approximated as a function of Re_p only. Kurose and Komori (1999) showed the drag force to be a function of the Reynolds particle number and the particle rotation speed. They showed that the effect of the rotation speed is relatively small, whence we neglect it in the present study. We adopt the empirical equation for the drag coefficient C_D proposed by Morsi and Alexander (1972)

$$C_D = a_0 + \frac{a_1}{Re_p} + \frac{a_2}{Re_p^2} \tag{3.2}$$

where a_0, a_1 and a_2 are coefficients dependent on Re_p. The values of a_0, a_1 and a_2 for different particle Reynolds numbers are given in Appendix A.

3.3.2 Lift force

Rubinow and Keller (1961) and Saffman (1965) analyzed the lift force acting on a rotating sphere in a linear unbounded shear flow using matched asymptotic expansions. In their analysis, the particle Reynolds number was assumed to be much less than unity. Saffman's expression for the lift force on a sphere derived by higher-order approximations is given by

$$F_L = 6.46\nu\rho(d/2)^2 u_r \left(|\alpha|/\nu\right)^{0.5} \text{sign}\,(\alpha) - \frac{11}{8}\rho u_r \alpha (d/2)^3 + \pi\rho u_r \Omega (d/2)^3 \tag{3.3}$$

where α is the shear rate of the mean flow, u_r is the relative velocity ($u_r = u_f - v_p$), and Ω is the angular speed of the sphere. The first and second terms on the right-hand side are due to the fluid shear, the third term represents the so-called Magnus effect, due to the rotation of the sphere. The lift force on a stationary ($\Omega = 0$) sphere in a linear shear flow always acts towards the higher-fluid-velocity side, and in uniform unsheared flow ($\alpha = 0$) a rotating sphere with its top part moving in the flow direction is always subject to an upward lift.

Saffman (1965) mentioned that, unless the rotational speed of a freely rotating sphere with a small particle Reynolds number is much greater than the shear rate, the lift force due to the rotation (Magnus effect) is at least an order of magnitude smaller than that due to the shear. Moreover, the second term in Equation (3.3) is much smaller than the first one, as it is of higher order in terms of the particle size. Therefore, in many previous studies the second and third terms on the right-hand side of Equation (3.3) were neglected. The lift coefficient for a spherical particle is defined by

$$C_L = \frac{F_L}{0.5\rho u_r^2 \pi (d/2)^2} \tag{3.4}$$

By substituting Equation (3.3) into Equation (3.4),

$$C_L = \frac{12.92}{\pi}\varepsilon - \frac{11}{8\pi}\frac{d}{u_r}\alpha + \frac{d}{u_r}\Omega \tag{3.5}$$

where ε represents the ratio of the square root of the shear Reynolds number to the particle Reynolds number, $\varepsilon = \mathrm{Re}_\alpha^{0.5}/\mathrm{Re}_p$.

Note that the following assumptions underly the derivation of Equation (3.3):

$$\mathrm{Re}_p = \frac{u_r d}{\nu} \ll 1 \tag{3.6}$$

$$\mathrm{Re}_\Omega = \frac{\Omega d^2}{\nu} \ll 1 \tag{3.7}$$

$$\mathrm{Re}_\alpha = \frac{\alpha d^2}{\nu} \ll 1 \tag{3.8}$$

$$\varepsilon = \frac{\mathrm{Re}_\alpha^{0.5}}{\mathrm{Re}_p} \gg 1 \tag{3.9}$$

Equation (3.3) can be used with confidence only if the above conditions are met. In practice, however, particle motion in turbulent flow often involves particle Reynolds numbers larger than 1, so that conditions (3.6) through (3.9) are no longer satisfied.

McLaughlin (1991) extended Saffman's analysis to remove the restriction given by Equation (3.9). In his analysis, ε does not need to be large compared to unity. Mei (1992) obtained the following relation from McLaughlin's results.

$$\frac{C_L}{C_{L,Sa}} = 0.443J \tag{3.10}$$

The index Sa denotes the corresponding result obtained by Saffman (1965), neglecting the second and third terms on the right hand side of Equation (3.3). Saffman's result is obtained for $J = 2.225$ and large ε. Mei (1992) fitted a curve through the data from the table in McLaughlin (1991), to obtain a relation for J for $0.1 \leq \varepsilon \leq 20$.

$$J = J(\varepsilon) \approx 0.6765 \left\{1 + \tanh\left[2.5\log_{10}(\varepsilon + 0.191)\right]\right\} \left\{0.667 + \tanh\left[6(\varepsilon - 0.32)\right]\right\} \tag{3.11}$$

Kurose and Komori (1999) studied the lift and drag forces on a rotating sphere in linear shear flow. They applied Direct Numerical Simulation (DNS), and investigated the effect of both shear and rotational speed of a sphere on the drag and lift forces for particle Reynolds numbers $1 \leq Re_p \leq 500$ and $0.1 \leq \alpha^* \leq 0.4$, where α^* is defined as

$$\alpha^* = \frac{d}{2u_r}\alpha \tag{3.12}$$

Their results are in a good agreement with those obtained by McLaughlin (1991). In the present study, we apply McLaughlin's relations to estimate the lift force on a sediment particle.

3.3.3 Submerged weight

Gravity and buoyancy forces are of major importance to the motion of sediment particles. The directions of gravity and buoyancy forces are opposite to each other, and the sum of gravity and buoyancy forces can be described as submerged weight. The submerged weight of a particle is given by

$$\vec{F}_G = \frac{\pi}{6} d^3 \left(\rho_p - \rho\right) \vec{g} \tag{3.13}$$

where ρ_p is the density of the sediment, ρ is the density of the fluid, and g is the gravitational acceleration.

3.3.4 Other forces

More forces, such as added mass and Basset forces, affect particle motion. Added mass or virtual mass is the inertia added to a particle because an accelerating or

decelerating particle must move some volume of surrounding fluid as it moves through it, since the particle and the fluid cannot occupy the same physical space simultaneously. For simplicity, this can be modelled as some volume of fluid moving with the object. The added mass force can be calculated by

$$\vec{F}_{add} = C_m \rho V_p \left(\frac{D\vec{u}_f}{Dt} - \frac{d\vec{v}_p}{dt} \right) \tag{3.14}$$

where $\vec{v}_p$ and $\vec{u}_f$ are the particle velocity and the fluid velocity at the particle centre of mass (if the particle was not present) respectively. The coefficient C_m is the added mass coefficient and is equal to 0.5 for spheres (Auton, 1987), V_p is the volume of the particle and ρ is the density of the fluid.

The Basset force is the force associated with past movements of the particle (interaction of the particle with its own wake). The Basset force is often relatively small (Armenio and Fiorotto, 2001), whence it is neglected in the present study.

3.4 Models for sediment movement

The motion of sediment on and above the river bed can be considered to follow three stages, namely, pick-up, transport and deposition. The transport is in suspension if the shear stress is sufficiently high, but in the form of a sliding behaviour if the shear stress is relatively low, albeit above the critical shear stress. In the next sections, we model these four modes of motion separately.

3.4.1 Sediment pick-up

The bed of a river can be approximated by interlocking layers of spherical particles. If the shear stress of the flow on the bed exceeds a certain value, the particles begin to rotate and may move from their positions. This stress level is called the critical shear stress, and the initiation of motion of particles is called incipient motion.

Figure (3.2) shows the bed schematically. Each spherical solitary particle is resting on three other closely packed spherical particles. It is the most stable three-dimensional configuration for spherical particles (Dey, 1999). The sizes of the particles are considered to be equal. Depending on the orientation of the three bed particles with respect to the direction of exerted forces, the solitary particle tends to roll either over the valley between two supporting particles, over the summit of a single particle, or somewhere in between.

The incipient motion of sediment is determined by the resultant of the mentioned forces. Figure (3.3) shows the forces acting on a spherical particle. The submerged weight is always in the downward direction. The drag force is parallel to the flow direction and the lift force is in the direction normal to the bed

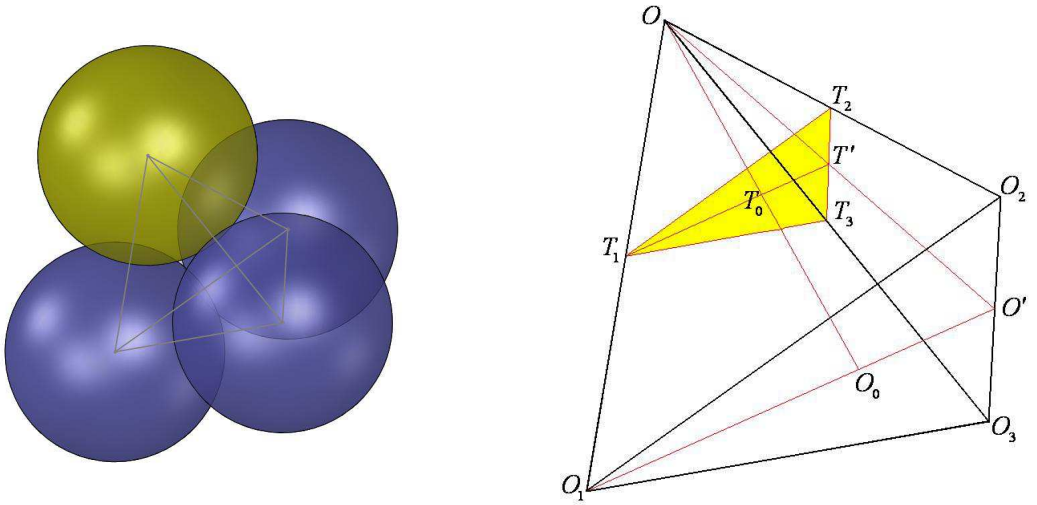

Figure 3.2: The configuration of a solitary particle on the three packed bed particles (left), and a tetrahedron formed joining the centres of the four particles (right).

at the pick-up point. The motion of spherical particles begins mostly by rolling, sometimes by sliding. For simplicity, incipient motion by sliding is ignored.

When a solitary particle is about to dislodge from its original position, the balance of moments about the point of contact M requires

$$\sum \vec{r} \times \vec{F} = 0 \tag{3.15}$$

or

$$F_n.x + F_t.y = 0 \tag{3.16}$$

where x and y are the tangential and normal lever arms and F_t and F_n are magnitudes of the tangential and normal forces respectively. The latter follow from

$$F_t = \vec{F}_{total} \,.\, \vec{t} \tag{3.17}$$

$$F_n = \vec{F}_{total} \,.\, \vec{n} \tag{3.18}$$

Here $\vec{n}$ and $\vec{t}$ are the unit normal and tangential vectors. $\vec{F}_{total}$ is defined as the resultant of all acting forces ($\vec{F}_{total} = \vec{F}_G + \vec{F}_{drag} + \vec{F}_{lift}$). By dividing F_t by the area of the particle, the exerted tangential particle shear stress τ can be found.

$$\tau = \frac{F_t}{\pi d^2/4} \tag{3.19}$$

The lever arms are determined according to Figure (3.2). T_1, T_2 and T_3 are the contact points of the three bed particles with the considered particle. As

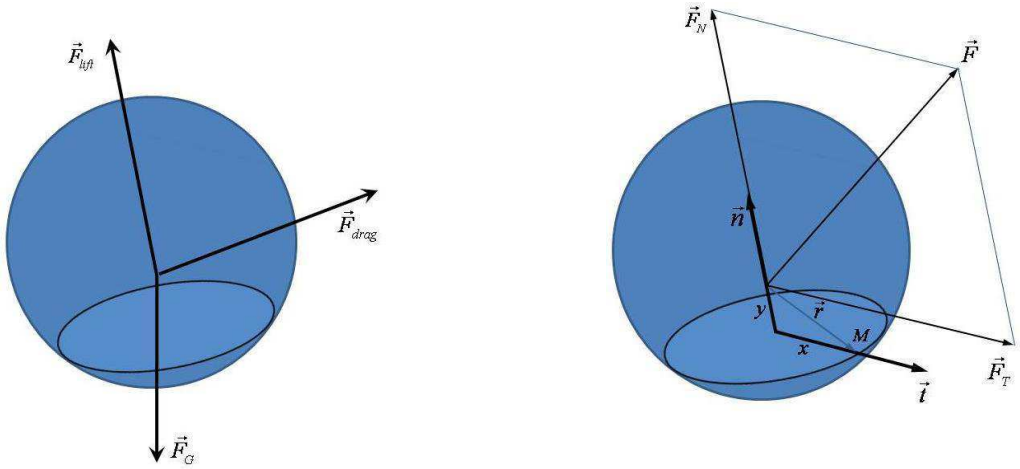

Figure 3.3: Forces on a solitary particle exerted by fluid and gravity (left) and the projection of the total force on normal and tangential directions (right).

mentioned before, depending on the orientation of the acting forces, this particle tends to roll over the valley, over the summit of a single particle, or somewhere in between. By considering the longest and shortest paths, the tangential lever arm will be

$$x_{min} = T_0T' = \frac{d}{4\sqrt{3}} \tag{3.20}$$

$$x_{max} = T_0T_1 = \frac{d}{2\sqrt{3}} \tag{3.21}$$

A solitary particle can choose different paths, according to the direction of the acting forces. As the number of the solitary particles is very large, the average particle path will correspond with the average tangential lever arm:

$$x = \frac{x_{max} + x_{min}}{2} = \frac{\sqrt{3}}{8}d \tag{3.22}$$

The normal lever arm y is equal to the distance between the centre of the solitary particle and the plane $T_1T_2T_3$, which passes through the contact points. The normal lever arm y is not related to the direction of motion. By considering Figure (3.3), y can be found as

$$y = \frac{d}{\sqrt{6}} \tag{3.23}$$

The acting point of moment changes its position during the rotation of the sphere. Figure (3.4) shows a particle during dislodge and rotation. The outer circles are the physical geometry of the spheres and the inner circles comes from the average effective radius coming from Equations (3.22) and (3.23) and equal to

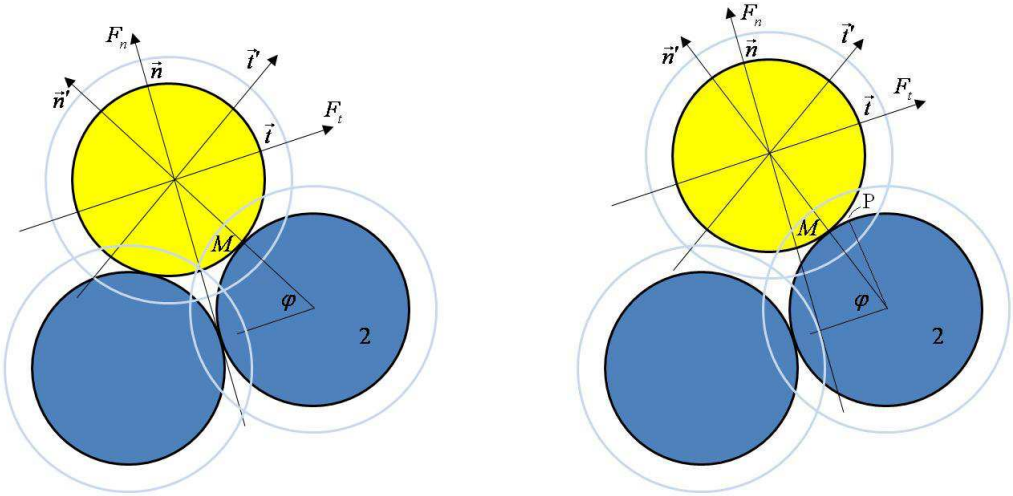

Figure 3.4: Presentation of forces and directions of the acting forces before moving (left) and during incipient motion (right).

$\sqrt{x^2+y^2}$. If φ is the angle of the tangential unit vector with the horizontal plane, the moment can be defined as

$$M = I\frac{d^2\varphi}{dt^2} \tag{3.24}$$

where I is the inertial moment; for a solid sphere $I = md^2/10$. By projecting the forces on the line passing from the centres of spheres and the line normal to it through the centre of the moving sphere ($\vec{n}'$ and $\vec{t}'$ in Figure 3.4), the moment at point M can be written as

$$M = r.\left(F_t \sin\varphi + F_n \cos\varphi\right) \tag{3.25}$$

in which r is the radius of rotation ($r = \sqrt{x^2+y^2}$). Inserting Equation (3.25) into Equation (3.24) yields,

$$\frac{d^2\varphi}{dt^2} = A\sin\varphi + B\cos\varphi \tag{3.26}$$

where

$$A = \frac{10F_t r}{md^2} \tag{3.27}$$

$$B = \frac{10F_n r}{md^2} \tag{3.28}$$

Equation (3.26) is nonlinear and has no direct analytical solution, but it is possible to find a solution for $d\varphi/dt$, which can be considered as the radial velocity of the moving particle related to the centre of the fixed particle. This solution reads

$$\frac{d\varphi}{dt} = \sqrt{-2A\cos\varphi + 2B\sin\varphi + C} \tag{3.29}$$

By applying the initial condition at $\varphi = \varphi_0$ as $d\varphi/dt|_{t=0} = 0$, this becomes

$$\frac{d\varphi}{dt} = \sqrt{-2A\left(\cos\varphi - \cos\varphi_0\right) + 2B\left(\sin\varphi - \sin\varphi_0\right)} \tag{3.30}$$

A complete dislodge of the sediment particle from the bed occurs when the rotating particle separates from the bed-particle. In that case, the reaction force of particle 2 tends to zero. By projecting the tangential and normal forces on the line passing from the centre of particles in Figure (3.4),

$$F_n \sin\varphi - F_t \cos\varphi = 0 \tag{3.31}$$

it follows that

$$\varphi = \tan^{-1}\left(\frac{F_t}{F_n}\right) \tag{3.32}$$

By substituting φ into Equation (3.30), the radial velocity can be found. The tangential velocity can be determined from:

$$V_{tan} = 2r\frac{d\varphi}{dt} \tag{3.33}$$

where V_{tan} is the particle velocity in the direction of $\vec{t}'$. The components of $\vec{V}_{tan}$ in x, y and z direction will be the initial velocities of the particle at the moment of its pick-up.

There is no consistent theoretical description for the amount of sediment pick-up. Most proposed formulations to derive pick-up functions are based on experimental approaches. Van Prooijen (2010) has derived a formulation for the instantaneous pick-up rate from the bed. According to this analysis, the particles are considered to be initially in rest. Due to lift and drag forces, the particles can accelerate. The acceleration is defined by a. To move over a distance equal to the grain diameter, d, a time $t = \sqrt{2d/a}$ is required. According to Newton's second law, the acceleration is the sum of the forces divided by the mass of the particle,

$$\vec{a} = \frac{\sum \vec{F}_{total}}{m_p} \tag{3.34}$$

where $\vec{F}_{total}$ is the resultant force on a single particle defined by $\vec{F}_{total} = \vec{F}_G + \vec{F}_{drag} + \vec{F}_{lift}$ and m_p is the mass of the particle. For uniform channel flow, the flow is determined by the friction velocity u_*. Both the lift and drag forces can be expressed by the shear stress ($\tau_b = \rho u_*^2$) as $\vec{F}_{lift} \sim \vec{\tau}_b d^2$ and $\vec{F}_{drag} \sim \vec{\tau}_b d^2$. The force balance can therefore be written as

$$\sum \vec{F} \sim d^2 \left(\vec{\tau} - \vec{\tau}_{cr} \right) \tag{3.35}$$

where $\tau_{cr} \sim \left(\rho_p - \rho \right) gd$, where ρ_p denotes the mass density of the particle.

From here on, we neglect the direction of the force, implying that we do not care about the direction of motion of the individual particle. As we are looking for the bulk quantity of bed entrainment, E, we consider a large number of particles. The exact position of a single particle is therefore of minor importance. Then the initial acceleration of the particle follows from

$$a \sim \frac{\sum F}{\rho_p d^3} = \frac{\tau - \tau_{cr}}{\rho_p d} = g \frac{\rho_p - \rho}{\rho_p} \left(\tau_* - \tau_{*cr} \right) \tag{3.36}$$

where τ_* denotes the dimensionless shear stress. Substituting this acceleration into the timescale definition $t = \sqrt{2d/a}$ gives

$$t \sim \sqrt{\frac{\rho_p}{\rho_p - \rho} \frac{2d}{\left(\tau_* - \tau_{*cr} \right) g}} \tag{3.37}$$

This means that the time scale is inversely proportional to the square root of the excess bed shear stress. The erosion rate then becomes

$$E \sim \rho_p \frac{d}{t} = \rho_p \sqrt{\frac{\rho_p - \rho}{\rho_p} gd \left(\tau_* - \tau_{*cr} \right)} \tag{3.38}$$

or

$$E = \epsilon \rho_p \sqrt{\frac{\rho_p - \rho}{\rho_p} gd \left(\tau_* - \tau_{*cr} \right)} \tag{3.39}$$

In dimensional form, the erosion rate becomes

$$E = \epsilon \sqrt{\rho_p \left(\tau - \tau_{cr} \right)} \tag{3.40}$$

The coefficient ϵ is a tuning parameter and contains among others the packing of the bed and the shape of the particles. Equation (3.40) is similar to the pick-up formula proposed by De Ruiter (1982, 1993), reading

$$E = \alpha_{Ruiter}\rho_p \sqrt{\frac{\rho_p - \rho}{\rho_p} g d \frac{\sigma}{\tau^0_{*cr}} \tan\phi} \tag{3.41}$$

in which τ^0_{*cr} is the instantaneous critical shear stress at a horizontal bed, ϕ is the angle of repose and α_{Ruiter} is a constant for uniform spherical particles. The angle of repose is constant. The critical shear stress at a horizontal bed can be determined by the balance of forces. The lift force can be neglected if it is small compared with the drag and gravity forces (which is not always true). Considering the drag parallel to the bed, and considering Equations (3.22) and (3.23), the following balance of forces applies in the critical state:

$$F_{cr}\frac{d}{\sqrt{6}} = \left(\rho_p - \rho\right)\frac{\pi}{6}d^3 g \frac{\sqrt{3}}{8}d \tag{3.42}$$

The particle shear stress is the acting force on a particle per unit effective surface area. The effective surface area is the projection of the particle surface in the direction of acting force, namely $2\left(\pi d^2/4\right)$. Hence

$$\tau^0_{*cr} = \frac{\tau_{cr}}{\left(\rho_p - \rho\right) dg} = \frac{\sqrt{2}}{8} \approx 0.177 \tag{3.43}$$

This means that the critical shear stress for a flat bed is also constant. Note that the shear stress in the current model is generally not constant, it is a function of the bed slope and the directions of the forces. Also note that the critical particle shear stress in Equation (3.43) is not the same as the Shields (1936) critical shear stress, which is based on the mean bed shear stress. This stress is almost half the average physical critical shear stress, because the effect of turbulent velocity fluctuations is not taken into account. Figure (3.5) illustrates this. Level A is the average shear stress which is used in the Shields diagram, whereas the value of the real shear stress at which sediments are picked is at level B. The peaks of the fluctuating shear stress amount to about twice the mean value (De Ruiter, 1982). After averaging of the particle shear stress over the bed area and comparing the result with the mean bed shear stress, we found a nearly linear relation between them. Figure (3.6) shows a comparison between the averaged particle shear stress and the mean bed shear stress for a large number of simulations with different bulk velocities and particle diameters. The constant of proportionality for the linear relation found turns out to be independent of the bulk velocity and is only a function of the particle diameter. The best fitting for this constant is found to be

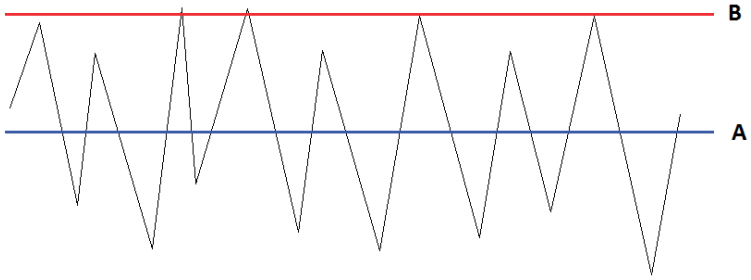

Figure 3.5: The critical shear stress on which the Shields diagram is based. The critical shear stress was considered at level A in the Shields diagram, whereas the peak of the shear stress is located at level B.

$$\beta = 0.1855 \left(\frac{\left(\rho_p/\rho - 1\right) g d^3}{36\nu^2} \right)^{0.1091} - 0.1043 \tag{3.44}$$

According to Van Rijn (1984a) the constant α_{Ruiter} in Equation (3.41) is equal to 0.016. This value of α_{Ruiter} has been derived from experiments and is particularly suitable for larger particles ($> 1,000\,\mu$m) (Van Rijn, 1984a). Therefore, the coefficient of proportionality in Equation (3.40) needs to be calibrated for small particles. In the current model, the pick-up rate formula proposed by Nakagawa and Tsujimoto (1980) is used for this calibration. The formulation they propose was validated against a range of physical observations. Moreover, their method yielded one of the best predictions of the pick-up function for fine sediment, as reported by Van Rijn (1984a). This approach was also effectively used by Onda and Hosoda (2004), Giri and Shimizu (2006) and Shimizu et al. (2009) in models of bedform development. According to Nakagawa and Tsujimoto (1980), the dimensionless pick-up rate is expressed by

$$P_S^* = \frac{P_S \sqrt{d}}{\sqrt{\left(\frac{\rho_p}{\rho} - 1\right) g}} = F_0 \bar{\tau}_* \left(1 - \frac{\bar{\tau}_{*cr}}{\bar{\tau}_*} \right)^3 \tag{3.45}$$

in which F_0 is an experimental constant. $\bar{\tau}_*$ and $\bar{\tau}_{*cr}$ are the dimensionless shear stress and the critical shear stress for incipient motion, respectively, both averaged over time and space. Here, the dimensionless shear stress $\bar{\tau}_*$ is defined as

$$\bar{\tau}_* = \frac{\bar{\tau}}{\left(\rho_p - \rho\right) g d} \tag{3.46}$$

According to the experimental studies of Nakagawa and Tsujimoto (1980), suitable values for the constants in Equation (3.45) are $F_0 = 0.03$ and $\bar{\tau}_{*cr} = 0.035$.

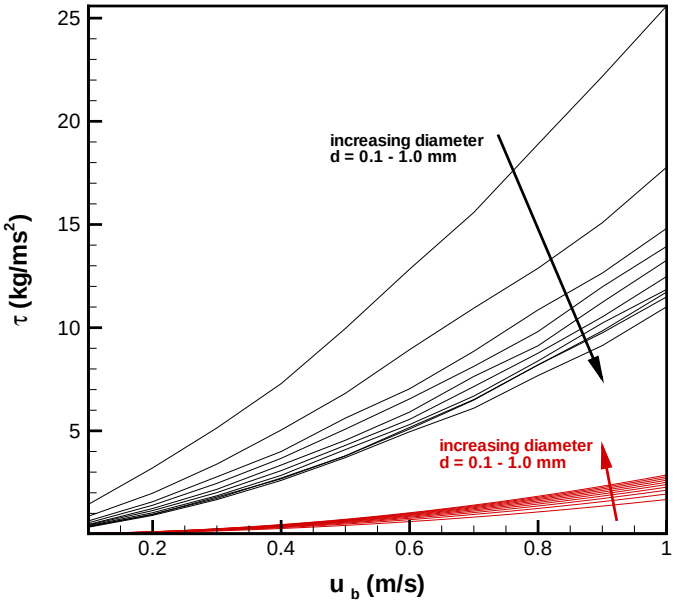

Figure 3.6: The averaged simulated particles shear stress (black) and the bed shear stress (red), for different particle diameters and bulk velocities.

The factor P_S can be considered as the probability density of sand particle dislodgement per unit time from the bed area occupied by one sediment particle (Nakagawa and Tsujimoto, 1980).

Equation (3.45) is based on unidirectional flow over a flat bed. Nagata and Muramoto (2005) used Tsujimoto's pick-up rate formula to find the volumetric rate of sediment pick-up from a specified area on the bed. Applying this approach to a cell covering part of the bed yields

$$\overline{V}_S = \frac{A_3}{A_2} P_S S d \tag{3.47}$$

Here $\overline{V}_S$ is the volume of sediment pick-up per unit time, S is the area of the cell on the bed-surface, and A_2 and A_3 are shape coefficients for spherical sand grains with two- and three-dimensional geometrical properties, namely $\pi/4$ and $\pi/6$ respectively.

In order to validate and calibrate the erosion rate in Equation (3.40), flow computations were made for different discharges over a flat bed, yielding different bed shear stress levels. The computed results were averaged over time and space to find the average entrainment rate and the average shear stress. The instantaneous volumetric pick-up rate over area S can be written as

$$\dot{V}_E = E \frac{S}{\rho_p} \tag{3.48}$$

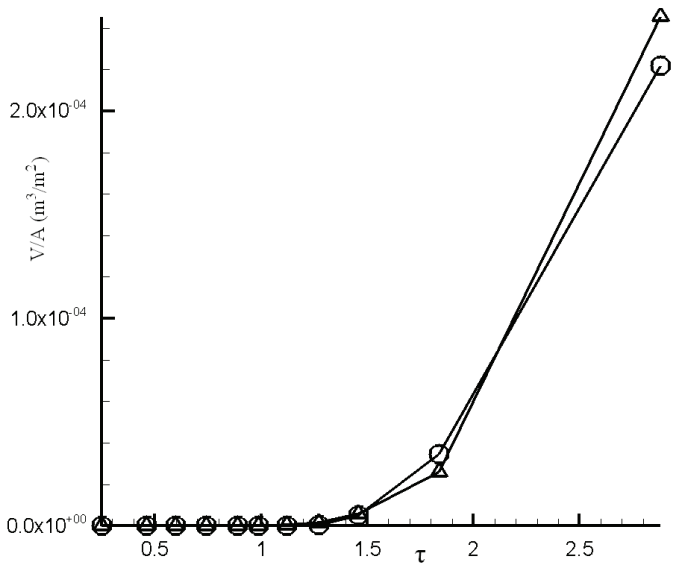

Figure 3.7: Comparison between present averaged formulation and the relation of Nakagawa and Tsujimoto (1980).

The computed average entrainment rates $\overline{\dot{V}}_S$ were compared with the entrainment according to Equation (3.45). Figure (3.7) shows that the computed average entrainment (based on the mean shear stress) agrees well with that derived from Equation (3.45). The best fitting tuning factor ϵ in Equation (3.40) is found to be 3.67×10^{-4}.

The volume of sediment pick-up in a time interval Δt will be

$$V_E = \dot{V}_E \Delta t = E \frac{S}{\rho_p} \Delta t \tag{3.49}$$

The number of particles involved can be determined by dividing the pick-up volume by the volume of a single particle V_p.

$$n_{pickup} = \frac{V_E}{V_p} \tag{3.50}$$

The number of particles picked up may be so large, that treating them one by one is beyond the capacity of existing computational resources. Hence we use a multiplication factor, usually much smaller than 1, to decrease the number of particles for computational efficiency. In this way, we consider a much smaller number of particles, but with the same total volume of pick-up: we assume each particle to carry the mass of a large number of its neighbours. The mass carried by a particle can be calculated as

$$m'_p = \frac{m_p}{C_{frac}} \tag{3.51}$$

where m_p is the mass of a physical particle, m'_p is the mass carried by the computational particle, and C_{frac} is the multiplication factor. Under the influence of drag, lift and gravity forces, particles are lifted and transferred with the water and finally deposited at other locations. Models for transport and deposition are necessary to find the particle trajectories and deposition locations. The next section describes the equations of motion of particles in flow.

3.4.2 Transport of sediment

After pick-up, the particles are transported by the forces exerted by the flow. The velocity of an individual sediment particle in the flow is described by

$$\begin{aligned}\rho_s V_p \frac{d\vec{v}_p}{dt} = (\rho_S - \rho)\, V_p \vec{g} + \rho V_p \frac{D\vec{u}_f}{Dt} + \frac{1}{2}\rho V_p \left(\frac{D\vec{u}_f}{Dt} - \frac{d\vec{v}_p}{dt} \right) \\ + \frac{3}{4}\frac{C_D}{d}\rho V_p \left|\vec{u}_f - \vec{v}_p\right| \left(\vec{u}_f - \vec{v}_p\right) \\ + \frac{3}{4}\frac{C_L}{d}\rho V_p \left(\left|\vec{u}_f - \vec{v}_p\right|^2_{top} - \left|\vec{u}_f - \vec{v}_p\right|^2_{bottom} \right) \vec{n}\end{aligned} \tag{3.52}$$

where $\vec{v}_p$ represents the velocity of the sediment particle, $\vec{u}_f$ is the fluid velocity at the particle location, C_D is the drag coefficient, C_L is the lift coefficient, d is the particle diameter, $D/Dt = \frac{\partial}{\partial t} + \vec{u}.\nabla$, $\vec{g}$ is the gravity vector, V_p is the particle volume and ρ and ρ_s are the densities of the fluid and particle respectively. The first term in the right-hand side of Equation (3.52) represents the gravity force, the second and third terms the effect of pressure forces and added mass, respectively (Maxey and Riley, 1983). The drag coefficient C_D can be found from Equation (3.2), but the lift coefficient C_L is difficult to determine. There is limited knowledge regarding the effect of solid boundaries on the particles. The effect of shear stress has been studied for very simple linear cases with $Re_p \ll 1$. Moreover the fluid velocity needs to be determined at the top and the bottom of the particle. In the model, the size of a particle is one or two orders of magnitude smaller than the size of a computational grid cell, which makes the difference between the interpolated velocities at the top and the bottom of a particle insignificant. We therefore replace the lift force term in Equation (3.52) by the theoretical and experimental relations introduced by McLaughlin (1991) and Mei (1992), which are given in Equations (3.10) and (3.11). These equations parameterise the total lift force, including Magnus effect and wall drift force.

A major simplification in the present study is neglecting the interactions between particles, and also neglecting the effect of particles on the fluid flow. This

simplification is valid if the sediment concentration in the mixture of water and sediment is low.

Equation (3.52) is solved using an implicit scheme to avoid instabilities. Each particle position is then calculated according to

$$\frac{d\,\vec{x}_p}{dt} = \vec{v}_p \tag{3.53}$$

where $\vec{x}_p$ is the position vector of the particle. The particles move according to Equations (3.52) and (3.53), until they settle. The mechanism of deposition is discussed in the next section.

3.4.3 Deposition

The mechanism of interparticle collision is a fundamental aspect of bed load transport. The observations of previous studies give conflicting assessments as to whether grains rebound partially elastically or are viscously damped (Schmeeckle et al., 2001). All researchers who have modelled the collision of saltating grains in water use the same simple model. The incoming velocity of the impacting grain is divided into a component normal and tangential to the colliding surface. The outgoing tangential velocity is equal to the incoming tangential velocity times a coefficient α_t, and the outgoing normal velocity is equal to incoming normal velocity multiplied by a factor $-\alpha_n$.

The mechanism of deposition is not clearly known yet. The particles can have different behaviour when they interact with the bed. Their motion may be viscously damped, they may be reflected or they may move tangentially to the bed. Schmeeckle et al. (2001) showed that the appropriate physical scaling of this problem is governed by a collision Stokes number:

$$St = \frac{m_p v_p}{6\pi\mu r_*^2} \tag{3.54}$$

where m_p is the mass of the single particle, μ is the dynamic viscosity of the water, v_p is the particle velocity when it contacts the bed and r_* is the relative particle radius ($1/r_* = 1/r_p + 1/r_{st}$). The variables r_p and r_{st} are the radiuses of the moving particle and the stationary particles located on the bed, respectively. The Stokes number (St) is a measure of the inertia of the particle relative to the viscous pressure force exerted on it by the fluid. Hence, if $St \ll 1$, the viscous pressure will stop the particle before significant elastic energy can be stored in the deformation of the particles. In this case, there will be no initial rebound velocity. At moderate values of St the elastic deformation will become significant enough to develop an initial rebound velocity but the rebounding particle will be arrested by negative pressures and cavitations in the gap between it and the bed. At still higher values of St, rebounding particles will separate completely.

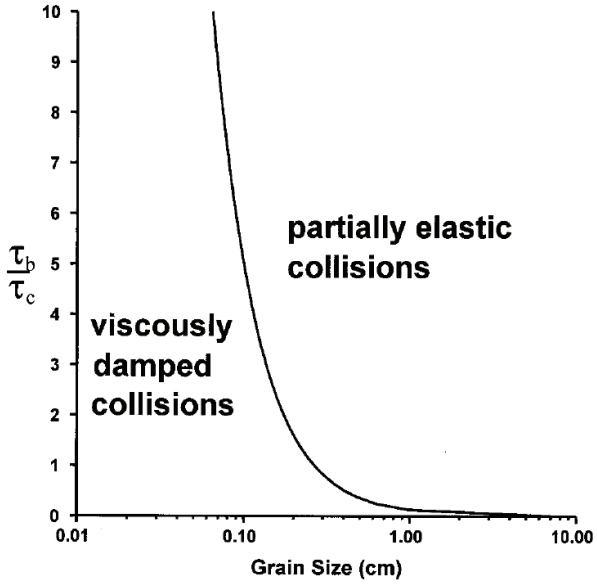

Figure 3.8: Graph of the transition from viscously damped to partially elastic collisions at typical bed load saltation velocities as a function of grain size and transport stage. Taken from Schmeeckle et al. (2001).

Figure (3.8), from an experimental study by Schmeeckle et al. (2001), shows a graph of the transition from viscously damped to partially elastic collisions. According to this figure, the transition between damped and un-damped particle collisions occurs at about the transition from medium to coarse sand. The corresponding critical sediment diameter size is 2.7 mm. Therefore, for sediment larger than sand (> 2 mm), saltation impacts will almost always be partially elastic, whereas for sand and smaller particles there is no significant normal rebound.

According to this information, for bed load transport of sand (< 2 mm) the normal elastic coefficient α_n will be zero, because the collisions are viscously damped. The tangential elastic coefficient α_t takes a value of about 0.9 (Schmeeckle et al., 2001). For particles larger than sand, the critical Stokes number ranges between 39 and 105. At Stokes numbers higher than 105, partially elastic collisions occur and the new velocities can be calculated as follows

$$V_{n,new} = -\alpha_n V_{n,old} \tag{3.55}$$

$$V_{t,new} = \alpha_t V_{t,old} \tag{3.56}$$

Here, V_n and V_t are the normal and tangential velocities of the particle during deposition, respectively. Schmeeckle et al. (2001) experimentally determined α_n at a value of 0.65. For Stokes numbers less than 39, the particle motion is viscously damped. In the range between 39 and 105, the behaviour is not clear be-

cause of the negative pressure and cavitations between the particle and the bed. Schmeeckle and Nelson (2003) did apply Equations (3.55) and (3.56) for a Stokes number less than 105, but set the normal rebound coefficient at zero ($\alpha_n = 0$). This approach is also taken in the present model for sediment deposition.

3.4.4 Sliding of sediment

Figure (3.4) shows a situation in which a particle separates from the bed. It is clear that the angle of particle separation must be in the range $\pi/3 \leq \varphi \leq 2\pi/3$. If the angle φ, calculated from Equation (3.32) does not fall within this range, the particle cannot separate and will slide along the bed. This can also be observed in flume experiments and in the field: a significant fraction of sediment transport occurs in this way. An extreme manifestation of this phenomenon is fluidization of the bed under high shear stresses.

This kind of sediment transport cannot be modelled in the same way as the transport of particles in the fluid described in section 3.4.2. Therefore we need another model, describing sediment sliding in layers over the upper part of the bed. Here we develop a simple sliding model, considering the sliding sediment as a sheet moving from one computational cell to the other. Figure (3.9) shows this model schematically for one cell on the bed. The sediment sheet can only move in the direction of the fluid force. Assuming the force exerted by the fluid to be constant over a time step Δt, Newton's second law yields

$$a_t = \frac{F_t}{m_p} \tag{3.57}$$

where a_t is the acceleration due to force F_t and m_p is the mass of a solitary particle. We suppose that the motion of each solitary particle starts from rotation as shown in Figure (3.4). If the forces exceed the critical level, but are not sufficient to separate the particle from the bed, the particle will roll or slide after it has reached point P in Figure (3.4). This point corresponds with angle $\pi/2$. According to Equation (3.30), the initial angular velocity can be determined as

$$\omega = \frac{d\varphi}{dt} = \sqrt{-2A\left(\cos\pi/2 - \cos\pi/3\right) + 2B\left(\sin\pi/2 - \sin\pi/3\right)} \tag{3.58}$$

The center of rotation of the particle is the centre of particle 2 located in the bed. Thus the tangential velocity $u_{0,tan}$ can be determined as

$$u_{0,tan} = d\omega \tag{3.59}$$

where ω is the radial velocity of the centre of the moving particle.

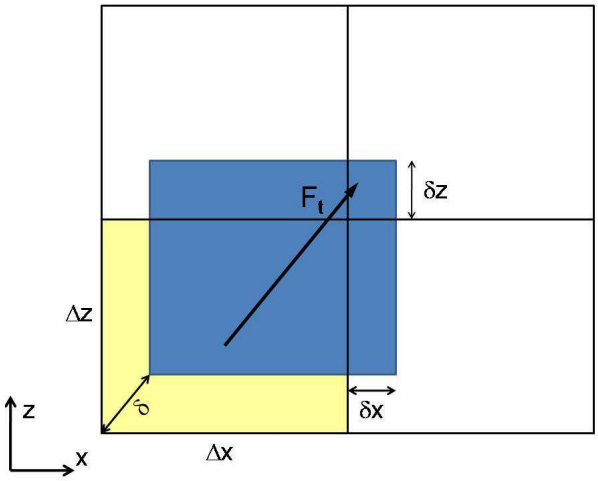

Figure 3.9: Model for sliding of sediment after pick-up, if sediment particles cannot leave the bed. A layer of sediment of the cell moves in the direction of the tangential force and slides to the neighboring cells.

We suppose that the time necessary to rotate the particle to the summit of the supporting particle (point P) is negligible. Thus the displacement δ can be calculated as follows

$$\delta = \frac{1}{2} a_t \Delta t^2 + u_{0,tan} \Delta t \tag{3.60}$$

It can be projected in x and z directions

$$\delta x = \delta \,.\, t_x \tag{3.61}$$

$$\delta z = \delta \,.\, t_z \tag{3.62}$$

where t_x and t_z are the components of the tangential unit vector $\vec{t}$ (in the direction of $\vec{F}_t$), respectively.

The amount of sediment pick-up is calculated by Equation (3.40). After displacement of the sediment layer, the amount of sediment given to the neighbouring cells can be determined as the ratio of the area displaced to the neighbour cell to the total area multiplied by the amount of sediment picked up. For example, the sediment passed on to the eastern cell in Figure (3.9) can be determined by

$$P_{S,east} = \frac{\delta x \, (\Delta z - \delta z)}{\Delta x \, \Delta z} P_S \tag{3.63}$$

By this model, bed load transport can be described. In combination with the other model components, it approximates the total sediment transport on and

above the bed.

3.5 Numerical validations

3.5.1 Particle fall velocity

Basically, the settling velocity is not a particle property, but rather a behavioural property. The terminal settling velocity (w_s) of a particle occurs when the fluid drag force on the particle is in equilibrium with the gravity force. Considering Equations (3.1) and (3.13) for the drag and gravity forces, the fall velocity takes the following form.

$$w_s = \sqrt{\frac{4}{3}\frac{\left(\rho_p/\rho - 1\right) dg}{C_D}} \tag{3.64}$$

In order to show how this constant velocity is reached, a particle of 0.25 mm diameter is released in the numerical model from a stationary state in a steady flow. Figure (3.10) shows the computed time evolution of the settling velocity and the drag coefficient. The velocity increases and approaches a constant value, the drag coefficient decreases and also approaches a constant value. In Equation (3.64) the drag coefficient C_D is a function of the settling velocity w_s, so this is an implicit relationship. It can be solved iteratively to determine the two quantities. Figure (3.11) shows the result for the same sediment diameter. Figures (3.10) and (3.11) clearly show that the numerical results agree well with the analytical ones.

3.5.2 Sediment avalanching

During the formation of dunes, the angle of the lee side can become relatively steep. If this angle is larger than the angle of repose, it is possible that the sediment slides along the lee side to the bottom. This process is called avalanching. Avalanching occurs because of instability of the sediment pack caused by gravity. If the direction of the gravity force falls outside the stability region of the particles, it tends to pull the particles downward. If opposing hydraulic forces are absent or not strong enough, avalanching occurs. Figure (3.12) shows the condition in which avalanching can occur. It has to be noticed that in the current model, the avalanching is based on the motion of solitary particles, and the effect of geometrical interactions between particle, which leads to pack avalanching, is not taken into account. This model is therefore suitable for non-cohesive uniform sediment, as the avalanching occurs by motion of solitary particles or in the form of small bulks.

In the present model, avalanching occurs automatically (by balance of forces) and no extra restrictions are applied. Yet, as geometrical sediment interactions

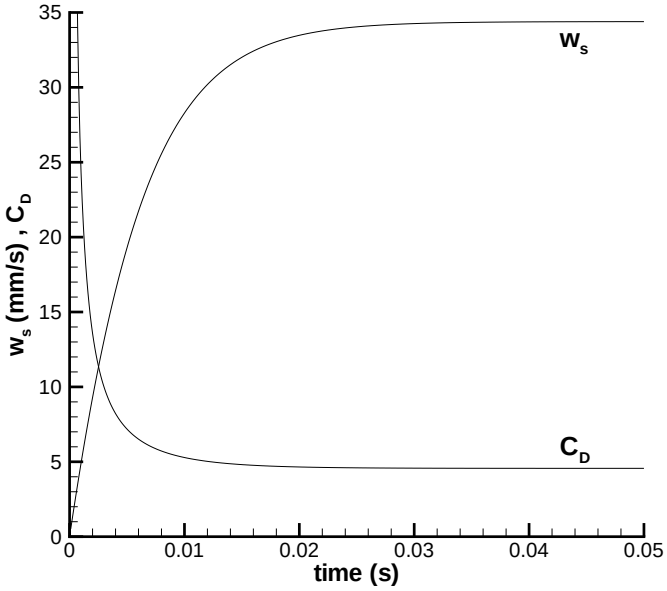

Figure 3.10: Simulation of fall velocity of a particle with diameter $d = 0.25\,\text{mm}$.

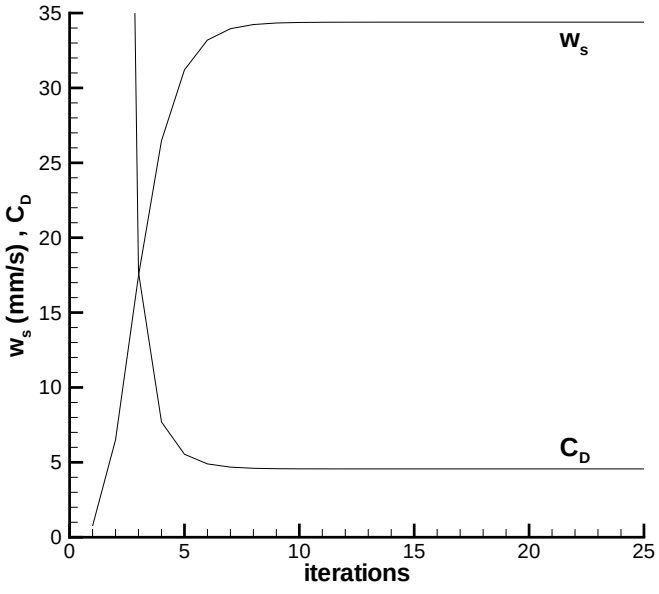

Figure 3.11: Fall velocity of a particle with diameter $d = 0.25\,\text{mm}$ by iteration of Equation (3.64).

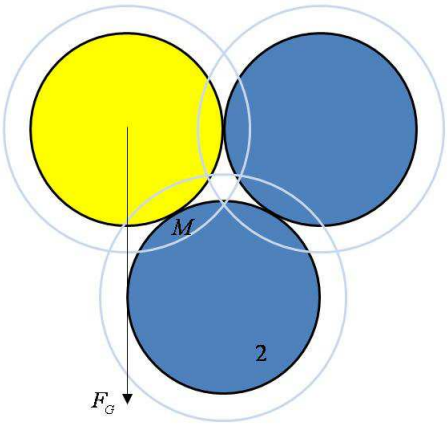

Figure 3.12: The situation in which an avalanche may occur. The gravity force falls outside the stability region of the particles (left side of point M), which lets the single particle rotate and fall downhill.

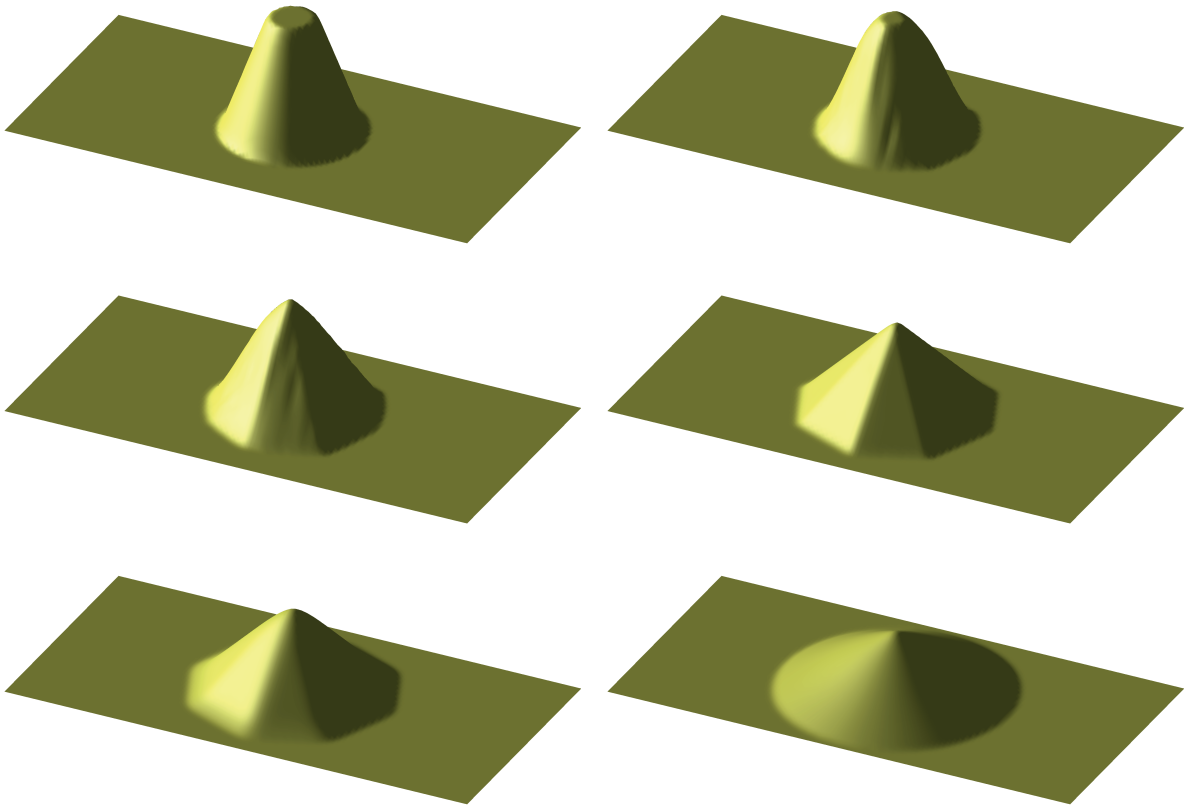

Figure 3.13: Three-dimensional views of the computed avalanche. It begins from a steep angle and the angle decreases until it reaches the angle of repose.

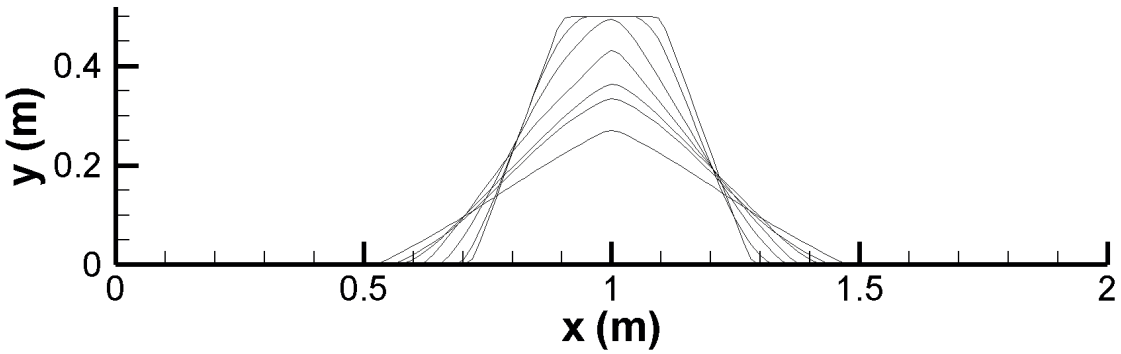

Figure 3.14: Cross sections of the bed during avalanching. It begins from a steep angle and the angle decreases until it reaches the angle of repose.

within the bed are not considered, this model is tested for its capability to reproduce empirical values of the angle of repose. As a test case, we start from a steep bedform in stagnant water. The initial slope of 75 degrees is much larger than the angle of repose. Figure (3.13) shows the initial condition of the bed. Although there is no ambient flow, the mound collapses. The particles move downhill, the height of the mound decreases and the width at the foot increases. Figure (3.14) shows the avalanching as a function of time. The slope of the deformed bed decreases until it reaches the angle of repose. Then the downhill transport of sediment stops and the bed reaches a steady state. The angle of repose in our model is 30 degrees, as can be seen in Figure (3.14).

3.5.3 Bedload sediment transport

Sediment transport can be divided into wash load transport, bed load transport of bed material and suspended transport of bed material. Wash load concerns very fine material which is transported in the water column and does not interact with the bed. This part of the transport does not affect morphology. Bed-material load concerns coarser particles that do interact with the bed. In general bedload transport concerns the part of the transported bed material that is in more or less continuous contact with the bed by rolling, jumping or sliding along the bed. Suspended load transport concerns the material that is transported in the water column, picked up and kept in suspension by turbulence. The sum of bed-load and suspended-load bed-material transport is called the total load transport of bed material.

Since more than a century, researchers have been developing methods to calculate the bulk bedload flux. One of the simplest bedload transport formulae was developed by Meyer-Peter and Müller (1948). They used flume measurements with a sediment bed of grains sized $d = 0.03 - 2.9\,\mathrm{cm}$, with varying sediment densities ($\rho_s = 1.3 - 4.2\,\mathrm{g/cm^3}$), and considered both well-sorted and naturally

sorted material. They found that at high shear stresses the bed load flux is given by

$$q_{*b} = 8\left(\tau_* - \tau_{*cr}\right)^{3/2} \tag{3.65}$$

Equation (3.65) represents a general bedload formula, where $\tau_{*cr} = 0.047$ is an average value of non-dimensional critical shear stress, τ_* is the non-dimensional shear stress, and q_{*b} is the non-dimensional bed load transport rate, defined as

$$q_{*b} = \frac{q_b}{d\sqrt{\left(\rho_p/\rho - 1\right) gd}} \tag{3.66}$$

Wiberg and Smith (1987) point out that the observed variation in the transport coefficient is well captured by a simple dependence on the Shields stress (τ_*), yielding a generalized bedload transport relation:

$$q_{*b} = \alpha\left(\tau_* - \tau_{*cr}\right)^n \tag{3.67}$$

where $n = 3/2$ and

$$\alpha = 1.6\ln\left(\tau_*\right) + 9.8 \approx 9.64\tau_*^{0.166} \tag{3.68}$$

A different approach was taken by Hans Albert Einstein and others, who tried to estimate sediment transport flux by accounting for the probability that any sediment particle within a population would be mobilized by the fluctuating flow field (Brown, 1950). This takes into account such things as the ability of small sediment grains to hide between larger ones, and the intensity of turbulent fluctuations at the bed. Under equilibrium conditions the number of grains deposited must be equal to the number of grains eroded, which, together with experimental data fitting, gives

$$q_{*b} = 40K\tau_*^3 \tag{3.69}$$

where

$$K = \sqrt{\frac{2}{3} + \frac{36\nu^2}{(\rho_p/\rho - 1)gd^3}} - \sqrt{\frac{36\nu^2}{(\rho_p/\rho - 1)gd^3}} \tag{3.70}$$

Van Rijn (1984b) proposed a different formula which can be used to estimate bed load transport rates with sediment mean sizes in the range between 0.2 and 2 mm. This formula is given as

$$q_{*b} = 0.053\frac{T^{2.1}}{d_*^{0.3}} \tag{3.71}$$

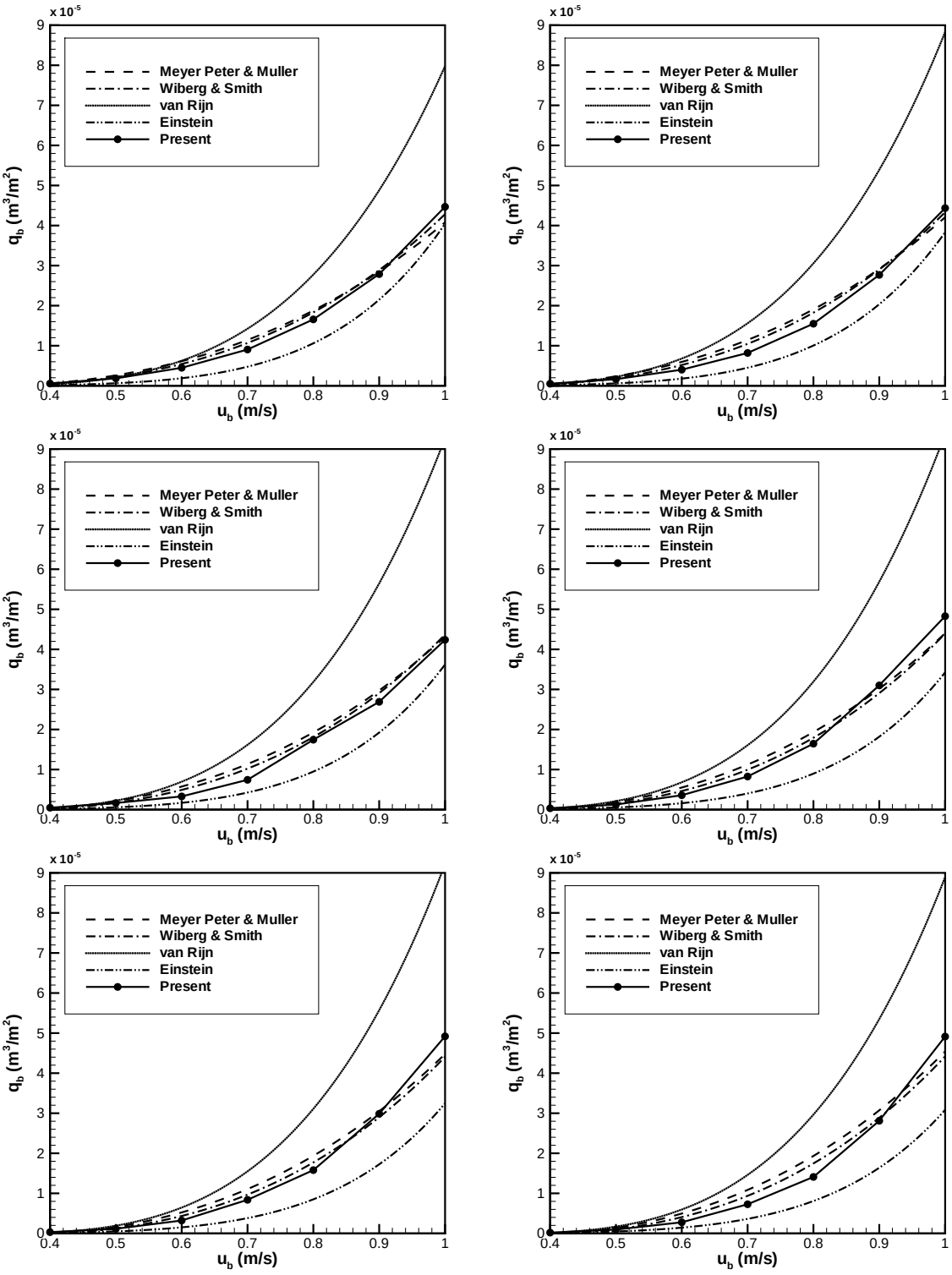

Figure 3.15: Sediment transport computed by the present model and compared with some parametric relations for different grain sizes varying between 0.3 mm and 0.65 mm.

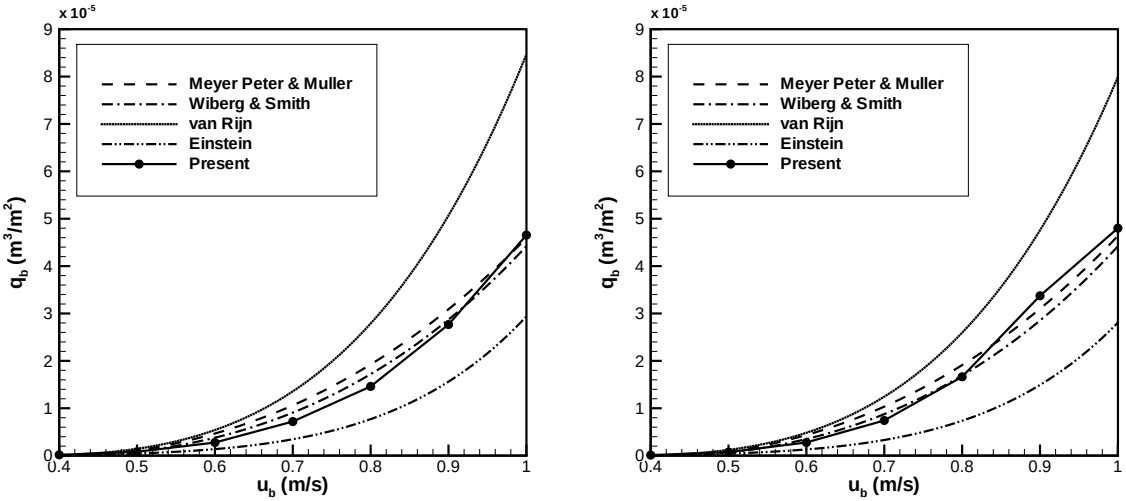

Continuing Figure 3.15.

where d_* and T are the dimensionless mean particle diameter and transport stage parameter, respectively, and defined as

$$d_* = d\left(\frac{g\left(\rho_p/\rho - 1\right)}{\nu^2}\right)^{1/3} \tag{3.72}$$

$$T = \frac{\tau_* - \tau_{*cr}}{\tau_{*cr}} \tag{3.73}$$

Here τ_{*cr} is the critical shear stress from the Shields diagram.

The aim of this section is to compare the sediment transport rate resulting from the present model with the empirical Meyer-Peter and Müller, Wiberg and Smith, Einstein and van Rijn formulae. In our numerical model, the sediments are transported as single particles in a Langrangian field. To estimate the bedload transport rate (or the total load transport rate), the total number of sediment particles passing through a plane normal to the flow direction is counted. As the model moves the particles each time step Δt, the passing volume is the volume of sediment which passes the intersection in a time interval Δt, over the width of the channel. Dividing the volume by Δt and the width gives the volumetric transport rate:

$$q = \frac{n_{pass} V_p}{b\,\Delta t} \tag{3.74}$$

in which n_{pass} is the number sediment particles passing, b is the width of the channel and q is the total load transport rate according to the numerical model.

The sediment transport is simulated for several flow rates and grain sizes (yielding different values of the Shields stress). Figure (3.15) shows a comparison of the sediment transport rates from the present model with Meyer-Peter and Müller's, Wiberg and Smith's, van Rijn's and Einstein's formulae. It is important to note, however, that the model simulations were done with a completely flat bed and that we used the zero velocity level as a calibration factor to tune the transport rate. Figure (3.15) shows a good agreement between the present numerical sediment transport calculations and the published empirical formulae. The zero velocity level is found to be $0.25d$ under the top of the particles on the bed, which agrees well with van Van Rijn (1984b).

3.5.4 Sediment concentration in a straight channel

By considering sediment with a constant settling velocity in uniform flow, the transport equation for the sediment concentration over the vertical reads

$$\frac{\partial \bar{c}}{\partial t} - w_s \frac{\partial \bar{c}}{\partial z} - \frac{\partial}{\partial z}\left(D_{zz} \frac{\partial \bar{c}}{\partial z} \right) = 0 \tag{3.75}$$

This further simplifies when considering stationary flow:

$$w_s \bar{c} + D_{zz} \frac{\partial \bar{c}}{\partial z} = 0 \tag{3.76}$$

This equation can be solved with a proper estimation of the eddy diffusivity D_{zz}. In accordance with a Reynolds analogy, the eddy diffusivity can be taken equal to the eddy viscosity, with an assumed vertical distribution, e.g. parabolic:

$$D_{zz} \approx \nu_t = \kappa u_* z \left(1 - \frac{z}{h} \right) \tag{3.77}$$

where u_* is shear velocity, z is the distance from the bed, h is the water depth, and κ is Von Kármán's constant, with a value of approximately 0.41. Using this expression in the above transport equation and integrating over z with the integration constant given by $c|_{z=a} = c_a$ results in the Rouse distribution (Rouse, 1937).

$$\bar{c} = c_a \left(\frac{h - z}{z} \frac{a}{h - a} \right)^{\frac{w_s}{\kappa u_*}} \tag{3.78}$$

The Rouse parameter (the exponent in Equation (3.78)) denotes the ratio of downward settling velocity to upward velocities caused by the turbulent fluctuations. The settling velocity can be found from Equation (3.64) and the shear velocity u_* corresponds with the logarithmic velocity profile

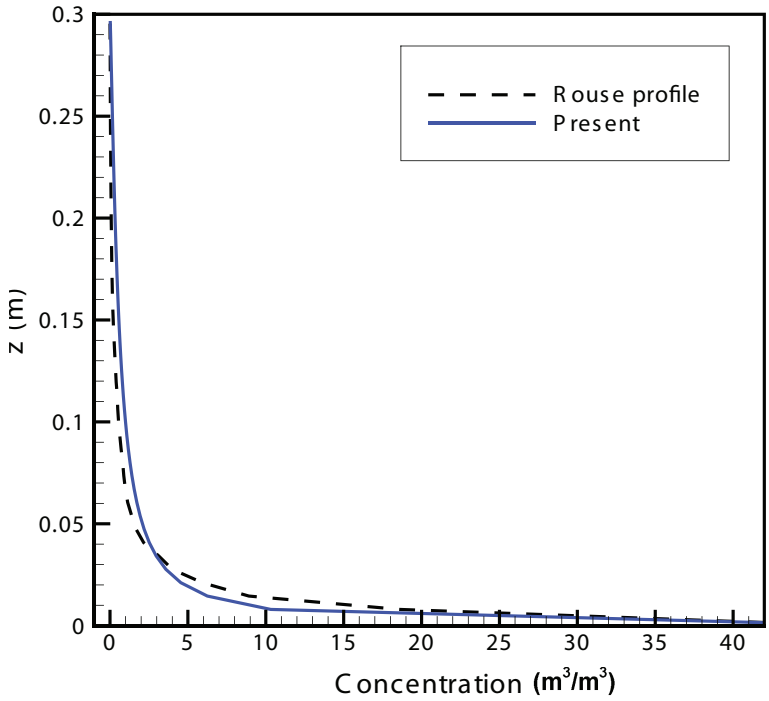

Figure 3.16: Comparison between theoretical and simulated Rouse profiles for sediments with diameter 150 μm in steady uniform flow with a bulk velocity of 0.9 m/s.

$$\frac{u}{u_*} = \frac{1}{\kappa} \ln\left(\frac{z}{z_0}\right) \tag{3.79}$$

where u is time averaged velocity at distance z above the bed, and z_0 is the level of zero intercept near the bed. The value of z_0 is related to the effective roughness height k_s and defined as $z_0 = k_s/30$ and $k_s = 2.5d$. Integration of both sides of Equation (3.79) yields,

$$u_b = \frac{u_*}{\kappa h}\left[h \ln\left(\frac{h}{z_0}\right) - h + z_0\right] \tag{3.80}$$

where u_b is the bulk velocity. The bulk velocity follows directly from the flow discharge via $u_b = Q/A$, where A is the cross-sectional area. Consequently, Equation (3.80) determines u_*.

In order to validate the sediment transport model, suspended sediment in a straight channel with uniform flow is simulated and the vertical sediment concentration profile is compared with the Rouse distribution. After the particles have reached statistically steady motion, the number of particles is determined

in thin layers parallel to the bed and the total volume of particles is divided by the total volume of the layer. Figure (3.16) compares the concentration profile thus obtained with the theoretical Rouse distribution for a grain size of 150 μm and a bulk velocity of 0.9 m/s. The simulated concentration profile is in a good agreement with the theoretical one.

3.6 Concluding remarks

We have developed a model for the simulation of sediment motion in turbulent flow. The sediment transport is modelled in a Lagrangian framework, which allows involving new concepts that are better suited for relatively small spatial and temporal scales. This approach gives a better insight into the physical transport phenomena and makes it possible to simulate details of the sediment motion, such as jumping, sliding and rolling.

The motion of sediment generally consists of three stages: (1) the particles begin to move (pick-up), (2) they get transported (moving in the water column or sliding over the bed), and (3) they are deposited at other locations. These stages are all governed by gravitational and flow-induced forces, which are simulated using theoretical and empirical relations.

The model has been validated for various well-documented aspects, such as the settling velocity of a single particle in stagnant water, the angle of repose after avalanching, and the bulk flux and the concentration profile in uniform flow. In all cases, the model results agree well with known formulae and relations. This model is to be used in high-resolution morphodynamic simulations. This means that the present process-oriented validation is necessary, but not sufficient. On top of this, the sediment transport model in combination with the flow model and the sediment balance will have to be validated against morphological information, such as bedform observations. This is the subject of the next chapter.

Chapter 4

Morphodynamics

4.1 Introduction

Early dune models were based on parameterized results from flume experiments. It was observed that a typical sequence of bedforms can be generated, depending on the flow conditions (Simons et al., 1961; Guy et al., 1966; Simons and Richardson, 1966). Figure (4.1) shows different types of bedforms. All features up to and including dunes are generally termed as lower-flow-regime bedforms and are characterized by small bed material transport rates and a high flow resistance. The lower flow regime sequence is plane bed, ripples and dunes (Figures 4.1a-e). The upper flow regime, characterized by large bed-material transport rates and small flow resistance, appears with restoration of a plane bed on which the lower regime bedforms are washed away (Figure 4.1d), Next, antidunes begin to form with upstream breaking waves over the dune crest. This type of bed is typically followed by the formation of a pool and chute morphology as described in Simons and Richardson (1966) (Figure 4.1f-h).

There is no clear distinction between ripples and dunes in the lower flow regime bedforms. The ripples scale with viscouse sublayer thickness whereas the dunes scale with water depth (Bridge, 2003). Extensive data compilations by Allen (1968) and Flemming (1988) demonstrate that there is a break in the continuum of observed bedforms defining ripples and dunes. Ripples are only present for fine sediment with $d < 1\,\mathrm{mm}$. There are no general techniques to divide ripples from dunes and some authors choose to make no distinction at all. Bennett and Best (1996) tried to generate a process-based separation of ripples and dunes, but this is not generally applicable.

Numerous approaches were developed in order to quantify sand wave induced morphology of alluvial channels. Most early investigations were conducted using theoretical, semi-empirical and empirical approaches (Engelund, 1970; Engelund and Fredsøe, 1982). Among them, theoretical studies were largely based on linear stability theory which is, in effect, not an appropriate approach for the determination of natural phenomena having finite amplitude. Empirical

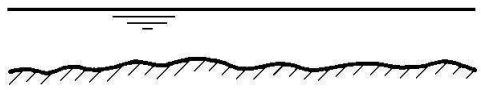

(a) Typical ripple pattern, $F \ll 1$.

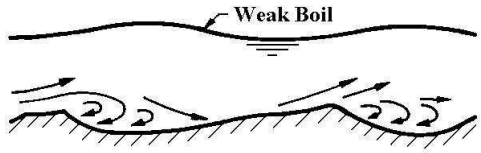

(b) Dunes with ripples superposed $F \ll 1$.

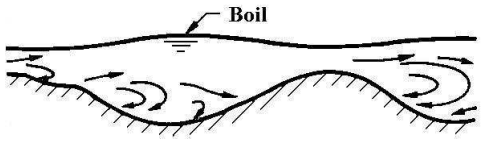

(c) Dunes, $F < 1$.

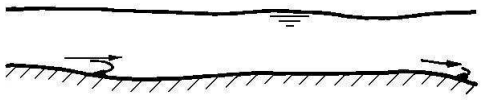

(d) Washed-out dunes or transition $F < 1$.

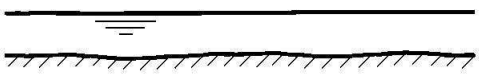

(e) Plane bed, $F < 1$ and $d < 0.4\,\text{mm}$.

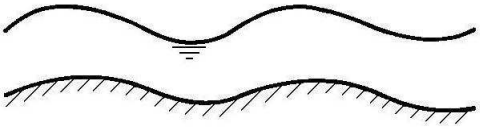

(f) Standing waves, ≥ 1.

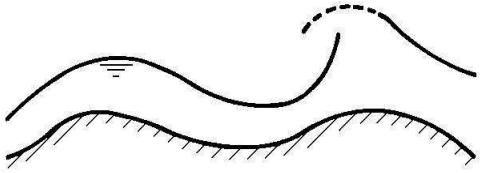

(g) Antidunes, $F \geq 1$.

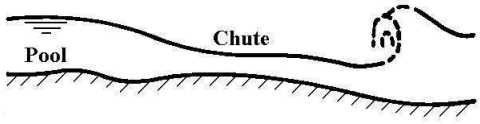

(h) Antidunes, $F > 1$.

Figure 4.1: Schematic representation bedforms formed by noncohesive sediments in alluvial channels. Flow velocity is increasing from (a) to (h) (Simons et al., 1961).

studies attempted to use the values of relevant flow and sediment properties to show what bedforms might be present under various conditions, and to derive parameterized relations. For instance, Southard and Boguchwal (1990) provide an extensive bedform phase diagrams and plotting methodology. Figure (4.2) shows the possible occurrence of ripples, dunes, antidunes or plan bed under different sediment size and flow conditions.

Morphodynamic numerical models are being increasingly employed in various river engineering research studies (Jang and Shimizu, 2005; Olsen, 2003; Shimizu, 2002; Darby et al., 2002; Shimizu and Itakura, 1989; Giri and Shimizu, 2006; Shimizu et al., 2009; Paarlberg et al., 2009; Niemann et al., 2011). Despite the considerable amount of work in this area, rather slow progress has been made regarding numerical computation of bed form dynamics (Giri and Shimizu, 2006). For instance, Giri and Shimizu (2006) and Shimizu et al. (2009) developed a ver-

tical two-dimensional flow model for simulating morphodynamics under steady and unsteady flows. The hydrodynamic model was coupled with a parameterized sediment transport model, proposed my Nakagawa and Tsujimoto (1980), and a mophodynamic model which is based on a balance between sediment pick-up and deposition. The flow model performance was enhanced by the use of a high-order Godunov scheme known as the cubic-interpolated pseudo-particle (CIP) technique to compute the advection term of the Navier-Stokes equation. They applied a nonlinear $k-\epsilon$ model and they found this to be adequate for reproducing flow and vorticity field in the separation region for the case of fixed dunes. Despite its attractiveness, this model shows some drawbacks: the effect of turbulent fluctuations is not considered, the step length coefficient in the sediment transport formula is unknown, and the model produces smooth two-dimensional bedforms.

Paarlberg et al. (2009) have developed a two-dimensional vertical model assuming hydrostatic pressure conditions. The sediment transport is computed using a Meyer-Peter-Müller type of equation, including gravitational bed slope effects and a critical bed shear stress. The flow model was simplified by parameterization of the flow in the recirculation zone and by considering the separation streamline as an artificial bed. This model successfully simulated the bedform evolution from a flat bed, with initial perturbations. However, in this model dunes keep merging until one dune covers the full domain, which is unrealistic. Moreover, bed load sediment transport is evaluated using the turbulence-averaged bed shear stress as flow parameter, which is not accurate in case of non-uniform flow with developing boundary layers associated with significant spatial variations in turbulence structures (Nelson et al., 1995).

More recently, Niemann et al. (2011) have developed a two-dimensional morphodynamics model. The flow is simulated using a $k-\omega$ model and the sediment transport is considered to be only bed-load using a "Meyer-Peter and Müller" sediment formula. The sediment transport is considered to be in equilibrium and they used a filter to remove the instabilities on the bedform. This filter imposes artificial erosion and deposition as it is argued by Niemann et al. (2011).

To the author's knowledge, numerical models so far have not been able to simulate detailed instantaneous three-dimensional bedform dynamics. Developing a model that provides detailed information of bedform migration and sediment transport can be very important for enhancing our insight into the dynamics of subaqueous dunes. The present model, which simulates detailed three-dimensional dune topography, is developed to complement the existing models.

This chapter describes a new approach to simulating three-dimensional dunes in unsteady flow, considering the effect of turbulent fluctuations and coherent structures on sediment transport. First, a model based on parameterization of sediment transport is applied. In a next step, the sediment model described in Chapter 3 is applied to evaluate the deformation of the bed.

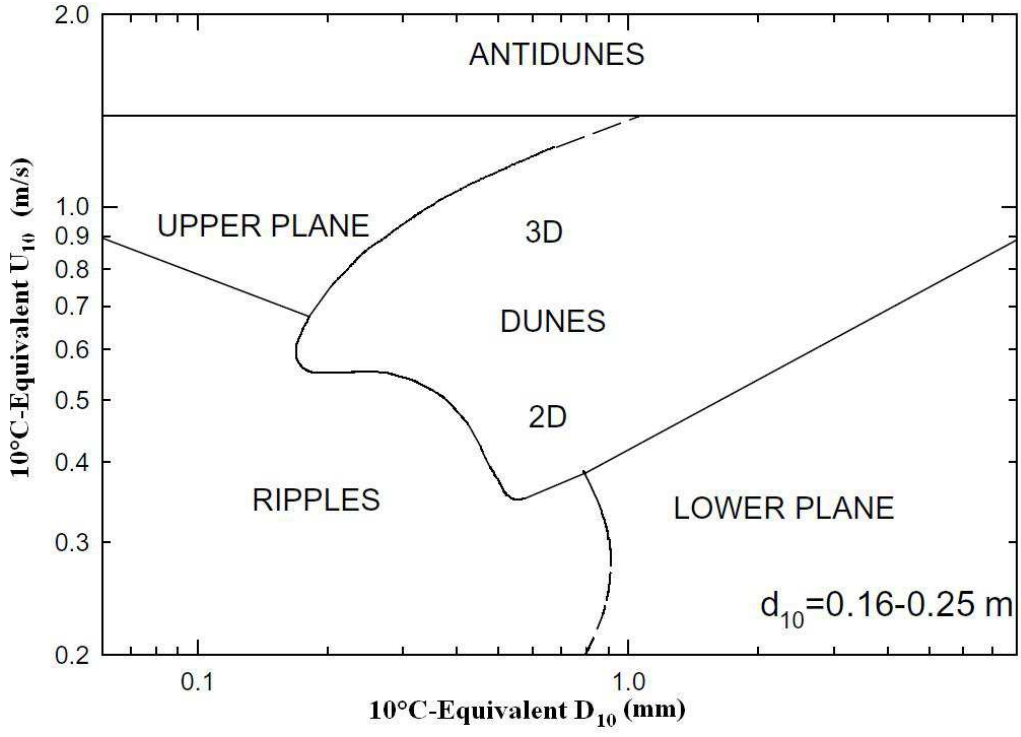

Figure 4.2: Bedform phase diagram digitised after Southard and Boguchwal (1990). The mean velocity U_{10} , flow depth, d_{10}, and grain size, D_{10}, have been adjusted to their $10°C$.

4.2 Numerical model

4.2.1 Overview

The 3D Large Eddy Simulation model described in chapter 2 is employed. Two sediment models are tested in combination with this hydrodynamic model. In the first case, a sediment model based on the parameterized sediment pick-up relations proposed by Nakagawa and Tsujimoto (1980) is employed. In the second case, this model is replaced by a more sophisticated model based on the discrete-element method for sediment pick-up, transport, deposition and sliding described in Chapter 3.

The computation of morphodynamic changes is based on the sediment balance equation, with the sediment pick-up and deposition obtained from the sediment model as source and sink terms. In the next sections, morphodynamic models based on parametric sediment transport relations and on the description of individual particle motion are discussed in more detail.

4.2.2 Morphology using parameterized sediment relations

Giri and Shimizu (2006) successfully used a two-dimensional vertical model for the evolution and migration of dunes. A Eulerian stochastic formulation of the evolution of bedforms proposed by Nakagawa and Tsujimoto (1980) is incorporated in their model. The dimensionless pick-up rate is expressed as follows (Nakagawa and Tsujimoto, 1980):

$$P_S^* = \frac{P_S\sqrt{d}}{\sqrt{(\rho_s/\rho - 1)\, g}} = F_0 \tau_* \left(1 - \frac{\tau_{*cr}}{\tau_*}\right)^3 \tag{4.1}$$

where d is the sediment grain size, ρ_s is the mass density of sediment, ρ is the mass density of water, g is acceleration due to gravity, P_S is the sediment pick-up rate, τ_* is the dimensionless local bed shear stress, τ_{*cr} is the dimensionless critical shear stress and F_0 is an empirical constant equal to 0.3. The sediment deposition rate is defined as

$$P_d = \int P_S f_s(s)\, ds \tag{4.2}$$

where P_d is the sediment deposition rate, and $f_s(s)$ is a distribution function of the step length. The latter is found to be given by

$$f_s(s) = \frac{1}{\Lambda} \exp(-s/\Lambda) \tag{4.3}$$

where Λ is the mean step length and s is the distance between the pick-up and deposition points. The mean step length can be calculated as $\Lambda = \alpha d$ in which α is an empirical constant. Here, the value of α is proposed to be 100 (after calibration). In order to calculate the evolution of the bed, the mass conservation equation for the bed is considered as

$$\frac{\partial y_b}{\partial t} = \frac{1}{1-\lambda}\left[\frac{A_3}{A_2}(P_d - P_S)\right] d \tag{4.4}$$

where y_b is the bed elevation, λ is the porosity factor of sediment, and A_2 and A_3 are shape coefficients for spherical particles in two and three dimensions, equal to $\pi/4$ and $\pi/6$, respectively.

The empirical equations mentioned above have been derived for unidirectional flow. Giri and Shimizu (2006) applied this formulation and assumed the flow to be unidirectional. They assume the flow in the recirculation zone (with negative streamwise velocity) to be weak, not exerting a significant shear stress on the bed. Therefore the pick-up of sediment in that zone is ignored.

In the first step of the present study, we apply the same formulations in three dimensions. We assume the flow to be unidirectional and ignore the transport

of sediment due to velocity components in transverse and negative streamwise directions. As we will show in the following sections, this approach is suitable for two-dimensional problems. In three-dimensional cases, the three-dimensionality of the dunes creates relatively large transverse velocities, whence the transverse sediment motion cannot be neglected. The empirical equations mentioned above are only applicable to three-dimensional flows with two-dimensional dunes (e.g. in narrow flumes). To avoid the shortcomings of this approach, a more realistic physics-based model is needed. In the next section, such a model is discussed.

4.2.3 Morphology using a sediment particle model

To avoid the shortcomings of the model proposed by Giri and Shimizu (2006), a more physics-based model is used. It describes sediment pick-up, transport, sliding and deposition, considering the sediment as rigid spherical particles and simulating particle motion in a Lagrangian framework as discussed in chapter 3. The resulting sediment model is likely to yield a more realistic description of the evolution and migration of bedforms.

The number of picked up and deposited particles is determined with the method described in chapter 3. In combination with a sliding model, it can be used to describe the evolution of the bed. The difference in the number of particles picked up and deposited for any portion of the bed indicates the amount of mass added to or taken away from that area. The change in bed level after time step Δt can be determined as

$$\Delta y = \frac{A_2}{A_3} \frac{V_p \left(n_{depos} - n_{pickup} \right)}{S.C_{frac}} + \frac{\delta P_S}{\Delta x \Delta z} \tag{4.5}$$

or

$$y_{new} = y_{old} + \Delta y \tag{4.6}$$

The first and second terms in the right hand side of Equation (4.5) indicate the effect of sediment transport by pick-up / deposition and sliding, respectively. y_{old} and y_{new} are the bed levels before and after deformation, n_{pickup} is the number of picked up particles and n_{depos} is the number of deposited particles in time step Δt, which can be found according to methods described in Chapter 3, using Stokes number and particle diameter as criteria for deposition. In the second term in the right hand part of Equation (4.5), $\delta P_S = P_{S,in} - P_{S,out}$ is the change in volumetric sediment transport for each cell associated with sliding. Here $P_{S,in}$ denotes the sum of sliding sediment coming into the control area from neighbouring cells, and $P_{S,out}$ is the sliding sediment going out from that control area to the neighbouring cells. Considering Figure (3.9),

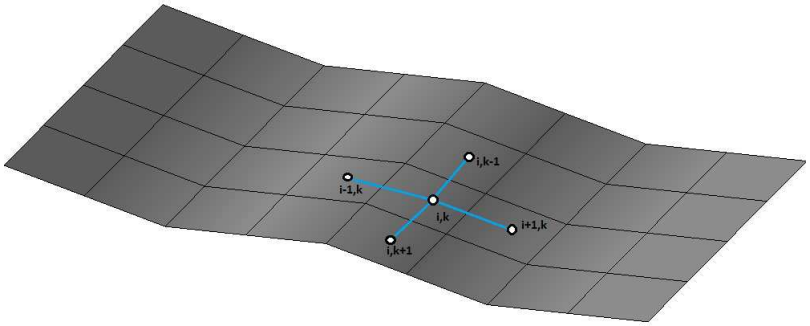

Figure 4.3: Bed topography is approximated by a surface grid.

$$P_{S,out} = \left(1 - \frac{\delta x\,(\Delta z - \delta z) + \delta z\,(\Delta x - \delta x) + \delta x \delta z}{\Delta x \Delta z}\right) P_S \tag{4.7}$$

The sliding model is discussed in more detail in section 3.4.4.

4.2.4 Bed geometry

The bed is considered as a structured surface grid (Figure 4.3). The resolution of the grid for Δx and Δz is the same as the resolution of the finest computational grid, which is attached to the bed. The bed level is defined in the centre of each cell and can be interpolated to other points. Here bilinear interpolation is applied, which conserves second-order accuracy of the bed geometry. On the other hand, mass conservation has to be taken into account as the bed deforms. In case of periodic boundaries upstream and downstream, the sum of mass in the bed and mass of moving particles must be constant. If the boundaries are not periodic, sediment has to be fed upstream to compensate for the outflow through the downstream boundary.

4.3 Numerical experiments

The formation and migration of ripples and dunes under turbulent flow conditions are presented in this section. The bedform changes are simulated by the approaches mentioned above, using a parametric sediment transport relation and a particle technique, respectively.

4.3.1 Simulation by parameterized sediment relations

First, the Eulerian stochastic formulation of the evolution of bedforms proposed by Nakagawa and Tsujimoto (1980) is considered. The dimensions of the com-

putational domain are identical to those in the experiment of Polatel (2006). In this experiment, the length of the 17^{th} of a train of 22 dunes is 400 mm, with a flume width of 8 cm. The water depth and the average bulk velocity are 8 cm and 0.394 m/s respectively, which yield a Reynolds number of 31520 and a Froude number of 0.44. The free surface is considered as a free-shear rigid lid. LES calculations using a level set method to model the free surface deformation show that the waves on the free-surface have a negligible effect on the flow, except on the streamwise turbulence intensities (Polatel, 2006).

To avoid instabilities from the steep angles, an avalanche model has been implemented based on the angle of repose of sediment. The angle of repose is taken to be 35 degrees. As soon as the angle of the lee side exceeds the angle of repose, it is forced artificially back to this angle. Sediment of diameter 100 μm has been used. Periodic boundary conditions are imposed in stream- and spanwise directions. The mass which leaves the domain enters the same domain from the other side. The flow is driven by a pressure gradient, the value of which is calculated such, that the bulk velocity at the entrance of the computational domain stays constant.

The bed is initially flat in the current numerical experiment. The shear stress fluctuations generate small perturbations of the bed surface by local pick-up and deposition. These perturbations grow higher and higher and ultimately lead to the generation of finite-amplitude bedforms. Figure (4.4) shows the resulting generation and migration of dunes. This simulation yields smooth dunes, because of the sediment transport description: it is divided into a pick-up and a deposition description, and the latter works by distributing the deposition of sediment over a certain region, thereby obtaining a filtering effect (Niemann et al., 2011).

This method is also applied in a wider domain to obtain a three-dimensional dune pattern. The same conditions of the above experiment were used (except the domain width). Figure (4.5) shows the resulting bed topography. Clearly, the irregularities found do not represent a physically realistic dune pattern, probably because the motion of sediment in spanwise direction is ignored (see above). In the next section, numerical experiments are discussed which make use of more sophisticated particle techniques to simulate the bed deformation.

4.3.2 Simulation using particle techniques

In this section, the generation and migration of dunes are simulated by using rigid spheres as sediment particles. The sediment is picked up from the bed, transported in the water, and settled at different locations. By considering the pick-up and deposition as mass sources and sinks, the deformation of the bed can be calculated. The configurations for this simulation are identical to a flume experiment carried out at the Department of Hydraulic Engineering of Delft University of Technology (Crosato et al., 2011). The total length of the flume is 25 m

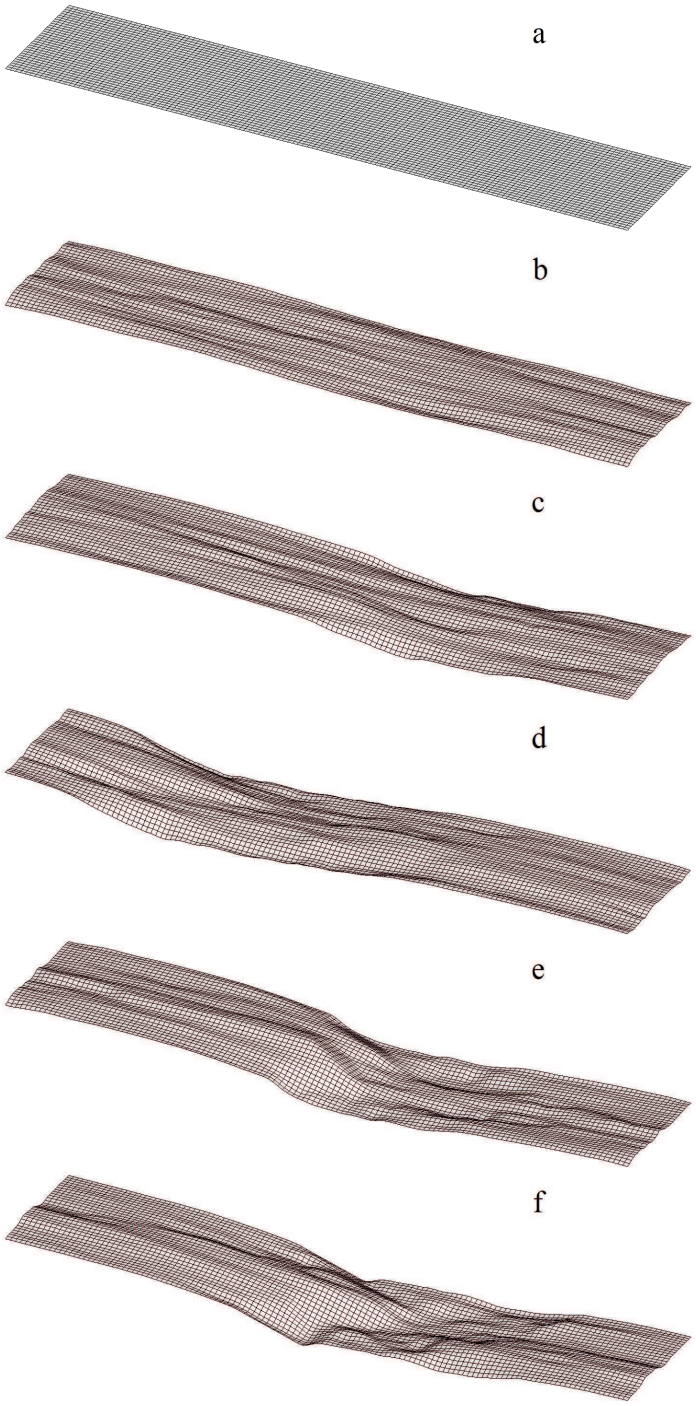

Figure 4.4: The evolution of the bed at different points in time simulated using a parametric sediment model. It begins from a flat bed (a), then longitudinal sand ridges form (b). Later on, these features become irregular (c), the irregularities keep on growing and dunes appear (d) which migrate in the streamwise direction (e and f).

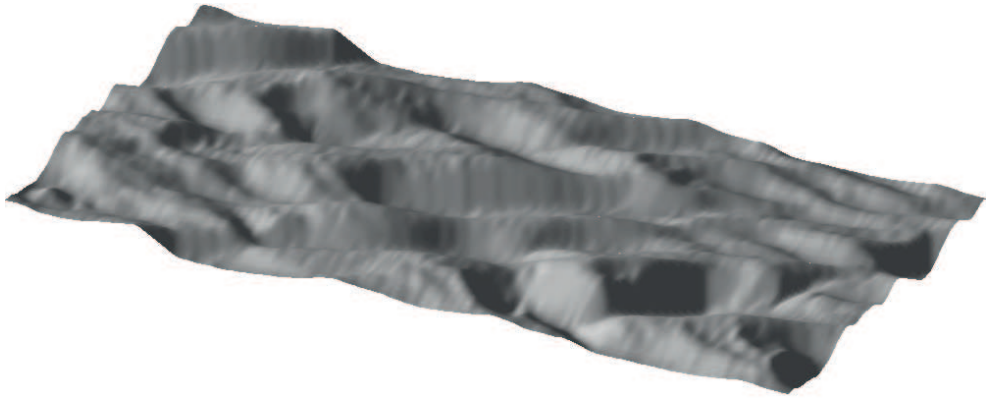

Figure 4.5: Simulation of bedforms in a wide channel using the formulations of (Nakagawa and Tsujimoto, 1980). The irregularities do not exhibit the typical dune features.

and the width is 60 cm, with a slope of 3×10^{-4}. The bottom of the flume is covered with a 20 cm thick sediment layer with 0.245 mm median diameter. The experiment began from a flat bed, with a water depth of 4.5 cm, and a discharge of 6.8 l/s. In the simulation only a part of the flume of 1.2 m length is modelled. The boundaries in streamwise direction are taken periodic. For generalization and also simplicity, the boundaries in spanwise direction are also taken periodic, thus ignoring the sidewall shear layers. The pick-up rate of sediment is calculated by Equation (4.1) instead of De Ruiter's formula (Equation 3.40 or 3.41). However, we replaced the overall bed shear stress and the critical shear stress in Equation (4.1) by the particle and instantaneous critical shear stresses. Similar to the experiment, the simulation begins from a flat bed, with the same water depth and discharge as in the experiment (Figure 4.6a). The bed gets instabilities because of fluctuating shear stress (Figure 4.6b). These instabilities lead to ripples (Figure 4.6c). The ripples grow (Figure 4.6d) and dunes are formed (Figure 4.6e). Dunes move and finally they attain a statistically steady state (Figure 4.6f). Figure (4.7a-f) shows instantaneous sediment distribution (suspended) in the water above the dunes. Figure (4.8) shows an instantaneous measurement of the bedform and its low-pass filtering in the centreline of the flume.

Bedform dimensions are determined from the bed-level profile using a 'zero-crossing' method (Van der Mark et al., 2008). Length and height are defined by two successive intersections of the bed profile with the baseline. In 2D situations, dunes are determined by comparing the downstream bed profile with its least-squares straight line. The height of an individual dune is defined as the difference between the highest and the lowest point between two successive zero crossings. The length of that dune is the distance between two successive zero crossings. The mean length and height of the dunes are found by averaging the length and height of all dunes present for several sections in streamwise

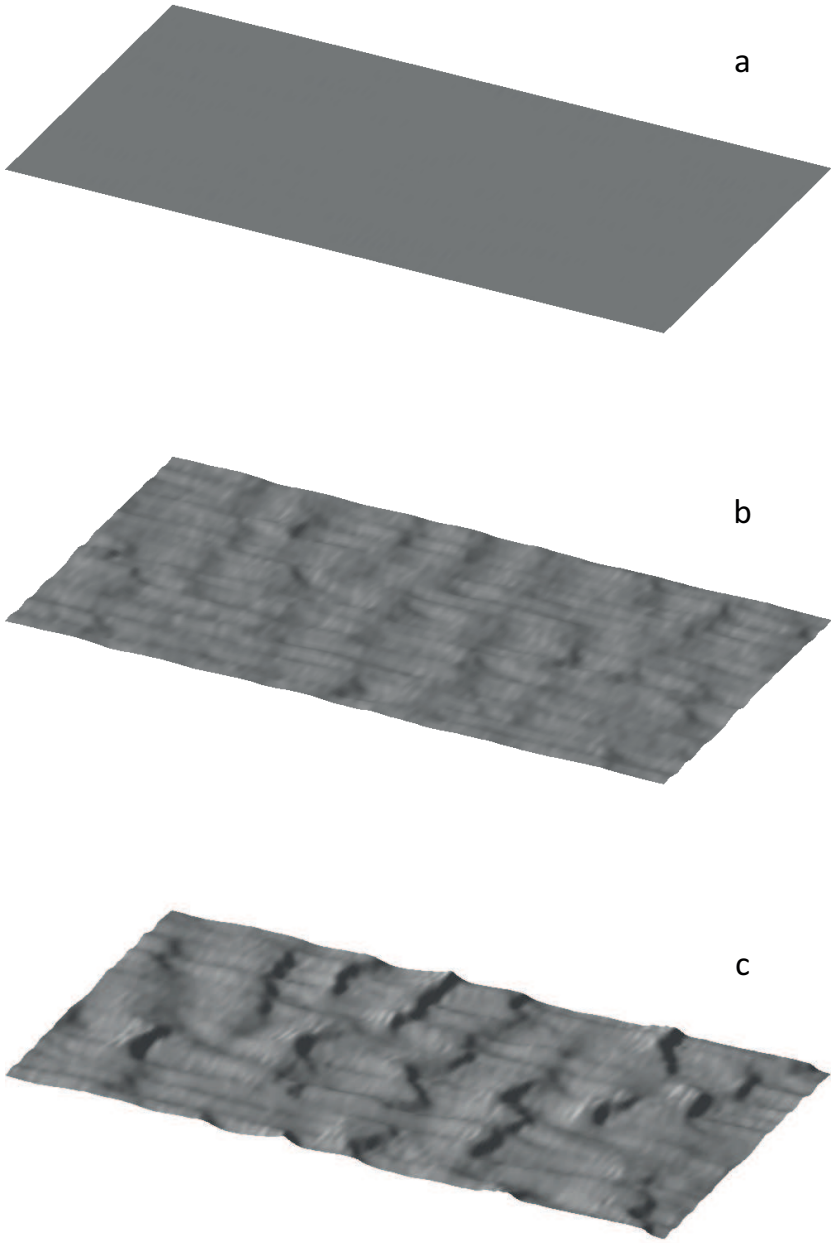

Figure 4.6: Simulation of morphology with sediment diameter of 245 μm. It starts from a flat bed (a), instabilities appear (b), then ripples are generated (c). The ripples grow (d), and lead to generation of dunes (e). The dunes grow and move as steady (f).

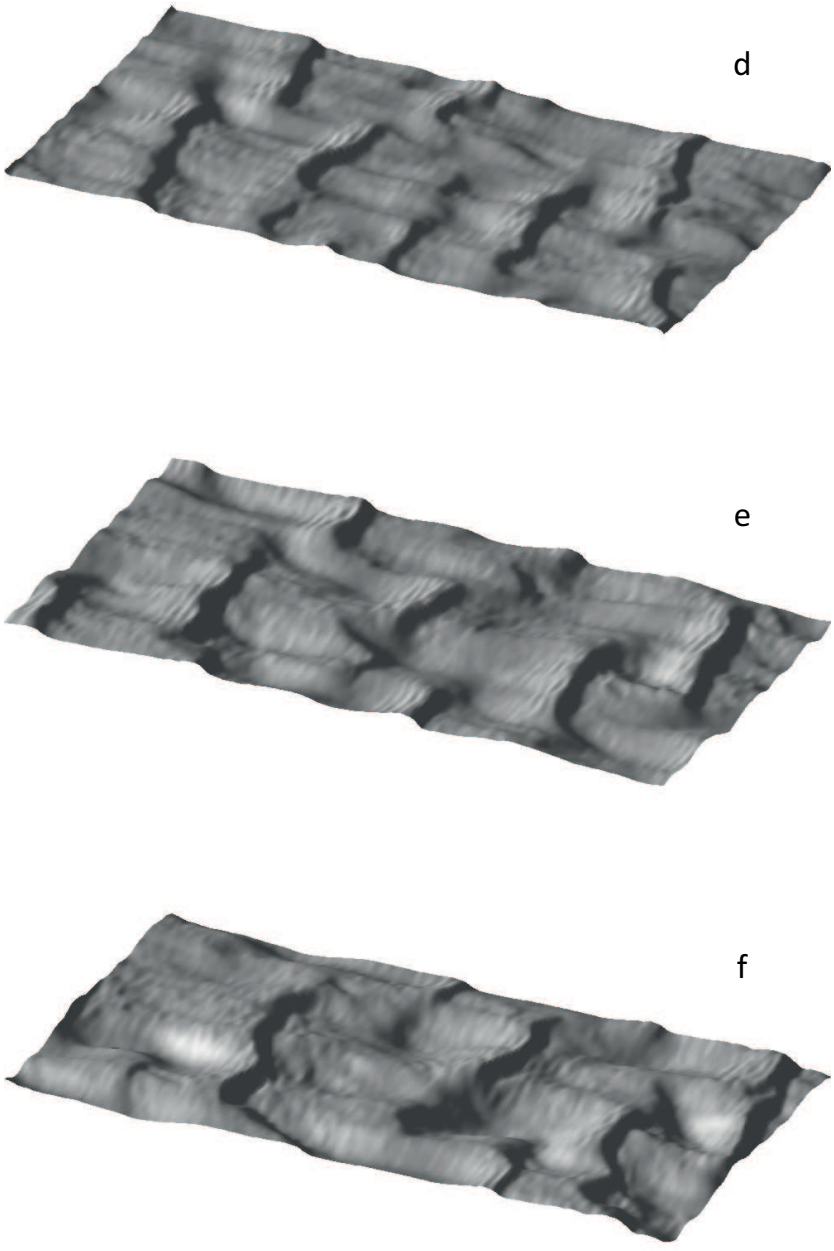

Continuing Figure (4.6)

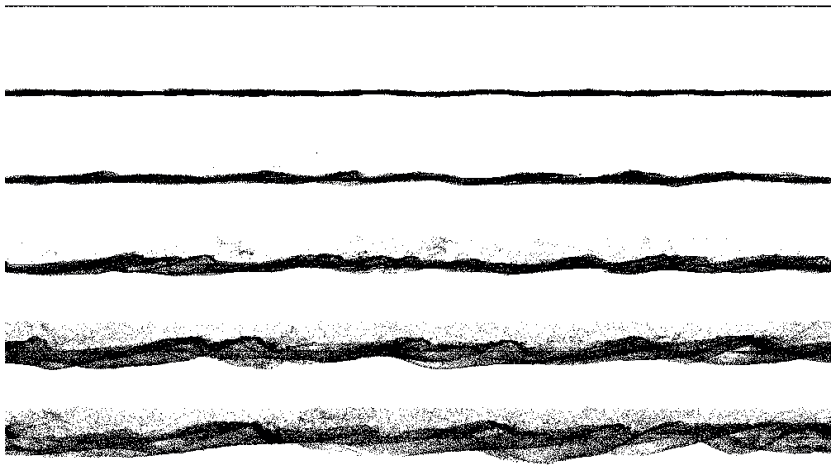

Figure 4.7: Computed distribution of sediment over the dunes (side view). The diameter of particles is 245 μm.

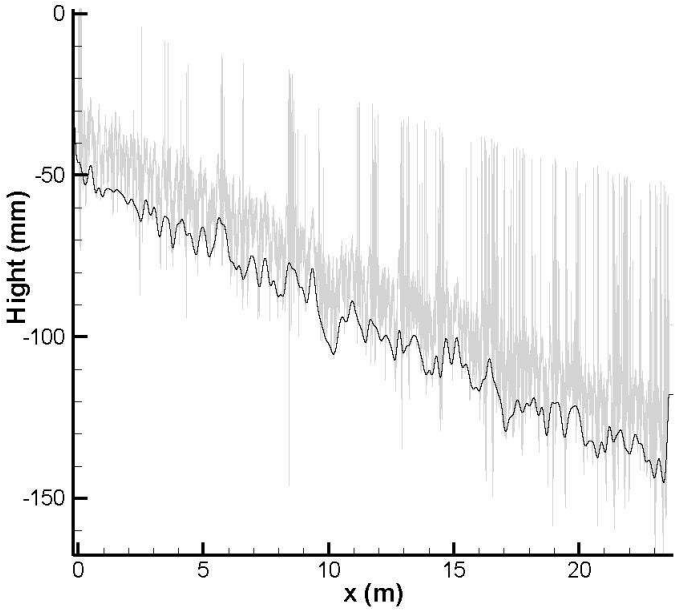

Figure 4.8: Measured dune height and length (grey) and low-pass filtered signal (black).

direction. The length and height of dunes in our simulation are found to be 26.6 cm and 24 mm, which agrees well with the experiment (30.5 cm and 26 mm, respectively). However, differences in average height and length can arise because different methods are used for averaging the measured and the simulated bedforms.

4.4 Concluding remarks

Two models for sediment transport were applied. First, a parameterized model based on the sediment transport relation of Nakagawa and Tsujimoto (1980) was employed. Although this method is capable of simulating two-dimensional (or nearly two-dimensional) bedforms under unidirectional flow, it fails to represent three-dimensional situations. Hence, a more advanced method for sediment transport, based on particle techniques, was employed. This model was shown to give physically more realistic and accurate results.

The bed morphology is derived from the sediment model by keeping track of sediment pick-up and deposition as sources and sinks in each cell. This sediment balance model was found to provide the best results to address the problem of bedform development.

In order to validate our model, the deformation and migration of the bedform is simulated and the results are compared with the experimental measurements. The model results were found to agree well with the experimental findings. It is found that the present model has the potential to constitute a basis for bed roughness under steady as well as varying flow conditions. This is extremely important, for instance, for the prediction of extreme flood levels in rivers, hence for the design of adequate flood protection measures. We elaborate this in the next chapters.

Chapter 5

Flow over fixed dunes

5.1 Introduction

The detailed simulation (eg. Large Eddy Simulation) of morphodynamic processes is computationally expensive and not applicable in practical engineering. Moreover, such simulations cannot be applied to large spatial and temporal scales by present computers. Parameterization of different aspects is necessary to be able to describe these larger-scale processes, such as the time-evolution of hydraulic roughness during a flood, in a more cost-efficient way.

Within this context, both statistically steady and unsteady morphodynamics are of eminent importance. The drag forces exerted by two- and three-dimensional dunes, respectively, are compared and parameterized relations with mean flow properties are derived.

5.2 Flow over fixed two-dimensional dunes

In order to validate the model for regular and irregular bedforms, the flow over two-dimensional dunes is simulated and further analyzed. Series of experiments were conducted by McLean et al. (1994) for the flow over two-dimensional dunes. The experiments were conducted in the Ocean Engineering Laboratory at the University of California. The experimental flume was 22 m long, 0.9 m wide, and 0.9 m deep and contained twenty fixed dunes of 0.8 m wavelength and 0.04 m height. The stoss side of the dunes was a half-cosine wave running from its low point at the trough to its high point at the crest. The angle of the lee slope was 30 degrees. Figure (5.1) shows the two-dimensional dune which is adopted for these experiments.Three flow conditions were investigated in these experiments, with the flow depth varying from 0.158 to 0.546 m. Table (5.1) shows the experimental conditions of these experiments.

Here we simulate runs 2 and 3 of these experiments. The boundaries in streamwise and transverse directions are taken periodic. A streamwise pressure

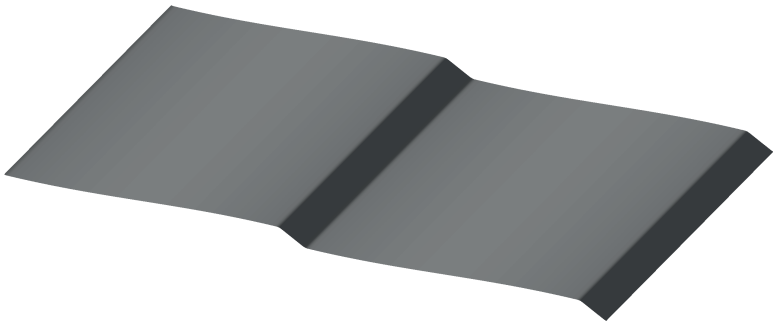

Figure 5.1: Schematic representation of the two-dimensional fixed, artificial dunes in McLean et al. (1994) experiments. The water flows from left to right.

Table 5.1: Experimental conditions for two-dimensional dunes (McLean et al., 1994)

Run	h (m)	U (m/s)	Fr	τ_T (Pa)	u_*^T (m/s)	c_f	Slope ($\times 10^4$)
1	0.210	0.482	0.336	1.49	0.0386	0.0064	8.3
2	0.158	0.377	0.303	1.20	0.0346	0.0084	9.4
3	0.546	0.284	0.123	0.45	0.0212	0.0056	0.81

gradient is adjusted such that the desired bulk velocity is achieved. Figure (5.2) shows the instantaneous streamwise velocity on this dune for runs 2 and 3. Figure (5.3) shows the spatially and temporally averaged streamwise velocity for runs 2 and 3. It can be seen that in run 2 no recirculation zone is found, whereas in run 3 a recirculation zone is formed in the lee of the dunes. Figure (5.4) shows the instantaneous vorticity for these two runs. The vorticity behind the dune crest probably reflects the boiling effect. Boils are generated on the stoss side of the dune, shed from the crest into the flow and finally reach the free surface, which they slightly deform (Best, 2005). Figure (5.5) shows the turbulent kinetic energy. The maximum turbulent kinetic energy for run 2 is located in the vicinity of the dune peak, whereas in run 3 the maximum is located around the recirculation zone.

In order to visualize the coherent structures of the flow we follow the approach developed by Hunt et al. (1988), based on the second invariant of ∇u, defined as

$$Q = -\frac{1}{2}\frac{\partial u_i}{\partial x_j}\frac{\partial u_j}{\partial x_i} = -\frac{1}{2}\left(|S|^2 - |\Omega|^2\right) \tag{5.1}$$

where S and Ω are the symmetric and antisymmetric components of ∇u. Figure

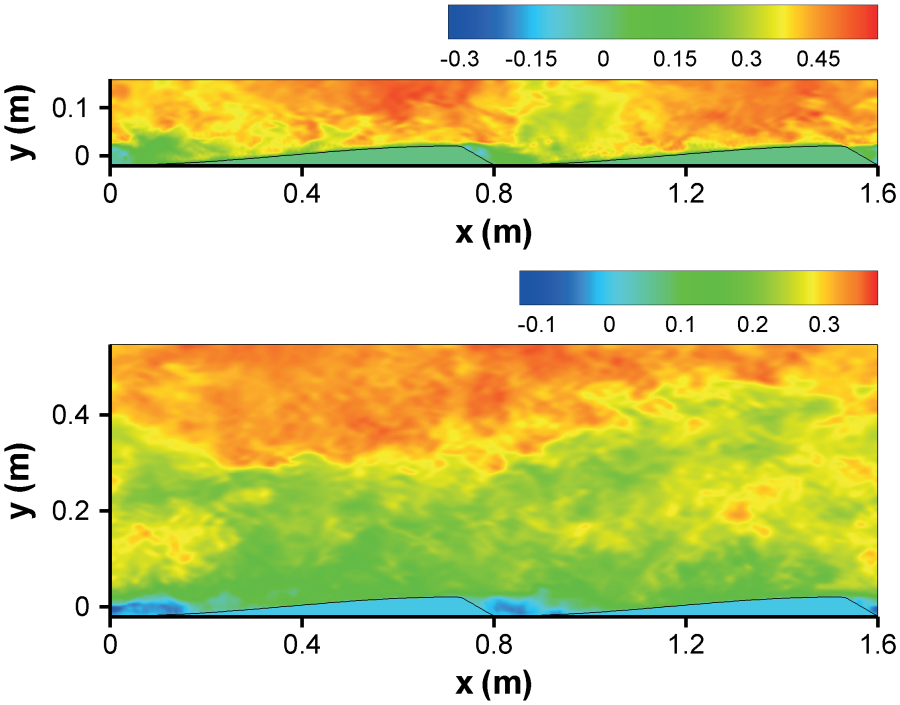

Figure 5.2: Instantaneous streamwise velocity for runs 2 and 3.

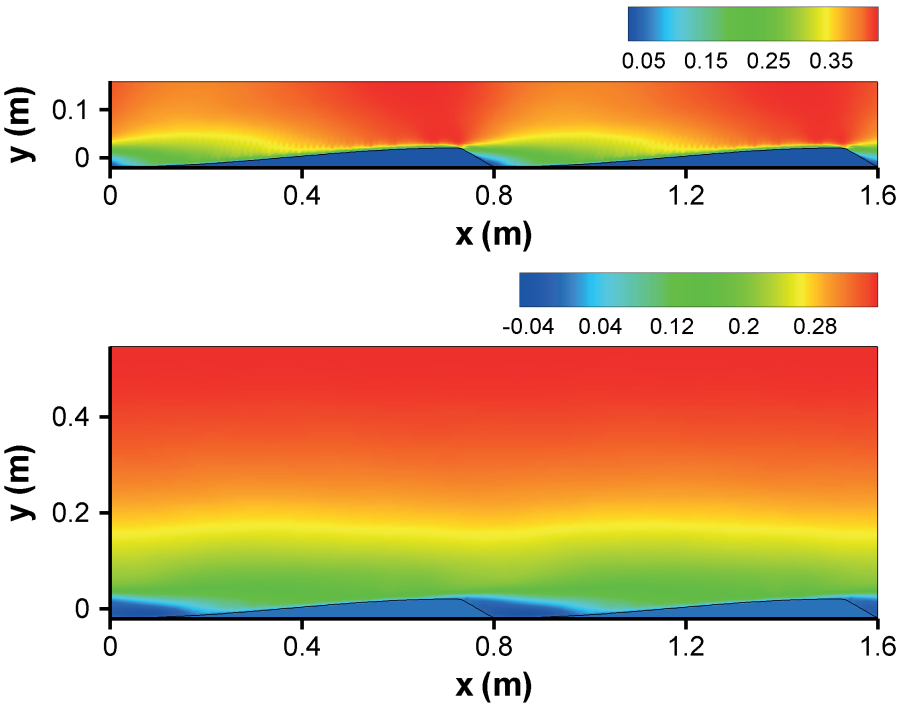

Figure 5.3: Space- and time-averaged streamwise velocity for runs 2 and 3.

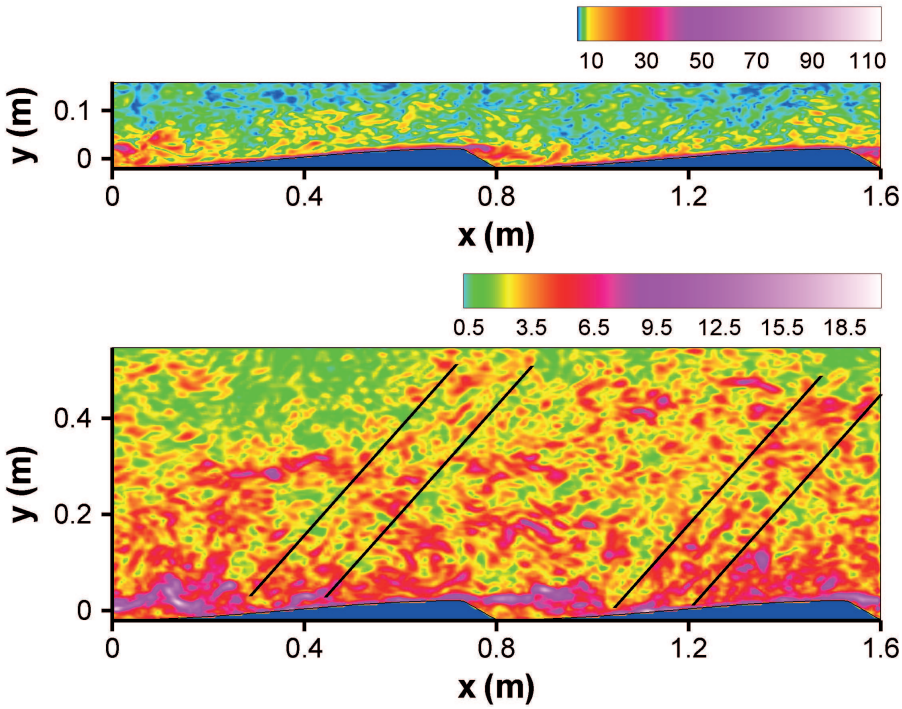

Figure 5.4: Instantaneous vorticity for runs 2 and 3.

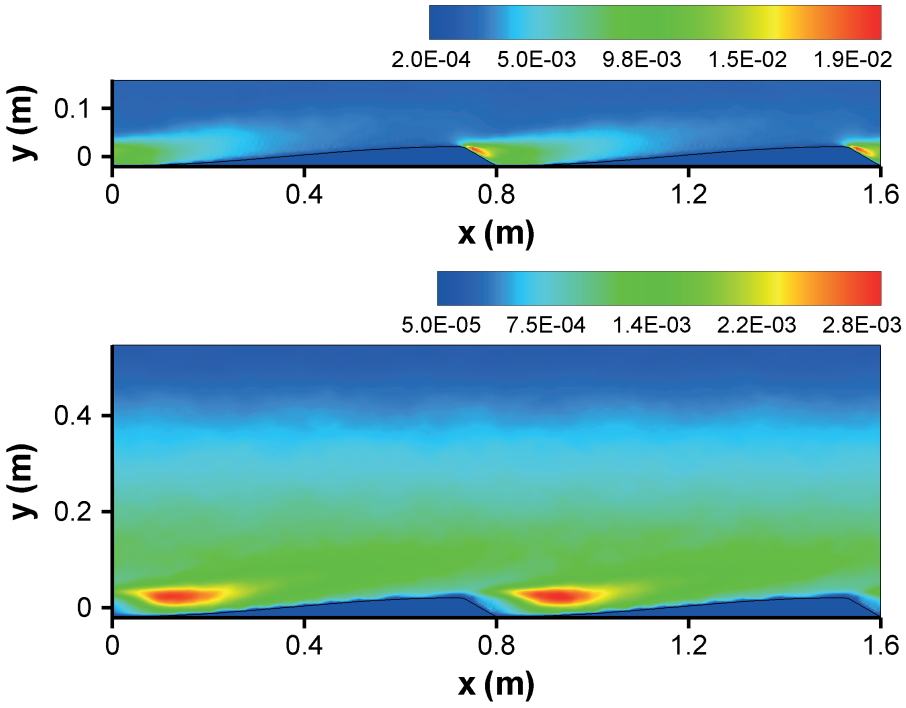

Figure 5.5: Space- and time-averaged turbulent kinetic energy for runs 2 and 3.

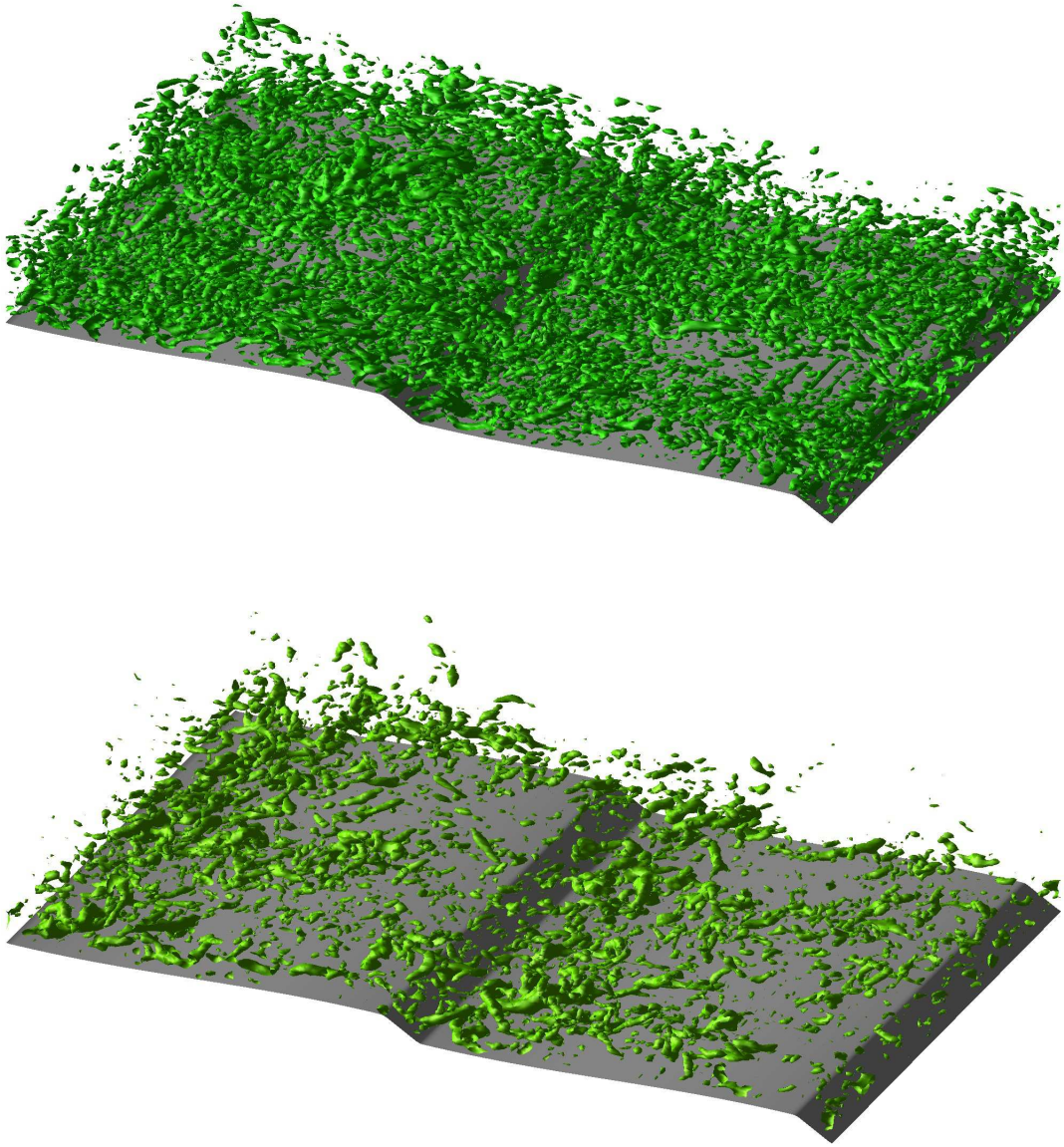

Figure 5.6: Coherent structure of turbulence over the dunes for runs 2 (top) and 3 (bottom) for the value of $Q = 8\,s^{-2}$.

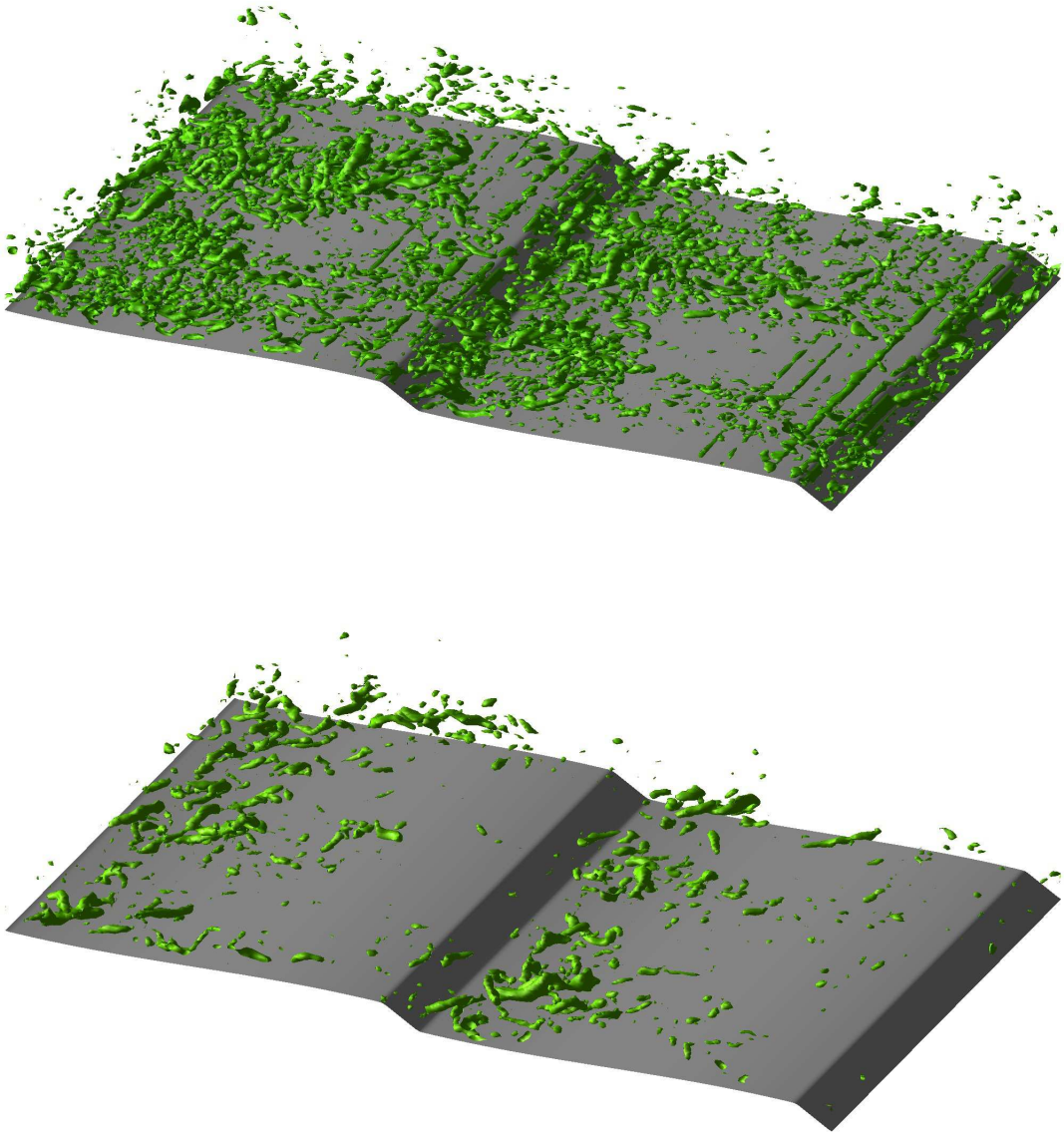

Figure 5.7: Coherent structure of turbulence over the dunes for runs 2 (top) and 3 (bottom) for the value of $Q = 20\,s^{-2}$.

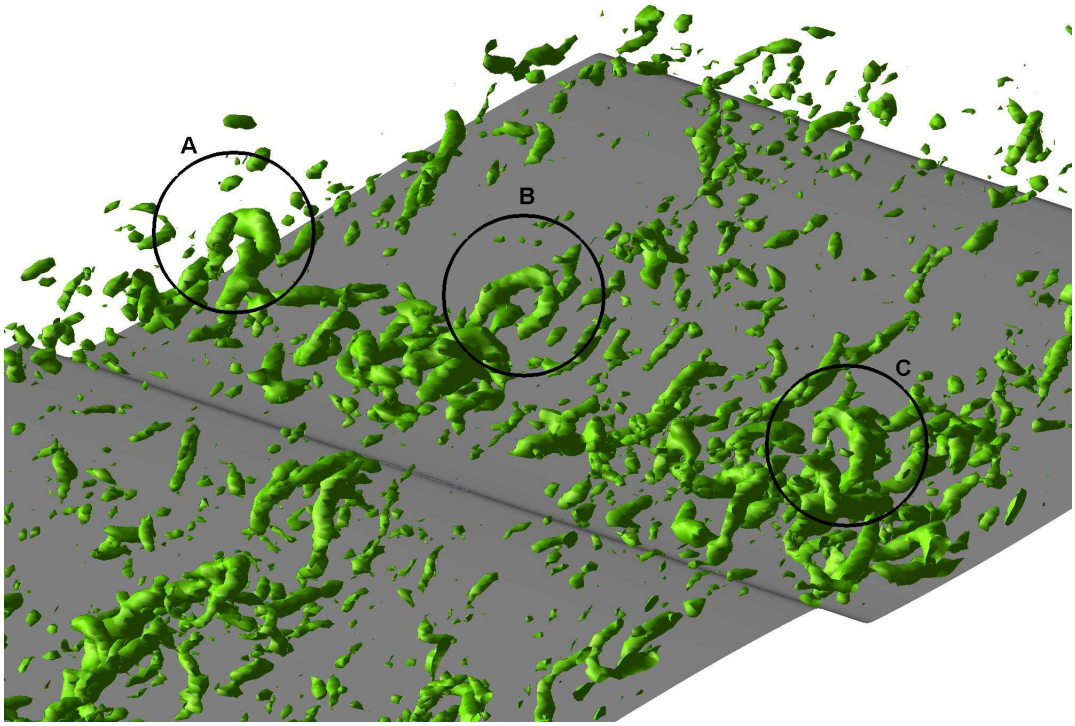

Figure 5.8: Horseshoe structure on the stoss side of a dune in run 3 for the value of $Q = 12\,s^{-2}$.

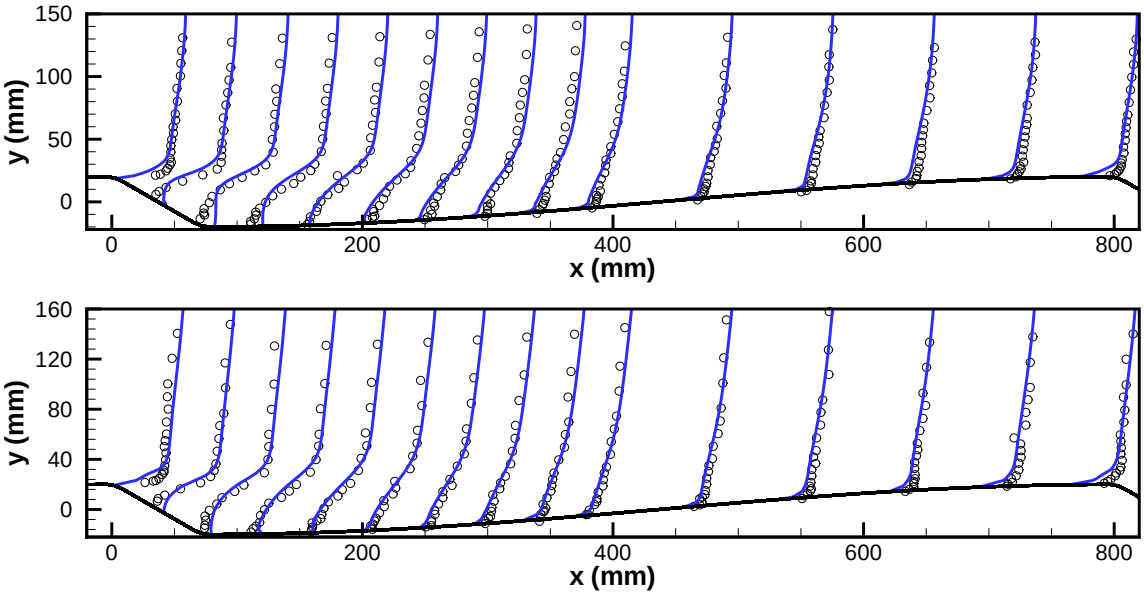

Figure 5.9: Comparison of non-dimensional time-averaged streamwise velocity profiles over two-dimensional dune for case 2 (top) and case 3 (bottom). McLean's experiment ○, and simulated results ——

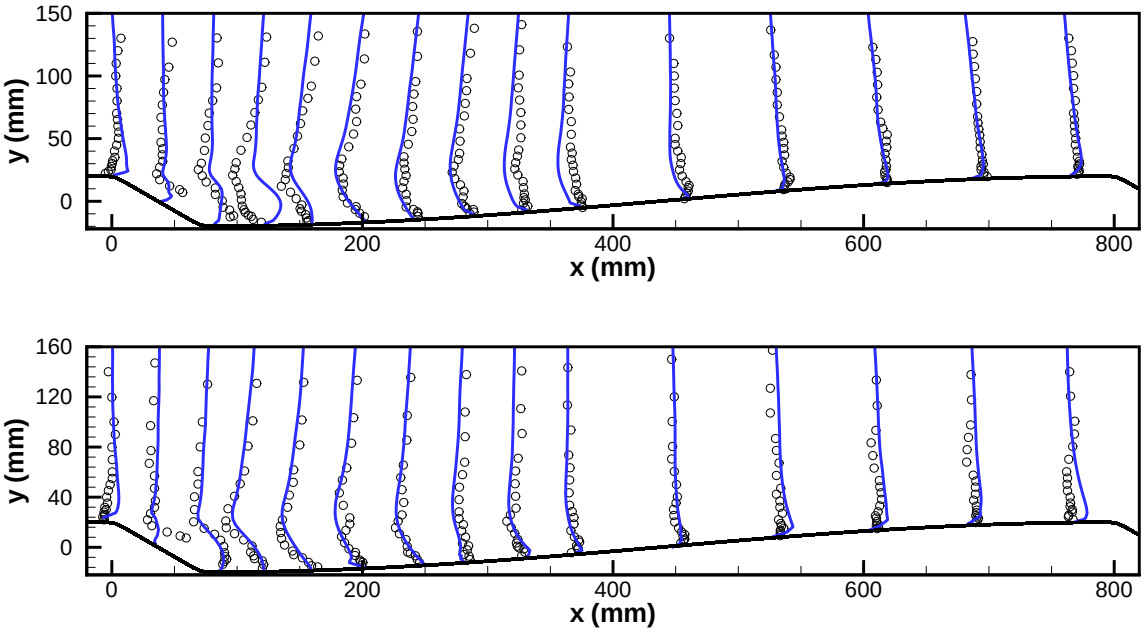

Figure 5.10: Comparison of non-dimensional time-averaged vertical velocity profiles over two-dimensional dune for case 2 (top) and case 3 (bottom). McLean's experiment ○, and simulated results ——

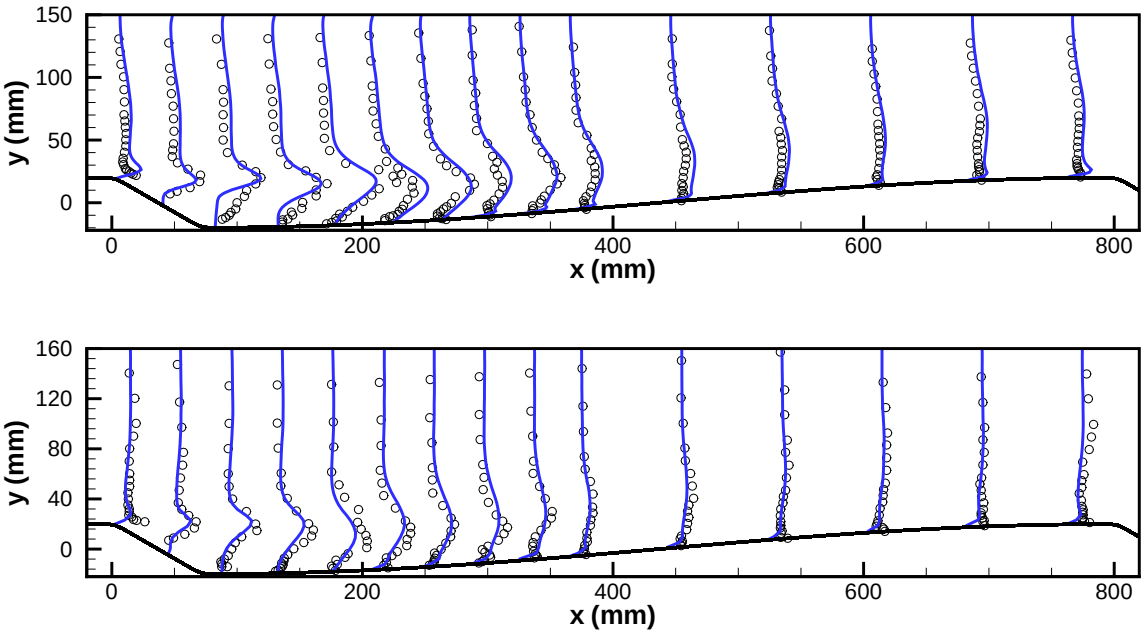

Figure 5.11: Comparison of non-dimensional time-averaged Reynolds stress profiles of $-\overline{u'u'}$ over two-dimensional dune for case 2 (top) and case 3 (bottom). McLean's experiment ○, and simulated results ——

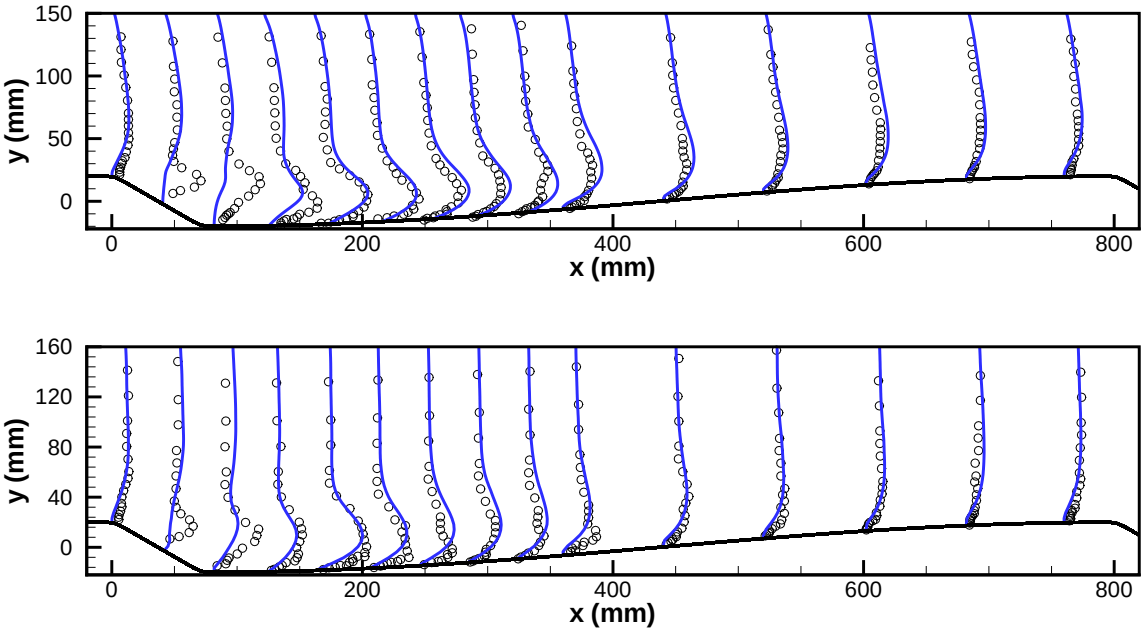

Figure 5.12: Comparison of non-dimensional time-averaged Reynolds stress profiles of $-\overline{w'w'}$ over two-dimensional dune for case 2 (top) and case 3 (bottom). McLean's experiment ○, and simulated results ——

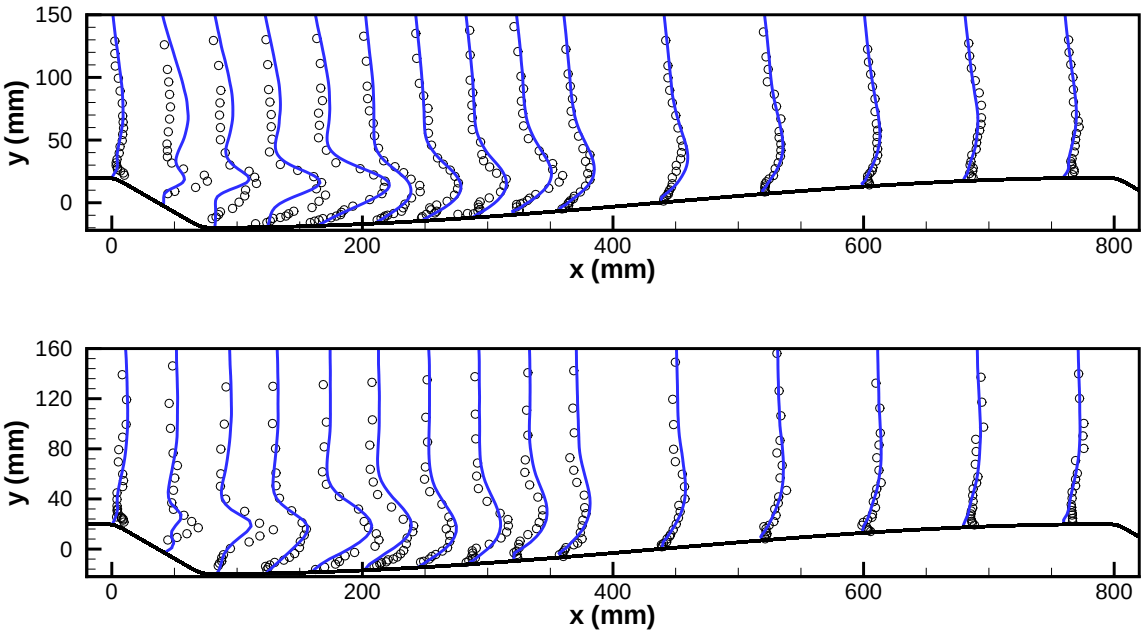

Figure 5.13: Comparison of non-dimensional time-averaged Reynolds stress profiles of $-\overline{u'w'}$ over two-dimensional dune for case 2 (top) and case 3 (bottom). McLean's experiment ○, and simulated results ——

(5.6) shows the coherent structure above the dune for runs 2 and 3 by plotting the isosurface for $Q = 8\,s^{-2}$. A slight difference in the form of these structures can be observed between these runs. The turbulence structures for run 2 are smaller than those for run 3. In run 3, the recirculation zone generates large eddies and these eddies break down to smaller eddies on the stoss side of the next dune. Because of absence of a significant recirculation zone in run 2, the large eddies can not be generated by the recirculation zone. To observe this phenomenon clearly, the coherent structure is plotted for a larger value of Q ($Q = 20\,s^{-2}$) in Figure (5.7). At $Q = 20\,s^{-2}$, the relatively small structures are filtered out and we observe large structures are formed behind the lee side of dunes in run 3, whereas the small structures in case 2 still dominate. Further downstream, these highly three-dimensional structures interact with the wall and generate disturbances with the same spanwise wavelength. These disturbances evolve into horseshoe vortical structures, and correspond to the horseshoe-like vortices. Figure (5.7) shows such kind of structures behind the lee side of a dune and on the stoss side of the following dune. Both legs of the horseshoe structure are associated with high levels of positive and negative streamwise vorticity (right and left leg, respectively, facing in the flow direction). As the two legs meet along the tip, regions of high spanwise vorticity are formed. As a result, strong vertical fluid motions are formed between the legs and close to the tip, lifting fluid from the wall region. In some instances, the intensity of these vertical fluid upwellings is as strong as 30% of the bulk flow velocity (Grigoriadis et al., 2009). This phenomenon has a strong effect on the pickup of sediment and hence in the reforming of the bed.

Figure (5.9) shows the averaged streamwise velocity normalized by the mean bed shear velocity u_*^T and compared with McLean's experiments. The normalized velocities for run 2 are generally slightly larger that those of run 3; however, considering the differences in depth and Froude number, the shapes of the individual profiles are remarkably consistent. Profiles of the vertical velocity for runs 2 and 3 are presented in Figure (5.10). The averaged streamwise and vertical velocities produced by the model are in a good agreement with the experiments. The agreement between simulated and experimental results is also extended to the Reynolds stress components shown in Figures (5.11), (5.12) and (5.13).

5.3 Flow over fixed three-dimensional dune

The interaction between flow field and bedforms is complex, involving as-yet poorly understood feedback mechanisms. One of these mechanisms is the effect of bedforms on turbulent flow. Due to the limited availability of turbulent flow measurements over three-dimensional dunes, so far we only considered measurements made over two-dimensional features of various types, including strongly asymmetric steep-angled dunes, relatively symmetric low-angled

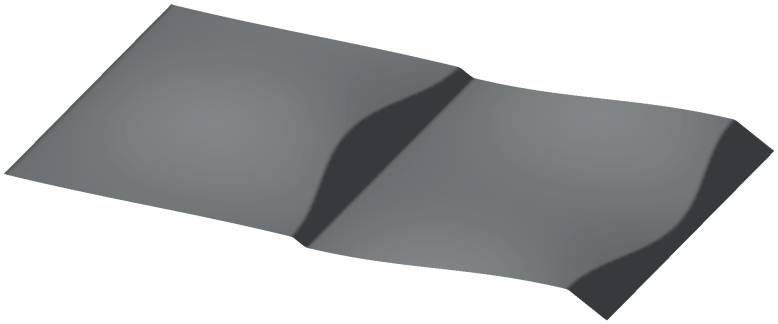

Figure 5.14: Fixed three-dimensional artificial dunes in the Maddux-experiments. The flow is from left to right.

dunes, and spatially accelerated flows. Maddux et al. (2003a,b) has performed series of experiments on fixed three-dimensional dunes. The configurations of these experiments are identical to those in McLean et al. (1994) experiments with two-dimensional dunes. Maddux's dunes were qualitatively similar to sine-crested three-dimensional dunes as observed in the field and in mobile-bed flumes (Gabel, 1993). The dunes had a mean wavelength λ of 0.8 m and a mean height δ at the crest of 0.04 m. The stoss side of the dunes was a half-cosine wave running from its low point at the trough to its high point at the crest. The angle of the lee slope was 30 degrees. The mean height, wavelength, and cross-section of these dunes matched those of the two-dimensional bedforms in McLean et al. (1994) experiments. Three-dimensionality of the dunes was introduced by making the crest line a full cosine wave in the spanwise direction (Figure 5.11). The dune height, δ, varied in the spanwise direction from 0.02 m to 0.06 m. Successive crestlines were 180 degrees out of phase, so that a dune that was high in the middle and low at the sides was followed by a dune that was low in the middle and high at the sides, as shown in Figure (5.14). It resulted in a crest-to-crest wavelength, λ, that varied in the spanwise direction from 0.73 m to 0.87 m. The resulting steepness of the dunes varied in the spanwise direction as well, with δ/λ values ranging from 0.025 to 0.075. These values matched well with values of δ/λ for real dunes observed in the field (Maddux et al., 2003b). While typical three-dimensional dunes are often more complex, with concave faces and other features, these dunes are sufficiently realistic while maintaining enough similarity to previous measurements to facilitate an understanding of the response of the flow to three-dimensional bed topography. Maddux et al. (2003b) shows a significant difference in turbulence structure and bed friction between two- and three-dimensional dunes, to the extent that this three-dimensionality must be taken into account in bedform modelling.

Maddux et al. (2003b,a) has extended the experiments over three-dimensional dunes for flow of similar depth and discharge as in experiments 2 and 3 over the

Table 5.2: Experimental conditions for three-dimensional dunes (Maddux et al., 2003a)

Run	h (m)	U (m/s)	Fr	τ_T (Pa)	u_*^T (m/s)	c_f	Slope ($\times 10^4$)
$T2$	0.173	0.357	0.275	1.71	0.0413	0.0134	10.6
$T3$	0.561	0.261	0.111	0.46	0.0215	0.0068	2.40

two-dimensional dunes. Table (5.2) shows the conditions for Maddux's experiments and they are named T2 and T3, referring to McLean's experiments 2 and 3, respectively. The water depth and the bulk velocities for T2 and T3 slightly differ from those in experiments 2 and 3.

Here we simulate the flow in experiment T2 and we call the simulation R2. The boundaries in streamwise direction are taken periodic. Smooth solid boundary conditions in spanwise direction are imposed to account for the glass side walls in Maddux's experiment. The free surface is considered as a rigid lid and the flow is driven by a pressure gradient to obtain the desire bulk velocity. The bed is considered as a rough boundary with sediment diameter of 1 mm on the bed as it is imposed in T2 (Maddux et al., 2003b). The simulations are done on a base grid of $128 \times 64 \times 32$ in streamwise, spanwise and normal direction, with one extra level of refining close to the bed.

Figure (5.15) shows the computed depth-averaged streamwise and spanwise velocities for run R2, compared with the contour graphs from Maddux's experiment T2. A qualitatively good agreement can be seen between the computed results and Maddux's measurements. The highest streamwise velocity is located on the crest line of the dunes but not at the crest point. The highest streamwise velocity is located halfway between the centreline and the walls, which is called the "node of the dune crest" in Maddux et al. (2003b). The lowest streamwise velocity is located in the trough parts directly downstream of the crest points, in the recirculation zone behind the crest. The largest absolute values of spanwise velocities are located halfway between the nodes of crest lines. The four quadrants of the spanwise velocity in Figure (5.15) are the results of the geometrical curvatures of the dunes.

Figure (5.16) shows the streamwise-averaged velocities for run R2, compared with those from Maddux's experiment T2. Like Figure (5.15), it shows that the streamwise velocity reaches its maximum at the nodes of the crest. Further, the validations are extended to the Reynolds stresses. Figure (5.17) shows a comparison between the Reynolds shear stresses for the current computations for run R2 and the measurement T2. All these figures show that the computed results qualitatively agree with the measurements.

Figure (5.18) shows the instantaneous streamwise velocity in the streamwise centre and node sections for run R2 and Figure (5.19) the time averaged velocity vectors. A relatively strong recirculation zone can be observed in the centre sec-

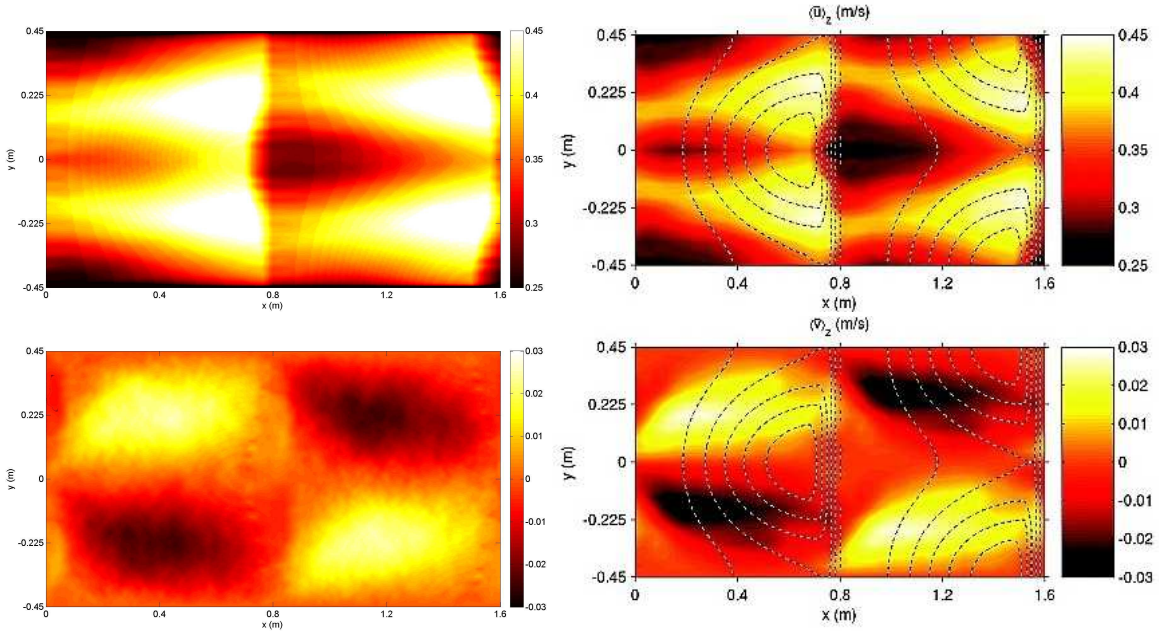

Figure 5.15: The computed depth-averaged streamwise (top left) and spanwise velocities (bottom left) for run R2, and comparison with T2 experiment from Maddux et al. (2003b) for streamwise (top right) and spanwise (bottom right) velocities.

tion, whereas in the node section this recirculation is much weaker. Although the streamwise velocity is stronger at the node, the height of the crest is lower there, whence the recirculation is weaker. Apparently, the size of the recirculation zone is more determined by the local dune height than by the velocity at the crest.

The spanwise and normal velocities form a secondary current pattern, which is shown clearly in Figure (5.20). Four counter-rotating secondary circulation vectors, with secondary current velocities, can be observed at $x = 0.8\,\mathrm{m}$, as it was also observed in experiment T2. These secondary currents appear to generate a net downward momentum flux. This flux could be carrying momentum that is not being carried by low levels of turbulence over the three-dimensional dunes (Maddux et al., 2003b).

Figure (5.21) shows the instantaneous vorticity in the centre and node sections. In the node section, boiling is less strong and the vorticity structures are pulled down. In the centre section, the vorticity is also pulled towards the bed, but behind the recirculation zone vorticity sheds and goes toward the water surface, again. This trend is observed in all instantaneous vorticity profiles of the current run.

Figure (5.22) shows the time-averaged turbulent kinetic energy (TKE) in the centre and node sections. Downstream of the crest point, a larger region of high turbulence kinetic energy is found, because of the larger recirculation zone. As

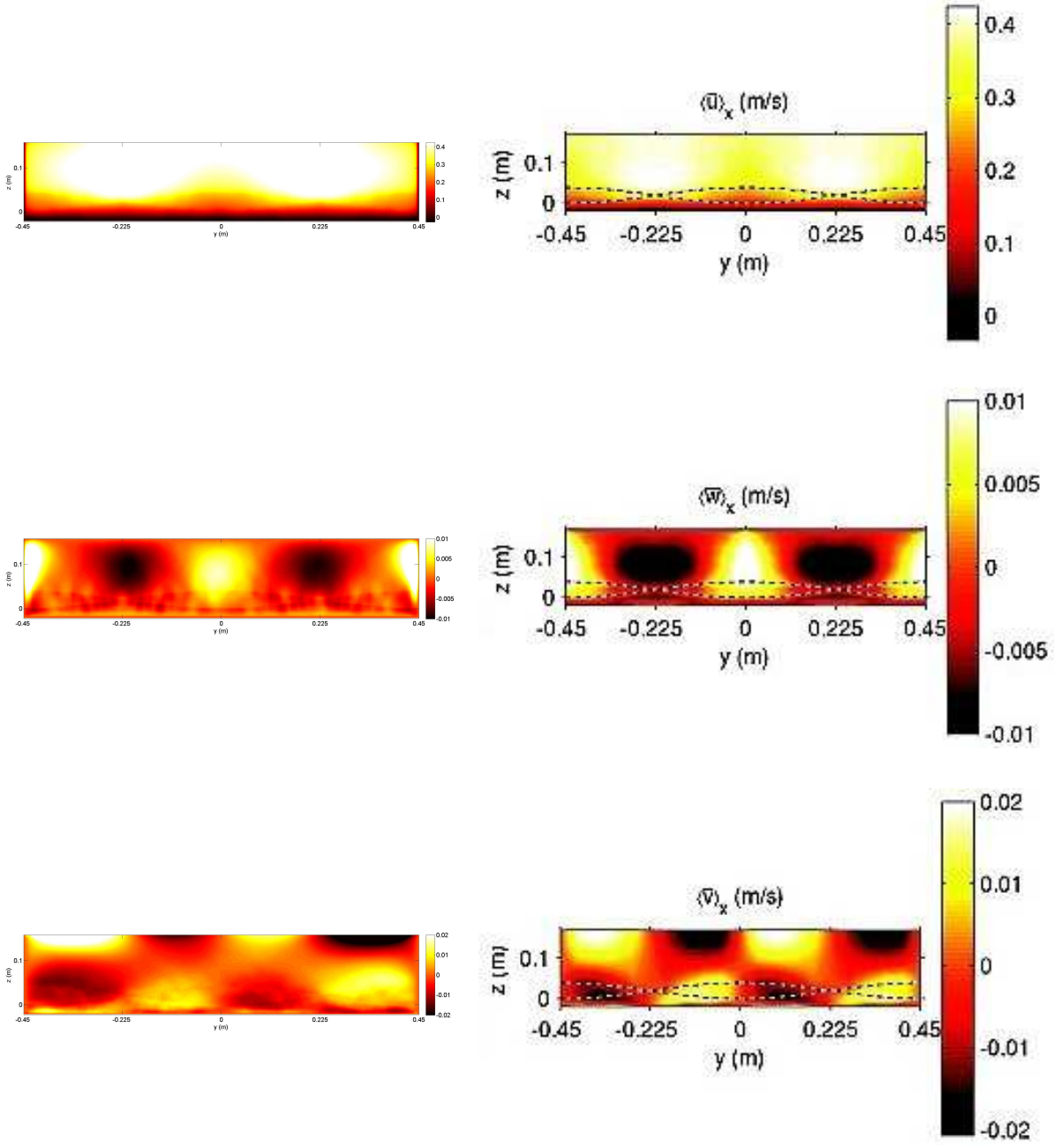

Figure 5.16: Computed streamwise-averaged patterns of the streamwise (top left), normal (middle left) and spanwise velocities (bottom left) for run R2, compared with the measured patterns from Maddux's experiment T2 (right).

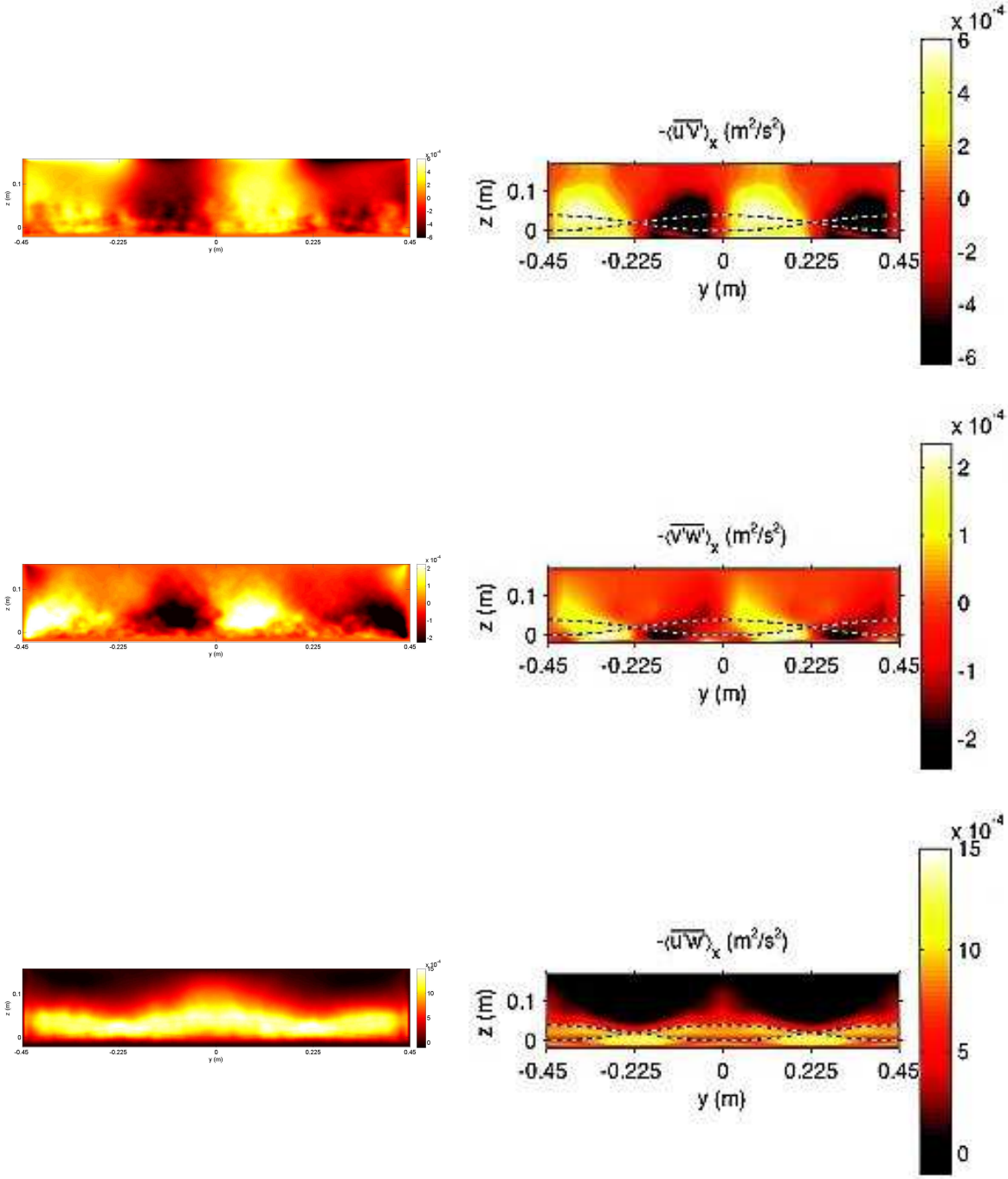

Figure 5.17: Computed streamwise-averaged Reynolds shear stress patterns $-\overline{u'v'}$ (top left), $-\overline{v'w'}$ (middle left) and $-\overline{u'w'}$ (bottom left) for run R2, compared with the measured patterns from Maddux's experiment T2 (right).

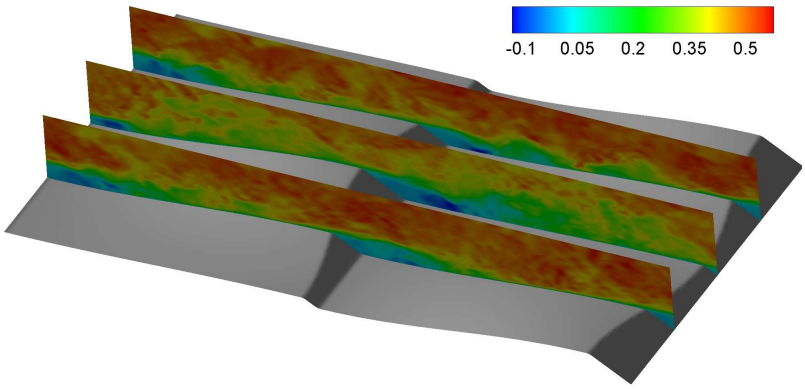

Figure 5.18: Instantaneous streamwise velocity at the centre-section and node-sections of the three-dimensional dune.

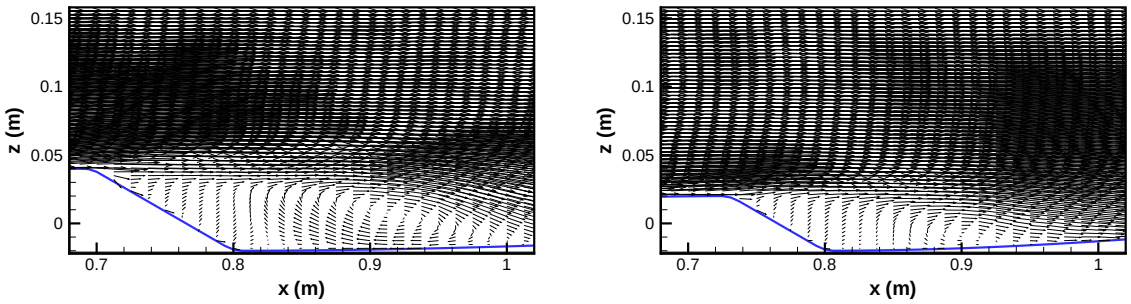

Figure 5.19: Time-averaged velocity vectors in the streamwise central section (left) and streamwise node section (right).

the recirculation zone gets smaller towards the node, the turbulent kinetic energy gets concentrated in a smaller region, although the turbulence intensity of these two regions are comparable.

5.4 Parameter study

In order to check the validity of the model against known parametric resistance models, and in order to derive parameterized relations for the bed resistance in case of irregular bedforms, the resistance in case of two- and three-dimensional dunes is calculated. Bed resistance is the total drag force exerted by the bed on the flow (Vanoni and Hwang, 1967). This resistance is important from a flood protection point of view, since an increased resistance leads to a reduced flood conveyance capacity of the river. The total bed resistance arises from skin friction on the sediment particles and form drag exerted by bed forms, via pressure gradients and energy losses in the flow separation zones (Einstein and Barbarossa,

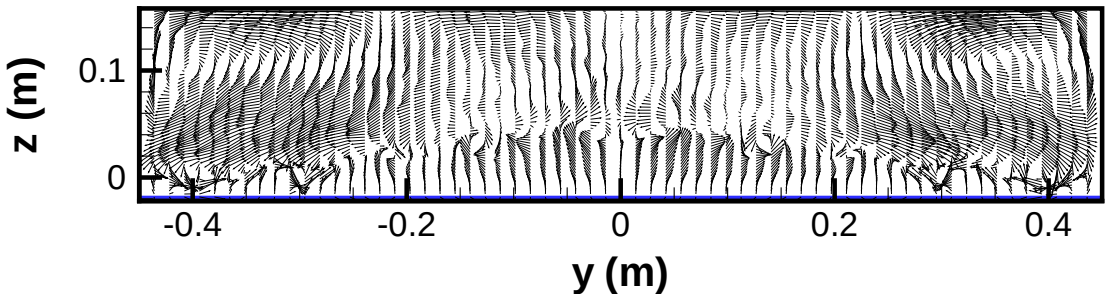

Figure 5.20: Time-averaged velocity vectors in the trough of the dune at $x = 0.8$ m. Four loops can be observed, rotating opposite to their neighbours.

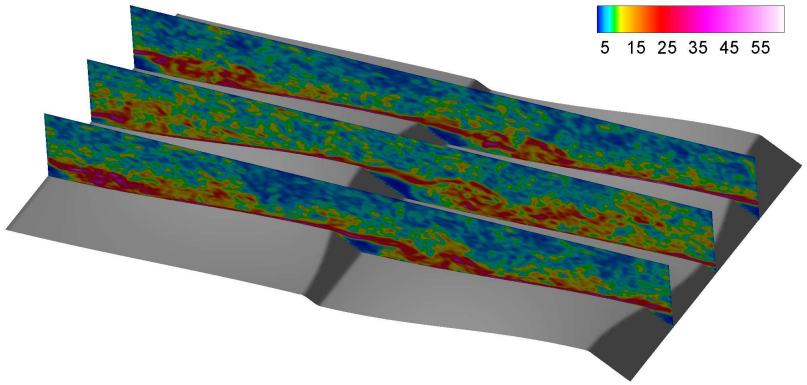

Figure 5.21: Instantaneous vorticity at the centre section and node sections of the three-dimensional dune.

1952). In the case of a flat bed, the effective shear stress is equivalent to the skin friction, but the contribution of form drag becomes significant in the presence of bed forms.

The boundary shear stress $\tau_b = \rho u_*^2$ indicates the skin friction (grain drag), where u^* is the averaged shear velocity in space (and also in time for steady flow) and can be obtained from the log-law wall function. The grain drag coefficient is defined as

$$c'_f = \frac{u_*^2}{U^2} \tag{5.2}$$

where U is the average velocity. The form drag can be determined in two different ways. In the most simple approach, the pressure gradient adjusted during the simulation to satisfy the required discharge can be used to determine the drag force. In a statistically steady state, the body force corresponding with this pressure gradient must balance the total drag force. For homogenous steady state turbulence and assuming the grain drag to be negligible compared to the form

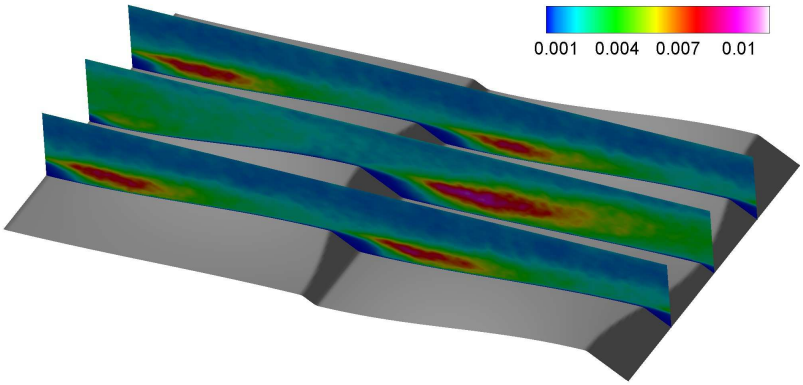

Figure 5.22: Time-averaged turbulent kinetic energy (TKE) at the centre section and node sections of the three-dimensional dune.

drag, the total drag coefficient c_f can be found as follows,

$$c_f = \frac{f_x R_h}{U^2} \tag{5.3}$$

where R_h is the hydraulic radius and f_x is the body force. Equation (5.3) is valid for steady state flows. More advanced methods have to be applied if the flow is unsteady. The pressure forces on the bed can be a suitable estimation for the form drag, as the form drag is the resulting force of the pressure acting on the bed. The pressure forces normal to the bed can be integrated over the bed, to yield

$$F = \int_S p.\vec{n}\, \mathrm{d}S \tag{5.4}$$

where p is the dynamic pressure and $\vec{n}$ is the normal unit vector on the bed surface. The dynamic pressure is calculated by subtracting the hydrostatic pressure from the total pressure. For the form drag, only the x-component of the force is important, and Equation (5.4) can be rewritten in the following form.

$$F = \int_S p\, n_x\, \mathrm{d}S \tag{5.5}$$

where n_x is the x-component of the normal unit vector. The drag form coefficient can be found as

$$c''_f = \frac{F}{\rho S u_b^2} \tag{5.6}$$

Where S is the area on which the force F is acting, and u_b is the bulk velocity.

Different analytical form drag models have been proposed based on physics-based approaches. An example of an analytical model is the form drag model developed by Yalin (1964) and Engelund (1966) (both authors independently developed the same model). They assume the effect of a bedform on the flow to be similar to that of a sudden expansion in pipe flow. The energy loss due to a sudden pipe flow expansion is determined from the cross-sectionally integrated momentum and energy balances over the expansion region. They also assume the bed shear stress, τ_b, the bed shear stress due to grain friction, τ', and the bed shear stress due to form drag, τ'', to be related to the same mean flow velocity, and the bed resistance coefficient, c_f, to be the sum of the resistance coefficients due to grain friction form drag,

$$c_f = c'_f + c''_f \tag{5.7}$$

in which c'_f and c''_f denote the grain friction coefficient and the form drag coefficient, respectively. For a reference situation with a standard bed form configuration, the form drag model developed by Yalin (1964) and Engelund (1966) yields

$$c''_f = \frac{\delta^2}{2\lambda h} \tag{5.8}$$

where δ is the dune height, λ is the dune length and h is the water depth. As such, the pressure is assumed to be constant over a cross section rather than hydrostatically distributed.

In the semi-analytical form drag model of Karim (1999), which is an extension of the Yalin (1964) and Engelund (1966) model, the effect of a bedform on the flow is assumed to be represented by a sudden expansion of a free surface flow rather than pipe flow. Although it seems to be more realistic, Karim's results deviate significantly from field measurements (Van der Mark, 2009).

Van der Mark (2009) has developed a semi-analytical form drag model for uniform bedforms. This model is similar to the model proposed by Yalin (1964) and Engelund (1966), but accounts for the effect of deviations from the reference situation by a correction factor γ_T:

$$c''_f = \gamma_T c''_{f,ref} \tag{5.9}$$

Van der Mark (2009) decomposed the correction factor γ_T into four different factors as

$$\gamma_T = \gamma_s \gamma_i \gamma_f \gamma_v \tag{5.10}$$

where γ_s, γ_i, γ_f, and γ_v denote the correction factors for four respective effects:

(a) the flow expansion is gradual rather than abrupt; (b) the flow pattern over a bedform is affected by upstream and downstream bedforms; (c) the height of the flow separation zone may deviate from the bedform height; and (d) the bedform geometry is irregular.

Engelund (1977) introduced another calibration coefficient to account for the free surface flow, the interactions between upstream and downstream bedforms, and the physical height of the separation zone

$$c''_f|_E = c_E \frac{\delta^2}{2\lambda h} \tag{5.11}$$

in which

$$c_E = 2.5exp\left(\frac{-2.5\delta}{h}\right) \tag{5.12}$$

Dune length, dune height, water depth and lee side slope may all affect the form drag. We have simulated flow over two-dimensional dunes, varying dune length, dune height, water depth and lee side slope. Starting point of our formulation is the analytical relation proposed by Yalin (1964) and Engelund (1966) with a correction factor. The correction factor is decomposed into two independent factors as follows

$$c''_f = \lambda_G \lambda_\theta \frac{\delta^2}{2\lambda h} \tag{5.13}$$

where λ_G and λ_θ represent the effects of dune dimensions (dune length, dune height, and water depth) and lee side slope, respectively.

Table (5.3) shows the settings for a series of simulations in which the dune height was changed. Figure (5.23) shows a comparison between the resulting form drag with the aforementioned analytical, parametrical and semi-analytical results. In Figure (5.23), the dune height is non-dimensionalized by the water depth. The computed form drag coefficient as a function of δ/h can be approximated by the second-order polynomial

$$c''_f = 0.25\,(\delta/h)^2 + 7.61 \times 10^{-3}\,(\delta/h) + 1.34 \times 10^{-4} \tag{5.14}$$

In Figure (5.24) the dune height is non-dimensionalized by the dune length. The computed form drag coefficient as a function of δ/λ can be approximated by

$$c''_f = 1.001\,(\delta/\lambda)^2 + 1.52 \times 10^{-3}\,(\delta/\lambda) + 1.34 \times 10^{-4} \tag{5.15}$$

In another series of simulations, the dune length was varied (see Table 5.4). Figure (5.25) shows the results compared with the aforementioned studies. The dune length is non-dimensionalized by the dune height. The resulting fit is again a second-order polynomial:

Table 5.3: Numerical simulations to determine the effect of dune height on form drag. The simulations are performed for $\lambda = 0.4$ m, $h = 0.2$ m, $\theta = 30^\circ$ and $u_b = 1$ m/s.

Run	δ (m)
RD01	0.000
RD02	0.005
RD03	0.010
RD04	0.015
RD05	0.020
RD06	0.025
RD07	0.030
RD08	0.035
RD09	0.040
RD10	0.045

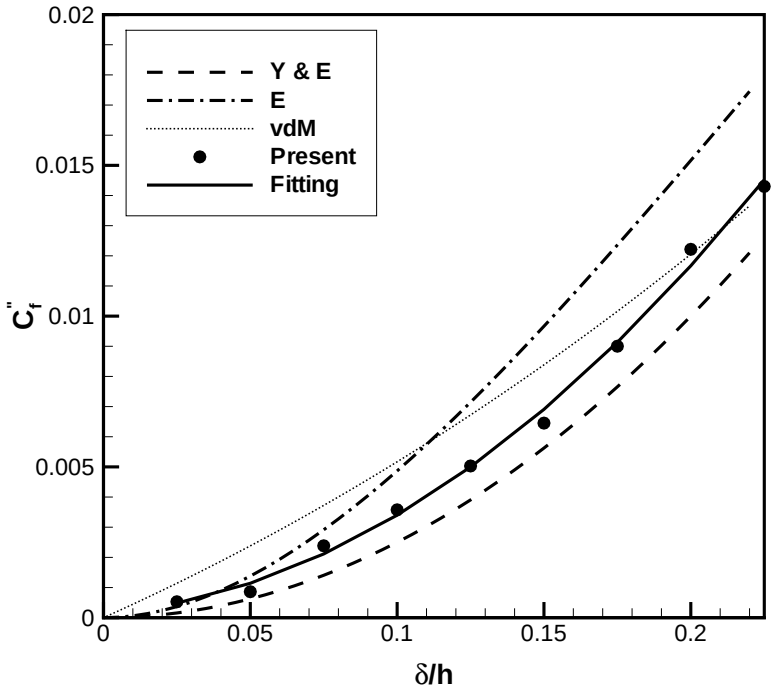

Figure 5.23: Variation of the form drag coefficient versus the ratio of dune height to water depth.

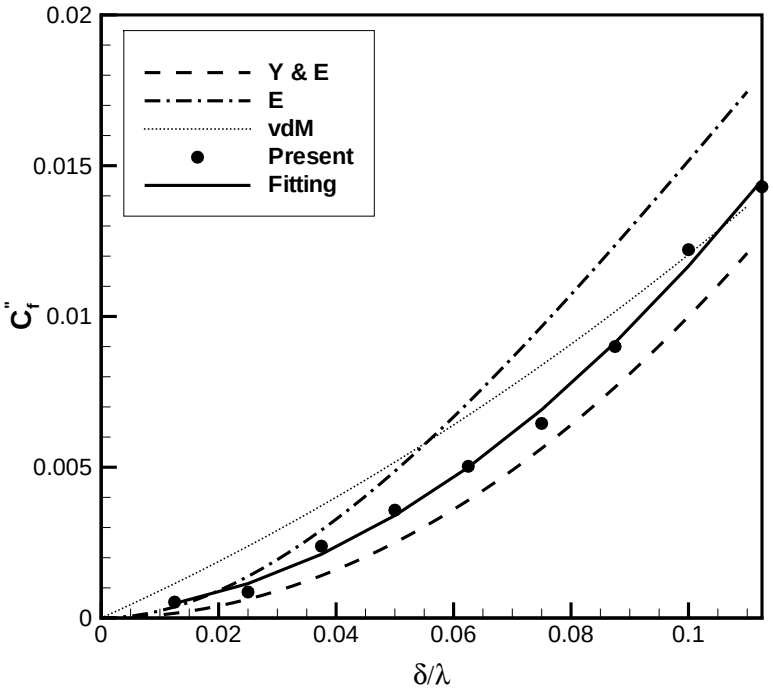

Figure 5.24: Variation of the form drag coefficient versus the ratio of dune height to dune length.

$$c''_f = 7.11 \times 10^{-5} (\lambda/\delta)^2 - 2.8 \times 10^{-3} (\lambda/\delta) + 3.45 \times 10^{-2} \tag{5.16}$$

Table (5.5) and Figure (5.26) show a series of computations in which the water depth was changed. The best fit for this curve is

$$c''_f = 2.137 \times 10^{-4} (h/\delta)^2 - 2.8 \times 10^{-3} (h/\delta) + 3.45 \times 10^{-2} \tag{5.17}$$

The relation between c''_f and each geometrical property should not be separated, as it is done in Equations (5.14) to (5.17). The form drag coefficient c''_f is affected by the combined effects of the dune height, dune length and the water depth as it is found in the form of Equation (5.8). In Figure (5.27) the numerical results for the form drag coefficient c''_f versus $\delta^2/(2\lambda h)$ have been plotted. A linear relation between c''_f and $\delta^2/(2\lambda h)$ is found, corresponding with a value of 1.293 for the geometrical correction factor λ_G.

As λ_G is constant, it can be concluded that the flow structure (eg. recirculation zone, interaction between upstream and downstream bedforms, etc.) acts linearly on the form drag coefficient and can be parameterized by a linear function. It has to be noted that the effects of flow expansion, consecutive dunes and size of the recirculation zone are implicitly included in the geometrical correction factor λ_G.

Table 5.4: Numerical simulations to determine the effect of dune length on form drag. The simulations are performed for $\delta = 0.04$ m, $h = 0.2$ m, $\theta = 30^\circ$ and $u_b = 1$ m/s.

Run	λ (m)
RL01	0.400
RL02	0.450
RL03	0.500
RL04	0.550
RL05	0.600
RL06	0.650
RL07	0.700
RL08	0.750
RL09	0.800

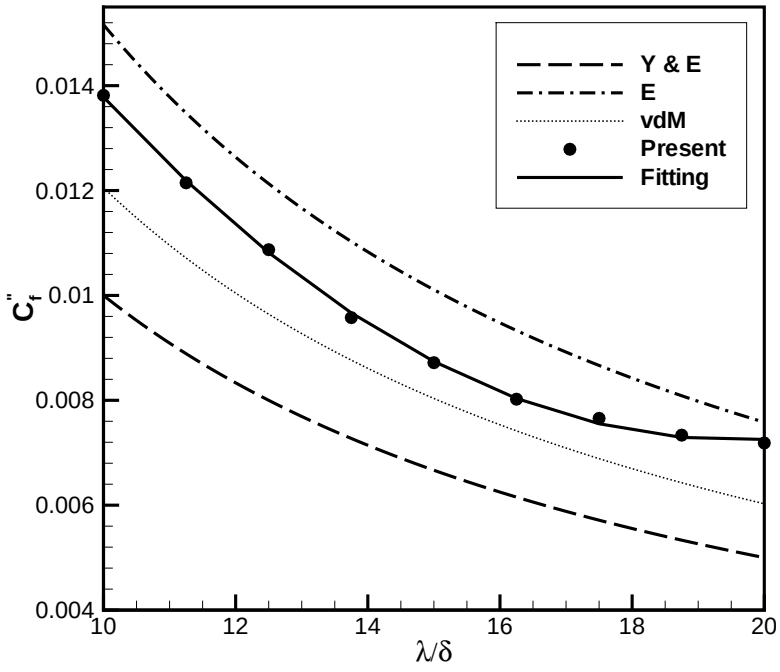

Figure 5.25: Variation of the form drag coefficient versus the ratio of dune length to dune height.

Table 5.5: Numerical simulations to determine the effect of water depth on form drag. The simulations are performed for $\delta = 0.04$ m, $\lambda = 0.4$ m, $\theta = 30^\circ$ and $u_b = 1$ m/s.

Run	h (m)
RH01	0.200
RH02	0.220
RH03	0.240
RH04	0.260
RH05	0.280
RH06	0.300
RH07	0.320
RH08	0.340
RH09	0.360

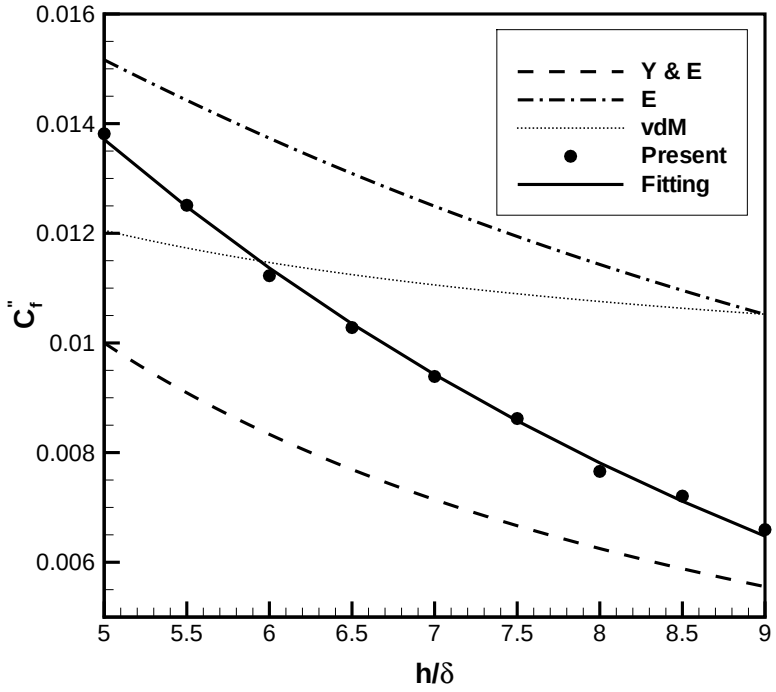

Figure 5.26: Variation of the form drag coefficient versus the ratio of water depth to dune height.

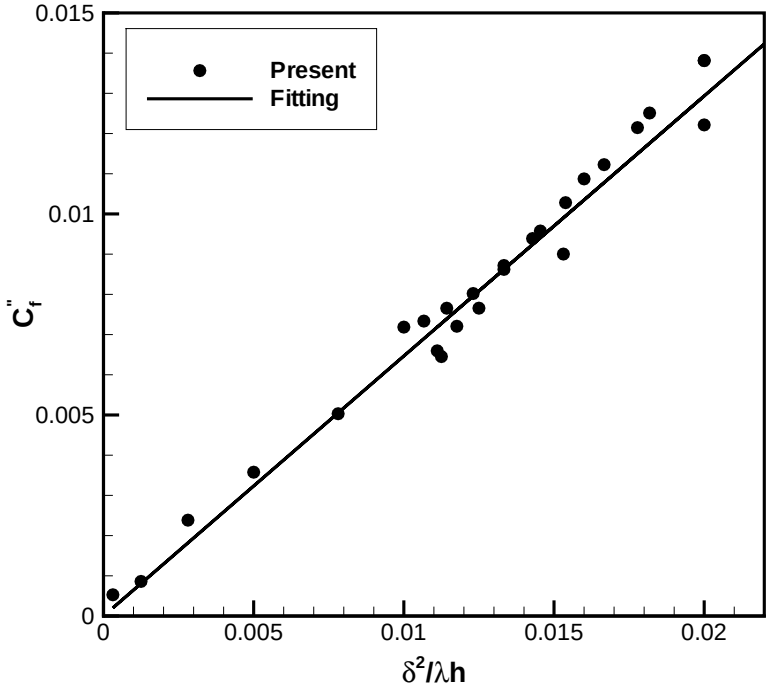

Figure 5.27: Variation of the form drag coefficient versus the ratio of $\delta^2/\lambda h$.

The correction factor for the lee side slope is found by a series of simulations as given in Table (5.6). The results have been plotted in Figure (5.27). The effect of variability of the slope is represented well by the following expression.

$$\lambda_\theta = \begin{cases} 1/\left[1 + 1.59 \times 10^7 \exp\left(-43.01 \frac{\theta\pi}{180^\circ}\right)\right] & \theta \leq 30^\circ \\ 1.125 - 0.165\left(\frac{\theta\pi}{180^\circ}\right) - 1.05 \times 10^{-2}\left(\frac{\theta\pi}{180^\circ}\right)^{-2} & \theta > 30^\circ \end{cases} \tag{5.18}$$

in which the lee side slop, θ, is expressed in degrees.

The correction factor for the angle of the lee side deviates significantly from the results provided by Van der Mark et al. (2008). According to the present results, the correction factor for the angle of lee side increases rapidly at small lee side angles. The maximum drag is associated with the lee side angle of 30 degrees. As this angle increases, the form drag decreases slowly in a form close to a linear function (although it has been fitted to a non-linear function). The experiments of Gibson (1910) support the results for our numerical simulations, as the behaviour of flow over dunes is similar to the flow expansion in a pipe flow.

The effect of grain size on the form drag has been neglected in these expressions, as we decomposed the form drag and the grain drag in Equation 5.7. Yet,

the grain size has a direct effect on the flow structure, and the flow structure in its turn has a direct effect on the form drag. To examine the validity of expression (5.7), a series of simulations was conducted with different grain sizes. The conditions of these simulation are given in Table (5.7). Figure (5.29) shows the form drag coefficient c''_f for different grain sizes. It is found that the effect of grain size on the form drag is negligible and Equation (5.7) can be applied safely.

Moreover, the effect of discharge (or bulk velocity) on the form drag coefficient c''_f has been examined, as shown in Table (5.8) and Figure (5.30). Apparently, the discharge has no effect on the form drag coefficient and c''_f stays constant for a range of discharges.

The above analyses and comparisons validate our form drag expression and shows that the current drag model agrees well with empirical and theoretical results from literature.

The above parametrization refers to two-dimensional dunes, but does not include the effect of three-dimensionality on the form drag. The form drag by three- dimensional dunes is expected to deviate significantly from that by two-dimensional ones. Although three-dimensionality of dune patterns may be very complex, with a wide range of possibilities, we consider only the cosine-shaped crest pattern discussed in section 5.3. This dune pattern is not all-encompassing, but realistic, as it has been found in the field (Gabel, 1993).

Two parameters define the cosine form of the crest: the wave length and the amplitude. The wave length of the present cosine-crest is equal to the channel width. The amplitude indicates the deviation of the dune crest geometry from its straight form in the two-dimensional case. At the same time, it determines the difference in the height between the highest and lowest points on the crest line (see Figure 5.14). We separate the effects of the wave length b and the amplitude β on the form drag coefficient, whence the drag coefficient relation can be improved for three-dimensionality of the bedform pattern by multiplication of these two effects with the relations found for two-dimensional drag.

$$c'''_f = \lambda_\beta \lambda_b c''_f = \lambda_\beta \lambda_b \lambda_G \lambda_\theta \frac{\delta^2}{2\lambda d} \tag{5.19}$$

where c'''_f is the form drag coefficient including three-dimensional features, and λ_β and λ_b represent the three-dimensionality of the bed.

Simulations with different crest wave lengths (different channel widths) and amplitudes were carried out. Table (5.9) shows the settings and Figure (5.31) the related diagram for the drag form coefficient. Based on the numerical simulations, we suggest the following expression for the correction factor for the crest wave length:

$$\lambda_b = 1.283 \sin\left[0.07463\left(\frac{b}{\delta}\right) + 0.1512\right] \tag{5.20}$$

Table 5.6: Numerical simulations to determine the effect of the lee side slope on the form drag. The simulations are performed for $\delta = 0.04$ m, $\lambda = 0.4$ m, $h = 0.2$ m, and $u_b = 1$ m/s.

Run	θ°
RT01	20.0
RT02	22.5
RT03	25.0
RT04	27.5
RT05	30.0
RT06	40.0
RT07	50.0
RT08	60.0
RT09	70.0

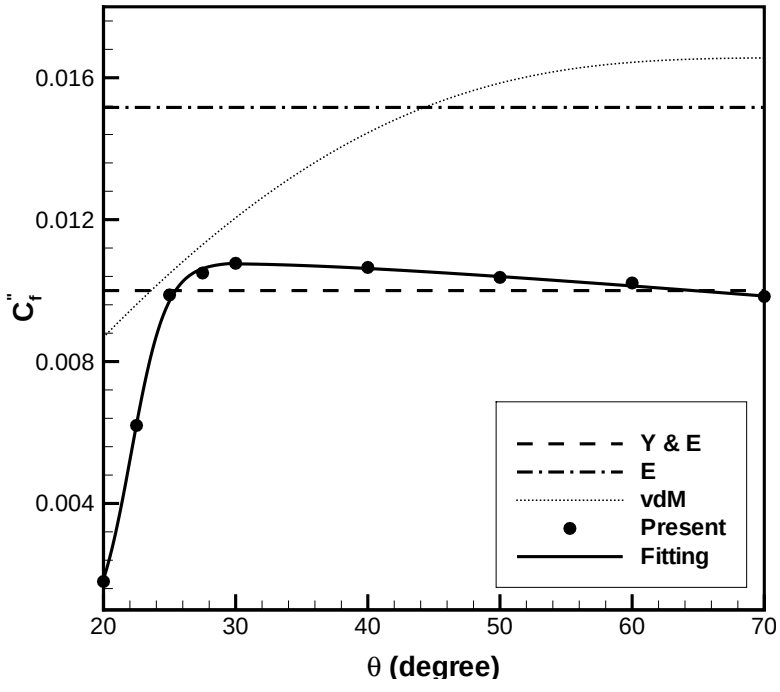

Figure 5.28: Variation of the form drag coefficient with the lee side slope.

Table 5.7: Numerical simulations to determine the effect of grain size on form drag. The simulations are performed for $\delta = 0.04$ m, $\lambda = 0.4$ m, $h = 0.2$ m, $\theta = 30^\circ$, and $u_b = 1$ m/s.

Run	d (μm)
RG01	100
RG02	150
RG03	200
RG04	250
RG05	300
RG06	350
RG07	400
RG08	450
RG09	500
RG10	550
RG11	600
RG12	650
RG13	700

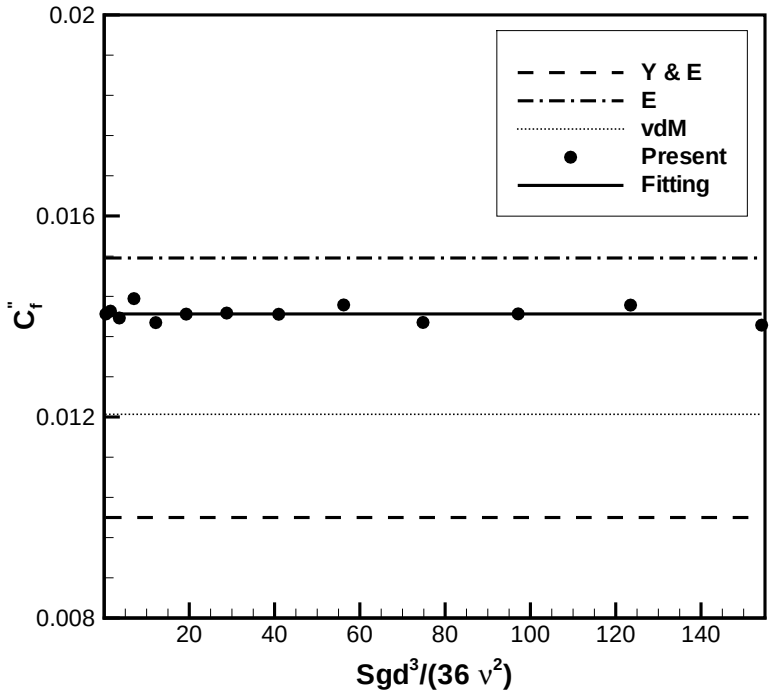

Figure 5.29: Variation of the form drag coefficient versus the non-dimensional sediment parameter.

For low values of b/δ, the form drag coefficient increases rapidly with b/δ. As the wave length increases, the effect of its variation decreases. Table (5.10) shows the settings for the cases with different amplitudes, and Figure (5.32) shows the form drag coefficient as a function of the crest amplitude coefficient. We suggest the following expression for the correction factor for the dune crest amplitude change:

$$\lambda_\beta = 0.8635\, e^{-0.61\beta} + 0.1167\, e^{1.878\beta} \tag{5.21}$$

This shows that three-dimensionality of the dunes does not always increase the form drag. For relatively low values of β, the form drag coefficient decreases with increasing crest amplitude. A minimum value of the drag coefficient is found near $\beta = 0.35$.

Finally, the parameterization above for the form drag can be summarized as below

$$c'''_f = \lambda_\beta \lambda_b c''_f = \lambda_\beta \lambda_b \lambda_G \lambda_\theta \frac{\delta^2}{2\lambda d}$$

$$\lambda_G = 1.239$$

$$\lambda_\theta = \begin{cases} 1/\left[1 + 1.59 \times 10^7 \exp\left(-43.01 \frac{\theta\pi}{180^\circ}\right)\right] & \theta \leq 30^\circ \\ 1.125 - 0.165\left(\frac{\theta\pi}{180^\circ}\right) - 1.05 \times 10^{-2}\left(\frac{\theta\pi}{180^\circ}\right)^{-2} & \theta > 30^\circ \end{cases}$$

$$\lambda_\beta = 0.8635\, e^{-0.61\beta} + 0.1167\, e^{1.878\beta}$$

$$\lambda_b = 1.283 \sin\left[0.07463\left(\frac{b}{\delta}\right) + 0.1512\right]$$

5.5 Concluding remarks

The flow over fixed two-dimensional dunes has been simulated and the results have been compared with the experimental measurements from previous studies. A good agreement has been obtained. The model shows sufficient capability to calculate the physical phenomena such as turbulence coherent structures and boiling vortices. Moreover, the flow over three-dimensional dunes is solved and the contours for velocities and the Reynolds shear stresses are compared with the previous experimental studies from literature. The contours show qualitatively good agreement with the experimental measurements. Furthermore, the model captured the recirculation zones and the currents of turbulence in a physics-based way.

Table 5.8: Numerical simulations to determine the effect of discharge (or bulk velocity) on form drag. The simulations are performed for $\delta = 0.04$ m, $\lambda = 0.4$ m, $h = 0.2$ m, and $\theta = 30^{\circ}$.

Run	$\overline{u}$ (m/s)
RQ01	0.300
RQ02	0.400
RQ03	0.500
RQ04	0.600
RQ05	0.700
RQ06	0.800
RQ07	0.900
RQ08	1.000

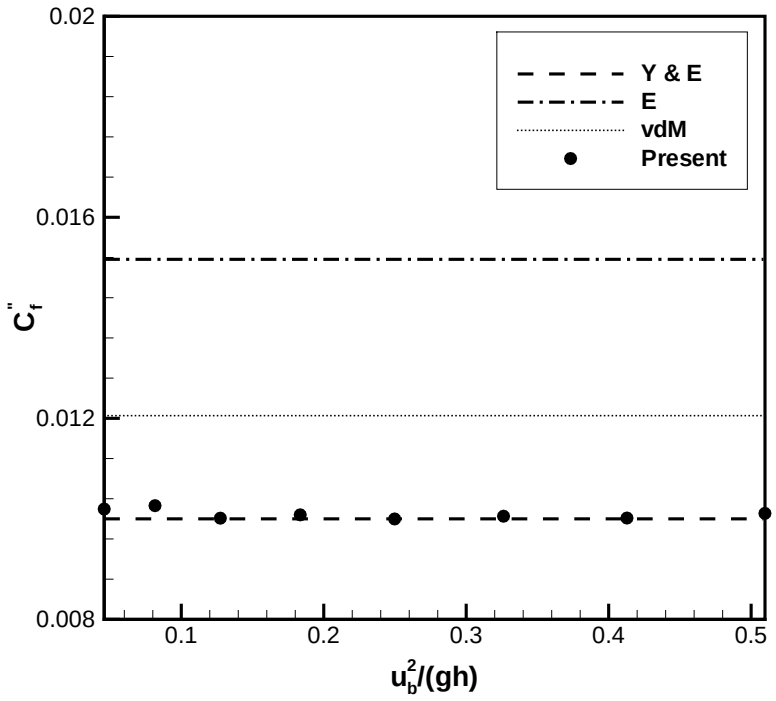

Figure 5.30: Variation of the form drag coefficient versus the change in the bulk velocity.

Table 5.9: Numerical simulations to determine the effect of crest wave length on form drag. The simulations are performed for $\delta = 0.04$ m, $\lambda = 0.4$ m, $h = 0.2$ m, $\theta = 30^\circ$, $u_b = 1$ m/s, and $\beta = 0$.

Run	b (m)
RB01	0.20
RB02	0.25
RB03	0.30
RB04	0.35
RB05	0.40
RB06	0.45
RB07	0.50
RB08	0.55
RB09	0.60
RB10	0.65
RB11	0.70
RB12	0.75
RB13	0.80

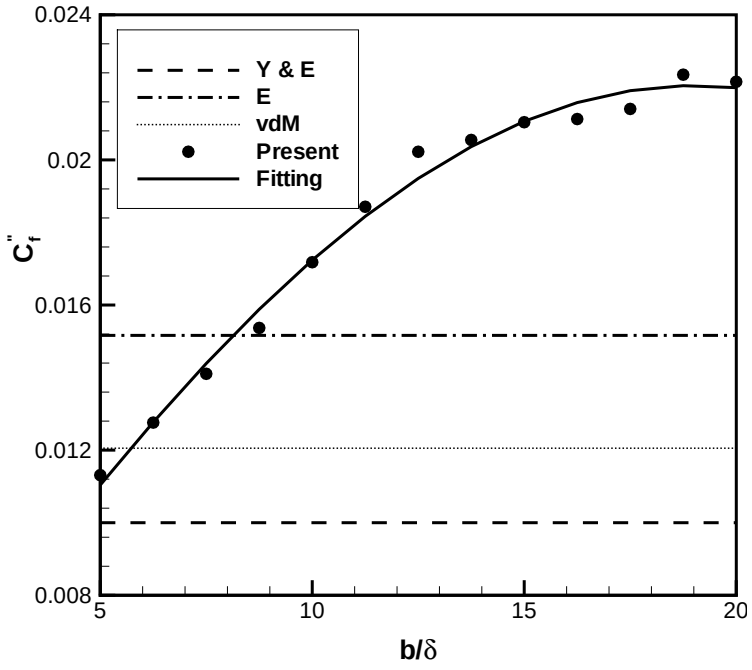

Figure 5.31: Variation of the form drag coefficient with the ratio of crest wave length to mean dune height.

Table 5.10: Numerical simulations to determine the effect of the crest amplitude on the form drag. The simulations are performed for $\delta = 0.04$ m, $\lambda = 0.4$ m, $h = 0.2$ m, $\theta = 30^\circ$, $u_b = 1$ m/s, and $b = 0.4$ m.

Run	β
RBT01	0.1
RBT02	0.2
RBT03	0.3
RBT04	0.4
RBT05	0.5
RBT06	0.6
RBT07	0.7
RBT08	0.8
RBT09	0.9
RBT10	1.0

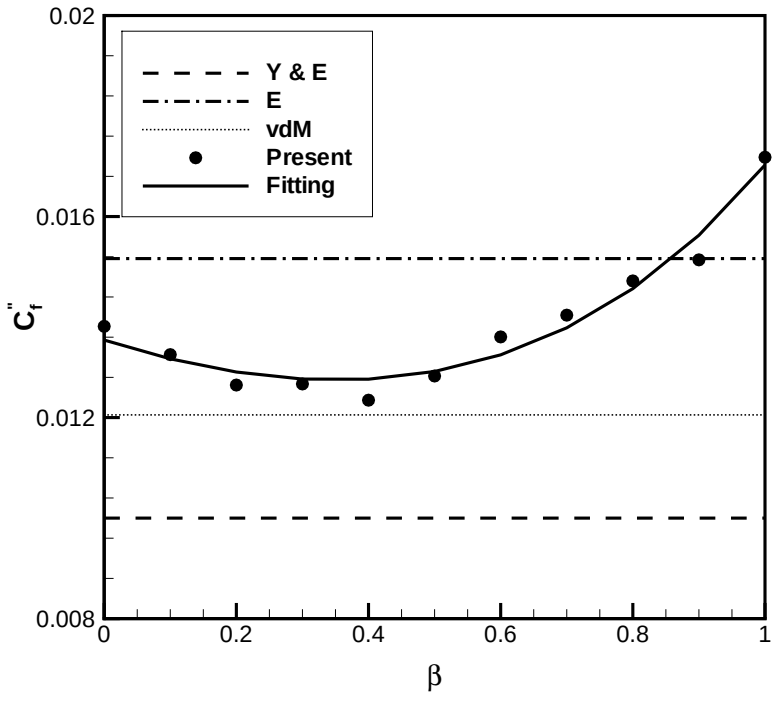

Figure 5.32: Variation of the form drag coefficient with the crest amplitude coefficient.

The simulations have been further extended to solve the flow over two- and three-dimensional dunes and parametric relations for the form drag have been derived. The analytical formula proposed by Yalin (1964) and Engelund (1966) was considered as the starting point for our parameterization study. The effects of dune dimensions and lee side angle were considered as correction factors in our study for the two-dimensional dunes. It is found that the flow structure (eg. recirculation zone, interaction between upstream and downstream bedforms, etc.) acts linearly on the form drag coefficient and the correction factor can be determined by a constant. The derived parametric relation for the effect of lee side angle has a good agreement with the experiments conducted by Gibson (1910) for a sudden expansion of flow in a pipe, and it deviates significantly from the results proposed by Van der Mark et al. (2008). The maximum form drag is found to be associated with a lee side angle of 30°. As the lee side angle increases, the form drag decreases slowly.

The effect of three-dimensionality has been decomposed into two factors, namely dune wave length and amplitude. It is found that the three-dimensionality of the dunes does not always increase the form drag. For relatively low crest amplitudes, the form drag coefficient decreases, increasing only later when further increasing the crest amplitude.

Chapter 6

Validation of morphodynamics at constant discharge

6.1 Introduction

Ripples and dunes are alluvial river bedforms at the smallest scales of fluvial morphodynamics. For flows of increasing strength, a typical sequence of bedforms occurs: lower flat bed $\rightarrow$ ripples $\rightarrow$ dunes $\rightarrow$ upper flat bed $\rightarrow$ antidunes (Simons et al., 1961; Guy et al., 1966; Simons and Richardson, 1966). Features up to and including dunes are generally termed lower-flow-regime bedforms, characterized by a low bed-material transport rate and a relatively high flow resistance. In the upper flow regime, first a plane bed is re-established, characterized by a high bed-material transport rate and a relatively low flow resistance. As the flow gets stronger, antidunes begin to form with upstream breaking waves over the dune crest. This type of bed is typically followed by the formation of a pool and chute morphology as described in Simons and Richardson (1966).

Early studies of river bedforms were based on results from flume experiments. They attempted to use mean flow and sediment properties to indicate what bedforms are to be expected under which conditions, and to derive parametric prediction formulae, called roughness predictors. Kennedy (1963) is considered to be the first to analyse the formation and the geometry of wave-like phenomena on mobile sand beds. He assumed two-dimensional potential flow over an erodible bed. To produce an unstable wave, he related the local sediment transport rate to the local fluid velocity, with a lag distance between sediment transport and flow velocity. Engelund (1970) investigated the stability of a sand bed by a two-dimensional mathematical model based on the vorticity transport equation. The model takes the internal friction into account and describes non-uniform suspended sediment concentration profiles. The inclusion of friction and a model for the sediment transport mechanism leads to results that differ substantially from those obtained previously by potential flow analysis. Richards (1980) added viscous effects to the flow model, including a one-

dimensional turbulence model for flow over a hydrodynamically rough bed, to study the formation of ripples and dunes. His results showed that ripple formation is independent of the flow depth. Sumer and Bakioglu (1984) extended this work to hydrodynamically smooth flows to analyze ripple formation.

Both two-dimensional and three-dimensional bedform patterns are observed in nature and laboratory experiments. Two-dimensional ripples and dunes are fairly regular in their spacing, height and length. Their crest lines are straight or weakly sinuous and are oriented perpendicular to the flow. Contrastingly, 3D features are more irregular in spacing, height and length, with highly sinuous or discontinuous crest lines (Ashley, 1990). Southard and Boguchwal (1990) provide a plotting methodology and extensive bedform phase diagrams, showing the occurrence of ripples, dunes, antidunes or plane bed for different sediment and flow properties. The formation and development of these bedforms are associated with local hydrodynamic and sediment transport characteristics, as well as with the flow-induced forces on the bed, which in their turn are influenced by the bedforms. Few attempts have been made so far to study the generation, migration, splitting, merging and superposition of dunes under constant or variable discharges. These phenomena are still not fully understood and difficult to study in the real world or even in the laboratory.

Recently, significant progress has been made in understanding bedform dynamics, thanks to significant advances in the ability to monitor flow and bedform morphology in the laboratory and the field, as well as in their numerical modelling. Nowadays, numerical modelling captures not only the characteristics of the mean flow field, but also those of turbulence, including coherent flow structures above non-flat beds. These advances of numerical modelling bring us into a position to make radical progress in quantifying, modelling and understanding the dynamics and kinematics of alluvial bedforms (Best, 2005). Thanks to the increased computer power and novel numerical techniques, detailed descriptions of turbulent flow and sediment motion can be used for process-based simulation of ripples and dunes. The local flow field is determined from well-established high-resolution hydrodynamic modelling concepts like DNS, LES or URANS. The description of the local and instantaneous sediment motion incorporated in these models is equally important, but much less well-established (see Chapter 3).

Several researchers have applied numerical methods to simulate the flow over fixed ripples, in order to understand the effects of bedforms on the flow field and the implications for the sediment transport. Zedler and Street (2001), for instance, focused on the initial entrainment and transport of suspended sediment in flows over fixed ripples. A well-resolved large-eddy simulation (LES) was employed to examine in detail the role and effect of coherent structures that occur near the bed.

None of the existing numerical models is capable of simulating the generation and migration of dunes in an entirely physics-based way. Yet, numerical models

were used to address these issues. Fredsøe (1982) proposed a model in which the dune height was determined by assuming the dune to move as a migrating front. The length of the dune was determined using a semi-empirical flow description. Tjerry and Fredsøe (2005) refined Fredse's model by describing the flow with a numerical flow model based on a two-equation turbulence closure. They were able to explain how the streamline curvature above the mildly sloping upstream part of the dune influences the dune length. The dune height, however, was not explained by this model; hence the earlier results from Fredsøe (1982) were employed.

Giri and Shimizu (2006) proposed a (vertically) two-dimensional morphodynamic model that successfully reproduces fluid and bedform dynamics in a coupled manner under steady flows. They described turbulence with a non-linear k-ϵ model. A non-equilibrium sediment transport approach, treating pick-up and deposition of sediment empirically, was used along with an assumed mean sediment particle step length. Despite its attractive features, it is difficult to get a realistic solution. The shape of the dune is strongly dependent on the definition of the particle step length. As the particle step length is unknown, this model cannot always predict the shape of the dunes correctly. Furthermore, this model uses a Reynolds Averaged Navier Stokes (RANS) turbulence closure, which removes the turbulent fluctuations. Hence, it removes the shear stress fluctuations and their effects on the sediment pick-up. The stress fluctuations are an important element in the formation of ripples on the stoss sides of the dunes, which cannot be simulated by RANS approaches (resulting in smooth dunes).

An interesting study on numerical modelling of dune dynamics was recently presented by Niemann et al. (2011). Their hydrodynamic model is based on a k-ω turbulence closure and the transport model is based on a conventional bed-load transport formula (Meyer-Peter and Müller), but including a slope effect and an avalanche model to stabilize the slope of the lee face. The model is found to be capable of predicting the dune evolution from an initial perturbation. The model uses a filter to smoothen the bedform. Niemann et al. (2011) argue that the filter locally "re-arranges" the sediment on the bed to some extent and that its effect can thus be interpreted as "artificial" erosion or deposition.

These detailed modelling approaches are all two-dimensional, but the nature of flow over three-dimensional dunes is very different from that in two dimensions, to the extent that the application of 2D models to field situations requires careful attention (Best, 2005). Field observations suggest that 3D models are necessary to describe natural bedforms.

It is against this background that we developed a high-resolution 3D numerical model for morphodynamic processes at small temporal and spatial scales, based on large eddy simulation, particles based transport of sediment, adaptive grid refinement and immersed-boundary techniques for mobile sediment beds. The flow and sediment transport submodels have been presented in chapters 2 and 3. In the present chapter we focus on the formation and development of

Table 6.1: Configurations of measurements for four experiments at Delft Hydraulics Laboratory.

Experiment	Discharge (m^3/s)	Water depth (m)	Flume width (m)	Flow velocity (m/s)
T01	0.151	0.197	1.500	0.511
T11	0.269	0.302	1.500	0.596
T31	0.116	0.208	1.125	0.495
T39	0.133	0.436	0.500	0.611

Table 6.2: Conditions for simulated cases.

Experiment	Related Exp.	Domain length (m)	$N_x \times N_y \times N_z$
R1	T01	5.10	$512 \times 64 \times 128$
R2	T11	6.00	$512 \times 64 \times 128$
R3	T31	4.75	$512 \times 64 \times 128$
R4	T39	4.00	$512 \times 128 \times 64$

ripples and dunes, presenting the first fully process-based 3D model for the simulation of bedform evolution and migration. We validate this model against four different laboratory flume experiments by Bakker et al. (1986).

6.2 Numerical experiments

A number of numerical tests were conducted to assess the capability of the proposed particle-based numerical model to simulate bedform evolution processes under steady discharges conditions. The results are compared with a series of experiments of Delft Hydraulics (Bakker et al., 1986).

Forty experiments were carried out in a straight flume with constant discharge in the period of 1974-1980 (Bakker et al., 1986). The length of the flume was 100 m with an adjustable width between 0.3 m and 1.5 m. The discharge was varied between the experiments. The material used in these experiments consisted of uniform sand with $d_{50} = 0.78\,\text{mm}$ and a density of $2660\,\text{kg/m}^3$. The sediment was supplied by means of a hydro-cyclone which discharges a predefined amount of sediment into the flume at regular intervals.

We have selected four experiments referenced by T01, T11, T31 and T39 in Bakker et al. (1986). Table 6.1 shows the experimental conditions for these cases. A part of the flume is simulated numerically by imposing periodic boundary conditions at the upstream and downstream ends of the model domain. This allows for using a relatively short domain length, so as to reduce the computational effort. A subset of the numerical runs was also performed by Shimizu et al. (2009), to check the effect of the domain length. Using domain lengths of 1.6 m, 4 m

Table 6.3: Observed and simulated average dune shape and percentage of error between numerical and experimental results.

		T01	T11	T 31	T39
Experiment	Av. dune height (m)	0.068	0.081	0.068	0.092
	Av. dune length (m)	1.270	1.194	1.183	1.284
		R1	R2	R3	R4
Simulation	Av. dune height (m)	0.071	0.077	0.070	0.081
	Av. dune length (m)	1.300	1.240	1.390	1.330
Error	Av. dune height (%)	−4.41	4.94	−2.94	11.96
	Av. dune length (%)	−2.36	−3.85	−17.50	−3.58

and 20 m, they showed the sensitivity of the model results to the domain length to be negligible. Yet, the domain length in our simulations covers several dune lengths, in order to minimize the effect of the periodic boundary conditions. The simulations indicated as R1, R2, R3 and R4 correspond to experiments T01, T11, T31 and T39, respectively. The domain length is chosen 5.1 m for R1, 6 m for R2, 4.75 m for R3, and 4 m for R4. Table (6.2) shows the conditions for the current simulations. Smooth solid boundary conditions in transverse direction are imposed, to account for the effect of the side walls in the experimental flume. In all simulations a rigid-lid boundary condition is imposed at the water surface. Niemann et al. (2011) showed that a rigid-lid water surface condition has only minor effects on the bed forms as long as the Froude number is relatively low. The flow is driven by a pressure gradient, chosen such that in each time step the discharge is kept constant. This means that the pressure gradient increases as the dunes grow and create more resistance. All simulations start from a flat bed without any initial perturbations.

In the first instance, the flow is simulated until it reaches a steady state. Subsequently, the sediment transport and morphology models are started. The steady state of the flow is determined by monitoring the residuals of velocity and pressure, until they reach statistically constant values. For all simulations a morphological factor of 20 is used, meaning that the time step in the morphological model equals 20 times the time step in the flow model .

Bedform dimensions are determined from the bed-level profile using a 'zero-crossing' method (Van der Mark et al., 2008). Length and height are defined by two successive intersections of the bed profile with the baseline. In 2D situations, dunes are determined by comparing the downstream bed profile with its least squares straight line. The height of an individual dune is defined as the difference between the highest and the lowest point between two successive zero crossings. The length of that dune is the distance between two successive zero crossings. The mean length and height of the dunes are found by averaging the length and height of all dunes present for several sections in streamwise direction. With this method, secondary bedforms (ripples migrating on the top of bedforms) can be

identified. In previous studies, such secondary bedforms were often removed, as one was only interested in the mean dune dimensions. The effect of not retaining secondary bedforms is that the reported dimensions will be somewhat smaller. The effect will be small, however, as the secondary bedforms will form on the crests of dunes, usually well above the mean bed level (Tuijnder et al., 2009).

Figure (6.1) shows the generation and migration of dunes for run R2. The bed evolves from flat to a stationary state, defined as a state in which the length and height of dunes remain statistically constant. The bed begins from a flat bed, later small deformations appear. These deformations grow in size and the dunes begin to be generated. In this simulation three-dimensionality ultimately dominates, although the initial dune pattern was closely two-dimensional. Figure (6.2) shows the generation and migration of dunes for case R4, in a narrow flume (0.5 m). In this case, the bedforms are much more two-dimensional. The bedforms begin as ripples evolving into dunes that are small in length and height. Later on, these dunes merge and form longer dunes. The height of these dunes grows until a stationary state is reached.

Figures (6.3) and (6.4) show the generation and migration of dunes for runs R1 and R3, respectively. Simulations R1 and R3 show clearly three-dimensional features of dunes. In all simulations, ripples are generated on the stoss side of the dunes, which leads to deformation of the dune profile. This phenomenon was already mentioned in Best (2005). Venditti and Michael (2005) define this structure as "sand sheets", without classifying these structures as ripples, dunes or bars. The sheets formed downstream of the reattachment point at a distance that was invariant to the dune size. Dunes and sand sheets represent distinct scales of sediment transport with different migration rates (Venditti and Michael, 2005).

Figure (6.5) shows the mean dune height evolution in time for all four simulations. The equilibrium dune height is found to be approximately 7.1 cm, 7.7 cm, 7 cm, and 8.1 cm for runs R1, R2, R3 and R4, respectively. This agrees fairly well the experimental results in Table (6.3). Figure (6.6) shows the evolution in time of the mean dune length. The equilibrium dune length is found to be approximately 1.3 m, 1.24 m, 1.39 m, and 1.33 m for runs R1, R2, R3 and R4, respectively. The experimental and numerical results for the average dune height and length in the equilibrium state are documented in Table (6.3). Moreover, the percentage of error between the experimental and the numerical results are given in this table. The simulated average dune height and length agree well with the experimental measurement. However, an over-prediction of 17.50% in the dune length for run R3, and an under-prediction of 11.96% in the dune height for run R4 can be observed.

The over-prediction in length for run R3 can be interpreted as the effect of three-dimensionality of dunes which cover the bed partially. Considering Figure (6.3) for run R3, four dunes can be observed, but the second dune from the upstream direction does not cover the width of the domain entirely. The parts of the

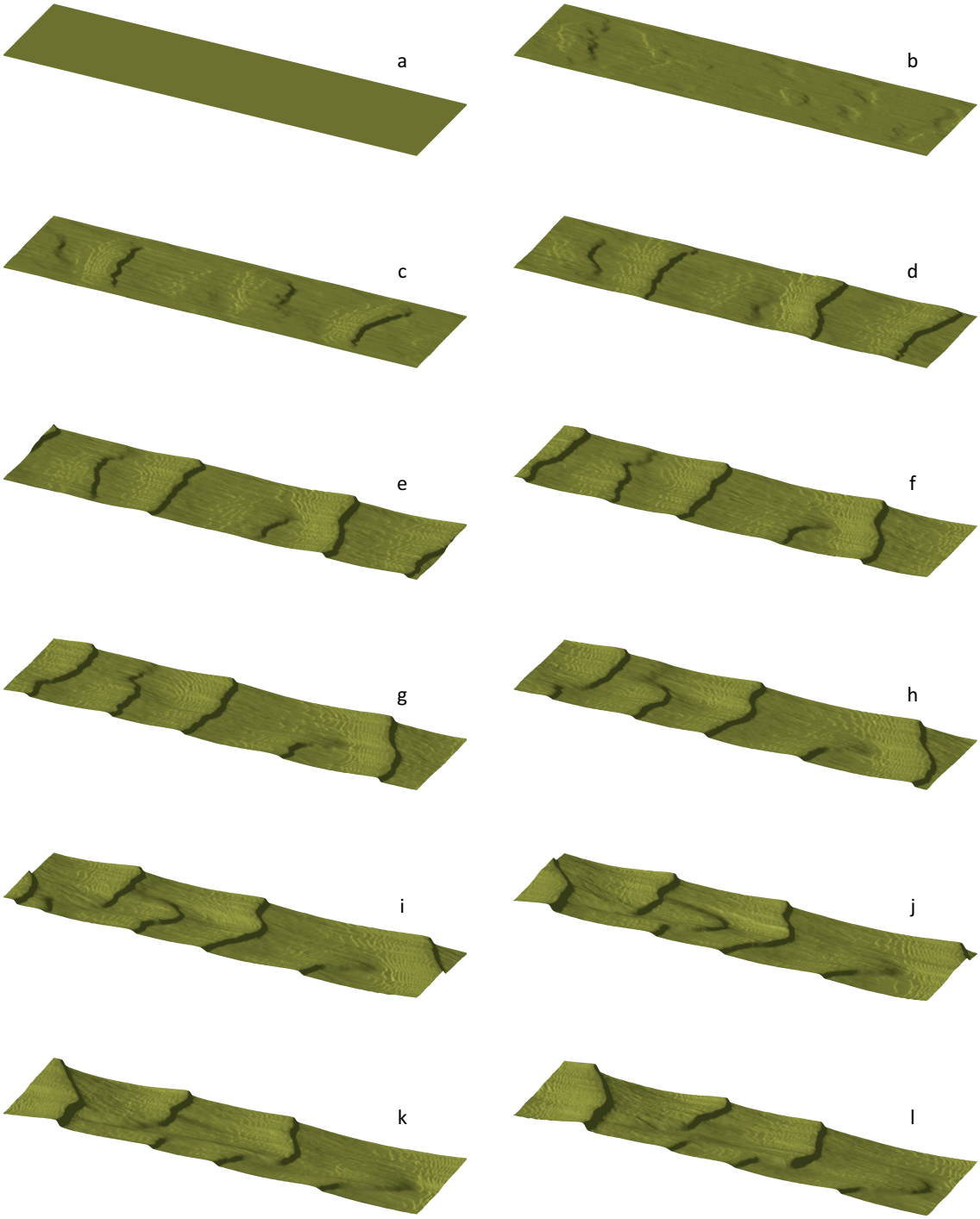

Figure 6.1: Bed form evolution simulated by numerical model for run R2. The bed begins from a flat bed (a), later small deformations appear (b). These deformations grow in size (c), and the dunes begin to be formed (d). Dunes are initially closely two-dimensional (e-g), but finally three-dimensionality dominates (h-l).

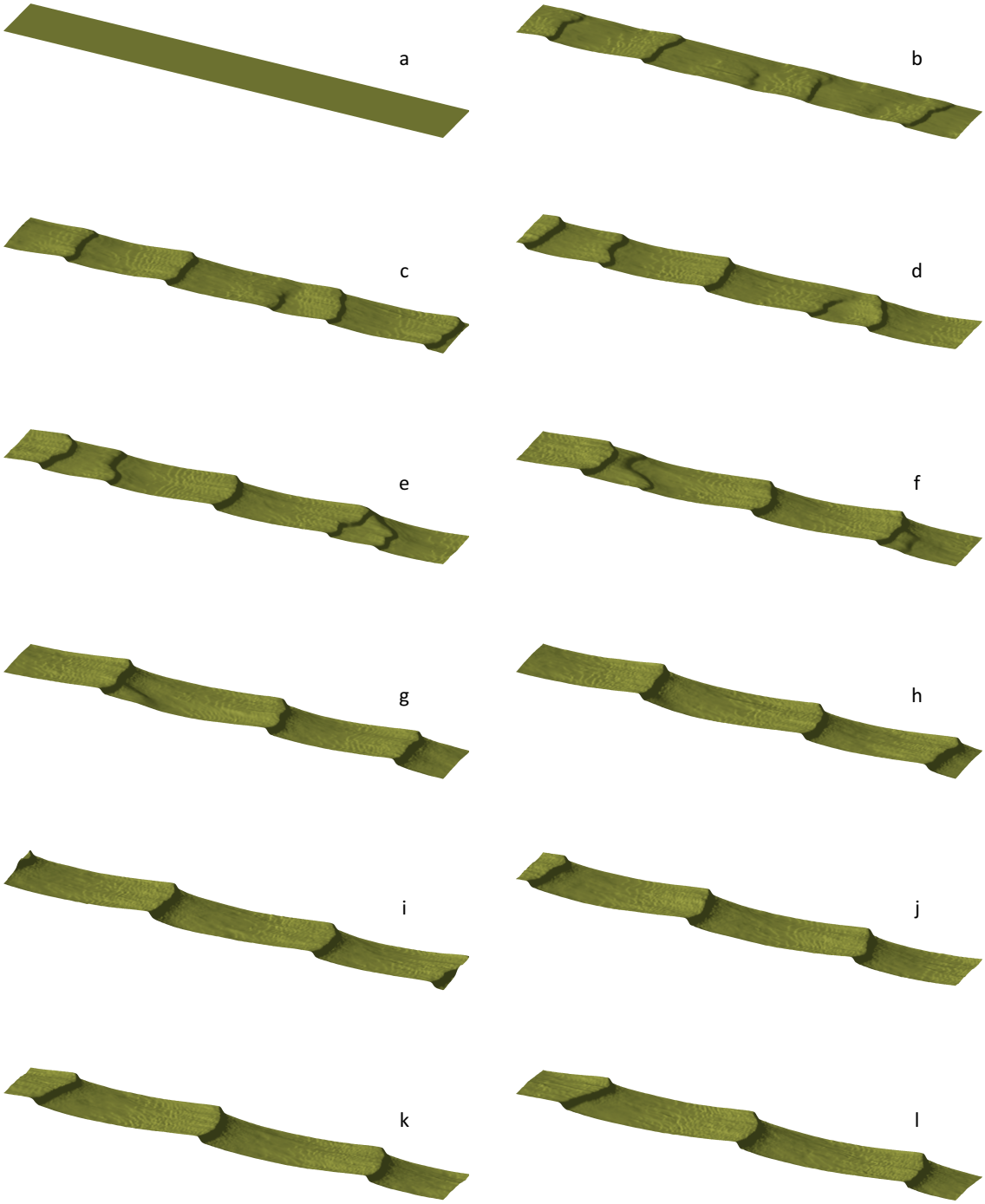

Figure 6.2: Bed form evolution simulated by numerical model for run R4. The bed begins from a flat bed (a), later ripples appear (b). These ripples grow in size and the dunes begin its formation (c). These dunes are merged (d-f) and dunes larger in length and height are formed (g). Finally, the bedform reaches its steady state and migrates in the form of two-dimensional dunes (h-l).

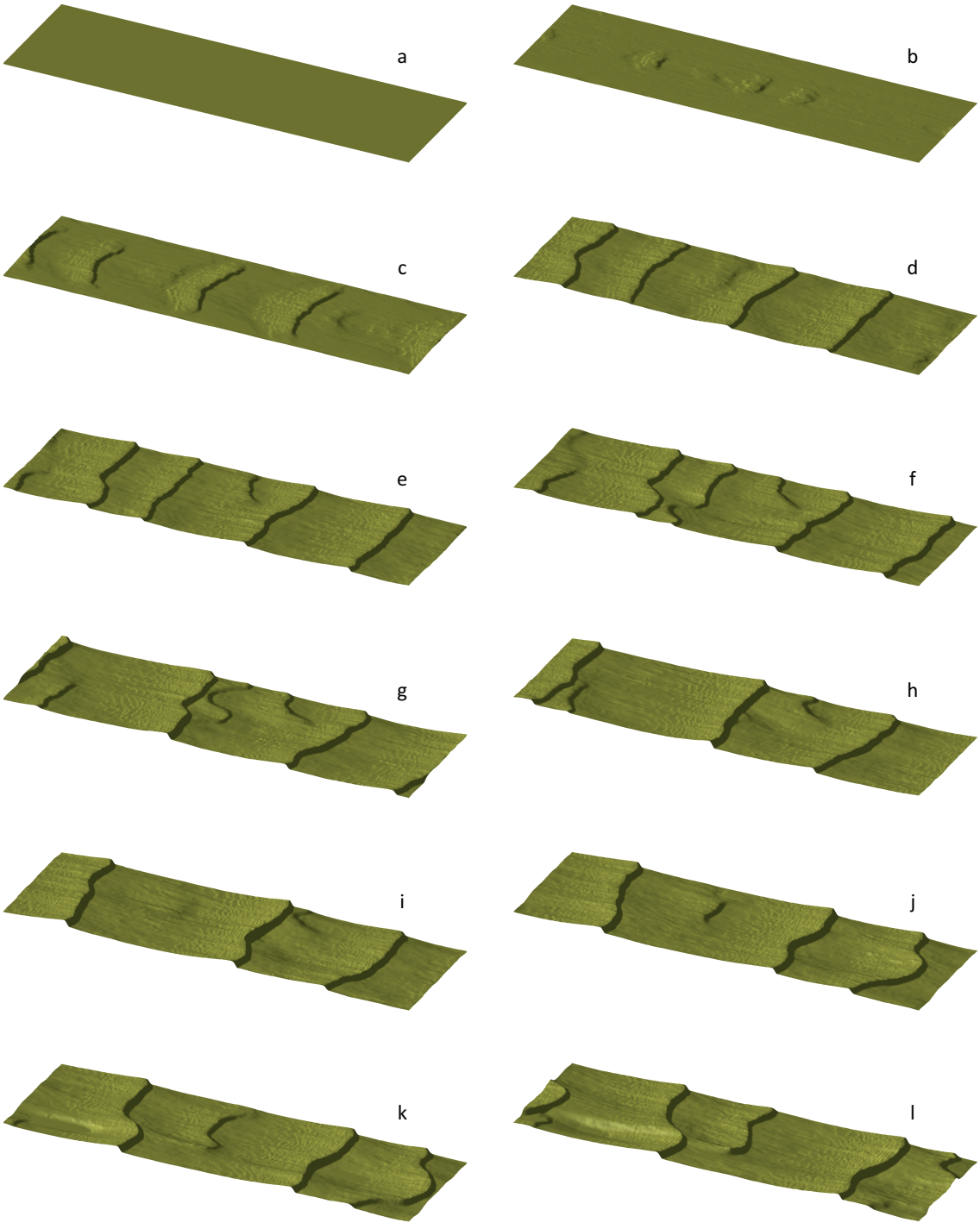

Figure 6.3: Bed form evolution simulated by numerical model for run R1.

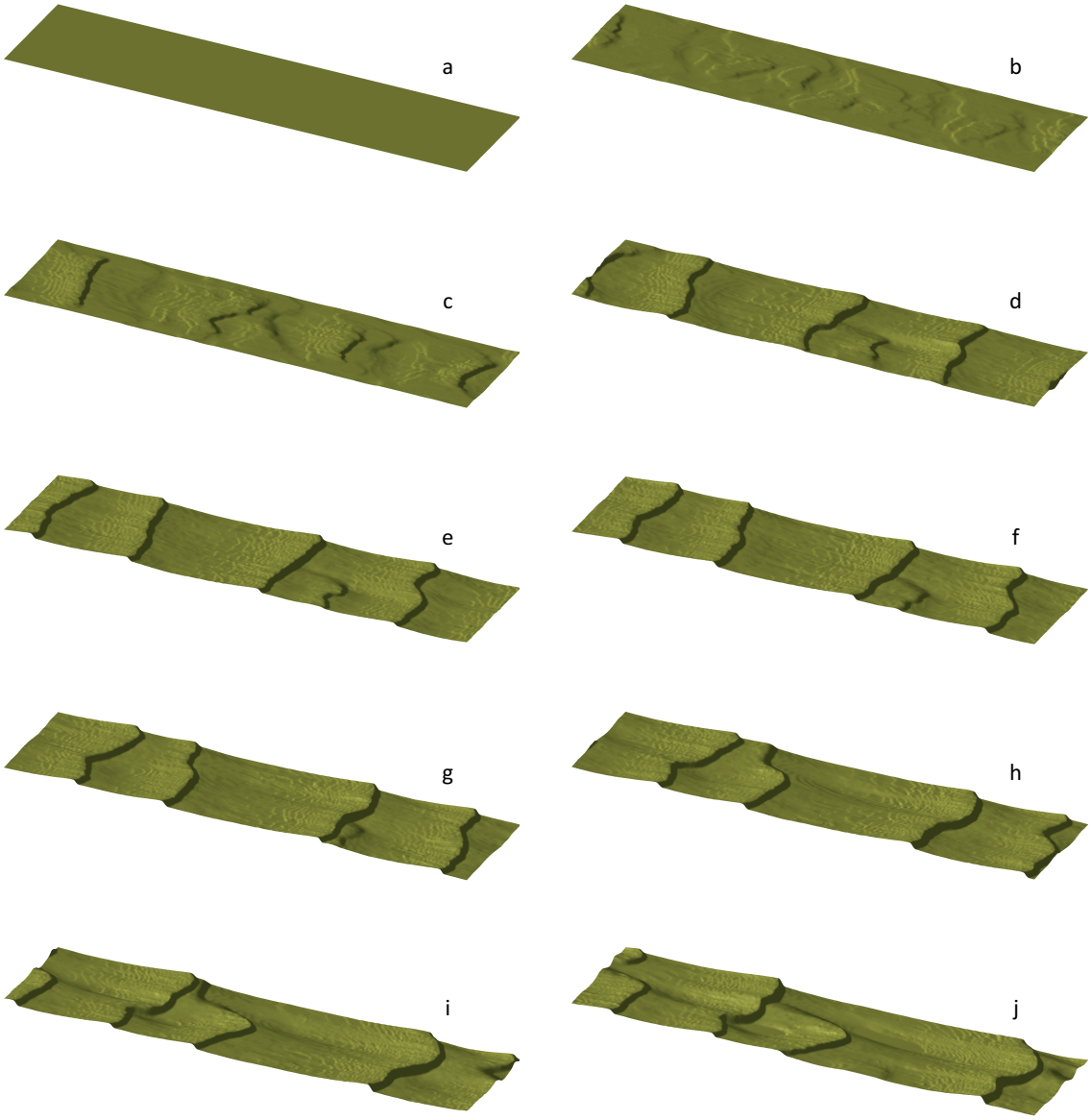

Figure 6.4: Bed form evolution simulated by numerical model for run R3.

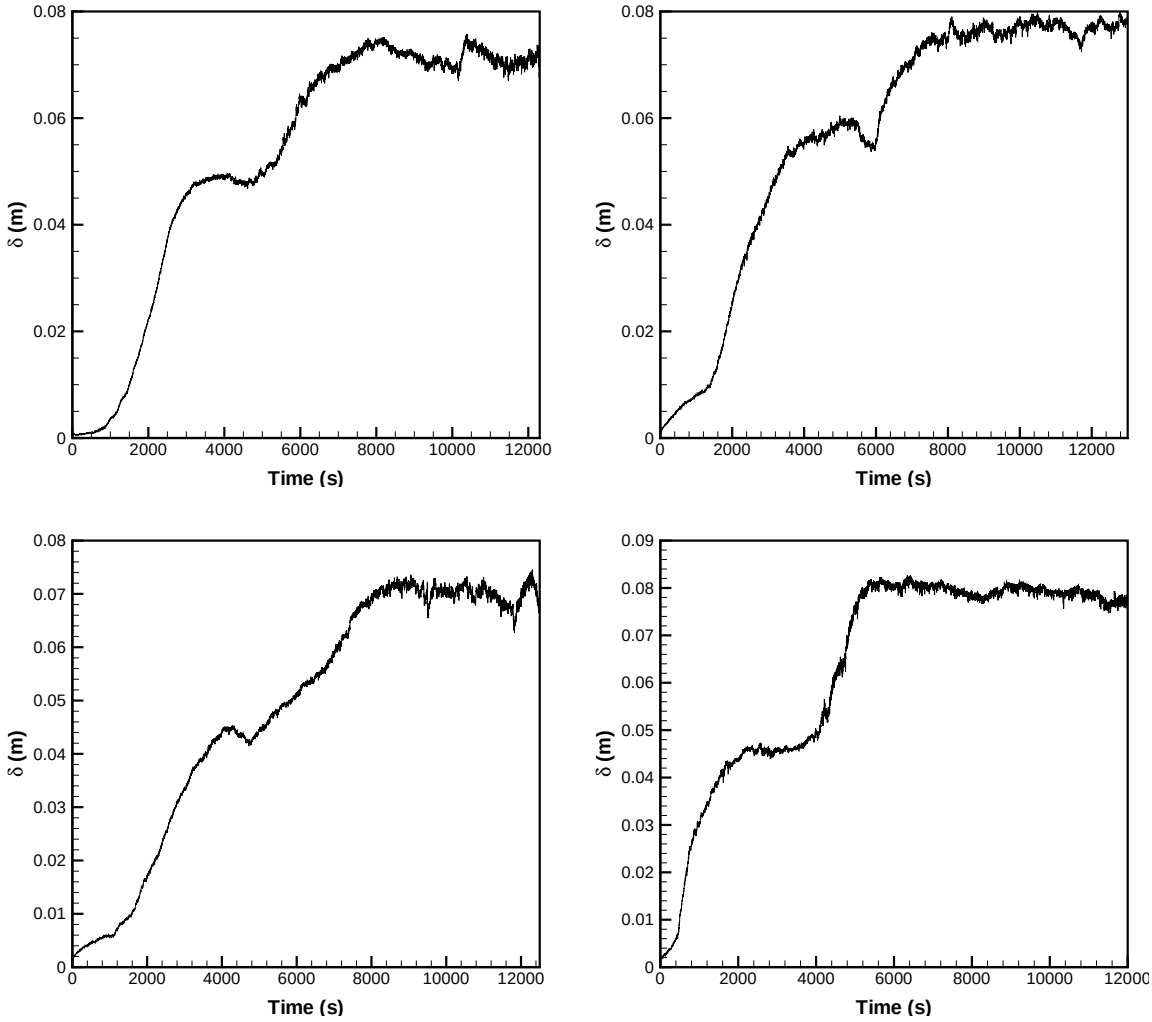

Figure 6.5: The evolution of the average dune height versus time for simulations R1 (top left), R2 (top right), R3 (bottom left) and R4 (bottom right).

dune which are almost flat do not count in the zero-crossing averaging approach, which yields an over-prediction of the average dune length. Moreover, the simulated results will be affected by the imposed periodicity of the boundary conditions, which forces an integer number of dunes in the domain. To avoid this, one may separately impose inflow and outflow boundary conditions in streamwise direction, but this was found not to change the results significantly.

There is a fundamental difference between the change in dune length and dune height. The change in height is related to individual dunes, whereas a change in length is related to the number of dunes in a certain stretch. This may involve higher and lower dunes superimposed onto one another. As the migration speed increases with decreasing dune height (Niemann et al., 2011), lower, faster moving dunes move over the stoss side of the higher dunes. When

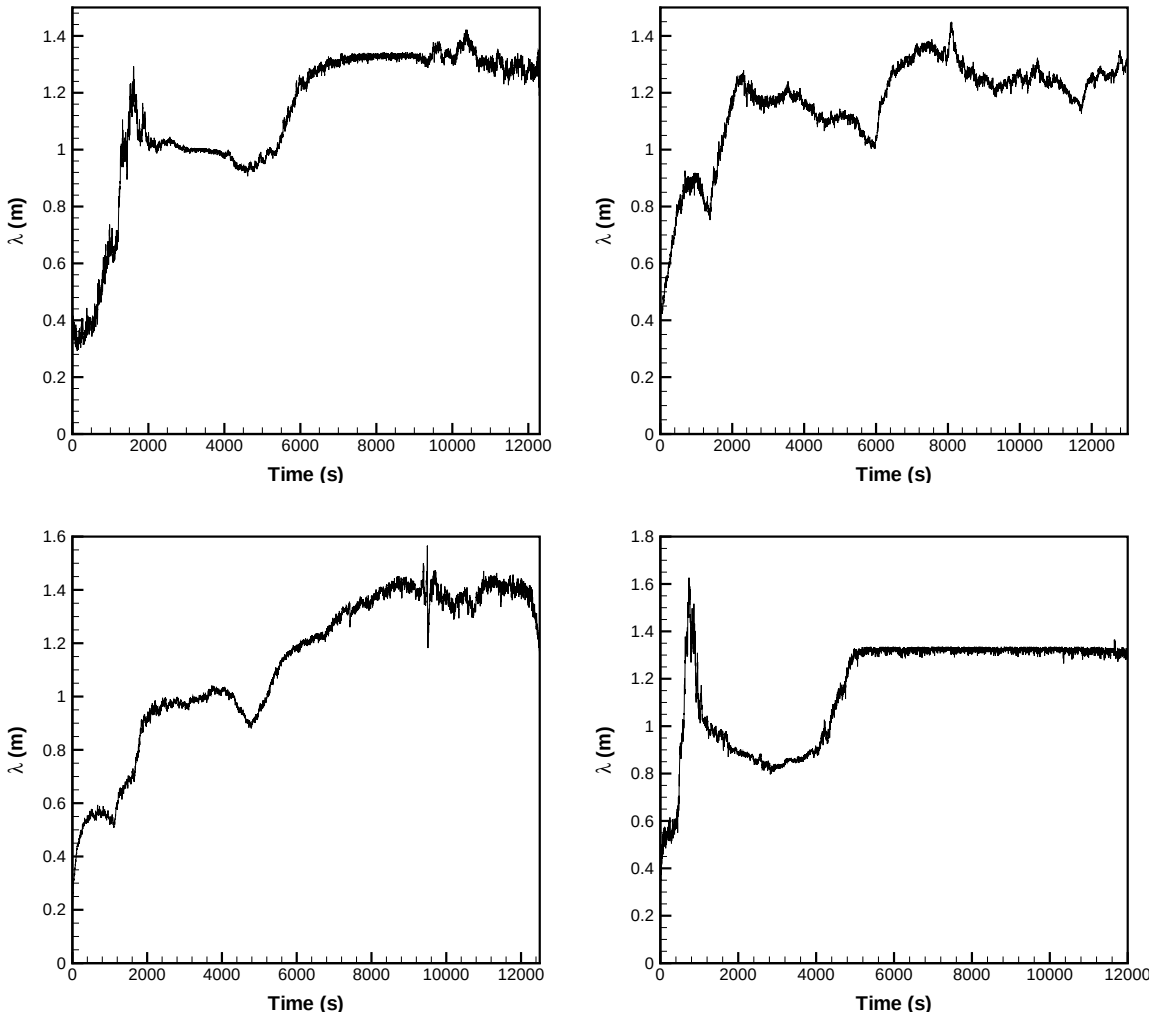

Figure 6.6: The evolution of the average dune length versus time for simulations R1 (top left), R2 (top right), R3 (bottom left) and R4 (bottom right).

they reach the crest, they merge with the higher dune and form a still larger dune. The sudden changes in height and length of dunes in Figures (6.5) and (6.6) can be attributed to this merging effect. This complicated phenomenon is enhanced by the presence of the side walls. Somehow, the secondary flow generated by the sidewalls complicates the bedform structure and initially generates dunes of different size. The present averaging procedure for dune height and length, involving different longitudinal bed profiles (not only the one in the centreline), includes the sidewall effect in Figures (6.5) and (6.6).

The behaviour of two-dimensional dunes in time is shown in Figure (6.7). This figure shows the centreline bed profile for all four runs. Phenomena such as splitting and merging clearly emerge from this figure. Cases R1, R2 and R3 yield three-dimensional dunes, whence the dunes in the centreline are not nec-

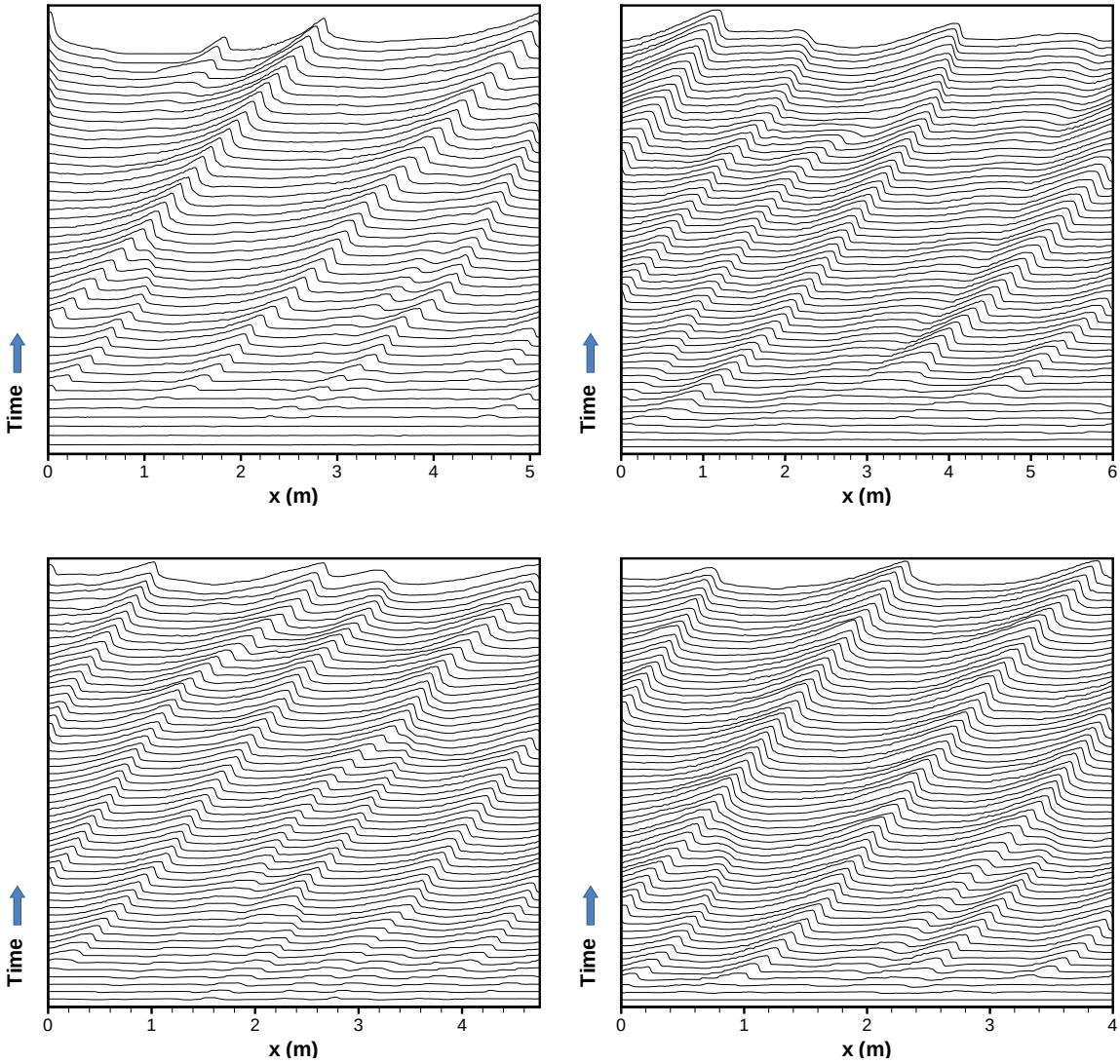

Figure 6.7: Visualization of evolution of dunes along the centreline for runs R1 (top left), R2 (top right), R3 (bottom left) and R4 (bottom right).

essarily of constant size. The dunes in case R4 are nearly two-dimensional and they approach a nearly constant size.

The evolution and migration of dunes are governed by sediment transport. In order to visualize this, the sediment particles above the dunes are shown in Figure (6.8). The concentration of sediment is highest close to the bed. Behind the sharp crests of the relatively high dunes, the sediment forms a kind of cloud, associated with the high-vorticity coherent structure separating from the dune crests and moving up to the water surface. These macroturbulent events are known to be a dominant mechanism for the suspension of sediment over dune beds (Jackson, 1976; Lapointe, 1992; Vendetti and Bennett, 2000; Best, 2005).

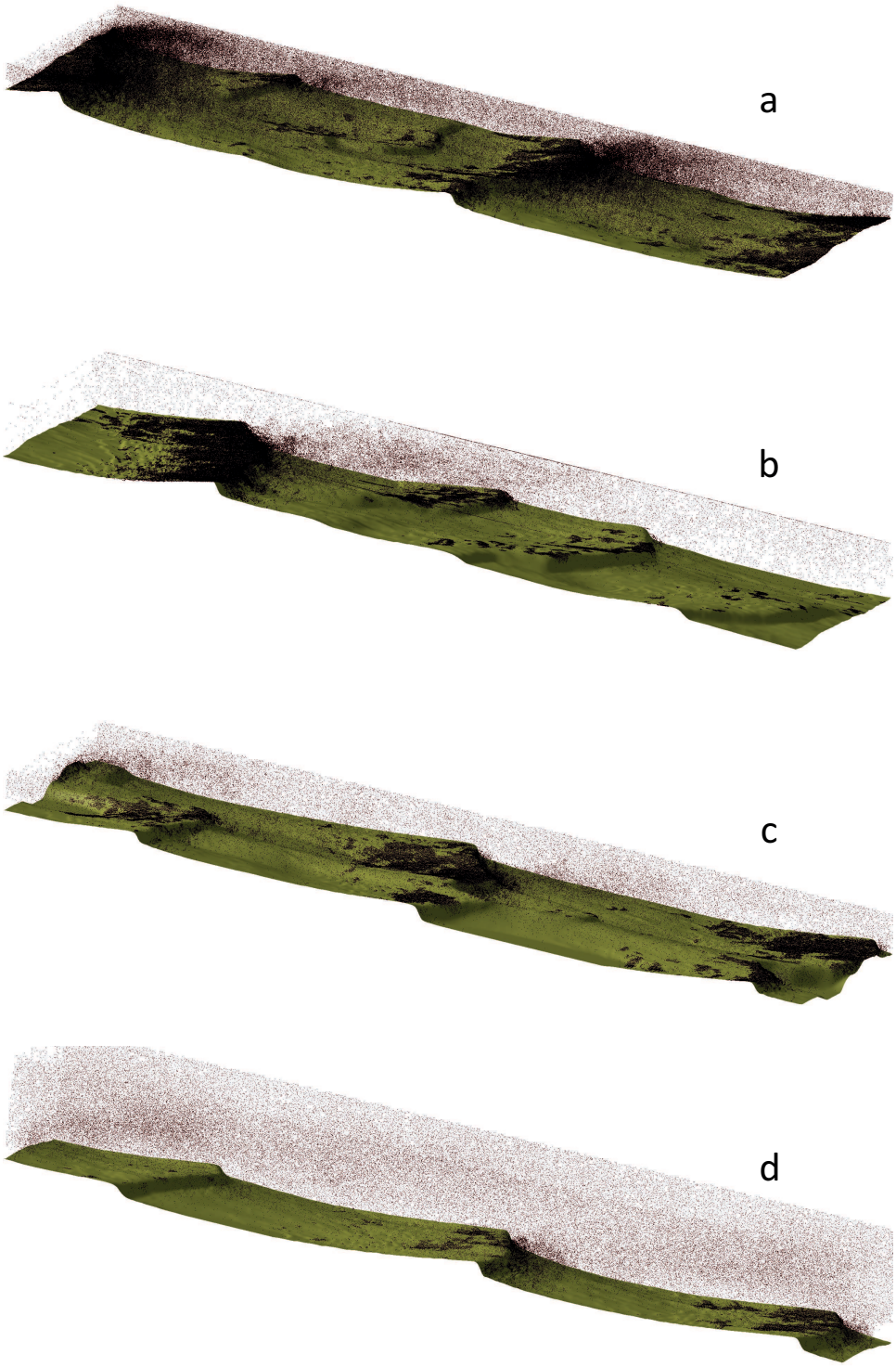

Figure 6.8: Visualization of the sediment particles above the bedforms for runs (a) R1, (b) R2, (c) R3 and (d) R4. Sediment concentrations are highest behind the crests of sharp dunes, because of the boiling effect.

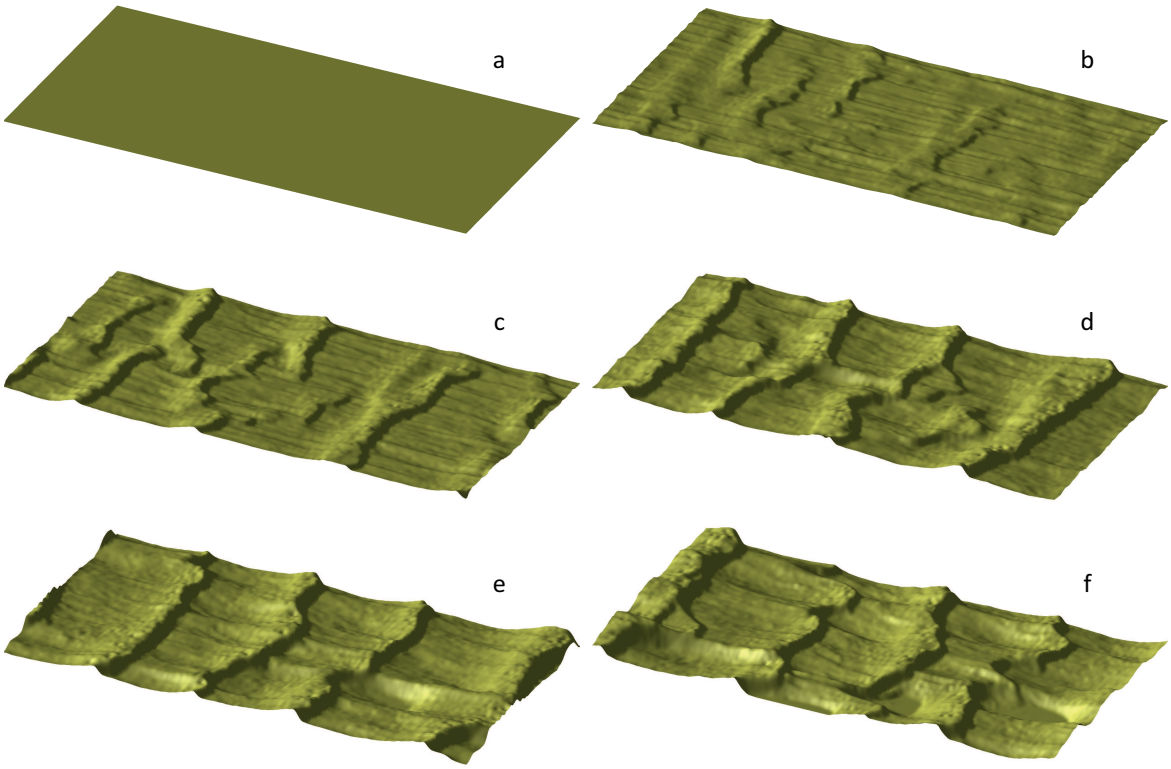

Figure 6.9: Simulation of evolution and migration of ripples and dunes with sediment diameter of 245 μm.

6.3 Effect of sediment size

In all experiments, mentioned above, the sediment size was constant. In order to investigate the effect of sediment diameter on dune topography, different cases are simulated, all with the same flow conditions and domain geometry as in a series of flume experiments carried out at Delft University of Technology (Crosato et al., 2011). Although these experiments were mainly meant to investigate the formation of steady bars in a straight channel, bedform dimensions were measured and made available to validate the present numerical model (Crosato et al., 2011) (personal communication). The total length of the flume was 25 m, its width 60 cm and its slope 3×10^{-4}. The bottom of the flume was covered with a 20 cm thick layer of sediment of 0.245 mm median diameter. The experiments started from a flat bed, with a water depth of 4.5 cm, and a discharge of 6.8 l/s.

The model domain covers only a 1.2 m long part of the flume and the upstream and downstream boundary conditions are taken periodic. The lateral boundaries are taken as smooth solid walls to account for the effect of the glass side walls in the flume. The simulation starts from a flat bed, with the same water depth and discharge as in the experiment (Figure 6.9). Initially, the bed gets per-

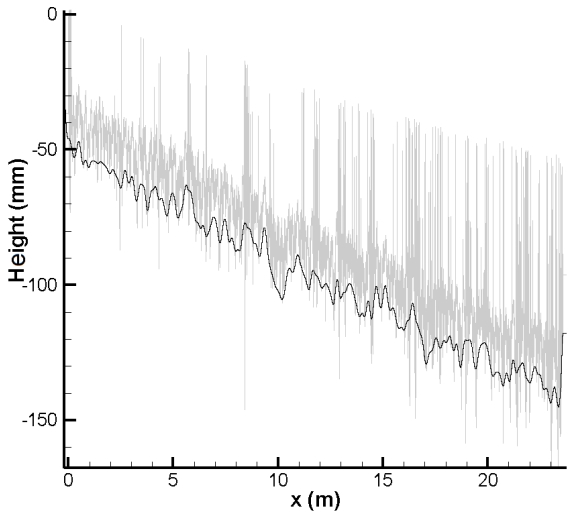

Figure 6.10: The measurement of dune height and length (grey) and low-pass filtering of the measurements (black).

turbed by shear stress fluctuations (Figure 6.9b), after which ripples are formed (Figure 6.9c). These ripples grow (Figure 6.9d) and dunes are formed (Figure 6.9e). These dunes migrate and grow and finally reach a statistically stationary state (Figure 6.9f). In Figures (6.9b) and (6.9c), long streamwise ribbon structures of the bedform can be noticed. This structure is generated under the effect of secondary currents which are generated by the non-homogeneity and anisotropy of turbulence. Cellular secondary currents might exist in a wide open-channel and lead to erode the bed cyclically in spanwise direction (Nezu and Nakagawa, 1993). Figure (6.3) shows a measured bed level profile in this state, along with the result of its low-pass filtering. The average length and height of the dunes according to the model, 33 cm and 28 mm, respectively, agree well with the experimental results (30.5 cm and 26 mm, respectively), although the measured dune length and height depend slightly on the filter length chosen.

Figure (6.11) shows the simulations with different sediment diameters (100, 120, 140, 160, 180, 200 and 220 μm). As can be seen in these figures, fine sediment yields superimposed ripples, which ultimately lead to deformed dunes (Best, 2005). This phenomenon can be explained by the bedform phase diagram of Southard and Boguchwal (1990). Given the bulk flow velocity, the conditions for fine sediment fall in the ripples regime. As the sediment diameter increases, conditions move toward the dune regime. Moreover, fine sediment is shown to yield almost two-dimensional bedforms. When increasing the sediment diameter, three-dimensionality increases and the bedforms become three-dimensional for the larger sediment sizes.

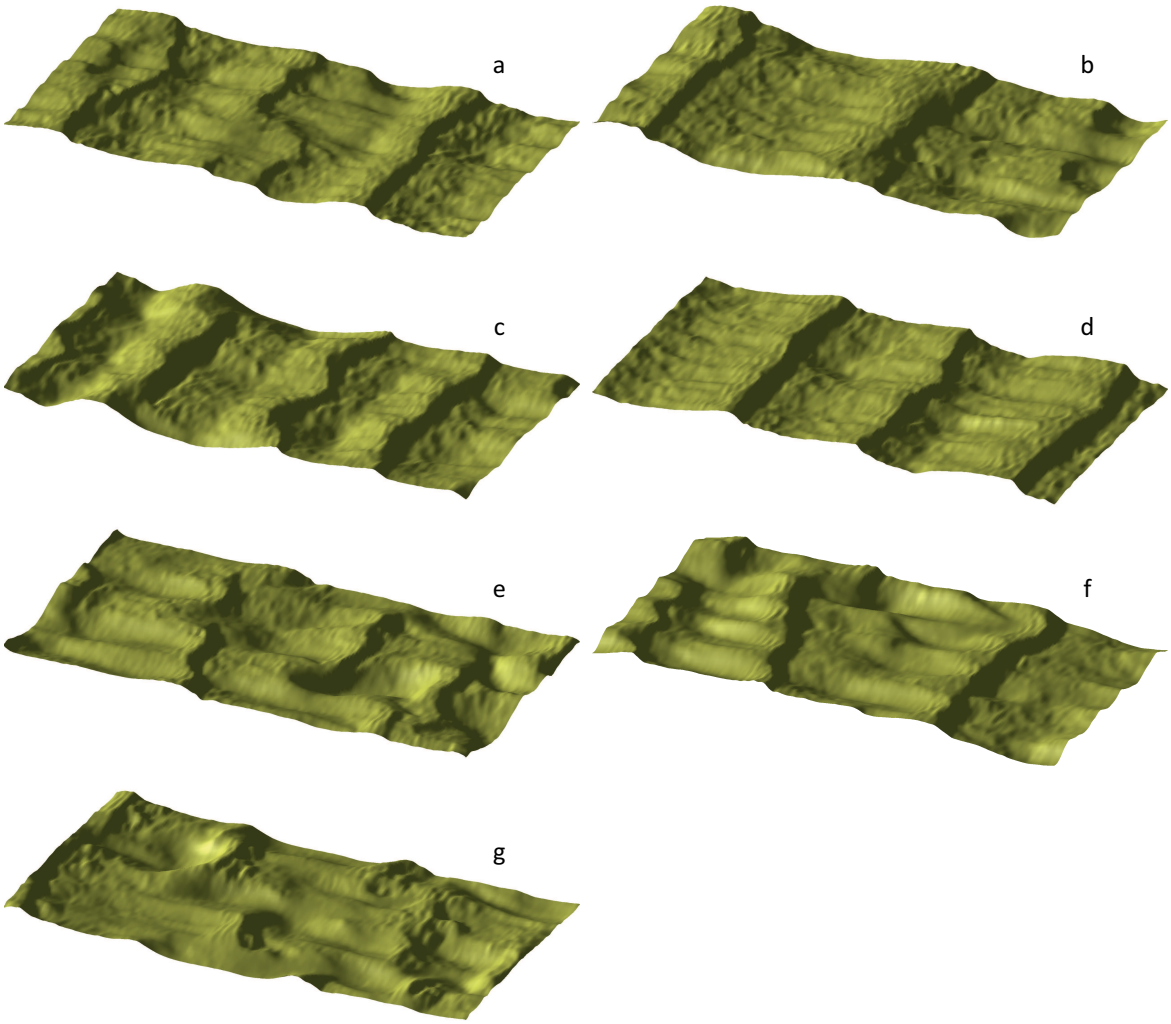

Figure 6.11: Simulation of dunes for different sediment diameters. (a) 100 μm, (b) 120 μm (c) 140 μm, (d) 160 μm, (e) 180 μm, (f) 200 μm, and (g) 220 μm.

6.4 Concluding remarks

Recent developments in state-of-the-art computational modelling enable simulating bedform evolution in rivers on the basis of detailed 3D process descriptions of turbulent flow and sediment transport. The turbulent flow is modelled by LES on a Cartesian grid with local refinements, which gives relatively accurate results while being computationally efficient.

In order to validate our model, five different experiments were simulated. The model results were found to agree well with the experimental findings. When considering the time evolution of dune length and height, merging of smaller and larger bedforms was found to yield irregularities in the evolution.

When changing the sediment grain size while keeping all other conditions the same, a smaller grain size was found to generate more and smaller ripples. As the sediment size increases, these ripples disappear and dunes dominate. Moreover, three-dimensionality increases with increasing sediment size.

The present model has the potential to constitute a basis for bed roughness and bed load transport parameterization under steady as well as varying flow conditions, even if this concerns rare extreme events. This is extremely important, for instance, for the prediction of extreme flood levels in rivers and the design of adequate flood protection measures.

Chapter 7

Morphodynamics under variable discharges

7.1 Introduction

An accurate prediction of bedform-induced flow resistance, including its role in flows with temporal variation, is essential from a practical engineering point of view, because the stage discharge relation in temporally varying flows with bedforms depends critically on the total drag. Many attempts have been made to improve both understanding and predictive capability of bedform evolution, transition and associated resistance under varying flow conditions. Most of the approaches are empirical or semi-empirical. There are still few prediction methods that can treat these phenomena in a coupled manner based on first physical principles.

A natural river involves discharge variations, which influence flow and sediment transport, hence the river bed topography. A constant discharge ultimately yields a statistically unique bedform pattern. As the discharge varies, the bedforms change. For a variable discharge, the form of the bed is not unique, due to a time lag between the discharge gradient and the bed deformation. The geometry of the bed is related to the history of the flow and different bedforms can exist with the same discharge if they have different histories. This is called hysteresis.

None of the existing numerical studies, except the fundamental study of Shimizu et al. (2009), considers the hysteresis effect that is apparent in many time-varying flows, despite the fact that predicting the form drag due to bedforms is often critically important for predicting stage variations during flood events. Few attempts have been made to analyze the hysteresis in bedform development during the rising and falling limbs of flood hydrographs. Yet, strong hysteresis between time-varying discharge and bed resistance has been observed in several studies. The discharge-roughness relationship is usually found to be in the form of a loop (Simons et al., 1961; Yamaguchi and Izumi, 2003). This phenomenon is attributed to the distinctive characteristics of bedform evolution and transition

and, in turn, differences in resistance to flow during rising and falling stages of flows, even under the same discharge conditions. Yamaguchi and Izumi (2002, 2003) provided a physical explanation of such a hysteresis using a weakly non-linear stability analysis. They stated that the hysteresis is characterized by a sub-critical bifurcation, and verified this against a laboratory experiment on transient bedforms under unsteady discharge conditions (Yamaguchi and Izumi, 2003). Shimizu et al. (2009) extended their previous studies (Giri and Shimizu, 2006) and proposed a morphodynamic model that successfully reproduces fluid and bed-form dynamics in a coupled manner under arbitrary steady or unsteady flow. The flow component of the morphodynamic model is two-dimensional, uses a non-linear $k - \epsilon$ model and includes non-hydrostatic effects. A non-equilibrium sediment transport approach that treats the pick-up and deposition of sediment empirically was used along with the imposition of an assumed mean sediment particle step length. Despite these attractive features, it is difficult to obtain a realistic solution. The dune shape in this model strongly depends on the definition of the particle step length. As the particle step length is unknown, this model cannot always predict the dune shape correctly. Furthermore, this model uses a RANS turbulence closure approach, which removes turbulent flow fluctuations and hence the effect of shear stress fluctuations on sediment pick-up, which is an important element in the formation of ripples on the stoss sides of the dunes. The interactions between flow field, bed geometry and sediment transport are quite complex and difficult to capture by simple models. The bedforms are created and altered by the flow and, conversely, the flow is influenced by the bedforms via form drag and significant variations in local mean flow and turbulence fields (Nelson et al., 1993). To the author's knowledge, no physics-based numerical model has been successful, so far, in reproducing these phenomena. A more sophisticated three-dimensional model is necessary to understand the physical phenomena and extract parameterized relations for practical use.

Not only the range of the discharge variation, but also its frequency has a major effect on the shape of dunes, and hence on the water level during a flood. The bed deformation for peak hydrographs of short duration is different from that for long-duration ones. Generally speaking, the change of form drag will be faster, and the variation in bedform behaves differently than the situation with long duration hydrographs. Understanding the features of bedform patterns caused by low and high frequency hydrographs is important for the prediction of the form and behaviour of dunes under unsteady discharge conditions.

The focus of this chapter is on the simulation of morphological changes caused by different hydrographs. To obtain a better understanding of the physical phenomena, the bedform and the form drag under variable discharges are studied and the effect of sediment diameter and the duration of hydrographs on the hysteresis are invistigated. Morover, extreme phenomena of dissipation of dunes in the high-flow regime (i.e. during flood) are simulated.

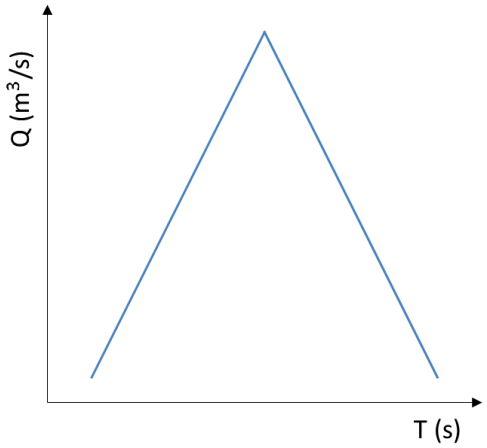

Figure 7.1: Schematic view of a hydrograph with linearly rising and falling limbs.

7.2 Numerical experiments

A number of numerical tests were conducted to assess the capability of the numerical model to simulate bedform evolution under unsteady discharges. These tests confirm the hysteresis effect and reveal the nature of their relation with hydrographs of different shape. Computations were carried out for a hypothetical flume of 1 m width. A variety of combinations of sediment particle size and discharge hydrograph was used.

As the upstream and downstream boundaries are taken periodic, a short domain length (2 m) is used for most numerical experiments to reduce the computational costs. All simulations begin from a flat bed with statistically homogenous turbulent flow. The boundaries in spanwise direction are also taken periodic. The free surface is considered as a free-slip rigid lid. This was shown to have a negligible effect on the bedforms, as long as the Froude number is relatively small (Niemann et al., 2011). The water depth is taken 0.4 m in all simulated scenarios. The discharge varies between 0.12 and 0.48 m^3/s, with symmetric linearly rising and falling limbs (Figure 7.1). This corresponds with a Froude number varying between 0.15 and 0.6 and a Reynolds number varying between 120,000 and 476,000. Although the maximum Froude number is relatively high for a free-slip water surface, the model shows still reasonable results. Niemann et al. (2011) has also shown that their model gives reasonable results with comparable Froude number under no-slip rigid-lid condition for the water surface. The present simulations are carried out using five different hydrographs and each hydrograph is combined with six different grain sizes. The grains diameters are chosen to be 300, 400, 500, 600, 700 and 800 μm, with flow periods of 2000, 3000, 4000, 5000 and 6000 s. Table (7.1) lists the settings for the various runs.

The height and length of the dunes are determined using the zero-crossing

Table 7.1: Calculation scenarios and conditions. All simulation are performed under variable discharge between 0.12 and 0.475 m^3/s

Run	Sediment size (μm)	Duration (s)
01	300	2000
02	300	3000
03	300	4000
04	300	5000
05	300	6000
06	400	2000
07	400	3000
08	400	4000
09	400	5000
10	400	6000
11	500	2000
12	500	3000
13	500	4000
14	500	5000
15	500	6000
16	600	2000
17	600	3000
18	600	4000
19	600	5000
20	600	6000
21	700	2000
22	700	3000
23	700	4000
24	700	5000
25	700	6000
21	800	2000
22	800	3000
23	800	4000
24	800	5000
25	800	6000

approach discussed in Chapter 6. Moreover, the form drag is calculated by integrating the streamwise component of the pressure on the bed, as discussed in Chapter 5. Figure (7.2) shows the results for the form drag for such a schematized hydrograph, with a flow period of 2000 seconds with uniform grain sizes varying from 300 to 700 μm. It can be seen that the form drag diagram has the form of an open loop. As the sediment size increases, the loop gets wider, i.e. the hysteresis effect gets stronger. The form drag increases in the rising flow stage because the dune height increases. In cases with coarser sediments, this increase is faster than in cases with finer sediment. In the falling flow stage, the form drag shows two different types of behaviour: (1) a fall starting immediately, but at a smaller rate than the increase in the rising stage, or (2) a first increase, followed by a decreasing stage, again at a smaller rate. Figure (7.3) shows the variation in the dune height and length under the mentioned hydrograph. In the rising stage, the dunes grow in height and the height at the peak of the hydrograph increases with sediment size, whereas the dune length remains almost the same.

In the falling stage, the dune height keeps on growing in the case with sediment of 300 μm. As the sediment size increases, a different behaviour is found: first, the dune height increases, but later it begins to decrease and finally it stays constant. The latter phenomenon can be explained from the sediment pick-up rate. The pick-up rate for coarser sediment is smaller than that for fine sediment, and as the flow velocity and bed shear stress decrease below the threshold of motion, the flow is unable to pick up the particles. This stage is reached for the coarser sediment only, which explains why the coarse-sediment bedforms no longer change as the flow slows down further. This phenomenon can also be observed in the dune length diagrams: after an initial growth in length during the falling stage, it reaches an equilibrium state.

In Figure (7.4) the duration of the hydrograph is slightly larger than in Figure (7.2): 3000 s. The behaviour is comparable with that in Figure (7.2). The same holds for Figures (7.6), (7.8) and (7.10), with durations of 4000, 5000 and 6000 s, respectively. In all these figures, the hysteresis loop gets wider as the sediment size increases, and the form drag during the rising and falling stage shows a similar behaviour as in Figure (7.2).

Similarly, Figures (7.5), (7.7), (7.9) and (7.11) are comparable with Figure (7.2). The height of the dunes during the rising flow stage increases and, as the flow rate reaches its maximum, the dune height for coarser sediments is greater than that for finer sediments. Moreover, after a deformation in the first part of the falling stage, the dunes reach an equilibrium state. For coarser sediment, the equilibrium stage is achieved earlier than for finer sediment.

The wider hysteresis loop for coarser sediment can be explained from a time lag between the flow and the motion of particles. As the particles are generally smaller than the relevant flow structures, the motion of particles will be dominated by the smallest scales of turbulence, the Kolmogorov time scales. Moreover, a time scale can be defined for the particles, viz. the characteristic time

needed for a particle to transit from one state to another state. The relaxation time is a function of the mass and mobility of the particle and can be defined as

$$\tau_p = \frac{\rho_p d_p^2}{18\mu} \tag{7.1}$$

in which ρ_p, d_p and μ are the particle density, particle diameter, and the kinematic viscosity of the flow respectively. The derivation of Equation (7.1) is given in Appendix B.

Pick-up and sliding of sediment particles occurs in the vicinity of the bed. The main part of the sediment transport also happens close to the bed. In that region, turbulence dissipation dominates and the eddy size is in the order of the Kolmogorov scale. Sediment pick-up, sliding and transport occurs by the small eddies which survive at a time scale in the order of the Kolmogorov time scale. If the particle relaxation time is much smaller than the Kolmogorov time scale, the particle can be carried into the flow without a significant time lag, which means that the particles always follow the flow. In the case of relatively large particles, however, the particle relaxation time is not much smaller than the Kolmogorov time scale. The flow cannot accelerate the particles immediately and there is a time lag between the motion of the eddies and the particles. The time lag increases rapidly with the particles size: according to Equation (7.1) the relaxation time is proportional to the particle diameter squared.

Comparing the cases with the same sediment size but different hydrographs gives an indication of the effect of the flow variations on form drag and dune dimensions. Hydrographs of longer duration lead to stronger hysteresis effects, in the dune geometry (height and length) as well as in the form drag. This effect is especially manifest for relatively coarse sediment, probably due to the larger time lag between the discharge variation and the bed deformations. The bed has not enough time to deform and adapt to the instantaneous discharge. This phenomenon becomes less pronounced for very longer hydrograph durations. As the discharge changes very slowly, the bedforms can adapt to the flow conditions and a weak hysteresis appears.

At relatively high discharge, the drag force exhibits strong fluctuations, as shown in Figures (7.2), (7.4), (7.6), (7.8) and (7.10). As the discharge increases, high-frequency ripples begin to appear. Thy are short-lived, emerge in a very short time and rapidly die out. These ripples directly contribute to the drag force and lead to a drag fluctuations. As the bed shear stress decreases in the falling limb, the drag fluctuations vanish again. The fluctuating drag is more prominent in long-duration hydrographs, because there is more time for the generation of high-frequency ripples. Note that these fluctuating bedforms are not visible in Figures (7.3), (7.5), (7.7), (7.9) and (7.13), where the shape of dunes are spatially averaged (by the zero-crossing approach), which filters out high-frequency effects.

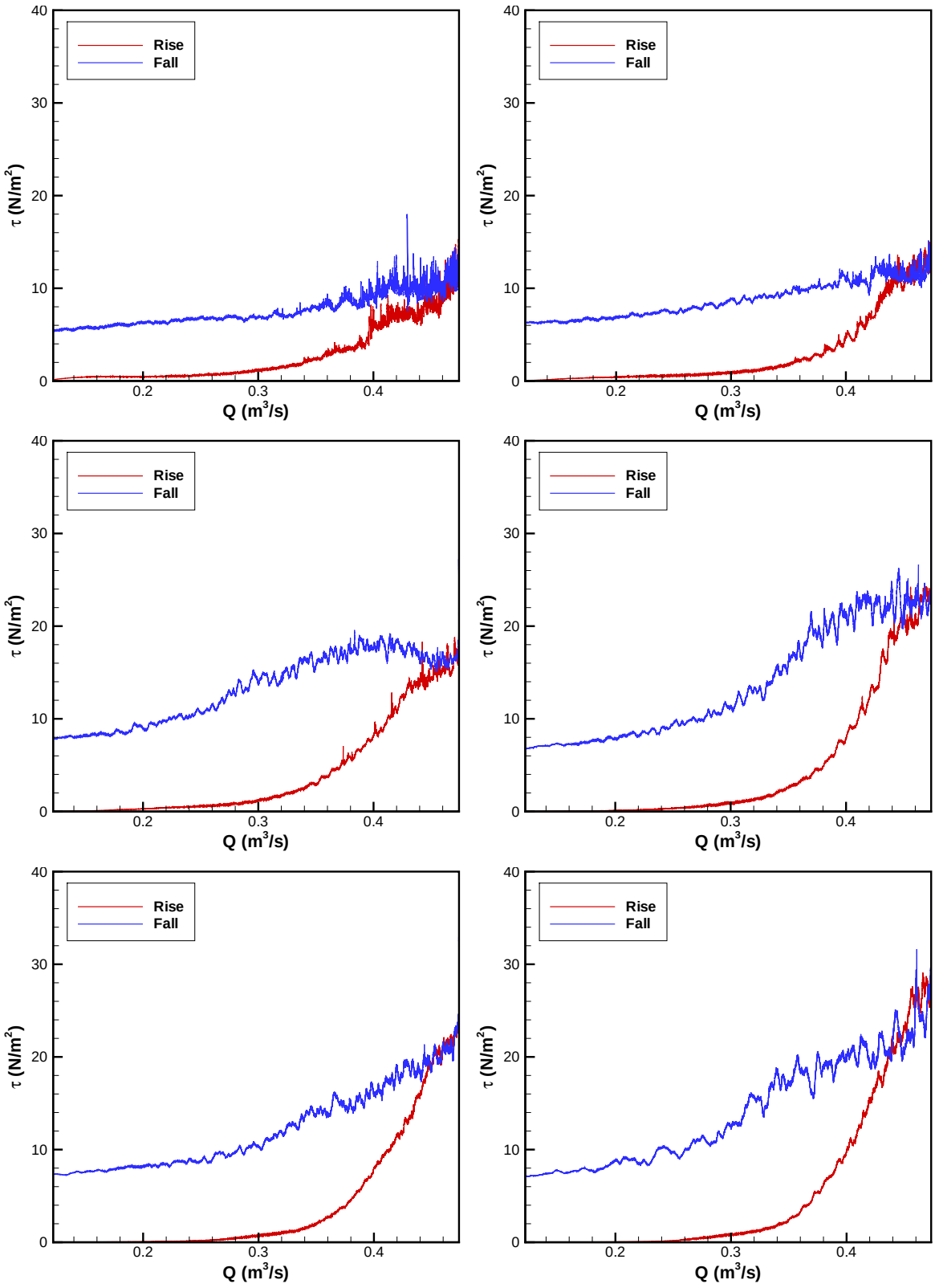

Figure 7.2: Form drag versus discharge in rising and falling stages of a schematized hydrograph with a period of 2000 seconds and sediment size of 300 μm (top left), 400 μm (top right), 500 μm (middle left), 600 μm (middle right), 700 μm (bottom left), and 800 μm (bottom right).

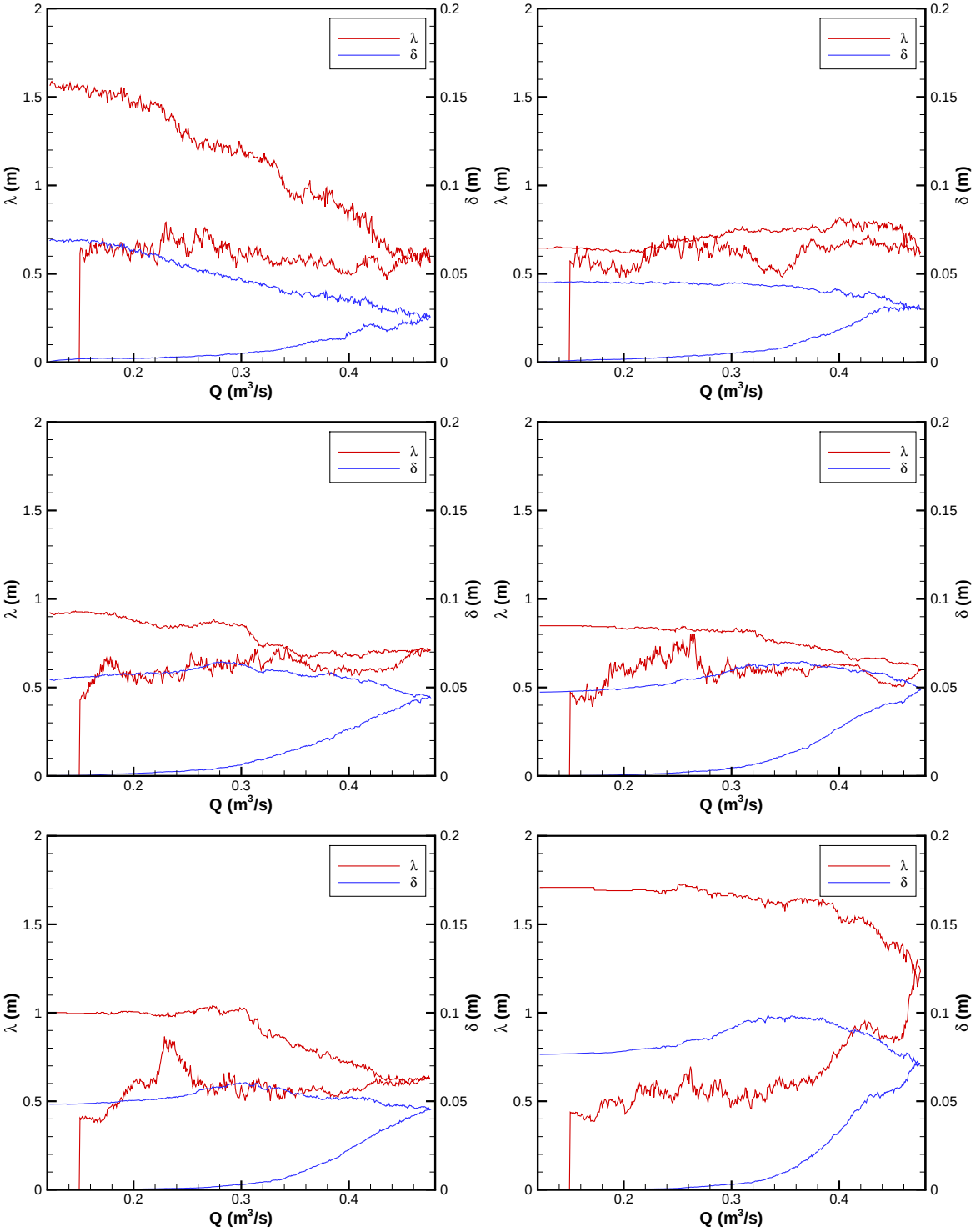

Figure 7.3: Dune height and length versus discharge in rising and falling stages of a schematized hydrograph with a period of 2000 seconds and sediment size of 300 μm (top left), 400 μm (top right), 500 μm (middle left), 600 μm (middle right), 700 μm (bottom left), and 800 μm (bottom right).

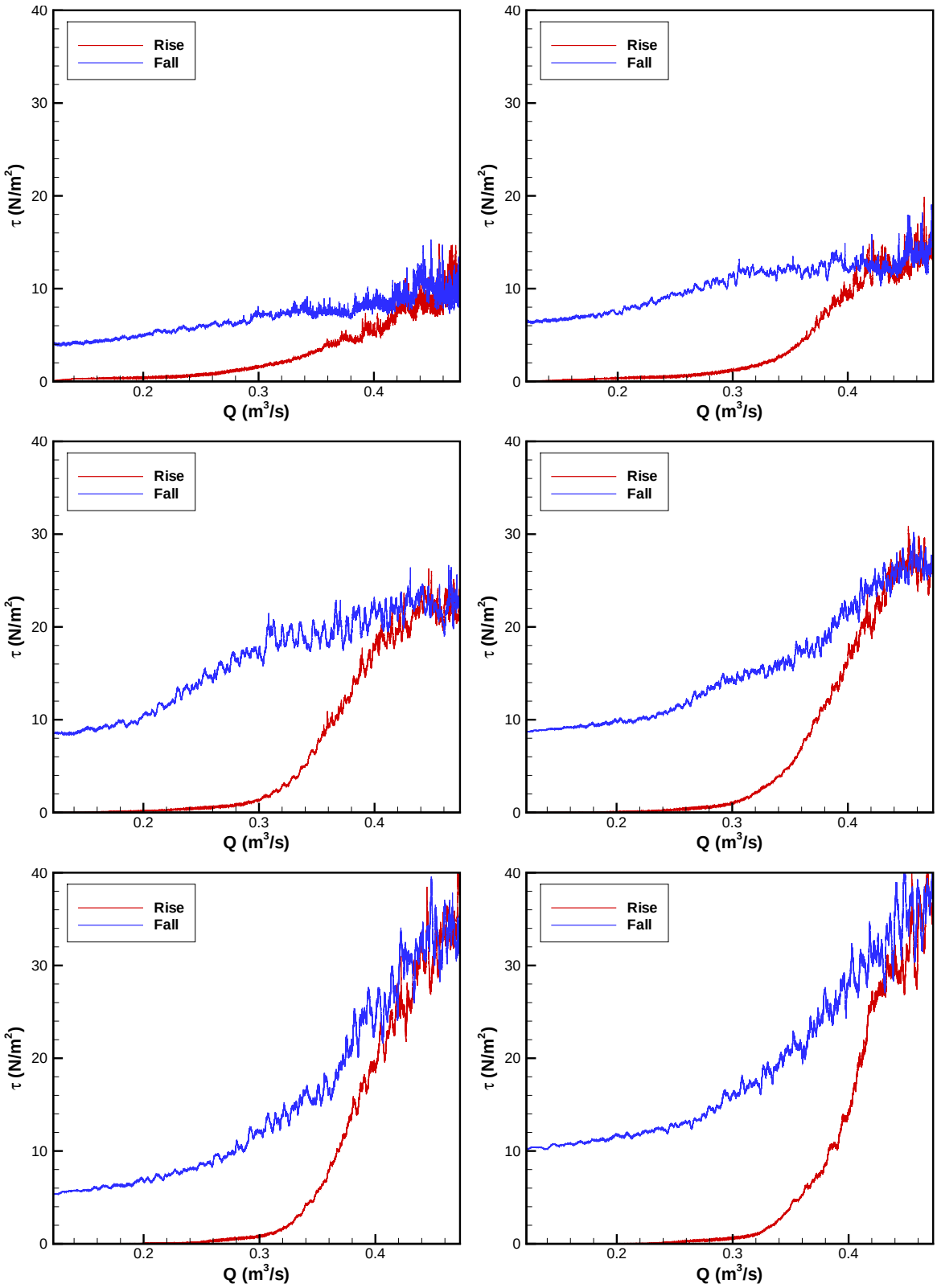

Figure 7.4: Form drag versus discharge in rising and falling stages of a schematized schematized hydrograph with a period of 3000 seconds and sediment size of 300 μm (top left), 400 μm (top right), 500 μm (middle left), 600 μm (middle right), 700 μm (bottom left), and 800 μm (bottom right).

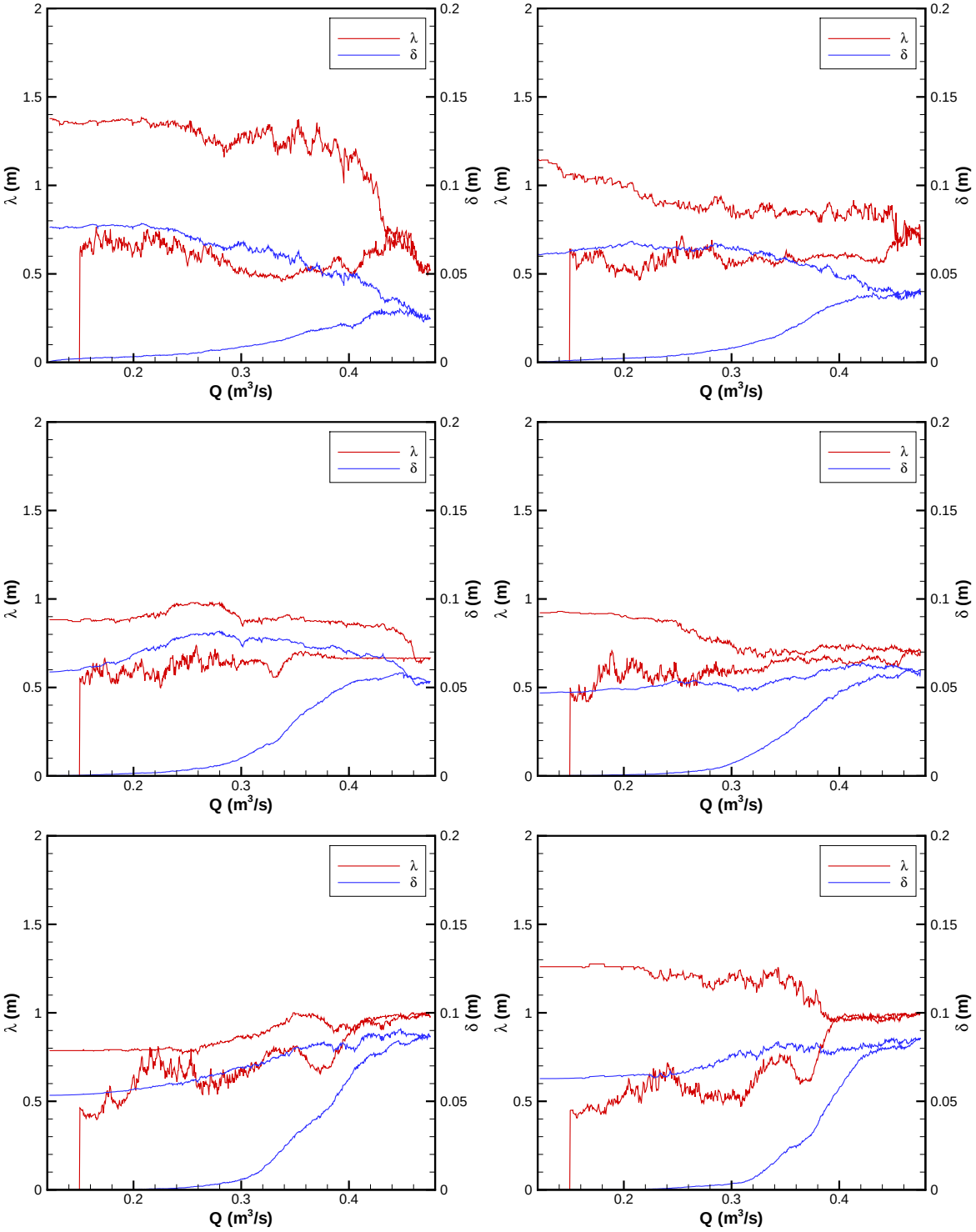

Figure 7.5: Dune height and length versus discharge in rising and falling stages of a schematized hydrograph with a period of 3000 seconds and sediment size of 300 μm (top left), 400 μm (top right), 500 μm (middle left), 600 μm (middle right), 700 μm (bottom left), and 800 μm (bottom right).

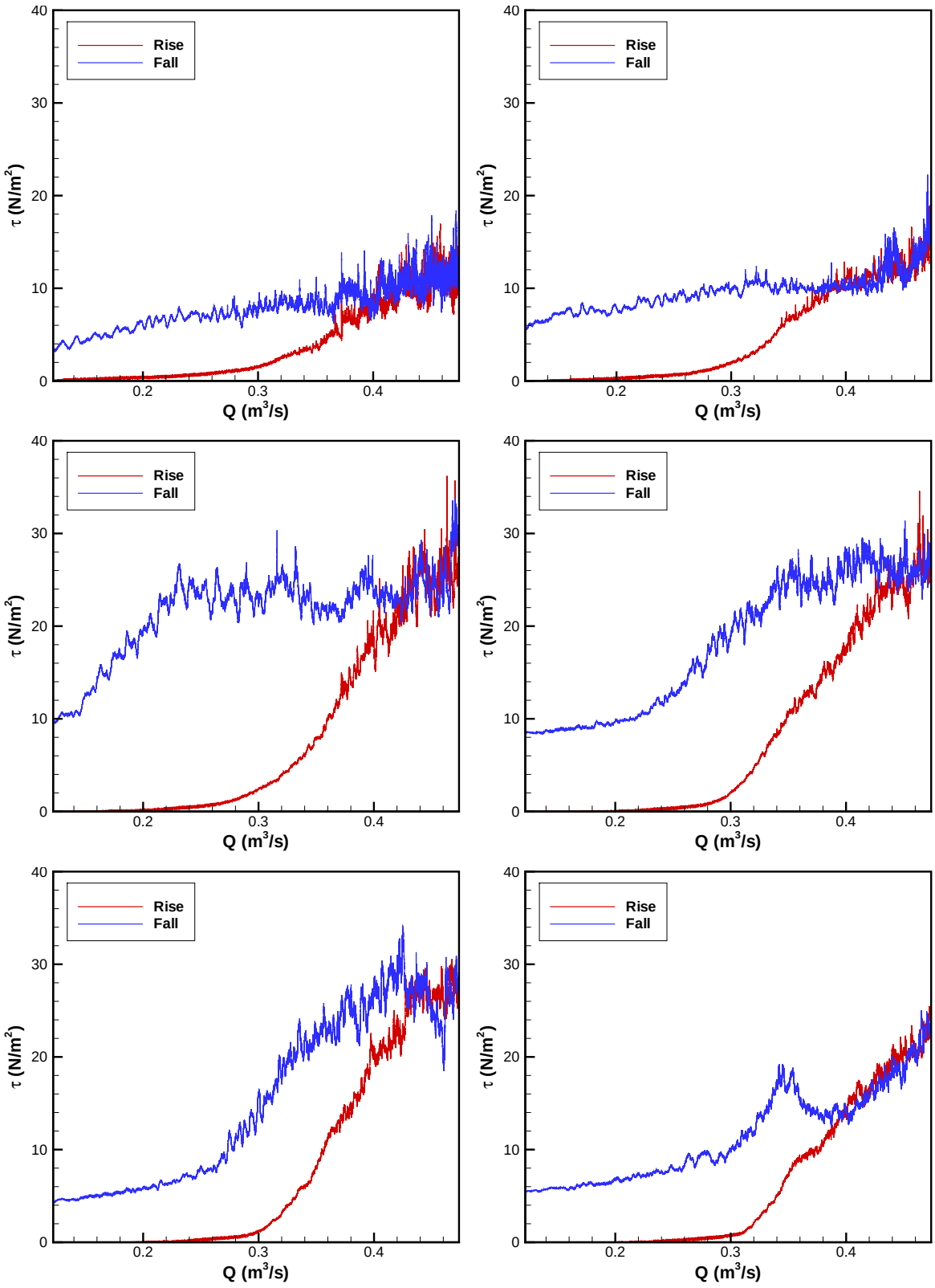

Figure 7.6: Form drag versus discharge in rising and falling stages of a schematized hydrograph with a period of 4000 seconds and sediment size of 300 μm (top left), 400 μm (top right), 500 μm (middle left), 600 μm (middle right), 700 μm (bottom left), and 800 μm (bottom right).

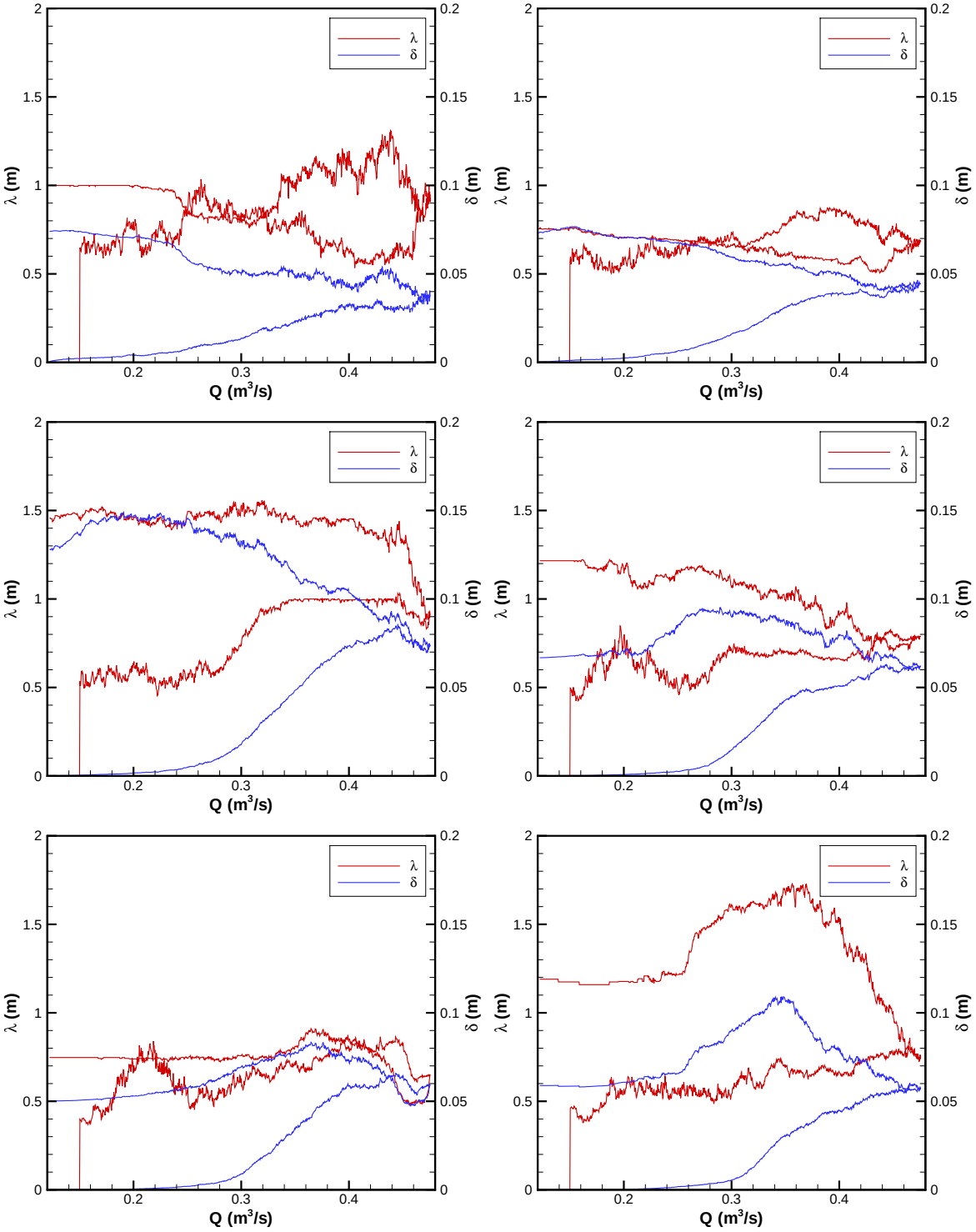

Figure 7.7: Dune height and length versus discharge in rising and falling stages of a schematized hydrograph with a period of 4000 seconds and sediment size of 300 μm (top left), 400 μm (top right), 500 μm (middle left), 600 μm (middle right), 700 μm (bottom left), and 800 μm (bottom right).

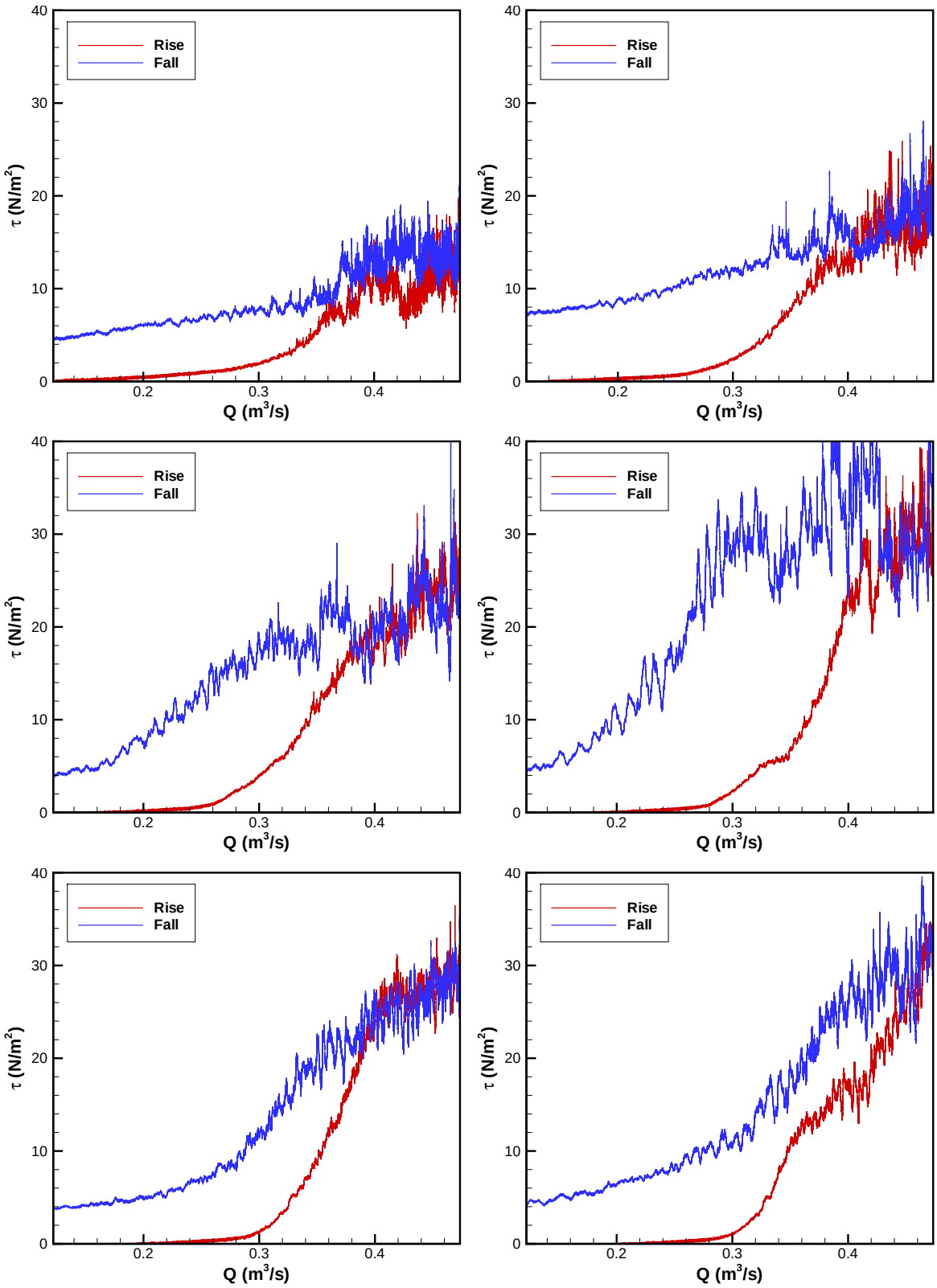

Figure 7.8: Form drag versus discharge in rising and falling stages of a schematized hydrograph with a period of 5000 seconds and sediment size of 300 μm (top left), 400 μm (top right), 500 μm (middle left), 600 μm (middle right), 700 μm (bottom left), and 800 μm (bottom right).

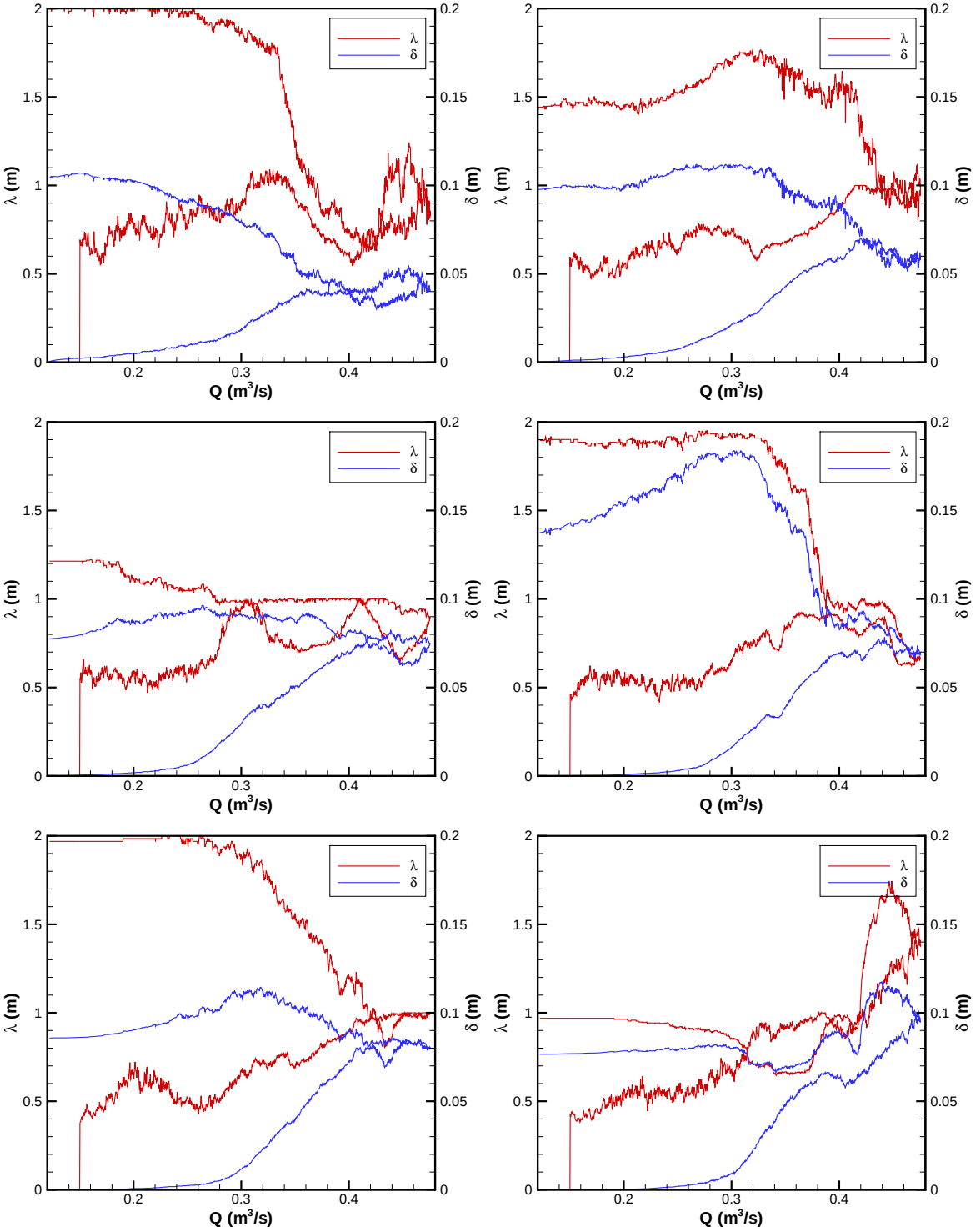

Figure 7.9: Dune height and length versus discharge in rising and falling stages of a schematized hydrograph with a period of 5000 seconds and sediment size of 300 μm (top left), 400 μm (top right), 500 μm (middle left), 600 μm (middle right), 700 μm (bottom left), and 800 μm (bottom right).

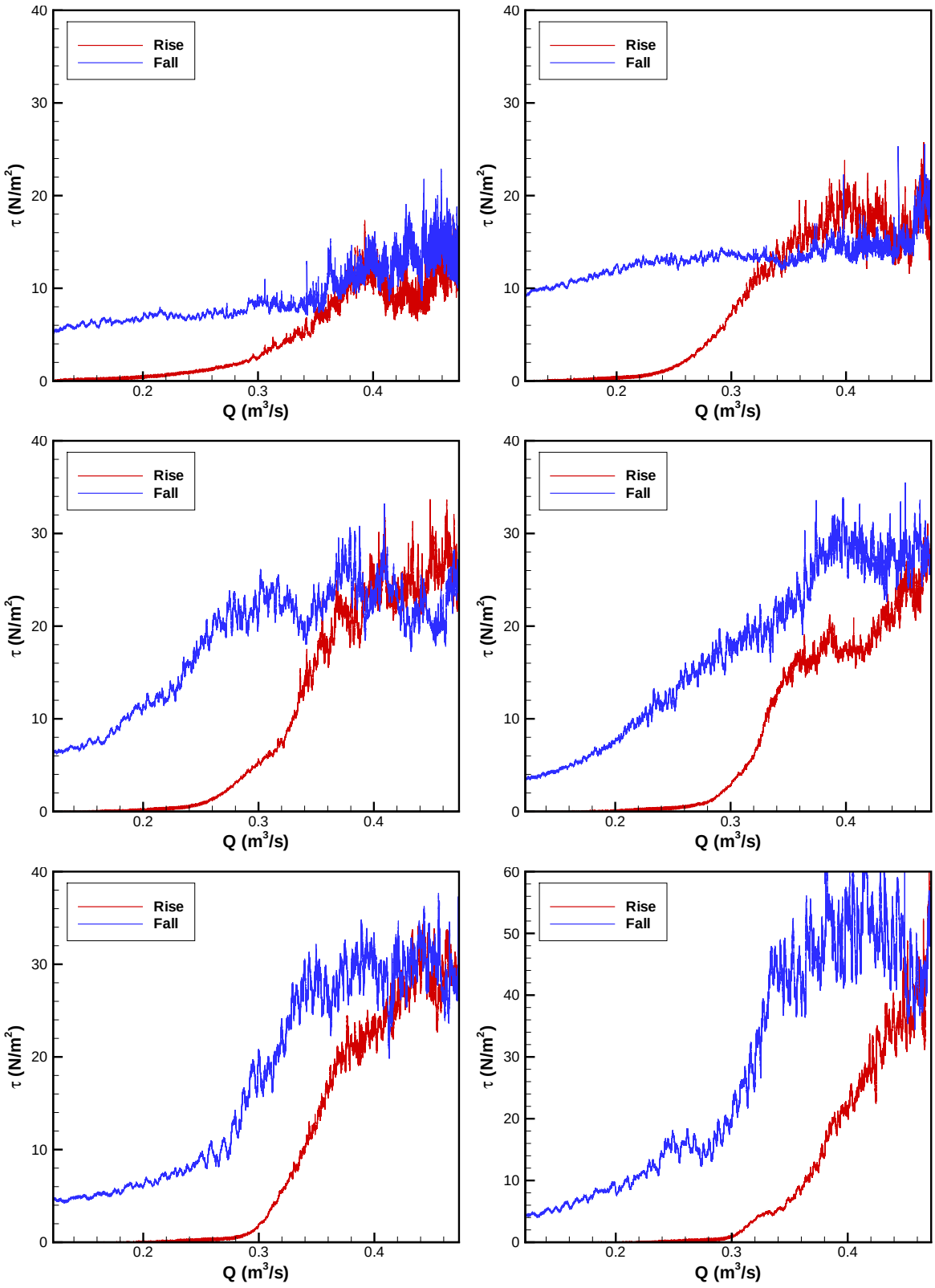

Figure 7.10: Form drag versus discharge in rising and falling stages of a schematized hydrograph with a period of 6000 seconds and sediment size of 300 μm (top left), 400 μm (top right), 500 μm (middle left), 600 μm (middle right), 700 μm (bottom left), and 800 μm (bottom right).

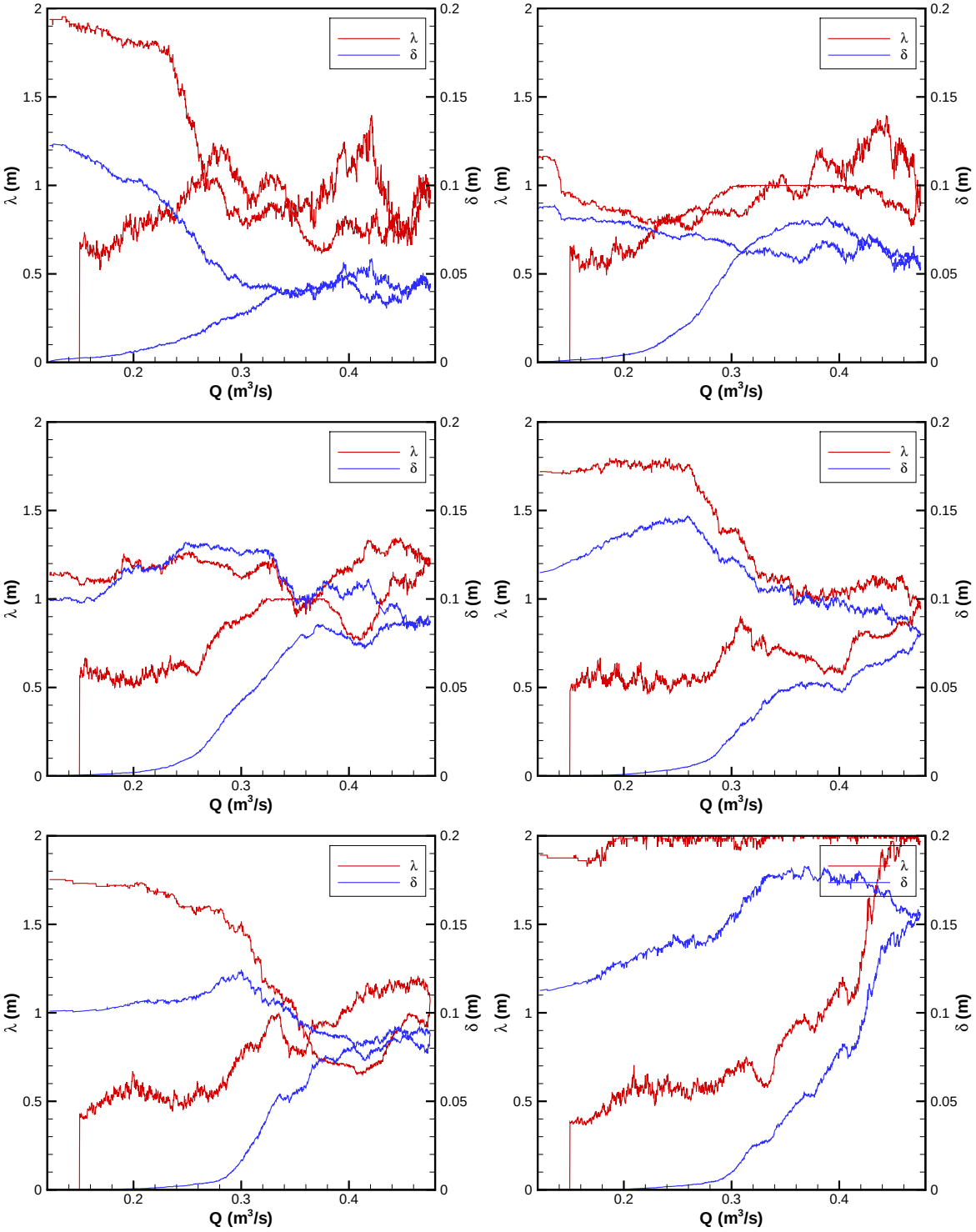

Figure 7.11: Dune height and length versus discharge in rising and falling stages of a schematized hydrograph with a period of 6000 seconds and sediment size of 300 μm (top left), 400 μm (top right), 500 μm (middle left), 600 μm (middle right), 700 μm (bottom left), and 800 μm (bottom right).

7.3 Upper-regime flat bed

The bed topography is a main factor determining flow resistance. It is therefore important to clarify the formation and dissipation mechanisms of dunes. Since transient phenomena like the formation and dissipation of sand waves occur during floods, it is necessary to clarify the effect of flow variations on the bed topography during floods.

Few experiments have been conducted to reproduce bedform evolution and transition processes under unsteady flow conditions. Sawai (1988); Izumi et al. (2003) performed laboratory experiments on transition processes from dunes to a flat bed. However, the experimental conditions considered did not lead to definitive conclusions. Sawai (1988), for instance, changed the experimental conditions by tilting the flume, instead of adjusting the discharge. This leads to a dramatic decrease in water depth by increasing the bulk velocity, which is not realistic in nature. The experiments conducted by Izumi et al. (2003) appear to be affected by ripples caused by very low flow velocities. A.Toyama and S.Giri (2009) conducted experiments to study the effect of flow variability on the bedform transition process. In these experiments, the discharge was varied stepwise, with a sudden change between consecutive discharge levels. Moreover, the experiments were conducted in a narrow flume, in order to enforce two-dimensional dunes. The abrupt change in discharge might have some additional effect on bedform evolution. The response of the bedform under the abrupt change (step hydrograph) cannot be generalized for bedforms under smooth hydrographs. Moreover, the side walls as well as the secondary flow had a significant effect on the bedforms. Recently, Nelson et al. (2011) carried out laboratory experiments with only two discharge levels to replicate rising and falling flow stages, and used the experimental observations to validate the numerical model proposed by Shimizu et al. (2009).

One of the most striking bedform transitions in response to an increasing flow intensity is the transition from a dune bed to a plane bed at high Froude numbers or high suspended sediment transport rates (Nelson et al., 2011) (because of suppression of turbulence by high near-bed sediment concentration, especially in the flow-separation zone as mentioned by Bridge and Best (1988)). As the flow intensity increases, bedforms decrease in amplitude and are eventually flattened out, resulting in a large decrease in form drag, hence in effective roughness. If the flow is subsequently decreased over the resulting flat bed, bedforms will reappear, but at a lower discharge than that at the time of bed flattening. This gives rise to another hysteresis effect in the stage-discharge relation during flood events, as discussed by Simons et al. (1961); Itakura et al. (1986); Julien et al. (2002) and many others. Using the Giri and Shimizu (2006) model for bedform evolution, Shimizu et al. (2009) were able to reproduce this behaviour. In the experimental study of Shimizu et al. (2009), the flume is so narrow (10 cm) that two-dimensional dunes are enforced. Moreover, the Giri and Shimizu (2006) model

Table 7.2: Simulated scenarios and conditions

Run	Duration (s)		
	Rising	Constant	Falling
R0	2000	8000	0
R1	2000	0	2000
R2	2000	1000	2000
R3	2000	2000	2000
R4	2000	3000	2000

is calibrated by adjusting the step length function, which reduces its predictive capability. Although this study confirms the capability of the model to describe two-dimensional bedform behaviour in time-varying flow, more advanced models are needed to predict this behaviour.

More recently, Hirai et al. (2011) conducted experimental studies on responses of bed topography to temporal flow changes. To some extent, they were able to generate a flat-bed regime after the formation of dunes. The applied discharge hydrograph varied stepwise with increasing and decreasing phases. Although they were able to generate a flat bed, the bed was not reproduced again after decreasing the discharge.

This section describes a number of numerical experiments to test the capability of the present to predict bedform evolution under varying discharge, including the transition to a flat bed and back. The numerical experiments concern a hypothetical flume of 2 m length, 1 m width and 0.4 m depth. To avoid side wall effects, the boundaries in spanwise direction are taken periodic. The boundaries in steamwise direction are also taken periodic and the flow is driven by a pressure gradient, such that the desired discharge hydrograph is achieved. In all simulations, a uniform sediment size of 400 μm is used. Table (7.2) shows the settings for the different model runs.

The starting point of each simulation is a flat bed under a relatively low discharge (0.12 m^3/s). Once the flow has reached its statistically steady state, we turn on the sediment transport and morphodynamic modules, and increase the discharge linearly in a time span of 2000 s to its maximum value of 0.48 m^3/s. Figure (7.12) shows the path of these simulations in the rising flow stage in the phase diagram of Southard and Boguchwal (1990). The maximum discharge for these simulations lies in the upper plane-bed regime. In the first simulation (R0), the discharge remains constant after reaching its maximum value. Figure (7.13) shows the hydrograph for this simulation. Figure (7.14) shows the bedform evolution during the rising stage and the following constant discharge, at 500, 1000, 1500, 2000, 2100, 2200, 2500 and 3000 s after the start of the mobile-bed run. As the discharge increases, first dunes start to appear, and subsequently high-frequency ripples are generated on the stoss sides of the dunes. These ripples cause a washout of the dunes, towards the upper-plane bed regime. Due to the time lag be-

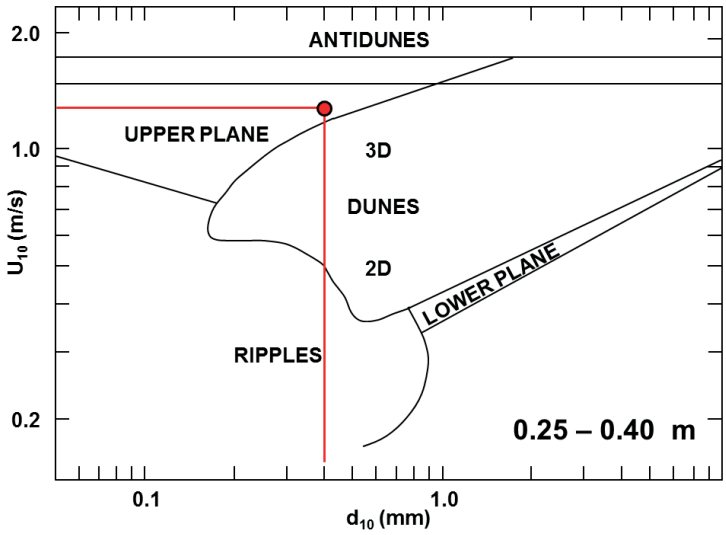

Figure 7.12: Path of the simulated cases in the rising flow stage in the phase diagram. The red point indicates the maximum flow discharge.

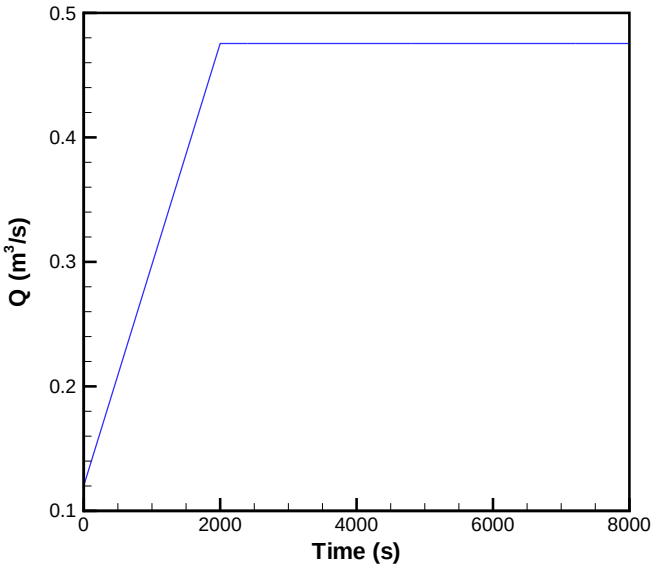

Figure 7.13: The hydrograph applied for run R0. The maximum value of the discharge falls in the upper plane-bed regime of the Southard phase diagram in Figure (7.12).

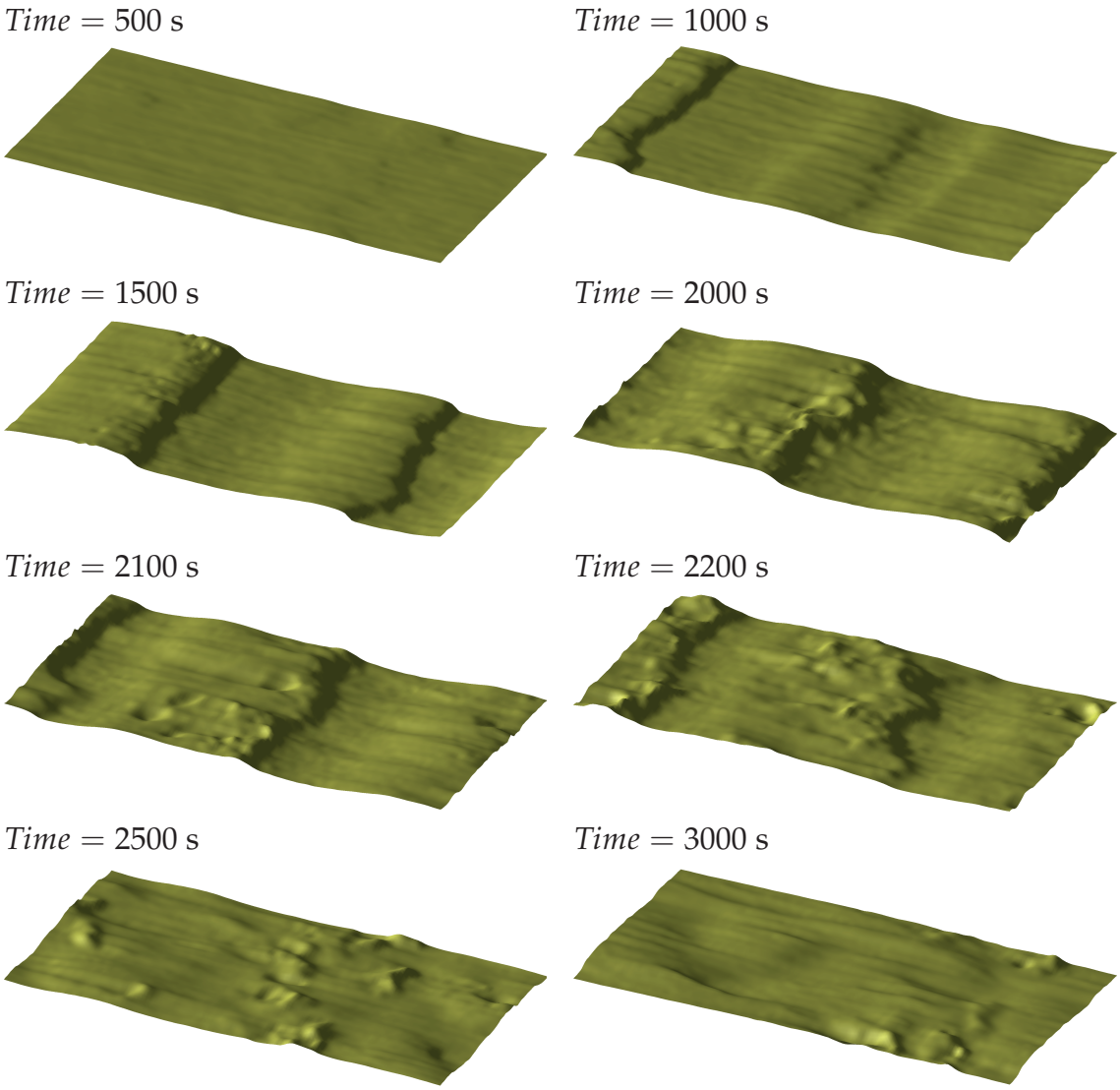

Figure 7.14: Bedform evolution under variable discharge for run R0. In the rising stage, dunes are generated and continue to grow. When the flow reaches the upper plane-bed regime, high frequency ripples are generated on the stoss sides of the dunes and they wash out the dunes.

tween the flow variations and the bed morphology, the bed needs time to adapt itself to that regime. After this transient stage, a flat bed is obtained.

Figure (7.15) shows the averaged dune height determined by the zero-crossing averaging technique described in Chapter 4. The dunes grow in height in the rising stage, but start losing height slightly before the discharge maximum is reached. This is because the point of maximum discharge falls inside the upper flat-bed region in Southard's phase diagram, which is reached already at a lower discharge (see Figure 7.12).

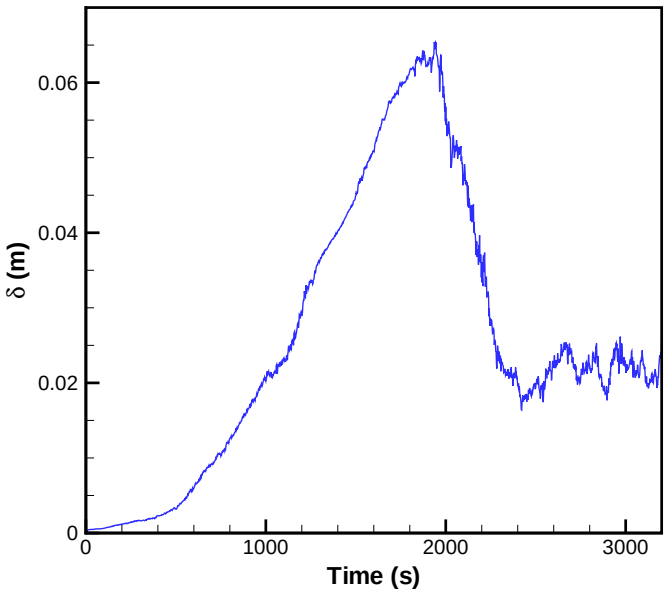

Figure 7.15: Average bedform height in R0. In the rising stage the height increases, in the constant discharge state (beyond 2000 s) the height decreases towards an almost flat bed.

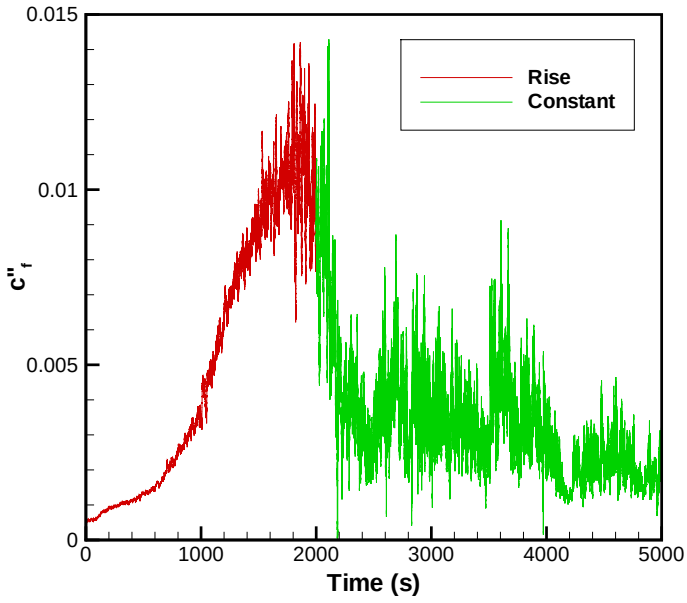

Figure 7.16: The form drag coefficient versus time in R0. When the height of dunes increases the form drag increases, in the constant discharge state (beyond 2000 s) the form drag decreases significantly because the dunes height decreases towards an almost flat bed.

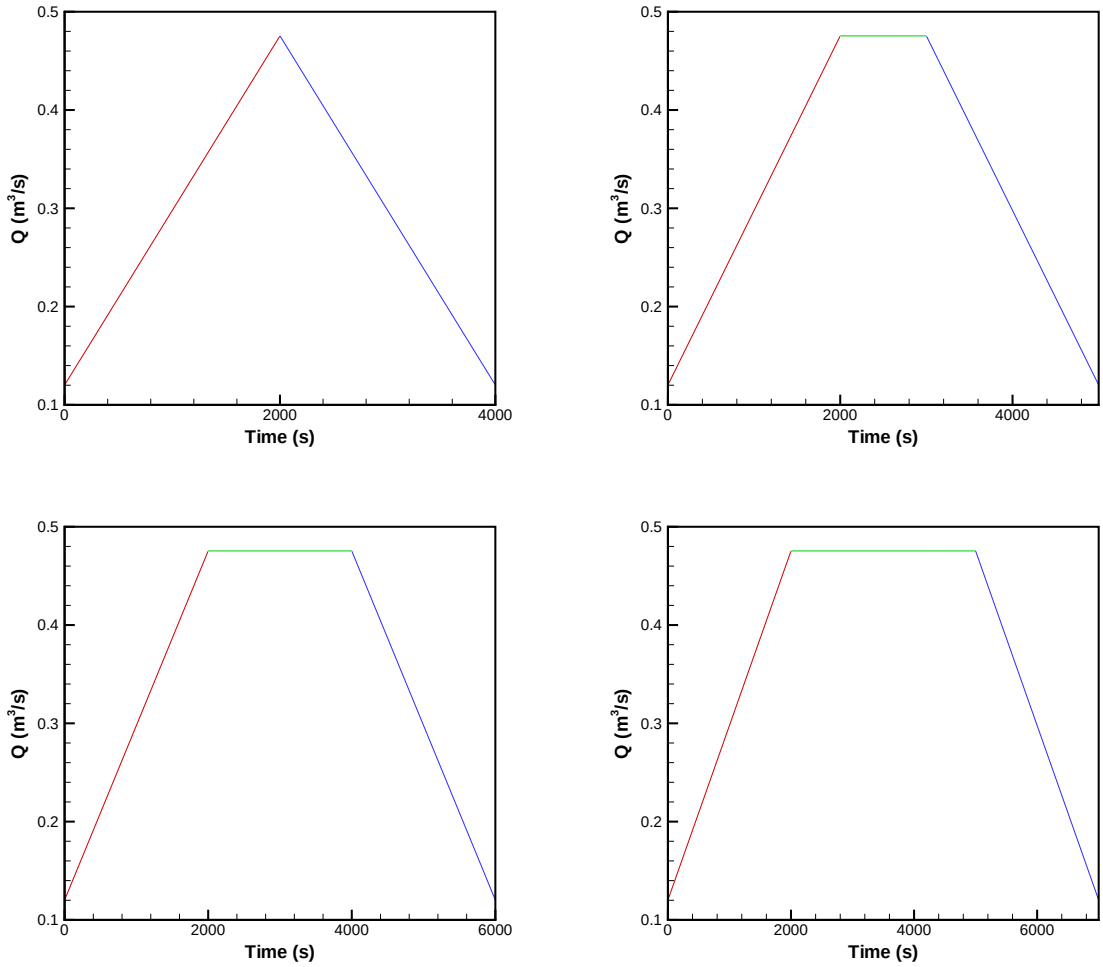

Figure 7.17: The hydrographs for runs R1 (top left), R2 (top right), R3 (bottom left) and R4 (bottom right).

Figure (7.16) shows the form drag coefficient c''_f in the rising stage and after the discharge gets constant. As the dunes grow in the rising stage, the form drag coefficient increases. By decreasing the dune height the form drag starts to decrease. In the constant discharge, as the dunes are washed out, the form drag coefficient drops significantly with a factor of 3 to 6 approximately. The form drag does not reach to zero because of existing high frequency ripple which lead to a small and fluctuating form drag.

In order to study bedform regeneration after flattening, we add a falling flow stage to the discharge hydrograph. Four numerical experiments R1, R2, R3 and R4 have been conducted, with the settings given in table (7.2). In case R1, the falling stage starts immediately after the rising flow stage, cases R2, R3 and R4 have a period of constant discharge in between. The duration of this period is

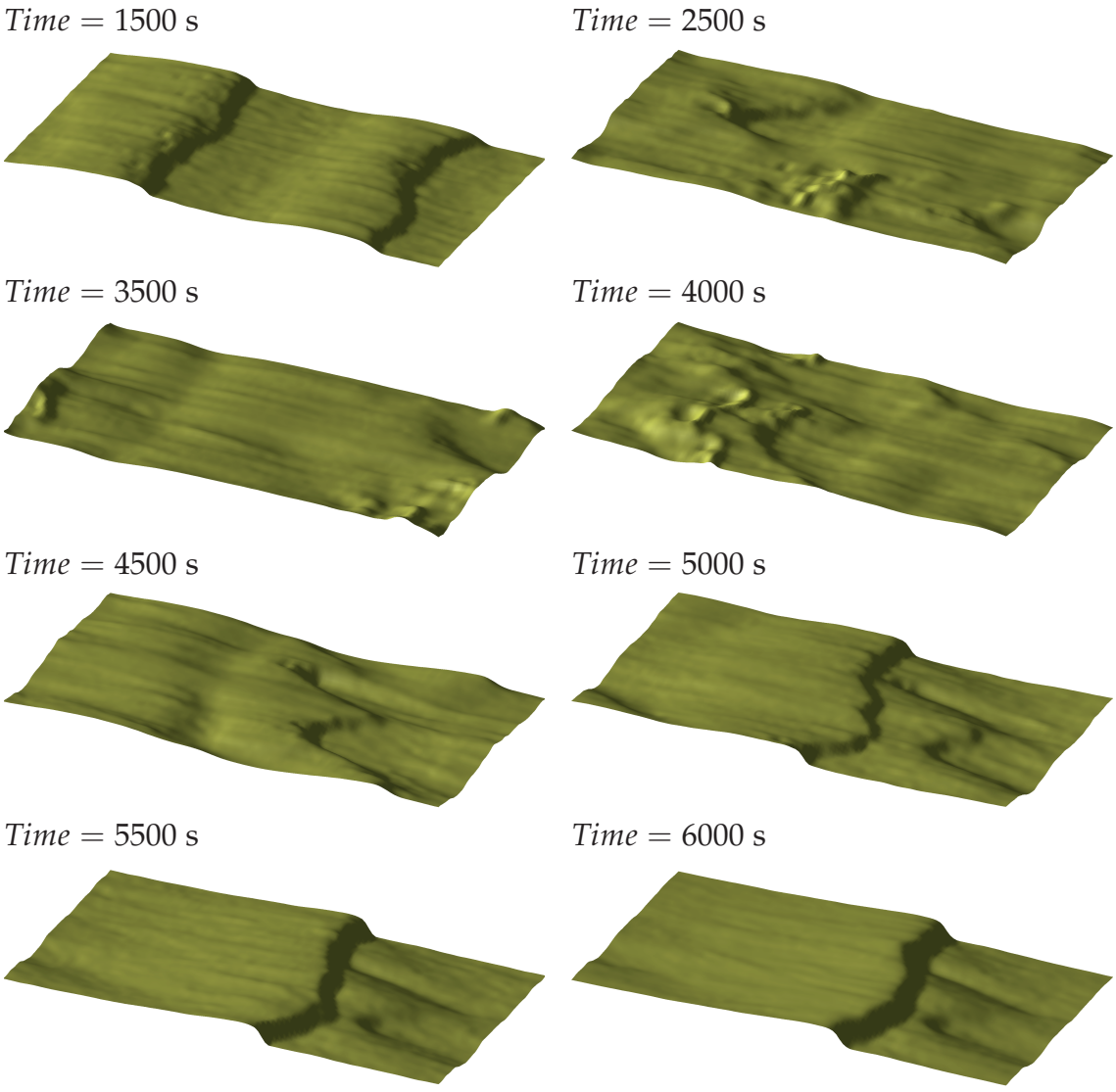

Figure 7.18: Evolution and migration of dunes under variable discharge for run R3. When the hydrograph is in the rising stage, dunes are generated. Under the constant discharge, the bed becomes flat and in the falling stage dunes are generated again.

1000, 2000 and 3000 s, respectively (Figure 7.14).

As an example, the bed topography in run R3 is shown in Figure (7.18). Similarly to Figure (7.14) the bedforms first grow and then disappear. In the falling stage, dunes begin to reappear. The regenerated dunes are higher than the dunes in the rising stage, because their generation starts under higher bed shear stress (from the maximum discharge). As the velocity gets smaller, the pick-up of sediment decreases and the dunes reach a steady state.

Figure (7.19) shows the average height of the dunes for runs R1, R2, R3 and

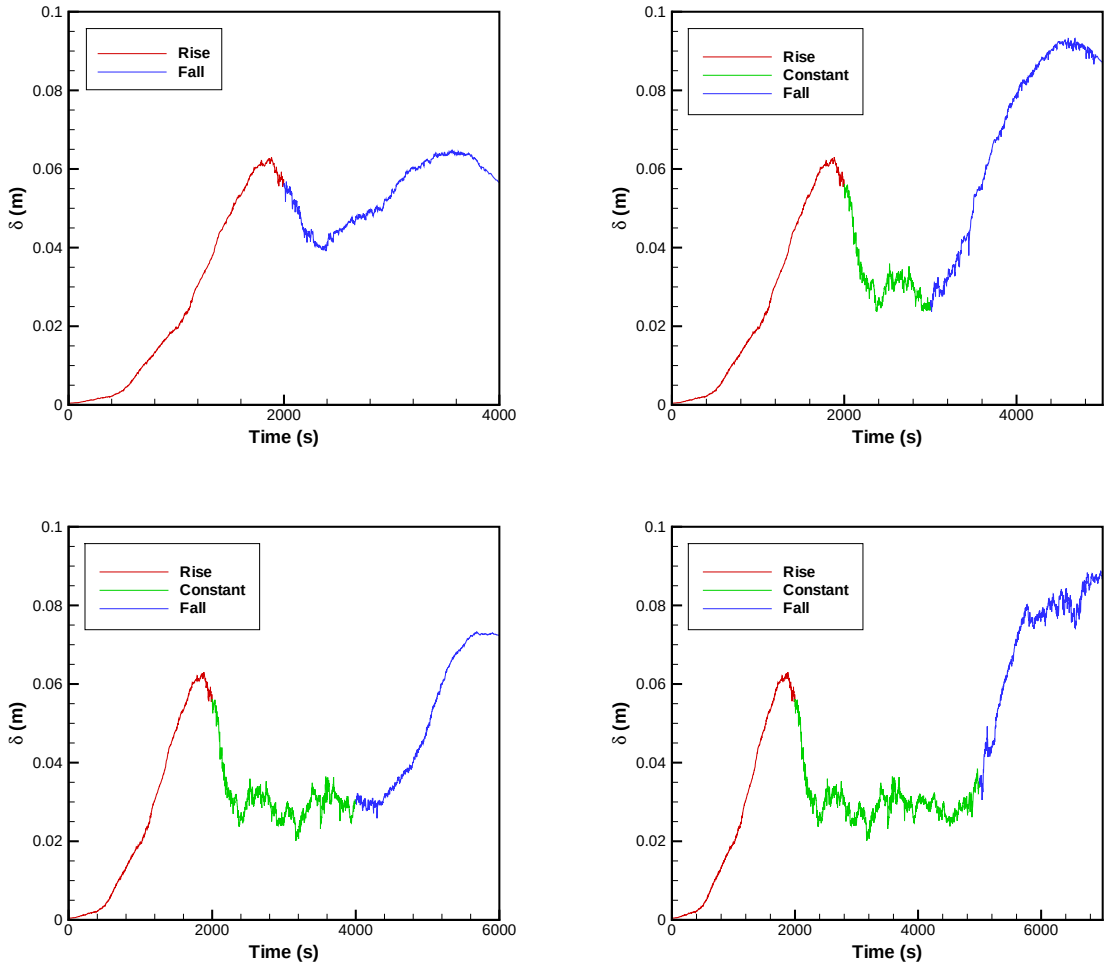

Figure 7.19: Average dune height for runs R1 (top left), R2 (top right), R3 (bottom left) and R4 (bottom right). The dune height decreases after the rising stage and increases again in the falling stage.

R4. For case R1, the falling flow stage is immediately after the rising flow stage, hence the bed has no time to be flattened completely. Before the dunes are completely washed out, the regeneration of dunes in the falling flow stage begins. For runs R2, R3 and R4, the dunes are washed out and later on, in the falling flow stage, higher dunes reappear. The remaining bedform height during the plane bed regime in R2, R3 and R4 does not concern dunes, but rather a combination of bed curvature and some high-frequency ripples, which are not filtered by the zero-crossing method.

In order to investigate the bedform behaviour if the hydrograph starts from a discharge value in the upper flat-bed regime and then falls to a lower discharge and stays constant there, another run was made: R5. This is a situation where

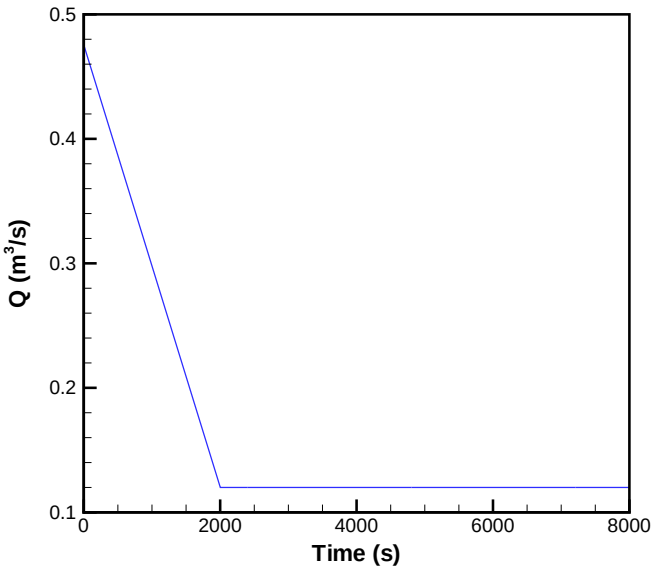

Figure 7.20: The hydrograph applied for run R5.

the flow discharge decreases from a flat-bed regime after the flood event, and later stays at a constant value. Figure (7.20) shows the hydrograph used. As the deformation of the bed begins at a high discharge, i.e. a high bulk velocity and a high bed shear stress, high-frequency ripples rapidly develop and die out again (Figure 7.22). Subsequently, as the discharge decreases, dunes begin to form. These dunes get higher and finally reach a steady state. This process is similar to that in the falling flow stage in runs R1 to R4.

Figure (7.21) shows the average dune height for run R5: the dunes first increase, reach a maximum and then decrease again. The height decay is slow, because the sediment pick-up rate is relatively low during low discharge. Yet, the bedforms finally reach a steady state.

7.4 Concluding remarks

The present model has been developed further to simulate the morphodynamics under unsteady discharges. Several numerical experiments with different grain sizes and different discharge hydrographs have been performed to analyse the hysteresis of drag under variable discharges. Our model results show that the bed can adapt itself to the discharge better in gradually varying discharges. Under rapidly varying discharge conditions, the bed does not have enough time to adapt to the flow variability.

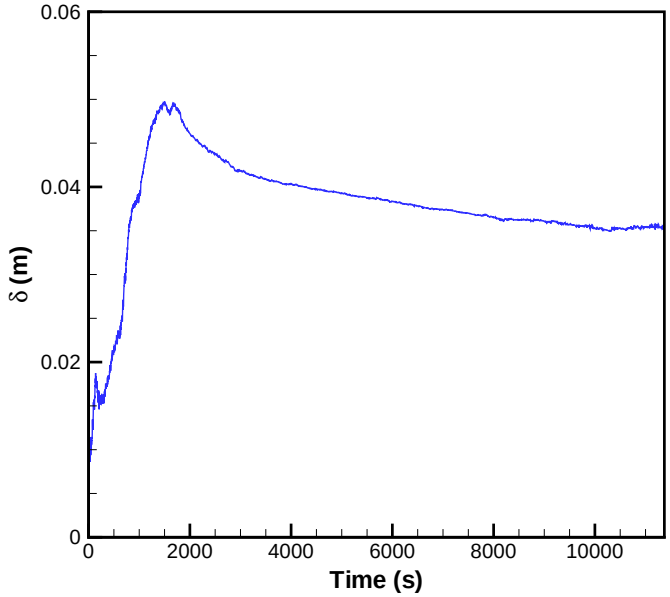

Figure 7.21: The average height of the dunes for run R5. In the falling stage, the height increases and reaches a maximum before the discharge has reached its minimum value. Later on, the dune height slowly decreases and finally reaches a steady state.

On the other hand, we observed that the size of sediment has a significant effect on the hysteresis of drag. Sediment with larger diameter enhances the hysteresis considerably. This is probably because of the difference between the particles relaxation time and the flow time scales. The large particles have a larger relaxation time. The time lag between flow and morphodynamics (which in effect determines the feature of hysteresis) appears to depend upon the difference between particle relaxation time and Kolmogorov time scale.

The hysteresis diagrams include instantaneous fluctuations for the cases with long-period hydrographs. This is because of the generation of ripples on the bed which are initially high in frequency. They change their form rapidly and produce fluctuating form drag.

The development of dunes and the associated hydraulic roughness during extreme events such as floods is complex. This situation has been simulated using different hydrograph forms, with combinations of increasing, constant and decreasing discharge. The discharge hydrograph and the size of sediment were chosen in such a way, that the peak discharge fell in the upper plane regime. The model generates growing dunes during the rising stage, but as the upper plane-bed conditions are reached, high frequency ripples are generated on the stoss side of the dunes. These ripples work in decreasing the height of dunes. The dunes start losing height and ultimately disappear. As the discharge decreases

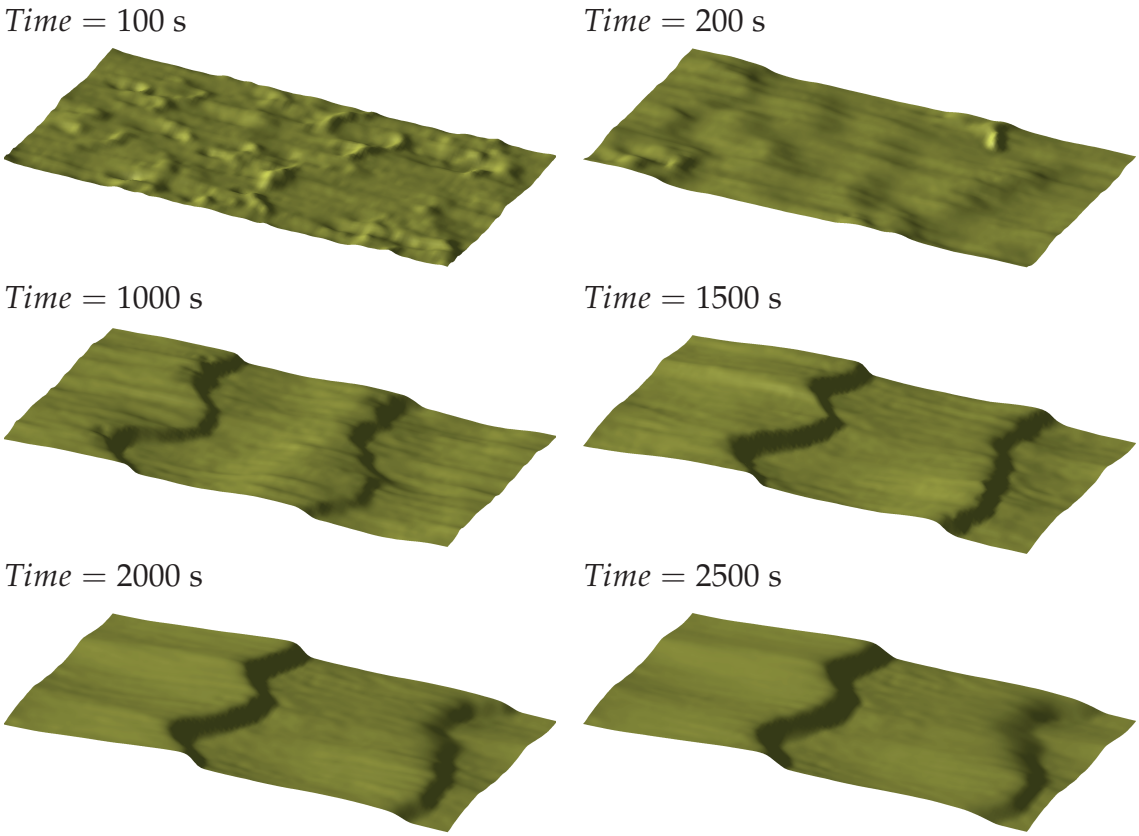

Figure 7.22: Evolution and migration of dunes under variable discharge for run R5. The bed first exhibits small high-frequency ripples. As the discharge decreases, dunes appear and grow until they reach a maximum and then slowly decay to a steady state.

again, dunes are regenerated in a realistic way. This provides confidence that the model can be used to extrapolate the existing knowledge on bedform behaviour to extreme flood events.

The studies in this chapter have been conducted to understand the response of bedforms to variable discharges. They could can be extended to derive parameterized relations for applications in flood mitigation design as well as in operational flood early warning systems.

Chapter 8

Conclusions and recommendations

This chapter summarizes the results of the present study; it is intended as a synthesis of the discussions already found in previous chapters. Section 8.1 gives an overview of the research procedure that has been followed. In section 8.2, conclusions stemming from the previous chapters are presented. Finally section 8.3 contains a number of recommendations and suggestions for further research.

8.1 General

This PhD study aims at a better insight into the mechanisms underlying bedform development and the corresponding hydraulic roughness in alluvial rivers, especially during floods. A proper understanding of these mechanisms allows for the development of parameterized models for larger spatial and temporal scales, to be used in operational models for flood early warning and the determination of design water levels. To that end, a detailed three-dimensional computational model has been developed that simulates river morphodynamics by employing a multiscale technique based on coupling a finite-volume method with a discrete particle method. The numerical model consists of three modules, describing hydrodynamics, sediment transport and morphodynamics.

8.1.1 Hydrodynamic module

The hydrodynamic module consists of an eddy-resolving model of turbulent flow using computationally efficient techniques capable of simulating detailed hydrodynamics. Accurate prediction of bedform evolution and migration requires an accurate flow prediction, including coherent turbulence structures. This is achieved using a finite-volume method combined with an isotropic unstructured Cartesian grid. The grid can be locally refined and adapted to the actual bed topography. The governing equations are discretized using a staggered grid and their solution is advanced in time using the fractional-step method. A ghost-

cell immersed-boundary technique has been implemented for the cells which intersect the immersed boundaries. In order to include the effects of coherent turbulence structures on sediment transport, the turbulence regime is modelled using Large Eddy Simulation (LES).

8.1.2 Sediment transport module

The motion of sediment generally consists of three stages: (1) the particles begin to move (pick-up), (2) they get transported (moving in the water column or sliding over the bed), and (3) are deposited at other locations. These stages are all governed by gravitational and flow-induced forces, which are simulated using theoretical and empirical relations.

The sediment transport module describes the motion of discrete particles. It involves modelling of sediment pickup, transport, deposition and sliding in a Lagrangian framework. The modelling is based on new concepts that are best suited for relatively small spatial and temporal scales (Schmeeckle and Nelson, 2003). The sediment particles are modelled as small rigid spheres in the water. This approach gives a better insight into the physical transport phenomena and makes it possible to simulate details of the sediment motion, such as jumping, sliding and rolling.

8.1.3 Morphodynamics

This module involves morphological modelling for bed-form evolution such as growth, decay and migration by implementing the pickup and deposition of sediment resulting from the sediment transport module.

The modules for hydrodynamics, sediment transport and morphodynamics are coupled to simulate time-dependent morphological processes in a physics-based way. The model results agree well with analytical solutions, experimental data, empirical relationships and observations published in the literature. The model has the potential to constitute the basis for bed roughness and bed load transport parameterization under steady and unsteady flow conditions. Thus it opens perspectives to important steps forward in fluvial and estuarine morphodynamics and engineering.

8.2 Conclusions

The hydrodynamics model has been validated against a number of well-documented flow cases:

1. An analytical solution of Stokes flow including source terms, to verify the order of accuracy of the model. The $\mathcal{L}_2$ norm shows second-order accuracy of the velocities and first-order accuracy of the pressure field.

2. Wannier flow to validate the applied ghost-cell immersed boundary technique. Again, second-order accuracy was shown for the velocity field.

3. Flow around a cylinder at different Reynolds numbers, to test the boundary layer treatment and the generation of complex flow structures such as von Kármán vortex street. The results for the length of the trailing bubble, the angle of separation, and the drag coefficient agree well with published results.

4. Driven cavity flow in a cube to test and validate the model in three-dimensional flows with recirculations and secondary flows. This validation shows the results agree well with published results.

5. Flow over a fixed smooth bed to test the capability of the model in resolving the boundary layer and the generation of a log-law velocity profile. The model was capable of capturing the log-law velocity profile.

6. Flow over a wavy bed to test the capability of the model in solving the flow over complex geometries, such as a rippled bed. A good agreement with past investigations was observed.

7. Flow over a two-dimensional fixed dune to test the capability of the model in generating strong recirculation zones behind the lee side and to validate the present numerical results with published results. The results fit well with the results provided by Yue et al. (2006).

8. Flow over fixed two- and three-dimensional dunes, which was shown to agree well with experimental data from literature. Although there is a lack of quantitative data available from experimental studies, it is shown that the model can produce results, at least, qualitatively similar to the measured data.

Moreover, the form drag for steady flow over two- and three-dimensional fixed dunes was computed and parameterized relations were derived. The resulting relations agree with the ones proposed by Yalin (1964); Engelund (1966, 1977); Van der Mark (2009).

The sediment transport model has been validated for various well-documented aspects, such as the settling velocity of a single particle in stagnant water, the angle of repose after avalanching, and the bulk flux and the suspended sediment concentration profile in uniform flow. In all cases, the model results agree well with known formulae and relations. As this model is to be used in small-scale morphodynamic simulations, this type of process-oriented validation is necessary, but not sufficient. Therefore, the sediment transport model in combination with the flow model and the sediment balance has also been validated against morphological information, such as bedform observations

In order to validate the morphodynamics model, four different experiments with steady flow were simulated. The model results were found to agree well with the experimental findings. When considering the time evolution of dune length and height, merging of smaller and larger bedforms was found to yield irregularities in the evolution.

When changing the sediment grain size while keeping all other conditions the same, a smaller grain size was found to generate more and smaller ripples. As the sediment size increases, these ripples disappear and dunes become dominant.

The bed morphology has been further simulated for variable discharge conditions, to study bedform and bed roughness evolution and the associated hysteresis effects. Hysteresis is shown for different types of hydrographs and is more pronounced if the rising and falling stages of the hydrograph have a relatively longer duration. This phenomenon becomes less valid for very long hydrograph durations. If the discharge changes very slowly, the bedforms can adapt to the flow conditions and the hysteresis effect may disappear. The sediment size also has a significant effect on the hysteresis: for coarser sediment the hysteresis loop becomes more pronounced. The hysteresis is found to be caused by the time lag between flow and bedform variation.

The development of dunes and the associated hydraulic roughness during extreme events such as floods is complex. Initially dunes grow higher and make the river bed rougher, but in later stages the dunes grow longer and make the river bed smoother again. Then, new bedforms may develop on top of the elongated dunes that make the river bed rougher again. These situations have been simulated using different hydrograph forms, with combinations of increasing, constant and decreasing discharge. The peak discharge and the size of sediment are chosen such, that they fall in the upper plane regime. Starting from a flat bed, the model generates growing dunes during the rising stage, but when the upper plane-bed conditions are reached, the dunes start losing height and ultimately disappear. As the discharge decreases again, dunes are regenerated in a realistic way. This provide confidence that the model can be used to extrapolate the existing knowledge on bedform behaviour to extreme flood events.

Finally, we can conclude that we have developed a sophisticated, physics-based, high-resolution and well-validated numerical model that can rightfully be claimed to describe bedform behaviour in rivers. This model can be used as a basis for parameterizations to be used in simpler, less computationally intensive models, and it can serve as a starting point for the incorporation of other physical effects, some of which are discussed below.

8.3 Suggestions for future research

Notwithstanding the results achieved and the knowledge acquired in this study, many issues remain unaddressed or unresolved. Here we mention some of them.

8.3.1 Bed morphodynamics in curved channels

Most natural rivers tend to meander and develop curved channels. The spiral flow in a bend has important effects on the bed morphology, not only by causing a cross-stream slope, but also by affecting the bedforms (e.g. oblique dunes). So far, few attempts have been made to study the morphodynamical behaviour of the bed in curved alluvial channels in a way that addresses both cross-stream slopes and bedforms. Consequently, the behaviour of ripples and dunes in curved channels remains to be fully understood.

The current numerical model can be employed to study these phenomena. The ghost-cell immersed-boundary technique, when applied to the banks, allows to follow any channel alignment, including bends. Hence there is no need to extend the present Cartesian approach with some kind of curved boundary-fitted grid system.

8.3.2 Morphodynamics under tides and waves

Combinations of (quasi-)steady and oscillatory flows commonly occur in coastal, lake, sea, and continental shelf environments and generate bedforms on sandy bottoms. In turn, the presence of dunes and ripples create hydraulic roughness felt by currents and waves. The bedforms also change the turbulence levels in the vicinity of the bed, thus affecting the transport of sediment and substances. All these facts point towards the strong couplings between surface waves, mean currents, sediment transport and bed morphology. Oscillatory flow ripples have intrigued researchers for more than a century, but many aspects remain to be understood. The present model, though restricted by its rigid-lid approximation, can help shedding more light on these phenomena.

On the other hand, from a geological point of view, not only the size but also the topography of bedforms is important in order to interpret sedimentary structures found in the subsoil. To the author's knowledge, no numerical studies have been made on the relationship between hydrodynamic conditions, bedform development and stratigraphy. The model presented here, extended with a bed stratigraphy module, can help addressing this kind of issues based on first physical principles.

8.3.3 Morphodynamics with non-uniform sediment

The beds of natural rivers are composed of various sizes of sediment grains, in other words, nonuniform sediment. Under identical flow conditions, coarse grains respond less strongly to the forces exerted by the water motion than the fine grains and slide further down steep slopes. Therefore, selective transport occurs, which produces many morphological processes such as vertical sorting, armouring and downstream fining. These phenomena cannot be captured by

a model with uniform sediment. The current model can easily be extended to graded sediments, provided that hiding and exposure are modelled and that a bed sediment composition administration module is included.

8.3.4 Bed morphodynamics at high Froude numbers

The free water surface has been shown to have a negligible effect on bed morphodynamics at relatively low Froude numbers (Niemann et al., 2011). As the Froude number increases, however, bedforms can be affected by accompanying undulations of the water surface. At higher Froude numbers, called the upper regime, first a plane bed establishes, characterized by a large bed-material transport rate and a relatively small flow resistance. As the flow gets even stronger, antidunes begin to form with upstream breaking waves over the dune crest. This type of bed is typically followed by the formation of a pool and chute topography. Few attempts have been made to model the morphodynamic behaviour under this kind of flow regimes. There is still limited knowledge regarding bedform behaviour at high Froude numbers and under supercritical flow conditions.

The current model does not include free surface effects, whence it is limited to low Froude number morphodynamics. Free-surface features could be added to the current model to be able to study the morphodynamics under near-critical as well as supercritical flows, but this extension is not entirely trivial, especially in the case of breaking waves.

8.3.5 Morphodynamics under laminar flow regime

Yalin (1992) attributes the formation of alluvial dunes and bars to bursting processes associated with the turbulent nature of the flow. Raudkivi and Witte (1990) contended that, but admitted that the initiation of bedforms must be associated with turbulence, since no ripples are formed in laminar flow. Raudkivi (1997) suggested that the initiation of ripples can probably be ascribed to turbulent bursting processes that exhibit certain orders. In contrast, Yalin (1992) claims that ripples are due to the viscous structures at the bed, defining ripples as the bed forms imprinted by viscous flow instabilities (undulations) at the bed of an otherwise turbulent flow. Coleman and Eling (2000) carried out experiments showing bedforms under laminar flow and argued that sand waves may form under laminar flow and that dune formation is therefore not associated with turbulence. The question arises, however, whether the flow in the experiments of Coleman and Eling (2000) is purely laminar, even in the vicinity of the bed.

Generation of purely laminar flow in the laboratory is a difficult task, but in a numerical model it is easily done. Thus one can investigate whether the dunes are the effect of turbulence or not. Although this study has no practical application as the flow in the field is always turbulent, it may give better insight into the physical phenomena associated with the generation of ripples and dunes.

8.3.6 Barchan ripples and dunes

As natural river beds consist of non-uniform sediment, it may happen that that the water flow picks up only sediment finer than a certain size. Fine sediment may be washed out and the remaining coarse sediment may cause an armouring effect. The sediment pickup will be limited and the morphological process will change to a process with limited supply of sediment. Similar situations occur when sediment is transported over a fixed layer, such as rockfill. Under a limited supply of sediment, the sediment particles tend to accumulate in so-called barchan dunes. The behaviour of barchan dunes is significantly different from that of normal mobile-bed dunes.

The current model can be employed to sediment transport over a fixed substrate and the generation of the corresponding bedforms. The only necessary modification is imposing a limited availability of sediment at the bed, depending on the deposition record.

8.3.7 Sediment transport on oblique dunes

In order to improve the prediction of river bend morphology, the influence of oblique dunes on the bed-load transport direction is to be quantified. Obliquely oriented dunes have been observed in laboratory experiments and have also been found by sidescan sonar measurements in natural rivers and estuaries. In such situations, dune crest orientations may deviate significantly (tens of degrees) from the direction perpendicular to the flow.

The flow in the lee of oblique dunes exhibits helical motion, instead of plane recirculation (Sieben and Talmon, 2011). This motion pulls the bed load sediment in cross-stream direction (in addition to a similar effect of sediments avalanching down the oblique slip face). The morphological behaviour in this kind of situations may differ significantly from that in a straight channel.

The flow and sediment transport on oblique dunes can be studied with the present model. A good understanding of this phenomenon will provide better insight into morphological processes in spatially non-uniform situations, like in river bends, but also in the vicinity of all kinds of engineering structures, such as groynes and bridge piers.

8.3.8 Step length of sediment

Einstein (1950) proposed a formulation for mean step length as $\Lambda = \alpha d$, in which Λ is the mean step length, d is the sediment diameter and α is an empirical constant. This simply suggests that particle trajectories in bed load transport are proportional to the grain size of the transported material. However, the mean step length is not a function of the grain diameter only. Grigg (1970) showed that particle trajectories were longer for longer dunes, even for identical grain

sizes. Observations of bed load motion suggest that, as boundary shear stress increases, there is a transition from no motion, to rolling, to saltation, indicating an increase in trajectories with increasing stress (Shimizu et al., 2009). Essentially all simple models for grain saltation suggest that grains go higher, faster, and farther as boundary shear stress or local flow velocities increase.

The exact relation between the mean step length and the flow condition (i.e. local shear stress) is still unknown. In the existing numerical models employed by Giri and Shimizu (2006) the mean step length is considered as a function of diameter only, and Giri and Shimizu (2006) calibrated the empirical coefficient α under steady flow. The coefficient α is not constant and varies strongly, especially in time-varying flow. To overcome this deficiency Shimizu et al. (2009) linked this coefficient to the local bed shear stress by a simple linear relation based on observations of Nelson et al. (2008). As the experiments conducted by Nelson et al. (2008) were rather limited (two experimental conditions), the real relation may easily deviate from this simple formulation.

The current model can handle sediment transport in a physics-based way and enables simulating the sediment transport under different flow conditions and deriving a parameterized relation to be employed in other, less detailed models.

References

Aftosmis, M. J., Berger, M. J., and Melton, J. E. (1998). Robust and efficient Cartesian mesh generation for component-based geometry. *AIAA Journal*, 36(6):952–960. doi:10.2514/2.464.

Allen, J. R. L. (1965). Sedimentation to the lee of small underwater sand waves: An experimental study. *J. Geology*, 73:95–116.

Allen, J. R. L. (1968). *Current ripples*. North Holland Publishing Company, Amsterdam,.

Armenio, V. and Fiorotto, V. (2001). The importance of the forces acting on particles in turbulent flows. *Phys. Fluids*, 13:2437–40.

Ashley, G. M. (1990). Classification of large-scale subaqueous bedforms: A new look at an old problem. *Journal of Sedimentary Petrology*, 60:160–172.

A.Toyama, S.Yamaguchi, Y. I. and S.Giri (2009). Experiments on bed form development and transition process under varying discharge. In *Proceedings of the 6th IAHR symposium on River, Coastal and Estuarine Morphodynamics (RCEM2009)*, pages 643–650, Santa Fe, Argentina. Universidad Nacional Del Litoral.

Auton, T. R. (1987). The lift force on a spherical body in a rotational flow. *J. Fluid Mech.*, 183:199–218.

Baas, J. H. (1999). An empirical model for the development and equilibrium morphology of current ripples in fine sand. *Sedimentology*, 46:123–138.

Bakker, B., Struijk, A. J., and Nijdam, H. (1986). Flume experiments on dunes under steady flow conditions (uniform sand, $D_m = 0.77\,\mathrm{mm}$), description of bed forms. Technical report volume I-III, TOW rivers R 657 - XIX / M 1314 part VIII, WL | Delft Hydraulics, Delft, the Netherlands.

Balachandar, R., Polatel, C., Hyun, B. S., Yu, K., Lin, C. L., Yue, W., and Patel, V. C. (2002). LDV, PIV, and LES investigation of flow over a fixed dune. In *Sedimentation and Sediment Transport*, Proc. Symp., Monte Verita, Switzerland. Kluwer Academic, Dordrecht, The Netherlands.

Balaras, E. (2004). Modeling complex boundaries using an external force field on fixed Cartesian grids in large-eddy simulations. *Computers & Fluids*, 33:375–404.

Barr, C. B., Slinn, D. N., Pierro, T., and Winters, K. B. (2004). Numerical simulation of turbulent, oscillatory flow over sand ripples. *J. Geophys. Res.*, 109. C09009, doi:10.1029/2002JC001709.

Batchelor, G. K. (2000). *An introduction to fluid dynamics*. Cambridge Mathematical Library. Cambridge University Press.

Bayyuk, S. (1996). *Euler flows with arbitrary geometries and moving boundaries*. Phd thesis, Dept. of Aero. and Mech. Eng., Univ. of Mich.

Benjamin, T. B. (1959). Shearing flow over a wavy boundary. *J. Fluid Mech.*, 6:161–205.

Bennett, S. J. and Best, J. (1996). Mean flow and turbulence structure over fixed ripples and the ripple-dune transition. In Ashworth, P. J., Best, J. L., and McLelland, S. J., editors, *Coherent Flow Structures in Open Channels*, pages 281–304. John Wiley and Sons Ltd.

Berger, M., Aftosmis, M. J., and Murman, S. M. (2005). Analysis of slope limiters on irregular grids. In *43rd AIAA Aerospace Sciences Meeting*, Reno, NV.

Berger, M. J., Aftosmis, M. J., and Adomavicius, G. (2000). Parallel multigrid on Cartesian meshes with complex geometry. In *Proceedings of the Parallel CFD Conference 2000*, Trodheim, Norway.

Best, J. (2005). The fluid dynamics of river dunes: A review and some future research directions. *Journal of Geophysical Research*, 110. F04S02, doi:10.1029/2004JF000218.

Best, J., Bennet, S., Bridge, J., and Leeder, M. (1997). Turbulence modulation and particle velocities over flat sand bed at low transport rate. *J. Hydraul. Eng.*, 123(12):1118–29.

Blom, A., Ribberink, J. S., and de Vriend, H. J. (2003). Vertical sorting in bed forms: Flume experiments with a natural and trimodal sediment mixture. *Water Resources Research*, 39(2):1025.

Brandt, A. (1977). Multi-level adaptive solutions to boundary-value problems. *Mathematics of Computation*, 31:333–390.

Brandt, A. and Yavneh, I. (1992). On multigrid solution of high-Reynolds incompressible entering flows. *Journal of Computational Physics*, 101:151–164.

Bridge, J. S. (2003). *Rivers and floodplains: Forms, processes, and sedimentary record*. Blackwell Publishing, Malden, MA.

Bridge, J. S. and Best, J. L. (1988). Flow, sediment and bedform dynamics over the transition from dunes to upper-stage plane beds: implications for the formation of planar laminae. *Sedimentology*, 35:753–763.

Brown, C. B. (1950). Sediment transportation. In Rouse, H., editor, *Engineering Hydraulics*, volume Chap. XII, New York, N.Y. John Wiley and Sons, Inc.

Calhoun, D. (2002). A cartesian grid method for solving the two-dimensional streamfunctionvorticity equations in irregular regions. *Journal of Computational Physics*, 176(2):231–275.

Capizzano, F. (2007). A compressible flow simulation system based on Cartesian grids with anisotropic refinements. In *45th AIAA Aerospace Sciences Meeting and Exhibit*, AIAA-2007-1450, Reno, Nevada.

Carling, P. A. (1999). Subaqueous gravel dunes. *Journal of Sedimentary Reserch*, 69:534–545.

Carling, P. A., Gölz, E., Orr, H. G., and Radecki-Pawlik, A. (2000a). The morphodynamics of fluvial sand dunes in the River Rhine near Mainz, Germany, Part I: Sedimentology and morphology. *Sedimentology*, 47:227–252.

Carling, P. A., Williams, J. J., Gölz, E., and Kelsey, A. D. (2000b). The morphodynamics of fluvial sand dunes in the River Rhine near Mainz, Germany, Part II: Hydrodynamics and sediment transport. *Sedimentology*, 47:253–278.

Cheng, N. S. and Chiew, Y. M. (1998). Pick-up probability for sediment entrainment. *Journal of Hydraulic Engineering, ASCE*, 124(2):232–235.

Clarke, D., Salas, M., and Hassan, H. (1986). Euler calculations for multi-element airfoils using Cartesian grids. *AIAA Journal*, 24.

Coirier, W. J. and Powell, K. G. (1996). Solution-adaptive Cartesian cell approach for viscous and inviscid flows. *AIAA Journal*, 34:938–945.

Coleman, N. L. (1967). A theoretical and experimental study of drag and lift forces acting on a sphere resting on a hypothetical stream bed. In *Proc. 12th IAHR Congr.*, volume 3, pages 185–192, Fort Collins, Colorado.

Coleman, S. E. and Eling, B. (2000). Sand wavelets in laminar open-channel flows. *J. Hydraulic Res.*, 38(5):331–338.

Coleman, S. E. and Melville, B. W. (1994). Bed form development. *J. Hydraul. Res.*, 120(4):544–560.

Coleman, S. E. and Melville, B. W. (1996). Initiation of bedforms on a flat sand bed. *J. Hydraul. Res.*, 122(6):301–310.

Coutanceau, M. and Bouard, R. (1977). Experimental determination of the main features of the viscous flow in the wake of a circular cylinder in uniform translation. *Journal of Fluid Mechanics*, 79(2):231256.

Crosato, A., Mosselman, E., Desta, F. B., and Uijttewaal, W. S. J. (2011). Experimental and numerical evidence for intrinsic nonmigrating bars in alluvial channels. *Water Resources Research*, 47. W03511, doi:10.1029/2010WR009714.

Dalrymple, R. W. and Rhodes, R. N. (1995). Estuarine dunes and bars. In Perillo, G. M. E., editor, *Geomorphology and Sedimentology of Estuaries*, pages 359–422, Amsterdam. Elsevier.

Darby, S. E., Alabyan, A. M., and Van de Wiel, M. J. (2002). Numerical simulation of bank erosion and channel migration in meandering rivers. *Water Resour. Res.*, 38(9):1163. doi:10.1029/2001WR000602.

De Ruiter, J. C. C. (1982). The mechanism of sediment transport on bed forms. In *Proceeding Euromech Conference 156*, Tech. Univ. of Istanbul, Istanbul, Turkey.

De Ruiter, J. C. C. (1993). Incipient motion and pick-up of sediment as function of local variables. Technical Report R 657-XI, Delft Hydraulics Laboratory, Delft, the Netherlands.

Dennis, S. C. R. and Chang, G. Z. (1970). Numerical solutions for steady flow past a circular cylinder at Reynolds numbers up to 100. *Journal of Fluid Mechanics*, 42(3):471–489.

Dey, S. (1999). Sediment threshold. *Applied Mathematical Modelling*, 23:399–417.

Dey, S. and Debnath, K. (2000). Influence of streamwise bed slope on sediment threshold under stream flow. *Journal of Irrigation and Drainage Engineering*, 126(4):255–263.

Dey, S. and Papanicolaou, A. (2008). Sediment threshold under stream flow: A state-of-the art review. *KSCE Journal of Civil Engineering*, 12(1):45–60.

Dinehart, R. L. (1989). Dune migration in a steep, coarsebedded stream. *Water Resources Research*, 25:911–923.

Donea, J. and Huerta, A. (2003). *The finite element method for flow problems*. John Wiley & Sons, Chichester (UK).

Drew, D. A. (1978). The force on a small sphere in slow viscous flow. *J. Fluid Mech.*, 88:393–400.

Einstein, H. A. (1950). The bedload function for sediment transportation in open channel flow. Tech. Bull. 1026, U.S. Dep. of Agric., Washington, D. C.

Einstein, H. A. and Barbarossa, N. L. (1952). River channel roughness. *Trans. ASCE*, 117:1121–46.

Einstein, H. A. and El-Samni, E. A. (1949). Hydrodynamic forces on rough wall. *Rev. Modern Phys.*, 21(3):520–524.

Engelund, F. (1966). Hydraulic resistance of alluvial streams. *J. Hydr. Eng. Div.*, 92(HY2).

Engelund, F. (1970). Instability of erodible beds. *J. Fluid Mech*, 42:225–244.

Engelund, F. (1977). Hydraulic resistance for flow over dunes. Progress report 44, Institute for Hydrodynamic and Hydraulic Engineering, Technical University Denmark.

Engelund, F. and Fredsøe, J. (1982). Sediment ripples and dunes. *Annu. Rev. Fluid Mech.*, 14:13–37.

Fadlun, E. A., Verzicco, R., Orlandi, P., and Mohd-Yusof, J. (2000). Combined immersed-boundary finite-difference methods for three-dimensional complex flow simulations. *Journal of Computational Physics*, 161:35–60.

Fernandez, F., Best, J., and Lopez, F. (2006). Mean flow, turbulence structure, and bed form superimposition across ripple-dune transition. *Water Resources Research*, 42. W05406, doi:10.1029/2005WR004330.

Flemming, B. W. (1988). Zur klassifikation subaquatistischer, stromungstrans versaler transportkorper. *Boch. Geol. U. Geotechn. Arb.*, 29:44–47.

Fornberg, B. (1980). A numerical study of steady viscous flow past a circular cylinder. *Journal of Fluid Mechanics*, 98(4):819–855.

Fredsøe, J. (1974). On the development of dunes in erodible channels. *J. Fluid Mech.*, 64:1–16.

Fredsøe, J. (1982). Shape and dimensions of stationary dunes in rivers. *J. Hydraul. Div. Am. Soc. Civ. Eng.*, 108(8):932–947.

Fredsøe, J. (1996). The stability of a sandy riverbed. In Nakato, T. and Ettema, R., editors, *Issues and Directions in Hydraulics*, pages 99–113. A. A. Balkema, Brookfield, Vt.

Fredsøe, J. and Tjerry, S. (2001). Morphological computation of dunes. In *Symposium on River, Coastal and Estuarine Morphodynamics*, Int. Assoc. for Hydraul. Res., Obihiro, Japan.

Gabel, S. L. (1993). Geometry and kinematics of dunes during steady and unsteady flows in the Calamus River, Nebraska, USA. *Sedimentology*, 40:237–269.

Ghosal, S., Lund, T. S., Moin, P., and Akselvoll, K. (1995). A dynamic localization model for large-eddy simulation of turbulent flow. *J. Fluid Mech.*, 286:229–255.

Gibson, A. H. (1910). On the flow of water through pipes and passages having converging or diverging boundaries. *Proc. of the Royal Society of London*, 83(563):366–376. Series A.

Gilmanov, A., Sotiropoulos, F., and Balaras, E. (2003). A general reconstruction algorithm for simulating flows with complex 3D immersed boundaries on Cartesian grids. *Journal of Computational Physics*, 191:660–669.

Giri, S. and Shimizu, Y. (2006). Numerical computation of sand dune migration with free surface flow. *Water Resources Research*, 42(10). W10422, doi:10.1029/2005WR004588.

Giri, S., Shimizu, Y., Yamaguchi, S., and Nelson, J. (2007). Simulating temporal response of bedform characteristics to varying flows. In *Proc. of Int. Conference on River, Coastal and Estuarine Morphodynamics*, pages 939–947.

Goda, K. (1979). A multigrid technique with implicit difference schemes for calculating two or three-dimensional cavity flows. *J. Comp. Phys.*, 30:76–95.

Grigg, N. S. (1970). Motion of single particles in alluvial channels. *J. Hydraul. Div. Am. Soc. Civ. Eng.*, 96:2501–2518.

Grigoriadis, D. G. E., Balaras, E., and Dimas, A. A. (2009). Large-Eddy Simulations of unidirectional water flow over dunes. *J. Geophys. Res.*, 114. F02022, doi:10.1029/2008JF001014.

Guy, H. P., Simons, D. B., and Richardson, E. V. (1966). Summary of alluvial channel data from flume experiments, 1956-1961. *USGS Professional Paper*, 462-I:1–96.

Ham, F. E., Lien, F. S., and Strong, A. B. (2002). A Cartesian grid method with transient anisotropic adaptation. *Journal of Computational Physics*, 179:469–494. doi:10.1006/jcph.2002.7067.

Harper, E. Y. and Chang, I. D. (1968). Maximum dissipation resulting from lift in a slow viscous shear flow. *J. Fluid Mech.*, 33:209–225.

Henn, D. S. and Sykes, I. (1999). Large-eddy simulation of flow over wavy surfaces. *Journal of Fluid Mechanics*, 383:75–112.

Hirai, Y., Yamaguchi, S., Shimizu, Y., and Kimura, I. (2011). A hydraulic experiment on small-scale bed topography in the flow-rate increase and decrease processes. In *River, Coastal and Estuarine Morphodynamics, RCEM2011*, pages 1780–1788.

Hosoda, T. and Tada, A. (1994). Free surface profile analysis on open channel flows by means of 1-D basic equations with effect of vertical acceleration. *Annu. J. Hydraul. Eng. JSCE*, 558(38):457–462.

Hunt, J. C. R., Wray, A. A., and Moin, P. (1988). Eddies, streams and convergence zones in turbulent flows. CTR Annual Research Briefs NASA Ames, Stanford University.

Iaccarino, G. and Verzicco, R. (2003). Immersed boundary technique for turbulent flow simulations. *Applied Mechanics Review*, 56(3):331–347.

Itakura, T., Yamaguchi, Y., Shimizu, Y., Kishi, T., and Kuroki, M. (1986). Observation of bed topography during the 1981-flood in the Ishikari River. *J. Hydrosci. Hydraul. Eng.*, 4(2):11–19.

Iwagaki, Y. (1956). Fundamental study on critical tractive force. *Trans. Jap. Soc. Civ. Eng.*, 41:1–21.

Izumi, N., Kawamura, S., and Igarashi, A. (2003). Experiments on the transition between dune and flat bed regimes. In *Proc. of Int. Conf. on Riv. Cosast. Est. Morph., RCEM*, pages 643–651.

Jackson, R. G. (1976). Sedimentological and fluid dynamic implications of the turbulence bursting phenomenon in geophysical flows. *J. Fluid Mech.*, 77:531–560.

Jang, C. L. and Shimizu, Y. (2005). Numerical simulation of relatively wide, shallow channels with erodible banks. *J. Hydraul. Eng.*, 131(7):565–575.

Jerolmack, D. J. and Mohrig, D. (2005). A unified model for subaqueous bed form dynamics. *Water Resour. Res.*, 41. W12421, doi:10.1029/2005WR004329.

Ji, Z. and Mendoza, C. (1997). Weakly nonlinear stability analysis for dune formation. *J. Hydraul. Eng.*, 123(11):979–985.

Julien, P. Y. and Klaassen, G. J. (1995). Sand-dune geometry of large rivers during floods. *Journal of Hydraulic Engineering*, 121(9):657–63.

Julien, P. Y., Klaassen, G. J., Ten Brinke, W. B. M., and Wilbers, A. W. E. (2002). Case Study: Bed resistance of Rhine River during 1998 flood. *J. Hydraul. Eng.*, 128(12):1024–50.

Karim, F. (1999). Bed-form geometry in sand-bed flows. *J. Hydraul. Eng.*, 125(12).

Kennedy, J. F. (1963). The mechanics of dunes and antidunes in erodible-bed channels. *Journal of Fluid Mechanics*, 16:521–544.

Kim, J., Kim, D., and Choi, H. (2001). An immersed-boundary finite-volume method for simulations of flow in complex geometries. *Journal of Computational Physics*, 171:132–150.

Kim, J., Moin, P., and Robert, M. (1987). Turbulence statistics in fully developed channel flow at low Reynolds number. *Journal of Fluid Mechanics*, 177:133–166.

Kirkpatrick, M. P., Armfield, S. W., and Kent, J. H. (2003). A representation of curved boundaries for the solution of the NavierStokes equations on a staggered three-dimensional Cartesian grid. *Journal of Computational Physics*, 184:1–36.

Kishi, T. and Kuroki, M. (1972). Bedforms and resistance to flow in erodible-bed channels (I). *Bull. Fac. Eng. Hokkaido Univ.*, 67:1–23.

Klaassen, G. J. (1990). Experiments with gradded sediments in a straight flume. Technical Report Q788 Vol. A and B, Delft Hydraulics.

Kleinhans, M. G. and van Rijn, L. (2002). Stochastic prediction of sediment transport in sand-gravel bed rivers. *Journal of Hydraulic Engineering, ASCE*, 128(4):412–425.

Kobayashi, N. and Madsen, O. S. (1985). Formation of ripples in erodible channels. *Earth Sci. Rev.*, 29:131–144.

Koh, E. P. C., Tsai, H. M., and Liu, F. (2003). Euler solution using Cartesian grid with least squares technique. In *41th AIAA Aerospace Sciences Meeting and Exhibit*, AIAA-2003-1120, Reno, Nevada.

Kreplin, H. and Eckelmann, H. (1979). Behavior of the three fluctuating velocity components in the wall region of a turbulent channel flow. *Physics of Fluids*, 22:1233.

Ku, H. C., Hirsh, R. S., and Taylor, T. D. (1987). A pseudospectral method for solution of the three-dimensional incompressible Navier-Stokes equations. *J. Comp. Phys.*, 70:439–462.

Kurose, R. and Komori, S. (1999). Drag and lift forces on a rotating sphere in a linear shear flow. *J. Fluid Mech.*, 384:183–206.

Lapointe, M. (1992). Burst-like sediment suspension events in a sand bed river. *Earth Surf. Process. Landf.*, 17:253–270.

Lilly, D. K. (1967). The representation of small-scale turbulence in numerical simulation experiments. In *Proc, IBM Sci. Comput. Symp. on Evviron. Sci.*, IBM Form 320-1951, pages 195–210.

Ling, C. H. (1995). Criteria for incipient motion of spherical sediment particles. *Journal of Hydraulic Engineering*, 121(6):472–478.

Lisle, T. E., E., P. J., Ikeda, H., Iseya, F., and Kodama, Y. (1997). Evolution of a sediment wave in an experimental channel. *Water Resources Research*, 33:1971–81.

Maaß, C. and Schumann, U. (1996). Direct numerical simulation of separated turbulent flow over a wavy boundary. In Hirschel, E. H., editor, *Flow simulation with high performance computers*, volume 52 of *Notes on numerical fluid mechanics*, pages 227–241.

Maddux, T. B., McLean, S. R., and Nelson, J. M. (2003a). Turbulent flow over three-dimensional dunes: 2. Fluid and bed stresses. *J. Geophys. Res.*, 108(F1). doi:10.1029/2003JF000018.

Maddux, T. B., Nelson, J. M., and McLean, S. R. (2003b). Turbulent flow over three-dimensional dunes: 1. Free surface and flow response. *J. Geophys. Res.*, 108(F1). doi:10.1029/2003JF000017.

Mahallati, A. and Militzer, J. (1993). Application of the piecewise parabolic finite analytic method to the three-dimensional cavity flow. *Numerical Heat Transfer, Part B*, 24:337–351.

Mandal, J. C. and Subramanian, J. (2008). On the link between weighted least-squares and limiters used in higher-order reconstructions for finite volume computations of hyperbolic equations. *Applied Numerical Mathematics*, 58(5):705–725.

Martin, D. F., Colella, P., and Graves, D. (2008). A cell-centered adaptive projection method for the incompressible Navier-Stokes equations in three dimensions. *Journal of Computational Physics*, 227(3):1863–1886.

Mavriplis, D. J. (2003). Revisiting the least-squares procedure for gradient reconstruction on unstructured meshes. In *16th AIAA Computational Fluid Dynamics Conference*, AIAA-2003-3986, Orlando, Florida.

Maxey, M. R. and Riley, J. J. (1983). Equation of motion for a small rigid sphere in a nonuniform flow. *Phys. Fluids*, 26(4):883–889.

McCormick, S. and Thomas, J. (1986). The fast adaptive composite grid (FAC) method for elliptic equations. *Math. Comp.*, 45:439–456.

McEwan, I. and Heald, J. (2001). Discrete particle modeling of entrainment from flat uniformly size sediment beds. *Journal of Hydraulic Engineering*, 127(7):588–597.

McLaughlin, J. B. (1991). Inertial migration of a small sphere in linear shear flows. *J . Fluid Mech.*, 224:261–274.

McLean, S. R., Nelson, J. M., and Wolfe, S. R. (1994). Turbulence structure over two-dimensional bed forms: Implications for sediment transport. *Journal of Geophysical Research*, 99(C6):12729–47.

McLean, S. R. and Smith, J. D. (1986). A model for flow over two-dimensional bedforms. *J. Hydraul. Eng.*, 112(4):300–317.

Mei, R. (1992). An approximate expression for the shear lift force on a spherical particle at finite reynolds number. *Int. J. Multlphase Flow*, 18(1):145–147.

Mendoza-Cabrales, C. (1987). *Refined modeling of shallow, turbulent flow over dunes*. Ph.d. dissertation, Colo. State Univ., Fort Collins.

Meneveau, C., Lund, T. S., and Cabot, W. H. (1996). A Lagrangian dynamic subgrid-scale model of turbulence. *J. Fluid Mech.*, 319:353–385.

Meyer-Peter, E. and Müller, R. (1948). Formulas for bed-load transport. In *Proceedings of the 2nd Meeting of the International Association for Hydraulic Structures Research*, pages 39–64.

Mittal, R., Dong, H., Bozkurttas, M., Najjar, F., Vargas, A., and von Loebbecke, A. (2008). A versatile sharp interface immersed boundary method for incompressible flows with complex boundaries. *Journal of Computational Physics*, 227:482552.

Mohd-Yusof, J. (1997). Combined immersed boundaries/B-splines methods for simulations of flows in complex geometries. CTR Annual Research Briefs, NASA Ames/Stanford University, Stanford.

Morsi, S. A. and Alexander, A. J. (1972). An investigation of particle trajectories in two-phase flow systems. *J. Fluid Mech.*, 55(2):193–208.

Nagata, N., T. H. T. N. and Muramoto, Y. (2005). Three-dimensional numerical model for flow and bed deformation around river hydraulic structures. *Journal of Hydraulic Engineering, ASCE*, 131(12):1074–1087.

Nakagawa, H. and Tsujimoto, T. (1980). Sand bed instability due to bedload motion. *J. Hydraul. Div. Am. Soc. Civ. Eng.*, 106(12):2029–51.

Nakayama, S. and Shimizu, Y. (2001). Numerical calculation of suspended sediment over bedforms. In *Symposium on River, Coastal and Estuarine Morphodynamics*, Int. Assoc. for Hydraul. Res., Obihiro, Japan.

Nelson, J. and Smith, J. D. (1989). Mechanics of flow over ripples and dunes. *J. Geophys. Res.*, 94(C6):8146–62.

Nelson, J. M., Logan, B. L., Kinzel, P. J., Shimizu, Y., Giri, S., Shreve, R. L., and McLean, S. R. (2011). Bedform response to flow variability. *Earth Surf. Process. Landforms*, 36:1938–1947.

Nelson, J. M., McLean, S. R., and Wolfe, S. R. (1993). Mean flow and turbulence over two-dimensional bedforms. *Water Resources Research*, 29:3935–53.

Nelson, J. M., Shimizu, Y., Giri, S., Logan, B. L., Konzel, P. J., Shreve, R. L., and McLean, S. R. (2008). Bedform response to flow variability. In Parsons, D., Garlan, T., and Best, J., editors, *Third International Workshop on Marine and River Dune Dynamics*, pages 241–248, Leeds, U.K. University of Leeds.

Nelson, J. M., Shreve, R. L., McLean, S. R., and Drake, T. G. (1995). Role of near-bed turbulence structure in bed load transport and bed form mechanics. *Water Resources Research*, 31(8):2071–2086.

Nezu, I. and Nakagawa, H. (1993). *Turbulence in Open-Channel Flows*, page 281. A. A. Balkema, Brookfield, Vt.

Niemann, S. L., Fredsø e, J., and Jacobsen, N. G. (2011). Sand dunes in steady flow at low Froude numbers: Dune height evolution and flow resistance. *Journal of Hydraulic Engineering*, 137(1):5–14.

Olsen, N. R. B. (2003). 3D CFD modeling of a self-forming meandering channel. *J. Hydraul. Eng.*, 129(5):366–372.

Onda, S. and Hosoda, T. (2004). Numerical simulation on development process of dunes and flow resistance. In *Proceeding of River Flow 2004*, volume 1, pages 245–52, Napoli, Italy.

Oosterlee, C. W. (1997). A GMRES-based plane smoother in multigrid to solve 3D anisotropic fluid flow problems. *Journal of Computational Physics*, 130(1):41–53.

Paarlberg, A. J., Dohmen-Janssen, C. M., Hulscher, S. J. M. H., and P., T. (2009). Modeling river dune evolution using a parameterization of flow separation. *Journal of Geophysical Research*, 114. F01014, doi:10.1029/2007JF000910.

Paintal, A. (1971). Concept of critical shear stress in loose boundary open channels. *J. Hydraul. Res.*, 9(1):91–113.

Pan, D. (2006). An immersed boundary method for incompressible flows using volume of body function. *Int. J. Numer. Meth. Fluids*, 50:733–750.

Papanicolaou, A., Diplas, P., Dancey, C., and Balakrishnan, M. (2001). Surface roughness effects in near-bed turbulence: Implications to sediment entrainment. *J. Eng. Mech.*, 127(3):211–218.

Papanicolaou, A. N., Diplas, P., Evaggelopoulos, N., and Fotopoulos, S. (2002). Stochastic incipient motion criterion for spheres under various bed packing conditions. *Journal of Hydraulic Engineering*, 128(4):369–380.

Paphitis, D. (2001). Sediment movementunder unidirectional flows: An assessment of empirical threshold curves. *Coastal Engineering*, 43:227–245.

Pereira, V. D. and Silva, J. B. C. (2005). Simulations of incompressible fluid flows by a least squares finite element method. *J. of the Braz. Soc. of Mech. Sci. & Eng.*, 100(3):274–282.

Polatel, C. (2006). *Large-scale roughness effect on free-surface and bulk flow characteristics in open-channel flows*. Phd thesis, Iowa Institute of Hydraulic Research, The Univ. of Iowa, Ames, Iowa.

Pope, S. B. (2004). *Turbulent flows*. Cambridge University Press.

Quirk, J. J. (1994). An alternative to unstructured grids for computing gas dynamic flows around arbitrary complex two-dimensional bodies. *Computer & Fluids*, 23:125–142.

Raudkivi, A. J. (1997). Ripples on stream bed. *Journal of Hydraulic Engineering*, 123:58–64.

Raudkivi, A. J. and Witte, H. H. (1990). Development of bed features. *J. Hydraulic Eng.*, 116(9):1063–1079.

Richards, K. J. (1980). The formation of ripples and dunes on an erodible bed. *Journal of Fluid Mechanics*, 99(3):597–618.

Richards, K. J. and Taylor, P. A. (1981). A numerical model of flow over bedforms in water of finite depth. *Geophys. J. R. Astron. Soc.*, 65:103–128.

Roden, J. E. (1998). *The sedimentology and dynamics of mega-dunes, Jamuna River, Bangladesh*. PhD thesis, Department of Earth Sciences and School of Geography, University of Leeds, Leeds, UK.

Rouse, H. (1937). Modern conceptions of the mechanics of fluid turbulence. *Trans. A.S.C.E.*, 102:463–543.

Rubinow, S. I. and Keller, J. B. (1961). The transverse force on a spinning sphere moving in a viscous fluid. *J. Fluid Mech.*, 11:447–459.

Russell, D. and Wang, Z. J. (2003). A Cartesian grid method for modeling multiple moving objects in 2D incompressible viscous flow. *Journal of Computational Physics*, 191:177–205.

Saad, Y. (2003). *Iterative methods for sparse linear systems*. SIAM.

Saffman, P. G. (1965). The lift on a small sphere in a slow shear flow. *J. Fluid Mech.*, 22(2):385–400.

Sawai, K. (1988). Transformation of sand waves due to the time change of flow conditions. *J. Hydrosci. Hydraul. Eng.*, 5(2):1–14.

Schindler, R. J. and Robert, A. (2005). Flow and turbulence structure over ripple-dune transition: An experiment under mobile bed condition. *Sedimentology*, 52:627–649.

Schmeeckle, M. W. and Nelson, J. M. (2003). Direct numerical solution of bedload transport using local, dynamic boundary condition. *Sedimentology*, 50:279–301.

Schmeeckle, M. W., Nelson, J. M., Pitlick, J., and Bennett, J. P. (2001). Interparticle collision of natural sediment grains in water. *Water Resources Research*, 37(9):2377–2391.

Schmeeckle, M. W., Shimizu, Y., Hoshi, K., Baba, H., and Ikezaki, S. (1999). Turbulent structures and suspended sediment over two-dimensional dunes. In *River, Coastal and Estuarine Morphodynamics*, Proceedings International Association for Hydraulic Research Symposium, pages 261–270.

Shields, A. (1936). Anwendung der Ähnlichkeitsmechanik und Turbulenzforschung auf die Geschiebebewegung. *Mitteilunger der Preussischen Versuchsanstalt für Wasserbau und Schiffbau*, 26:5–24.

Shimizu, Y. (2002). A method for simultaneous computation of bed and bank deformation of a river. In *International Conference on Fluvial Hydraulics*, Louvainla-Neuve, Belgium. Univ. Catholique de Louvain.

Shimizu, Y., Giri, S., Yamaguchi, S., and Nelson, J. (2009). Numerical simulation of duneflat bed transition and stage-discharge relationship with hysteresis effect. *Water Resources Research*, 45. W04429, doi:10.1029/2008WR006830,.

Shimizu, Y. and Itakura, T. (1989). Calculation of bed variation in alluvial channel. *J. Hydraul. Eng.*, 115(3):367–384.

Shimizu, Y., Schmeeckle, M. W., and Nelson, J. M. (2001). Direct Numerical Simulation of turbulence over two-dimensional dunes using CIP method. *Journal of Hydraulic Engineering*, 19:85–92.

Sieben, J. and Talmon, A. M. (2011). Bed-load transport in obliquely dune-covered riverbeds. *Journal of Hydraulic Research*, 49(3):317–324.

Simons, D. B. and Richardson, E. V. (1966). Resistance to flow in alluvial channels. *USGS Professional Paper*, 422-J:1–61.

Simons, D. B., Richardson, E. V., and Albertson, M. L. (1961). Flume studies using medium sand (0.45 mm). *USGS Professional Paper*, 1498-A:1–76.

Smith, J. D. (1970). Stability of a sand bed subjected to shear flow of low Froude numbers. *J. Geophys. Res.*, 75:5928–40.

Southard, J. B. and Boguchwal, L. (1990). Bed configurations in steady unidirectional water flow part 2. Synthesis of flume data. *Journal of Sedimentary Petrology*, 60:658–679.

Stoesser, T., Braun, C., Garcia-Villalba, M., and Rodi, W. (2008). Turbulence structures in flow over two-dimensional dunes. *Journal of Hydraulic Engineering,*, 134(1):42–55.

Sumer, B. M. and Bakioglu, M. (1984). Formation of ripples on an erodible bed. *Journal of Fluid Mechanics*, 144.

Ten Brinke, W. B. M., Wilbers, A. W. E., and Wesseling, C. (1999). Dune growth, decay and migration rates during a large-magnitude flood at a sand and mixed sand-gravel bed in the Dutch Rhine river system. In Smith, N. D. and Rogers, J., editors, *Fluvial Sedimentology VI*, volume 28 of *Spec. Publs Int. Ass. Sedimentol.*, pages 15–32.

Thomas, J., Diskin, B., and Brandt, A. (1999). Textbook multigrid efficiency for the incompressible Navier-Stokes equations: High Reynolds number wakes and boundary layers. Tech. rep. 99-51, ICASE.

Thompson, M. and Ferziger, J. (1989). An adaptative multigrid technique for the incompressible Navier-Stokes equations. *Journal of Computational Physics*, 82:94–121.

Tjerry, S. and Fredsøe, J. (2005). Calculation of dune morphology. *J. Geophys. Res.*, 110. F04013, doi:10.1029/2004JF000171.

Tritton, D. J. (1959). Experiments on the flow past a circular cylinder at low Reynolds numbers. *Journal of Fluid Mechanics*, 6(4):547–567.

Trottenberg, U., Oosterlee, C. W., and Schüller, A. (2001). *Multigrid*. Academic Press.

Tseng, Y. H. and Ferziger, J. H. (2003). A ghost-cell immersed boundary method for flow in complex geometry. *Journal of Computational Physics*, 192:593–623.

Tuijnder, A. P., Ribberink, J. S., and Hulscher, S. J. M. H. (2009). An experimental study into the geometry of supply-limited dunes. *Sedimentology*, 56:1713–1727.

Udaykumar, H. S., Mittal, R., Rampunggoon, P., and Khanna, A. (2001). A sharp interface Cartesian grid method for simulating flows with complex moving boundaries. *Journal of Computational Physics*, 174:345–380.

Van der Mark, C. F. (2009). *A semi-analytical model for form drag of river bedforms*. Phd thesis, Twente University, Twente, the Netherlands.

Van der Mark, C. F., Blom, A., and H., H. S. J. M. (2008). Quantification of variability in bedform geometry. *Journal of Geophysical Research*, 113. F03020, doi:10.1029/2007JF000940.

Van Prooijen, B. C. (2010). On the erosion of non-cohesive sediment. Personal communication.

Van Rijn, L. C. (1984a). Sediment pick-up function. *Journal of Hydraulic Engineering*, 110(10):1494–1502.

Van Rijn, L. C. (1984b). Sediment transport, part I: Bed load transport. *Journal of Hydraulic Engineering*, 110:1431–56.

Van Rijn, L. C. (1984c). Sediment transport, part III: Bed forms and alluvial roughness. *Journal of Hydraulic Engineering*, 110(12):1733–54.

Vanka, S. P. (1986). Block-implicit multigrid solution of Navier-Stokes equations in primitive variables. *Journal of Computational Physics*, 65:138–158.

Vanoni, V. A. and Hwang, L. S. (1967). Relation between bed forms and friction in streams. *J. Hydr. Div.*, 93:121–144.

Vendetti, J. G. and Bennett, S. J. (2000). Spectral analysis of turbulent flow and suspended sediment transport over dunes. *J. Geophys. Res.*, 105:22035–47.

Venditti, J. G. and Michael, C. (2005). Morphodynamics of small-scale superimposed sand waves over migrating dune bed forms. *Water Resources Research*. doi:10.1029/2004WR003461.

Wannier, G. H. (1950). A contribution to the hydrodynamics of lubrication. *Quart. Appl. Math.*, 8:1–32.

Waymel, F., Monnoyer, F., and William-Louis, M. J. P. (2006). Numerical simulation of the unsteady three-dimensional flow in confined domains crossed by moving bodies. *Computers & Fluids*, 35:525–543.

Wesseling, P. (2000). *Principles of computational fluid dynamics*. Springer.

Wesseling, P. (2004). *An introduction to multigrid methods*. R.T. Edwards INC.

Wewetzer, S. F. K. and Duck, R. (1999). Bedforms of the middle reaches of the Tay Estuary, Scotland. In Smith, N. D. and Rogers, J., editors, *Fluvial Sedimentology VI*, volume 28 of *Spec. Publs Int. Ass. Sedimentol.*, pages 33–41.

White, C. M. (1940). The equilibrium of grains on the bed of a stream. *Phil. Trans. Royal Soc.*, 174A:322–338.

Wiberg, P. L. and Smith, J. D. (1987). Calculations of the critical shear stress for motion of uniform and heterogeneous sediments. *Water Resources Research*, 23(8):1471–80.

Wilbers, A. (2004). *The development and hydraulic roughness of river dunes*. PhD thesis, University of Utrecht, Utrecht, The Netherlands.

Wu, F. C. and Chou, Y. J. (2003). Rolling and lifting probabilities for sediment entrainment. *Journal of Hydraulic Engineering*, 129(2):110–119.

Xu, S. and Wang, Z. J. (2006). An immersed interface method for simulating the interaction of a fluid with moving boundaries. *Journal of Computational Physics*, 216:454–493.

Yalin, M. S. (1964). Geometrical properties of sand waves. *J. Hydr. Eng. Div.*, 90:105–109.

Yalin, M. S. (1992). *River Mechanics*, page 219. Elsevier, New York.

Yamaguchi, S. and Izumi, N. (2002). Weakly nonlinear stability analysis of dune formation. In Bousmar, D. and Zech, Y., editors, *Proceedings of the International Conference on Fluvial Hydraulics*, pages 843–850, Swets and Zeitlinger, Lisse, Netherlands.

Yamaguchi, S. and Izumi, N. (2003). Weakly nonlinear analysis of dunes including suspended load. In Sánchez-Arcilla, A. and Bateman, A., editors, *Proceedings of the 3rd IAHR Symposium on River, Coastal and Estuarine Morphodynamics*, pages 172–183, Madrid.

Yamaguchi, S. and Izumi, N. (2005). Weakly nonlinear analysis of dunes by the use of a sediment transport formula incorporating the pressure gradient. In *4th IAHR Symposium on River, Coastal and Estuarine Morphodynamics*, Int. Assoc. for Hydraul. Res., Urbana,Il.

Yang, J. and Balaras, E. (2006). An embedded-boundary formulation for large-eddy simulation of turbulent flows interacting with moving boundaries. *Journal of Computational Physics*, 215:12–40.

Ye, T., Mittal, R., Udaykumar, H. S., and Shyy, W. (1999). An accurate Cartesian grid method for viscous incompressible flows with complex immersed boundaries. *Journal of Computational Physics*, 156:209–240.

Yoon, J. Y. and Patel, V. C. (1996). Numerical model of turbulent flow over sand dune. *Journal of Hydraulic Engineering*, 122(1):10–17.

Yue, W., Lin, C. L., and Patel, V. C. (2005). Large Eddy Simulation of turbulent open-channel flow with free surface simulated by level set method. *Physics of Fluids*, 17. doi:10.1063/1.1849182.

Yue, W., Lin, C. L., and Patel, V. C. (2006). Large-Eddy Simulation of turbulent flow over a fixed two-dimensional dune. *Journal of Hydraulic Engineering*, 132(7):643–51.

Zanke, U. (1990). Der Beginn der Sedimentbewegung als Wahrscheinlichkeitsproblem (The start of sediment motion as a probability problem). *Wasser + Boden*, 42(1):40–43.

Zedler, E. A. and Street, R. L. (2001). Large-Eddy Simulation of sediment transport: Currents over ripples. *Journal of Hydraulic Engineering*, 127:444–52.

Zeeuw, D. D. and Powell, K. G. (1993). An adaptive refined Cartesian mesh solver for the Euler equations. *Journal of Computational Physics*, 104:56–68.

Zijlema, M., Segal, A., and Wesseling, P. (1995). Finite volume computation of incompressible turbulent flows in general coordinates on staggered grids. *Int. J. Numer. Meth. Fluids*, 20:621–640.

Appendix A

Drag coefficient

According to Figure (3.1), Morsi and Alexander (1972) derived the following relations for the drag coefficient.

$$
\begin{aligned}
&C_D = 24.0/Re && ; && Re < 0.1 \\
&C_D = 3.69 + 22.73/Re + 0.0903/Re^2 && ; && 0.1 < Re < 1 \\
&C_D = 1.222 + 29.1667/Re - 3.8889/Re^2 && ; && 1 < Re < 10 \\
&C_D = 0.6167 + 46.5/Re - 116.67/Re^2 && ; && 10 < Re < 100 \\
&C_D = 0.3644 + 98.33/Re - 2778/Re^2 && ; && 100 < Re < 1000 \\
&C_D = 0.357 + 148.62/Re - 4.75 \times 10^4/Re^2 && ; && 1000 < Re < 5000 \\
&C_D = 0.46 - 490.546/Re + 57.87 \times 10^4/Re^2 && ; && 5000 < Re < 10000 \\
&C_D = 0.5191 - 1662.5/Re + 5.4167 \times 10^6/Re^2 && ; && 10000 < Re < 50000
\end{aligned}
$$

Appendix B

Particle relaxation time

Based on experimental results of Morsi and Alexander (1972), the drag coefficient for $Re < 1$ can be defined as

$$C_D = \frac{24}{Re} = \frac{24\mu}{\rho d v_p} \tag{B.1}$$

This is the Stokes's law where Re is the Reynolds number, ρ and μ are the density and viscosity of flow, d is the particle diameter, and v_p is the particle velocity relative to the flow. For a spherical particle under Stokes's law, which is generally valid for the sediment particles in the ambient flow the drag force is

$$F_D = 3\pi\mu d v_p \tag{B.2}$$

Assumptions for the above relationships:

1. The particles are rigid spheres.
2. Stokes's law or inertial force is much smaller than viscous force.
3. The fluid is continuum.
4. The flow is without wall effects.
5. The density of the flow is constant.
6. The flow is in steady state.

The particle velocity in a still air when released from rest can be derived as (based on Newton's second law):

$$m_p \frac{dv_p}{dt} = m_p g - F_D = m_p g - 3\pi\mu d v_p \tag{B.3}$$

By integration of Equation (B.3), considering $v_p(t = 0) = 0$,

$$v_p = \frac{\rho_p d^2 g}{18\mu}\left(1 - e^{-t/\tau_p}\right) \tag{B.4}$$

where

$$\tau_p = \frac{\rho_p d^2}{18\mu} \tag{B.5}$$

is the particle relaxation time. Thus, particle relaxation time characterizes the time required for a particle to adjust or relax its velocity to a new condition of forces. It is an indication of the particle ability to quickly adjust to a new environment or condition. It depends on the mass and mechanical mobility of the particle, and is not affected by the external forces acting on the particle.

List of Symbols

Roman Symbols

a_i	polynomials coefficient	–
b	the width of 3D dunes	m
c_f	total drag coefficient	–
C_{frac}	a multiplication factor equal or smaller than unity	–
C_D	drag coefficient	–
C_L	lift coefficient	–
$C_{L,Sa}$	Saffman's lift coefficient	–
C_m	added mass coefficient	–
C_s	Smagorinsky's constant	–
c'_f	grain drag coefficient	–
c''_f	form drag coefficient	–
c'''_f	form drag coefficient for 3D dunes	–
d	sediment particle diameter	m
e_{ij}	stress tensor (various uses) or	kg/ms^2
e_{ij}	error tensor for SGS model	m^2/s^2
f_i	volume force on flow in x_i direction	N
F_0	an empirical constant	–
F_{add}	added mass force	N
F_{drag}	drag force	N
F_G	submerged weight	N
F_L	lift force	N
F_n	normal force	N
F_t	tangential force	N
Fr	Froude number	–
g	gravitational acceleration	m/s^2
h	water depth	m
J	empirical variable for lift coefficient	–
k_s	roughness height	m
L_{ij}	Germano identity tensor	m^2/s^2
$\vec{n}$	normal unit vector	–
n_{depos}	number of deposited particles	–
n_{pickup}	number of picked up particles	–
m_p	mass of particle	kg

p	pressure	N/m^2
P_d	sediment deposition rate	s^{-1}
P_S	dimensional pick-up rate	s^{-1}
P_S^*	dimensionless pick-up rate	–
$P_{S,in}$	volumetric sliding sediment transport to a cell	m^3
$P_{S,out}$	volumetric sliding sediment transport from a cell	m^3
Q	turbulent coherent structure function	s^{-2}
R_h	hydraulic radius	m
Re_p	particle Reynolds number	–
Re_α	shear Reynolds number	–
Re_Ω	rotational particle Reynolds number	–
s	distance between pick-up and deposition points	m
S	area of a cell on the bed (various uses) or	m^2
S	symmetric component of Δu	s^{-1}
S_{ij}	strain rate tensor	s^{-1}
t	time	s
T	time scale (various uses) or	s
T	duration cycle of a hydrograph	s
u^+	non-dimensional parallel velocity to wall	–
u_b	bulk velocity	m/s
u_f	flow velocity in particle level	m/s
u_i	velocity component in x_i direction	m/s
u_r	relative velocity of particle to flow	m/s
U	average velocity	m/s
U_∞	far-field stream velocity	m/s
v_p	particle velocity	m/s
V_p	volume of particle	m^3
V_E	parameterized volumetric pickup rate	m^3/s
V_S	computed volumetric pickup rate	m^3/s
x_i	coordinates	m
y_b	bed elevation	m
y_{new}	bed level after deformation	m
y_{old}	bed level before deformation	m
z^+	non-dimensional normal distance to wall	–
z_0	roughness length	m

Greek symbols

α	shear rate of the mean flow	s^{-1}
α^*	dimensionless shear	–
β	a coefficient for crest amplitude (various uses) or	–
β	proportionality variable	–
δ	dune height	m
δ_{ij}	Kronecker delta	–

δp	pressure correction scalar	N/m^2
Δ	filter length	–
Δt	time step	s
ε	$= Re_\alpha^{0.5}/Re_p$	–
θ	angle of lee side (various uses) or	degree
θ	angle of separation	degree
κ	von Kármán constant	–
λ	dune length (various uses) or	m
λ	porosity factor	–
λ_G	drag correction factor for geometry effects	–
λ_θ	drag correction factor for angle of lee side	–
λ_β	drag correction factor for crest line curvature	–
λ_b	drag correction factor for dune width	–
Λ	mean step length	m
μ	dynamic viscosity	kg/ms
ν	kinematic viscosity	m^2/s
ν_t	turbulent viscosity	m^2/s
ξ	a scalar	–
ρ	fluid mass density	kg/m^3
ρ_p	particle mass density	kg/m^3
ρ_s	mass density of the sediment	kg/m^3
τ_*	dimensionless local bed shear stress	–
τ_{cr}^*	dimensionless critical shear stress	–
τ_b	boundary shear stress	N/m^2
τ_{ij}	sub-grid-scale stress	m^2/s^2
τ_p	particle relaxation time	s
τ_T	bed shear stress	N/m^2
φ	angle of particle rotation (various uses) or	degree
φ	scalar	–
ϕ	angle of repose	degree
Ω	rotation angular particle velocity (various uses) or	rad/s
Ω	antisymmetric component of Δu	s^{-1}

Mathematics

C	spatial advection operator
D	spatial diffusion operator
G	spatial operator for pressure

Abbreviations

2D	two-dimensional
3D	three-dimensional
BiCGStab	Biconjugate Gradient Stabilized method
CFL	Courant Friedrichs Lewy
CIP	Cubic-Interpolated Pseudo-particle
DNS	Direct Numerical Simulation
FAC	Fast Adaptive Composite grid
FAS	Full Approximation Storage
GMRES	Generalized Minimal Residual method
IMEX	Implicit-Explicit method
MLAT	Multi-Level Adaptive refinement Techniques
RANS	Reynolds-Averaged Navier-Stokes
RHS	Right Hand Side
SGS	Sub-Grid Scale
TKE	Turbulent Kinetic Energy
URANS	Unsteady Reynolds-Averaged Navier-Stokes

List of Figures

List of Tables

Acknowledgements

This doctoral dissertation is a final product of the work done in several years at the Section of Hydraulic Engineering, Delft University of Technology (TUDelft), where I benefited a lot from the inspiring and friendly atmosphere, for which I am greatly indebted to many people, who have inspired and supported me during my studies.

My great gratitude addresses to Prof. Huib de Vriend, my promoter, for his guidance and giving me the continues support and providing me freedom to trying out new ways in doing research. I highly appreciate his profound knowledge and precious input into our research works, his encouragement and their constant help. I also would like to express my great gratitude to dr. Erik Mosselman and dr. Kees Sloff, my copromoter and supervisor, for their constant help and giving me direction, freedom and contentious encouragement.

I am very grateful to Prof. Yasuyuki Shimizu for his support, advices and providing me all facilities during my stay in Japan. During my stay in his laboratory I gained a strong background on morphodynamics and obtained my first results on dune simulation. Moveover, I would like to thank him for his challenges providing me Postdoctoral position in his lab and giving me freedom, encourage and direction in doing research.

I would like to thank Dr. Ichiro Kimura for his continuous help, scientific discussions, and cooperation. He is not only a good colleague, but also a good friend, who helped me very much before and during my stay in Japan.

I would like to express my gratitude to dr. Sanjay Giri, from whom I could get both great mentorship and friendship, for sharing his ideas and detailed advices on morphodynamics. He spent his R&D hours as well as his free time to gives me direction in my research work. His input has been helpful to shape my research.

I known dr. Jonathan Nelson as a scientific, colleague and a friend. We spent nice periods during conferences as well as during his stay in Netherlands. He always encouraged me and gave me new ideas in my work.

I would like to thank Dr. Rafid Al-Khoury for his contentious help, reviewing my reports and giving me new ideas.

The financial support for this PhD project came from Delft Cluster project ”Safety against flooding”, financed by the Netherlands government and supported by Rijkswaterstaat Waterdienst. I would like to appreciate their support.

I am indebted to many of my colleagues to support me. I would like to show my gratitude to Marcel Zijlma, Guus Stelling, Robert Jan Labeur, Wim Uijttewaal and Kees Oosterlee for supporting me and give me continue help in my research.

At last but not at least, special thanks goes to my colleagues who supported me directly and indirectly in my work, Willem Ottevanger, Wei Li, Bram van Prooijen, and Shahid Ali for our scientific discussions, and all other colleagues who made a friendly atmosphere during my PhD period.